

On the Role of Nitride and Oxide Supports for the Charge State of Isolated Palladium Catalysts

Dissertation

zur

Erlangung des akademischen Grades

Doktor rerum naturalium (Dr. rer. nat.)

der Mathematisch-Naturwissenschaftlichen Fakultät

der Universität Rostock

vorgelegt von

Junhao Huang

Geb. am 27. Januar 1994 in Shandong, China

Die vorliegende Arbeit wurde am Leibniz-Institut für Katalyse e. V. an der Universität Rostock unter der Leitung von Prof. Dr. Jennifer Strunk (Abteilungsleiterin „Heterogene Photokatalyse“) in der Zeit von Januar 2020 bis April 2023 angefertigt.

The present work was accomplished at the Leibniz Institute for Catalysis e. V. at the University of Rostock under the supervision of Prof. Dr. Jennifer Strunk (Head of the Department “Heterogeneous Photocatalysis”) during the period from January 2020 to April 2023.

Gutachter

Prof. Dr. Jennifer Strunk, Leibniz-Institut für Katalyse e.V., Rostock, Germany

Prof. Dr. Alexander A. Auer, Max-Planck-Institut für Kohlenforschung, Germany

Dr. Andrew Logsdail, Cardiff University, UK

Datum der Einreichung: 17. April 2023

Datum der Verteidigung: 21. November 2023

Erklärung der Urheberschaft

Hiermit erkläre ich, dass ich diese Dissertation selbstständig verfasst und keine anderen als die im Literaturverzeichnis aufgeführten und als Referenzen gekennzeichneten Quellen benutzt habe. Diese Arbeit wurde bisher keinem anderen Prüfungsausschuss zur Bewertung vorgelegt.

I hereby declare that I have written this doctoral thesis independently and that I have not used any sources other than those listed in the bibliography and identified as references. This thesis was not previously presented to any other examination board for assessment.

Place, date, signature

Rostock, 17.04.2023, Junhao Huang

Acknowledgement

I would like to express my gratitude to my esteemed supervisor Prof. Jennifer Strunk for your invaluable advice, continuous support, and patience during the course of my PhD study. Thank you for offering me plenty of opportunities to communicate and exchange ideas with the catalysis community and for providing an environment where I could thrive as an independent researcher. I am so glad to have been a part of your research group, and I am sure that our cooperation in the scientific field will continue in the future.

I would like to extend my gratitude to the Leibniz Institute for Catalysis for providing me a scholarship to complete my PhD studies. I would also like to express thanks for the supportive and collaborative environment, the friendly colleagues, and the effective communication within the institute.

I would like to thank Dr. Marcus Klahn for his treasured support, which was influential in shaping my experiment methods and critiquing my results. I am grateful to Prof. Haijun Jiao and Dr. Xinxin Tian for their guidance on DFT calculations and for being very patience in helping me overcome my knowledge gaps in this area. I would also like to thank Dr. Andrew J. Logsdail at Cardiff University, from whom I have learned so much about DFT calculations. I extend my thanks to everyone from the theoretical computing teams at Cardiff University, who have greatly contributed to my understanding of this field. I would like to acknowledge the travel funding from the UK Catalysis Hub, which supported my academic visit to Cardiff University.

My sincere thanks must also go to the members of the department “Heterogeneous Photocatalysis” for their support on my research. I would like to acknowledge Dr. Tim Peppel for the SEM measurement, Dr. Norbert Steinfeldt and Michael Sebek for the advice on the laboratory instrument operation, Dr. Pawel Naliwajko for the training on FT-IR instrument, and Shuoping Ding for the help on operation of electrochemical workstation.

I would like to express my thanks to the LIKAT Analytical Services Group: Dr. Stephan Bartling for the XPS measurements, Dr. Nils Rockstroh for the STEM measurements, Dr. Henrik Lund for the XRD measurements, Reinhard Eckelt for the sorption measurements, Anja Simmula and Astrid Lehmann for the elemental analysis, Christine Rautenberg for the thermogravimetry measurements.

I am also pleased to say thanks to my collaborators. It wouldn't have been possible to conduct this research without their precious support. Thanks to Prof. Jan-Dierk Grunwaldt, Dr. Anna

Zimina, and Dr. Martin Radtke for the XAS measurements and data analysis. Thanks to Dr. Jabor Rabeah and Dr. Xingchao Dai for the EPR measurements and discussion. Thanks to Prof. Björn Corzilius and Dr. Victoria Aladin for the solid-state NMR measurements and analysis. Thanks to Prof. Zhenyu Sun and Prof. Song Hong from Beijing University of Chemical Technology, as well as Dr. Kevin Oldenburg from ELMI-MV at the University of Rostock, for their contributions to the STEM measurements and discussions. Thanks to Dr. Armin Springer from EMZ at the University of Rostock for the help in SEM measurements.

I would like to say thanks to all my friends and colleagues for their help and support over the past three years. I will always remember the moments we spent together and the accomplishments we celebrated together.

In the end, I would like to express my grateful thanks to my parents, who gave me enough moral support, encouragement, and motivation to achieve my personal goals.

Abstract

Heterogeneous palladium catalysts have gained enormous relevance in various applications, particularly in organic coupling synthesis, hydrogen detection, purification, and storage. However, the price of Pd remains above economically feasible levels for large-scale commercial applications. Isolated Pd catalysts have the potential to provide superior and cost-effective solutions to meet the requirements of present and evolving thermochemical, photochemical and electrochemical applications. In this thesis, a series of isolated Pd catalysts were constructed, and the effect of supports types (oxide and nitride supports) on the charge state of the Pd center was thoroughly investigated.

The first section of the thesis focuses on the modification of polymeric carbon nitride (PCN) to create a nanosheet structure with a large surface area, which will be taken as support for anchoring isolated Pd atoms. Exfoliation of PCN into a 2D nanosheet structure could enhance its surface activity and lead to unique optical and electrical properties. Four common exfoliation strategies (liquid ultrasonication, thermal oxidation, hydrothermal oxidation, and chemical oxidation) were adopted, and their effects on the structural and electronic changes in PCN were analyzed in detail. Depending on the exfoliation method used, different factors, such as morphology, surface area, crystal and molecular structure, band edge positions, and charge carrier generation and mobility, can be influenced. By comparing the properties of differently exfoliated PCN, conclusions can be drawn about the suitability of exfoliation methods for providing more sites for Pd deposition.

Using a simple wet impregnation method, PCN nanosheets supported isolated Pd atoms were successfully synthesized. In addition to the PCN support, three other nitride supports (hBN, Si₃N₄, and TiN) were employed for anchoring Pd atoms. For comparison, upon deposition of Pd with the same procedure, five oxides (TiO₂, ZnO, Al₂O₃, SiO₂, and B₂O₃) were used as supports to prepare Pd single-atom catalysts. By investigating the oxidation state using XAS, XPS, CO-DRIFTS, and Bader charge analysis, it was found that Pd atoms prefer to interact with surface hydroxyl groups to form Pd(OH)_x species on oxide supports, whereas on nitride supports, Pd atoms are incorporated into the surface structure in the form of Pd–N bonds. Moreover, a bridge was successfully built between the experimental oxidation state and the calculated Bader charge based on the periodic trend in electronegativity, allowing the determination of the appropriate models for understanding the coordination and electronic structure of isolated Pd catalysts.

Zusammenfassung

Die heterogene Palladiumkatalyse hat für verschiedene Anwendungen enorme Bedeutung erlangt, insbesondere für die Synthese organischer Verbindungen, sowie den Nachweis, die Reinigung und die Speicherung von Wasserstoff. Allerdings liegt der Preis für Pd nach wie vor über dem für großtechnische Anwendungen akzeptablen Niveau. Isolierte Pd-Atome haben das Potenzial, überlegene und kosteneffiziente Lösungen für die Anforderungen heutiger und künftiger thermochemischer, photochemischer und elektrochemischer Anwendungen zu bieten. Im Rahmen der Arbeit sollen isolierte Pd-Zentren hergestellt und der Einfluss verschiedener oxidischer und nitridischer Trägermaterialien auf den Ladungszustand und die nächste Umgebung des abgeschiedenen Pd-Zentrums untersucht werden.

Der erste Abschnitt der Arbeit befasst sich mit der Modifizierung des polymeren Kohlenstoffnitrids, um dünne PCN-Schichten mit hoher spezifischer Oberfläche zu erhalten, auf denen isolierte Pd-Atome verankert werden können. Daneben kann die Exfolierung in eine 2D-nm dicke Blattstruktur zu einer erhöhten Oberflächenaktivität und einzigartigen optischen und elektronischen Eigenschaften von polymerem Kohlenstoffnitrid (PCN) führen. Vier gängige Exfolierungsstrategien (Flüssigphasen-Ultraschallbehandlung, thermische Oxidation, hydrothermale Oxidation und chemische Oxidation) wurden angewandt, und ihre Auswirkungen auf die strukturellen und elektronischen Veränderungen des PCN wurden im Detail analysiert. Je nach eingesetzter Exfolierungsmethode werden die Morphologie und Oberfläche, die Kristall- und Molekülstruktur, die Bandkantenpositionen, die Ladungsträgererzeugung und -beweglichkeit unterschiedlich beeinflusst. Durch die Untersuchung der Eigenschaften von unterschiedlich exfoliertem PCN lassen sich Rückschlüsse auf die Eignung der Exfolierungsmethoden zur Erzielung einer Vielzahl von Stellen für die Pd-Abscheidung ziehen.

Mit einer einfachen Nassimprägnierungsmethode wurde atomar dispergiertes Pd auf nanometerdicken PCN-Blättern erzeugt. Außer dem PCN wurden noch drei weitere Nitridträger (hBN, Si₃N₄ und TiN) zur Aufbringung der Pd-Atome eingesetzt. Das gleiche Verfahren wurde auch zur Pd Abscheidung auf oxidischen Trägern (TiO₂, ZnO, Al₂O₃, SiO₂ und B₂O₃) angewandt, um auf deren Oberfläche isolierte Pd-Zentren zu synthetisieren. Durch die Untersuchung des Oxidationszustandes mittels XAS, XPS, CO-DRIFTS und Bader-Ladungsanalyse wurde festgestellt, dass die Pd-Atome bevorzugt mit den auf der Oberfläche vorhandenen Hydroxylgruppen interagieren, wodurch auf dem Oxidträger eine Pd(OH)_x-Spezies gebildet wird. Dagegen sind auf dem Nitridträger die Pd-Atome in Form einer Pd-N-

Bindung in die Oberflächenstruktur eingebunden. Darüber hinaus wurde erfolgreich eine Brücke zwischen dem experimentellen Oxidationszustand und der berechneten Bader-Ladung auf der Grundlage des periodischen Trends der Elektronegativität geschlagen, was die Bestimmung geeigneter Modelle für das Verständnis der koordinativen und elektronischen Struktur isolierter Pd-Katalysatoren ermöglicht.

Table of Contents

Acknowledgement	III
Abstract.....	V
Zusammenfassung.....	VI
List of Figures	X
List of Figures in the Appendix.....	XII
List of Tables.....	XVI
List of Tables in the Appendix	XVI
List of Abbreviations.....	XVII
List of Symbols	XVIII
1. Introduction	1
1.1 Catalysis with palladium	1
1.2 Introduction of palladium and palladium compounds.....	2
1.3 Synthesis of isolated Pd catalysts	4
1.4 Characterization of isolated Pd catalysts.....	4
1.5 Nitride supported isolated Pd catalysts.....	18
1.6 Oxide supported isolated Pd catalysts	19
2. Objectives and strategies of this thesis	22
2.1 Modification of PCN support through four different exfoliation strategies	22
2.2 Investigation of the role of nitride and oxide supports for the charge state of isolated Pd catalysts	24
3. Experiments and methods	25
3.1 Catalyst synthesis	25
3.1.1 Synthesis of PCN nanosheet through four exfoliation strategies	25
3.1.2 Synthesis of nitride and oxide supported isolated Pd catalysts	26
3.2 Experimental characterization.....	27
3.3 Theoretical calculation	37
3.4 Catalytic testing.....	40
3.4.1 Photocatalytic phenol degradation	40
3.4.2 Suzuki-Miyaura coupling reaction	40
4. Results and discussion.....	43
4.1 Catalyst characterization	43
4.1.1 Experimental characterization for exfoliated PCN catalysts.....	43
4.1.2 Experimental characterization for isolated Pd catalysts.....	59
4.2 Theoretical investigation	80

4.2.1 Structural investigation for exfoliated PCN catalysts	80
4.2.2 Structural investigation for isolated Pd catalysts.....	82
4.3 Catalytic activity.....	87
4.3.1 Exfoliated PCN catalysts for phenol photodegradation	87
4.3.2 Isolated Pd/PCN catalysts for Suzuki-Miyaura reaction	88
4.4 Catalytic mechanism	91
4.4.1 Mechanism of exfoliated PCN catalysts for phenol photodegradation	91
4.4.2 Mechanism of isolated Pd/PCN catalysts for Suzuki-Miyaura reaction	92
5. Summary	94
6. Outlook.....	97
List of Reference.....	99
Appendix	113
List of Writing/Experiments/Calculations to Highlight Own Work and Contributions by Other Researchers.....	154
Curriculum Vitae	156

List of Figures

Figure 1. HAADF-STEM images of isolated Pd atoms on PCN; arrows indicate location of single atoms.	9
Figure 2. Schematic illustration of regions of different CO adsorption modes in FT-IR spectroscopy.	11
Figure 3. Schematic illustration of the regions in XAS.	13
Figure 4. (a) Heptazine structures of PCN, (b) in-plane repeats between heptazine units, and (c) out of plane π - π stacking motif of the same heptazines on top of each other.	23
Figure 5. Schematic illustration of different exfoliation processes for synthesizing nanolayered PCN.	25
Figure 6. Horizontal Attenuated Total Reflectance (HATR) accessories with flow-through cell and ZnSe plate, implemented in a Nicolet iS50 FT-IR spectrometer.	30
Figure 7. Schematic representation of the ATR set-up used to monitor the Suzuki-Miyaura reaction.	31
Figure 8. DRIFTS cell with Praying Manti accessory, implemented in a Nicolet iS50 FT-IR spectrometer; the outlet is connected to QMS GAM400.	32
Figure 9. (a) Hydrogen-bonded PCN model, and (b) the sheet staggered arrangement of ideal PCN model with AB stacking with P63/mmc space group.	37
Figure 10. Schematic illustration of Pd atom and Pd nanocluster (0.5 nm) anchored on hydrogen-bonded PCN model.	38
Figure 11. Candidate binding sites for Pd atoms on a TiO ₂ anatase (101) surface.	38
Figure 12. Photocatalytic reaction set-up for phenol degradation.	40
Figure 13. Batch reaction set-up for Suzuki-Miyaura reaction.	41
Figure 14. Continuous flow reactor for Suzuki-Miyaura reaction.	42
Figure 15. Schematic representation of the continuous flow reactor set-up used for Suzuki-Miyaura reaction.	42
Figure 16. (a) TGA-MS of pristine PCN. (b) <i>In situ</i> DRIFTS spectra of PCN heated to 150 °C for 60 min (10 °C min ⁻¹) in Ar atmosphere.	43
Figure 17. Density comparison of differently exfoliated PCN. Each sample is 50 mg.	44
Figure 18. SEM images of (a) PCN, (b) t-CN, (c) c-CN, (d) u-CN and (e, f) h-CN. Scale bar, 1 μ m.	46
Figure 19. AFM images and the corresponding height profiles of pristine PCN.	46
Figure 20. AFM images and the corresponding height profiles of u-CN-16.	47
Figure 21. AFM images and the corresponding height profiles of t-CN-6.	47
Figure 22. AFM images and the corresponding height profiles of c-CN-16.	47
Figure 23. Nitrogen adsorption-desorption isotherms of differently exfoliated PCN.	48
Figure 24. (a) XRD patterns and (b) DRIFTS spectra of differently exfoliated PCN.	49
Figure 25. (a) XPS survey spectra, high-resolution XPS spectra of C1s (b) and N1s (c), and (d) VBXPS spectra of differently synthesized PCN.	52
Figure 26. (a) ¹³ C CPMAS NMR spectra at 8 kHz, recorded with the near-quantitative Multi-CP sequence,[221] and (b) ¹ H MAS NMR at 60 kHz rotational frequency of differently exfoliated PCN. * mark a impurity signal from isopropanol. (c) Chemical structures of heptazine unit. * represent atomic connectivity to the next heptazine unit.	54
Figure 27. EPR spectra of differently exfoliated PCN with (Red line) and without (Black line) the light (> 420 nm) irradiation.	55
Figure 28. UV-vis absorption spectra of t-CN (a), c-CN (b), u-CN (c) and h-CN (d), which were calculated from the reflectance data with the Kubelka-Munk function.	56
Figure 29. Bandgap calculation of differently exfoliated PCN according to Tauc's method.	57
Figure 30. Electronic band structure of differently exfoliated PCN.	58

Figure 31. (a) Transient photocurrent (I–T) curves and (b) photoluminescence (emission) spectra of differently exfoliated PCN.	59
Figure 32. UV-Vis absorption spectra of various Pd samples and their corresponding pure supports.	60
Figure 33. XRD pattern of various Pd samples and their corresponding pure supports.	61
Figure 34. TPDE patterns of various Pd samples (intensely colored line) and their corresponding pure supports (pale line) in helium atmosphere.....	62
Figure 35. Pd 3d photoemission spectra of (a) different Pd/nitride samples, (b) different Pd salts, and (c) Pd/PCN samples prepared with different Pd salts.	63
Figure 36. Pd 3d photoemission spectra of Pd/PCN samples before and after washing.	64
Figure 37. Pd 3d photoemission spectra of 2 wt% Pd/PCN-200 °C and 2 wt% Pd/PCN-400 °C.	65
Figure 38. Pd 3d photoemission spectra of Pd/oxide samples.	66
Figure 39. Pd 3d photoemission spectra of 1 wt% Pd/PCN-200 °C and 1 wt% Pd/PCN-400 °C.	66
Figure 40. Binding energy of Pd 3d _{5/2} peaks obtained from X-ray photoelectron spectra of various Pd catalysts.	67
Figure 41. Representative HAADF-STEM images of 0.5 wt% (a and b), 2 wt% (c and d), 4 wt% (e and f), and 16 wt% Pd/PCN samples (g and h).	68
Figure 42. Representative HAADF-STEM images of 2 wt% Pd/PCN sample before (a and b) and after washing (c and d). Unstable Pd nanoclusters highlighted by the white ellipses.	69
Figure 43. Representative HAADF-STEM images of 1 wt% Pd/TiO ₂ sample.	70
Figure 44. CO-DRIFTS spectra of Pd/TiO ₂ , Pd/ZnO, and Pd/Al ₂ O ₃ samples, marked with intensely colored line, and CO-DRIFTS spectra of their corresponding pure supports, marked with pale line.	71
Figure 45. CO-DRIFTS spectrum of Pd (TFA) ₂	71
Figure 46. CO-DRIFTS spectra of 1 wt% Pd/TiO ₂ -200 °C and 1 wt% Pd/TiO ₂ -400 °C.	72
Figure 47. DRIFTS spectra of CO removed from Pd/TiO ₂ upon O ₂ exposure at 25 °C (a) and during heating process to 200 °C (b).	73
Figure 48. NAP-XPS of the Pd 3d core line of Pd/TiO ₂ during the CO adsorption process.	73
Figure 49. CO-DRIFTS spectra of Pd/PCN, Pd/hBN, and Pd/Si ₃ N ₄ samples, marked with intensely colored line, and CO-DRIFTS spectra of their corresponding pure supports, marked with pale line.	74
Figure 50. CO-DRIFTS spectra of various Pd/PCN samples, marked with pale line, and CO-DRIFTS spectra of the washed Pd/PCN catalysts, marked with intensely colored line.	75
Figure 51. CO-DRIFTS spectra of 2 wt% Pd/PCN-200 °C and 2 wt% Pd/PCN-400 °C.	75
Figure 52. (a) Pd K-edge XANES spectra and (b) EXAFS magnitude of the Fourier transform (FT) for various Pd samples.	77
Figure 53. (a) Pd K-edge XANES spectra and (b) EXAFS magnitude of the Fourier transform (FT) for various Pd/PCN samples.	78
Figure 54. Wavelet transform analysis of Pd K-edge EXAFS oscillations of various Pd/PCN samples.	79
Figure 55. Two exfoliation process of PCN: (a) interlayer exfoliation, (b) in-plane structure fragmentation.....	80
Figure 56. The total density of states and projected orbital density of states (DOS) images of hydrogen-bonded model (a) and ABAB-stacking ideal model (b).	81
Figure 57. (a) Bader charge for Pd models with different oxidation state (+1, +2, +3, and +4), plotted against the electronegativity of different type of bonding atom (C, N, O, and F). (b) Bader charge-oxidation state plots for different Pd models.....	83

Figure 58. Plots of Bader charge and CO stretching frequencies for Pd/PCN (a) and Pd/TiO ₂ (101) (b), respectively.....	84
Figure 59. (a) Photocatalytic activity and (b) pseudo first-order rate constants of phenol degradation with differently exfoliated PCN.	87
Figure 60. (a) Biphenyl formation over bulk PCN, Pd/PCN catalysts, commercial 5% Pd/Al ₂ O ₃ , and commercial 20 wt% Pd/C. (b) The mole specific activity (mol Biphenyl per mol Pd per second, left axis, black) and mass specific activity (mol Biphenyl per unit mass of the catalyst per second, right axis, red) of the different Pd/PCN catalysts.....	88
Figure 61. Continuous flow experiments of Suzuki coupling of bromobenzene with phenylboronic acid over 2 wt% Pd/PCN in Ar and O ₂	89
Figure 62. Biphenyl formation over different Pd catalysts with and without light: (a) 2 wt% Pd/PCN, (b) 2 wt% Pd/PCN-200 °C, and (c) 2 wt% Pd/PCN-400 °C.....	90
Figure 63. Representative DMPO spin trapping EPR spectra of PCN, t-CN-6, c-CN-16 and u-CN-16 suspension under successive treatment of O ₂ during the visible-light irradiation.	91
Figure 64. (a) <i>In situ</i> ATR-IR spectra of 2 wt% Pd/PCN for the coupling reaction of bromobenzene and phenylboronic acid. (b) <i>In situ</i> ATR-IR spectra of the substrate calibration (bromobenzene, phenylboronic acid, and K ₂ CO ₃). The bands related to the functional groups from bromobenzene and phenylboronic acid are marked with black and red dashed lines, respectively. The yellow dashed lines mark the IR bands present in both substrates. New bands derived from boron-related group are marked with dark blue square, and new bands related to biphenyl is marked with dark red spheres.	92
Figure 65. ¹¹ B NMR spectra of phenylboronic acid with (green line) and without (red line) K ₂ CO ₃ . ..	93
Figure 66. The connection between computation, theory, and experiment.....	95

List of Figures in the Appendix

Figure A. 1. SEM images of PCN(a), t-CN (b), c-CN (c), u-CN (d) and h-CN (e, f). Scale bar, 200 nm.	113
Figure A. 2. SEM images of bulk PCN (a), c-CN-8 (b) and c-CN-16 (c). Scale bar, 10 μ m.	113
Figure A. 3. AFM image and the corresponding height profile of t-CN-3.....	114
Figure A. 4. Sample picture of t-CN-3 before and after grinding.	114
Figure A. 5. Mott-Schottky plots of differently exfoliated PCN.....	115
Figure A. 6. (a) Color changes of Pd(TFA) ₂ before and after 24 h of standing in various organic solvents. (b) Boiling points and relative polarity of various organic solvents.	116
Figure A. 7. Nitrogen adsorption-desorption isotherms of nitride and oxide supports.	117
Figure A. 8. UV-Vis absorption spectra of Pd/PCN samples before (a) and after (b) washing.	117
Figure A. 9. XRD patterns of Pd/PCN samples before and after washing.....	118
Figure A. 10. DRIFTS spectra of Pd/PCN samples before and after washing.	119
Figure A. 11. DRIFTS spectra of various Pd samples and their corresponding pure support.....	120
Figure A. 12. Corresponding QMS response during TPDE measurements of different Pd/nitride samples (left) and pure nitride supports (right).	121
Figure A. 13. Corresponding QMS response during TPDE measurements of different Pd/oxide samples (left) and pure oxide supports (right).....	122
Figure A. 14. Pd 3d photoemission spectra and CO-DRIFTS spectra of 4 wt% Pd/TiO ₂ (a and c) and 4 wt% Pd/Al ₂ O ₃ (c and d).....	123
Figure A. 15. Representative HAADF-STEM images of the washed 2 wt% Pd/PCN sample.	124

Figure A. 16. SEM images of (a) PCN, (b) 1 wt% Pd/PCN, (c) TiO ₂ and (d) 1 wt% Pd/TiO ₂ .	124
Figure A. 17. DRIFTS spectra of CO desorbed from Pd/Al ₂ O ₃ upon O ₂ exposure at 25 °C (a) and during heating process to 200 °C (b).	125
Figure A. 18. DRIFTS spectra of CO desorbed from Pd/ZnO upon O ₂ exposure at 25 °C (a) and during heating process to 200 °C (b).	125
Figure A. 19. (a) XRD patterns and (b) UV-Vis DRS spectra of 1 wt% Pd/TiO ₂ -200 °C and 1 wt% Pd/TiO ₂ -400 °C.	126
Figure A. 20. (a) XRD patterns and (b) UV-Vis DRS spectra of 2 wt% Pd/PCN-200 °C and 2 wt% Pd/PCN-400 °C.	126
Figure A. 21. (a) Layer-by-layer exfoliation diagram of the hydrogen-bonded PCN model. (b) the calculated model energy and average interlayer energy. (c) optimized model energy and (d) average interlayer energy over different layer number.	127
Figure A. 22. (a) Schematic illustration of the process of hydrogen bond calculation. (b) the calculated model energy and zero-point energy (ZPE). (c) hydrogen bond energy calculation process.	128
Figure A. 23. Projected density of states (PDOS) of the monolayer hydrogen-bonded PCN.	129
Figure A. 24. Bader charge for different Pd ²⁺ models, plotted against the electronegativity of different type of bonding atom (C, S, N, and O). All models are obtained from the Cambridge Crystallographic Data Centre (CCDC).	130
Figure A. 25. CO adsorbed (left) on (PdN ₂) _{surface} and (PdN ₂) _{surface} (right) with top view (top) and side view (bottom). Pd, C, N, O, H atoms are dark green, grey, blue, red and white spheres, respectively.	131
Figure A. 26. CO adsorbed (left) on (PdN ₃) _{surface} and (PdN ₃) _{surface} (right) with top view (top) and side view (bottom). Pd, C, N, O, H atoms are dark green, grey, blue, red and white spheres, respectively.	131
Figure A. 27. CO adsorbed (left) on (PdN ₄) _{surface} and (PdN ₄) _{surface} (right) with top view (top) and side view (bottom). Pd, C, N, O, H atoms are dark green, grey, blue, red and white spheres, respectively.	132
Figure A. 28. (PdN ₄) _{interlayer} with top view (top) and side view (bottom). Pd, C, N, H atoms are dark green, grey, blue and white spheres, respectively. The Bader charge of the model is +0.51, and the calculated oxidation state is +1.8. The CO vibration frequency analysis was not performed on this model, because CO molecules would interact with the PCN support rather than Pd atoms, which is in subsurface layer.	132
Figure A. 29. CO adsorbed (top) on Pd (Atop) model and Pd (Atop) model (bottom) with top view (left) and side view (right). Pd, Ti, C, O atoms are dark green, light-grey, grey, and red spheres, respectively.	133
Figure A. 30. CO adsorbed (top) on Pd(O _{2c} -vacancy) model and Pd(O _{2c} -vacancy) model (bottom) with top view (left) and side view (right). Pd, Ti, C, O atoms are dark green, light-grey, grey, and red spheres, respectively.	133
Figure A. 31. CO adsorbed (top) on Pd(O _{3c} -vacancy) model and Pd(O _{3c} -vacancy) model (bottom) with top view (left) and side view (right). Pd, Ti, C, O atoms are dark green, light-grey, grey, and red spheres, respectively.	134
Figure A. 32. CO adsorbed (top) on Pd(O _{3c} *-vacancy) model and Pd(O _{3c} *-vacancy) model (bottom) with top view (left) and side view (right). Pd, Ti, C, O atoms are dark green, light-grey, grey, and red spheres, respectively.	134

Figure A. 33. CO adsorbed (top) on Pd(Ti _{5c} -vacancy) model and Pd(Ti _{5c} -vacancy) model (bottom) with top view (left) and side view (right). Pd, Ti, C, O atoms are dark green, light-grey, grey, and red spheres, respectively.	135
Figure A. 34. CO adsorbed (top) on Pd(Ti _{6c} -vacancy) model and Pd(Ti _{6c} -vacancy) model (bottom) with top view (left) and side view (right). Pd, Ti, C, O atoms are dark green, light-grey, grey, and red spheres, respectively.	135
Figure A. 35. CO adsorbed (top) on PdOH model and PdOH model (bottom) with top view (left) and side view (right). Pd, Ti, C, O, H atoms are dark green, light-grey, grey, red, and white spheres, respectively.	136
Figure A. 36. CO adsorbed (top) on Pd(OH) ₂ model and Pd(OH) ₂ model (bottom) with top view (left) and side view (right). Pd, Ti, C, O, H atoms are dark green, light-grey, grey, red, and white spheres, respectively.	136
Figure A. 37. CO adsorbed on PCN-position 1 with top view (top) and side view (bottom). C, N, O, H atoms are grey, blue, red and white spheres, respectively.	137
Figure A. 38. CO adsorbed on PCN-position 2 with top view (top) and side view (bottom). C, N, O, H atoms are grey, blue, red and white spheres, respectively.	137
Figure A. 39. CO adsorbed (top) on TiO ₂ (101)-position 1 with top view (left) and side view (right). Ti, C, O, H atoms are light-grey, grey, red, and white spheres, respectively.	138
Figure A. 40. CO adsorbed on TiO ₂ (101)-position 2 with top view (left) and side view (right). Ti, C, O, H atoms are light-grey, grey, red, and white spheres, respectively.	138
Figure A. 41. CO adsorbed on TiO ₂ (101)-position 3 with top view (left) and side view (right). Ti, C, O, H atoms are light-grey, grey, red, and white spheres, respectively.	139
Figure A. 42. CO adsorbed on TiO ₂ (101)-position 4 with top view (left) and side view (right). Ti, C, O, H atoms are light-grey, grey, red, and white spheres, respectively.	139
Figure A. 43. CO adsorbed on TiO ₂ (101)-position 5 with top view (left) and side view (right). Ti, C, O, H atoms are light-grey, grey, red, and white spheres, respectively.	140
Figure A. 44. CO bonded to one Pd atom of Pd _{cluster} /PCN with top view (top) and side view (bottom). Pd, C, N, O, H atoms are dark green, grey, blue, red and white spheres, respectively. .	141
Figure A. 45. CO bonded to two Pd atom of Pd _{cluster} /PCN with top view (top) and side view (bottom). Pd, C, N, O, H atoms are dark green, grey, blue, red and white spheres, respectively. .	141
Figure A. 46. CO bonded to three Pd atom of Pd _{cluster} /PCN with top view (top) and side view (bottom). Pd, C, N, O, H atoms are dark green, grey, blue, red and white spheres, respectively. .	142
Figure A. 47. CO bonded to one Pd atom of bulk Pd (111) with top view (top) and side view (bottom). Pd, C, O atoms are dark green, grey, and red spheres, respectively.	142
Figure A. 48. CO bonded to two Pd atom of bulk Pd (111) with top view (top) and side view (bottom). Pd, C, O atoms are dark green, grey, and red spheres, respectively.	143
Figure A. 49. CO bonded to three Pd atom of bulk Pd (111) with top view (top) and side view (bottom). Pd, C, O atoms are dark green, grey, and red spheres, respectively.	143
Figure A. 50. (a) Sample photographs (b) CO-DRIFTS spectra, (c) Pd 3d photoemission spectra, (d) XRD pattern, and (e) UV-Vis DRS spectra for 2 wt% Pd/PCN_Ar and 2 wt% Pd/PCN_O ₂	144
Figure A. 51.(a) EPR spectra of t-CN-3 before and after visible-light irradiation and (b) Selected DMPO spin trapping EPR spectra of t-CN-3 suspension under successive treatment of O ₂ during the visible-light irradiation.	145
Figure A. 52. ¹³ C NMR spectra of substrates, referenced to Ethanol-d ₁ (58.05 ppm).	146
Figure A. 53. ¹ H NMR spectra of substrates, referenced to D ₂ O (4.79 ppm).	146

Figure A. 54. (a) *In situ* ATR-IR spectra of 2 wt% Pd/PCN for the coupling reaction of iodobenzene and phenylboronic acid. (b) *In situ* ATR-IR spectra of the substrate calibration (Iodobenzene, Phenylboronic acid, and K_2CO_3). The bands related to the functional groups from bromobenzene and phenylboronic acid are marked with black and red dashed lines, respectively. The yellow dashed lines mark the IR bands present in both substrates. New bands derived from boron-related group are marked with dark blue square, and new bands related to biphenyl is marked with dark red spheres. 147

List of Tables

Table 1. Production yield of differently exfoliated PCN ^a	44
Table 2. Characterization data of differently exfoliated PCN.	53
Table 3. EXAFS fitting parameters at the Pd K-edge for various Pd samples ($S_{O_2}=0.7$).....	77
Table 4. EXAFS fitting parameters at the Pd K-edge for various Pd/PCN samples ($S_{O_2} = 0.7$).....	79
Table 5. Bader charge of Pd ($Q e $), calculated Pd oxidation state, CO adsorption energy (E_{ads} , eV), C–Pd distance (R_{PdC} , Å), C–O bond length (R_{CO} , Å), and CO stretching frequency (ω_e , cm^{-1}) for CO adsorption on Pd atom on a hydrogen-bonded PCN. The corresponding structure is shown in Figure A.25 – A.27.....	86
Table 6. Bader charge of Pd ($Q e $), calculated Pd oxidation state, CO adsorption energy (E_{ads} , eV), C–Pd distance (R_{PdC} , Å), C–O bond length (R_{CO} , Å), and CO stretching frequency (ω_e , cm^{-1}) for CO adsorption on Pd moieties on a TiO_2 (101) terrace sites. The corresponding structure is shown in Figure A.29– A.36.....	86
Table 7. Conversion of experimental CO stretching frequencies to the Bader charge and oxidation state of Pd for 2 wt% Pd/PCN and 1 wt% Pd/ TiO_2 , respectively.	86

List of Tables in the Appendix

Table A. 1. XPS high-resolution C1s data of differently exfoliated g- C_3N_4	148
Table A. 2. XPS high-resolution N1s data of differently exfoliated g- C_3N_4	149
Table A. 3. ICP and XPS data of Pd/PCN samples with different loading.	150
Table A. 4. Comparison of atomic ratio of F to Pd over different Pd samples.	150
Table A. 5. ICP and XPS data of Pd/PCN samples with different loading.	151
Table A. 6. Comparison of atomic ratio of F to Pd over Pd/PCN samples.	151
Table A. 7. CO adsorption energy (E_{ads} , eV), C–Pd distance (R_{PdC} , Å), C–O bond length (R_{CO} , Å), and CO stretching frequency (ω_e , cm^{-1}) for CO adsorption on support PCN and TiO_2 (101) terrace sites. The corresponding structure is shown in Figure A.37 – A.43.	152
Table A. 8. Comparison of Bader charge and CO stretching frequencies of Pd/PCN and Pd/ TiO_2 with different Pd oxidation state (+4, +2, +1, and 0). Bader charge of Pd ($Q e $), experimental CO stretching frequency (ω).....	152
Table A. 9. CO adsorption energy (E_{ads} , eV), C–Pd distance (R_{PdC} , Å), C–O bond length (R_{CO} , Å), and CO stretching frequency (ω_e , cm^{-1}) for CO adsorption on Pd nanoparticle (0.5 nm) on PCN model and bulk Pd (111). The corresponding structure is shown in Figure A.44 – A.49.	153
Table A. 10. High performance liquid chromatography (HPLC) data of 2 wt% Pd/PCN for continuous flow reaction in Ar and O_2 atmosphere after 2h.....	153
Table A. 11. XPS and ICP data of spent catalysts.....	153

List of Abbreviations

acac	Acetylacetonate
AFM	Atomic force microscopy
at. %	Atomic percentage
ATR	Attenuated total reflection
BET	Brunauer-Emmett-Teller
CB	Conduction band
c-CN	Exfoliated PCN by chemical oxidation method
CN	Coordination number
DFT	Density functional theory
DRIFTS	Diffuse reflectance infrared Fourier transform spectroscopy
DRS	Diffuse reflectance spectroscopy
DSC	Differential scanning calorimetry
EPR	Electron paramagnetic resonance
EXAFS	Extended X-ray absorption fine structure
EELS	Electron energy loss spectroscopy
FESEM	Field emission scanning electron microscopy
FT	Fourier transform
GC	Gas chromatography
GGA	Generalized gradient approximation
h-CN	Exfoliated PCN by hydrothermal oxidation method
HPLC	High-performance liquid chromatography
ICP-OES	Inductively coupled plasma optical emission spectroscopy
IR	Infrared
LDA	Local-density approximation
MCT	Mercury-cadmium-tellurium
MFC	Mass flow controller
MS	Mass spectrometry
NAP	Near-ambient pressure
NMR	Nuclear magnetic resonance
MAS	Magic angle spinning
OAc	acetate
P25	Mixed-phase titanium dioxide (ca. 80% anatase and 20% rutile)
PAW	Projector augmented wave
PBE	Perdew-Burke-Ernzerhof
PCN	Polymeric carbon nitride
PL	Photoluminescence

continued on next page

QMS	Quadrupole mass spectrometry
SACs	Single-atom catalysts
sccm	Standard cubic centimeters per minute
SEM	Scanning electron microscopy
SMSI	Strong metal-support interaction
STEM	Scanning transmission electron microscopy
t-CN	Exfoliated PCN by thermal oxidation method
TEM	Transition electron microscopy
TFA	Trifluoroacetate
TGA	Thermogravimetric analysis
TOF	Turnover Frequency
TPD	Temperature-programmed desorption
u-CN	Exfoliated PCN by liquid ultrasonic method
UV	Ultraviolet
VASP	Vienna ab initio simulation package
VB	Valence band
Vis	Visible
wt%	Weight percent
XAS	X-ray absorption spectroscopy
XPS	X-ray photoelectron spectroscopy
XRD	X-ray diffraction

List of Symbols

Symbol	Quantity	Unit
λ	Wavelength	nm
ν	Wavenumber	cm^{-1}
θ	Diffraction angle	$^{\circ}$
c	Instant concentration	mg L^{-1}
c_0	Initial concentration	mg L^{-1}
E_1	Energy of monolayer model	eV
E_a	Average interlayer energy	eV
E_g	Band gap energy	eV
E_n	Corresponding energy of n-layer model	eV
G	g factor (EPR)	
N	Number of layers in the model	
T	Temperature	$^{\circ}\text{C}$
V	Volume	L

1. Introduction

1.1 Catalysis with palladium

Catalysis has received enormous interest from the perspectives of both scientific research and industrial applications. It contributes to 30 – 40% of the global gross domestic product (GDP), and approximately 90% of chemicals are manufactured through catalytic processes [1, 2]. It shapes modern society in many ways, such as the development of the “Haber-Bosch” process, the invention of Ziegler-Natta catalysts, and the introduction of the three-way catalytic converter in vehicles [3-7].

Heterogeneous palladium catalysts are an important class of catalysts used in a wide variety of applications, particularly in industrial synthesis, hydrogen storage, and energy conversion [8-10]. For example, automobile exhaust from burning fossil fuels is processed through a catalytic converter, usually composed of palladium, platinum, and rhodium, to break down some harmful byproducts [11, 12]. In the field of organic reactions, the palladium-catalyzed Suzuki-Miyaura cross-coupling reaction fundamentally changed the practice of organic synthesis, leading to the joint award of the 2010 Nobel Prize in Chemistry to Richard F. Heck, Ei-ichi Negishi, and Akira Suzuki [13, 14]. Moreover, palladium is a key component of fuel cells, in which hydrogen and oxygen react to produce electricity, heat, and water [15]. However, Pd-based heterogeneous catalysts are expensive and in limited supply. The abundance of Pd within the crust of the Earth is 0.015 ppm by weight [16], and the cost is at ca. \$1431 per ounce (Kitco Gold Index, March 3, 2023), which is even higher than the cost of platinum (\$958 per ounce). So, the price of Pd is above acceptable levels for large-scale commercial applications. Therefore, improving the utilization efficiency of heterogeneous Pd catalysts and maintaining their reactivity and selectivity has become a challenge in their application.

In recent years, with the rapid development of synthetic methods, characterization techniques, and computational chemistry, researchers are able to investigate the structure-reactivity relationship of heterogeneous catalysts at the nanoscale, molecular scale, and even atomic scale [17]. Studies on the size of supported metal catalysts have demonstrated that it is critical factor in determining the local geometries and electronic structures, thereby governing the catalytic properties. Especially when the metal size is decreased to the single-atom scale, the utilization efficiency of each metal atom can reach up to 100% [18]. In this way, the maximum atom-utilization efficiency allows a noteworthy decrease in the utilization of Pd. Therefore, it is of great significance to achieve the controllable synthesis of heterogeneous Pd catalysts with

atomic precision and get a deeper understanding of their coordination and electronic structure, as well as the structure-reactivity relationship.

When the supported Pd is atomically dispersed, it is usually in covalent coordination or in ionic interaction with the supports, thereby possessing a partial charge due to the metal-support interactions [19, 20]. However, the surface free energy of Pd increases as its particle sizes decrease, which leads to the undesired aggregation of individual atoms into nanoparticles during synthesis and reaction processes [21]. One effective and straightforward strategy is to decrease the Pd loading, which allows for the spatial isolation of Pd atoms on the support and prevents aggregation. Of course, this is based on sacrificing more active sites. Therefore, developing a viable strategy to enhance the presence of active atomic centers and inhibit the aggregation of Pd atoms on the support remains a significant challenge.

The stabilization of Pd atoms on supports requires specific anchoring sites on their surface, such as surface vacancies, unsaturated surface atoms, doped heteroatoms, and surface cavity sites [22]. Among the various types of isolated Pd catalysts, those based on nitride and oxide supports have attracted significant interest. Generally, the oxide surface consists of oxygen/metal vacancies, hydroxyl groups, and step sites, *etc.*, which can provide anchoring sites for stabilizing isolated metal atoms [23]. On nitride supports, the metal atoms can be stabilized on these anchoring sites by directly bonding to surface nitrogen atoms without removing a cation. To confirm the coordination and electronic structure of the Pd center, atomic-scale structure characterizations, such as advanced electron microscopy, structure-sensitive spectroscopy, and even *in situ/operando* methodologies, are often required [24, 25].

1.2 Introduction of palladium and palladium compounds

The physicochemical properties of palladium are relatively unique due to its $[\text{Kr}]4d^{10}$ outer electron configuration [26]. The fully filled d orbitals of palladium make it energetically stable and endow palladium unique electronic properties, making it useful for catalytic applications. Palladium has the appearance of a silvery-white metal, and it has the lowest melting point (1554.8 °C) among the platinum group metals [27]. It is soft and ductile when annealed, but its strength and hardness are significantly increased when cold-worked [28]. It is relatively stable and resistant to oxidation at room temperature. However, when palladium sponge metal is heated in oxygen at 350 °C, it can be transformed into palladium(II) oxide (PdO). PdO is the only oxide of palladium that has been well characterized [29].

The synthesis of heterogeneous Pd catalysts usually requires the use of homogeneous Pd complexes as precursors. Pd compounds exist mainly in the 0 and +2 oxidation states, like tris(dibenzylideneacetone)dipalladium(0) ($\text{Pd}_2(\text{dba})_3$), bis(tri-tert-butylphosphine)palladium(0) ($\text{Pd}(\text{t-Bu}_3\text{P})_2$), tetrakis(triphenylphosphine)palladium(0) ($\text{Pd}(\text{PPh}_3)_4$), palladium(II) chloride (PdCl_2), palladium(II) acetate ($\text{Pd}(\text{OAc})_2$), palladium(II) bis(acetylacetonate) ($\text{Pd}(\text{acac})_2$), and palladium(II) trifluoroacetate ($\text{Pd}(\text{TFA})_2$). A few palladium(III) compounds are also known to exist in mononuclear and dinuclear forms [30]. Pd(IV) compounds are relatively rare, with sodium hexachloropalladate(IV) (Na_2PdCl_6) and potassium hexachloropalladate (IV) (K_2PdCl_6) as examples. Although the homogeneous Pd complexes, especially Pd (II) compounds, have been widely used for the synthesis of fine chemicals, supported heterogeneous Pd catalysts are more advantageous from the perspective of sustainable catalysis and circular economy [31].

To date, heterogeneous catalysts account for ca. 80% of industrial catalytic processes due to their easy recovery and robustness [32]. Studies on heterogeneous catalysts have confirmed that the size of nanoparticles plays a significant role in governing the catalytic properties. In 1989, Haruta's group discovered that gold catalysts exhibit ultra-high catalytic activity for the low-temperature oxidation of CO when their size is reduced to 10 nm [33]. Before that, gold, as well as the platinum-group metals (palladium, ruthenium, rhodium, osmium, iridium, and platinum), had been considered inert metals. Moreover, it has been found that when the size of metal is reduced to the level of a few atoms, the metal cluster exhibit the structural characteristics with discrete energy bands. Sitja *et al.* [34] demonstrated that when the size of Pd particles is larger than 2.3 nm, CO adsorption energy increases quasi-monotonically with particle size. While the Pd particles below 1.8 nm, the CO adsorption energy shows irregular oscillation since the electronic and geometric structures of metal clusters strongly depend on their atomicity [35]. Wang *et al.* [36] demonstrated a conjugated microporous polymer-supported Pd nanoparticles photocatalyst with particle sizes ranged between 5 and 10 nm that exhibited efficient performance for visible-light catalytic Suzuki coupling at room temperature. The authors found that the immobilized Pd nanoparticles formed an interface with the support to facilitate the charge carrier transfer through the Schottky effect.

When the size of the supported metal is further decreased to individual atoms, the geometric and electronic properties become distinguishable from those of nanoparticles due to different interaction ways with the support [37]. The isolated metal atoms are often stabilized through covalent interactions with coordinating atoms on the support. Thus, the supports have an extraordinary influence on determining the electronic state of the catalytic metal sites, thereby affecting their overall catalytic properties [38-40]. In 2011, after the term "single-atom catalysts"

proposed by Zhang *et al.* [18], it has recently become one of the most energetic research frontiers in the field of heterogeneous catalysis. Especially for noble-metal-based catalysts, it is a great advantage that the isolation of metal sites achieves a maximum atom utilization efficiency [41, 42]. Besides, single-atom catalysts also exhibit additional distinctive characteristics, including the ability to suppress undesired side reactions commonly observed at multiple metal sites, and in some cases, enhance stability by optimizing the metal-support interface [43-46].

1.3 Synthesis of isolated Pd catalysts

To prevent the agglomeration of isolated Pd atoms into particles, it is crucial to establish strong covalent interactions between the central Pd atoms and the surrounding coordination atoms from the supports. Various methods have been reported for the synthesis of isolated Pd catalysts, and these can be categorized as “bottom-up” (direct-synthesis) and “top-down” (post-synthesis) synthetic routes [47]. In the direct-synthetic route, Pd nanoparticles or bulk Pd are used as starting precursors, and the key point is to break the Pd–Pd bond of the Pd nanoparticles or bulk Pd and form new and strong bonds between the Pd atom and the support [48]. Conversely, in the post-synthetic route, homogeneous Pd complexes are often used as starting precursors, and the key point is to achieve atomic dispersion of these Pd complexes on the support and maintain as isolated atoms during the post-treatment process [49]. Usually, controlling the Pd loading content and employing the supports with high specific areas and abundant anchoring sites are effective approaches to achieve isolated Pd catalysts.

Impregnation method

The impregnation strategy is the most widely used wet-chemistry method for the synthesis of SACs. To prevent metal aggregation during synthesis, it is vital to control the metal loading and select suitable supports with high specific surface areas [18, 50, 51]. Sun *et al.* [52] reported a simple wet impregnation method for synthesizing single-atom Au, Pd, Ru, and Pt catalysts using low-boiling-point, low-polarity solvents such as acetone. The atomic dispersion of cationic metal species is due to (1) the increased wetting of the carbon support by the hydrophilic/hydrophobic nature of the solvents, (2) the lower drying temperature to avoid metal agglomeration, and (3) the absence of water to keep a high-valent metal species. In addition, Ma *et al.* [53] developed a mixture of Pd species, consisting of isolated Pd atoms, subnanometer Pd clusters, and Pd nanoparticles, on nanodiamonds by controlling the Pd loading through a wet chemistry method. The suspension temperature (100 °C) and the adjustment of pH (~10,

with Na_2CO_3 solution) are the key points to achieve the various surface Pd species on the surface of nanodiamond support.

Spatial confinement strategy

Metal-organic frameworks (MOFs) are a current new type of porous material that has drawn considerable attention due to their regular pore structures, extremely high surface area, and distinct designability as well as tailorability [54, 55]. The well-defined porous structures in MOFs are able to encapsulate mononuclear metal precursors within its cavity through the microporous confinement effect [56-58]. Meanwhile, abundant coordination sites can be generated after the post-treatment of MOFs, which can also be used for stabilizing metal atoms [59, 60]. For example, high-temperature pyrolysis of ZIF-8 can result in the formation of nitrogen-doped porous carbon materials [61-63]. Li *et al.* [64] reported a highly stable single-atom Pd catalyst using a strategy of cage-encapsulated precursor pyrolysis. First, the $\text{Pd}(\text{acac})_2$ was *in situ*-trapped in the cages of ZIF-8 during the crystallization process, denoted as $\text{Pd}(\text{acac})_2@\text{ZIF-8}$. To remove the ligand of $\text{Pd}(\text{acac})_2$ and generate isolated Pd atoms, a high-temperature pyrolysis of $\text{Pd}(\text{acac})_2@\text{ZIF-8}$ at 900 °C in Ar was performed. During the pyrolysis process, ZIF-8 transformed into nitrogen-doped porous carbon, while $\text{Pd}(\text{acac})_2$ was reduced *in situ* through the carbonization of the organic linkers of ZIF-8. The individual Pd atoms were stabilized by the nitrogen species present in the nitrogen-doped porous carbon derived from ZIF-8.

Moreover, polymers or polymer-derived materials usually contain a significant number of heteroatoms with lone pairs of electrons, such as nitrogen (N), phosphorus (P), and sulfur (S) [47]. These heteroatoms can serve as coordination atoms for anchoring Pd atoms through strong coordination interactions [65-69]. He *et al.* [70] developed a precursor-dilution strategy to synthesize various isolated metal catalysts supported on N-doped porous carbon ($\text{M}_1/\text{N-C}$). Specifically, the tetraphenylporphyrin (TPP) chelated with metal cations was copolymerized with excessive metal-free TPP to dilute the metal ions. This process helps increase the distance between the supported metal atoms, thereby preventing the tendency to aggregate during pyrolysis. The authors demonstrated the excellent versatility of this precursor-dilution strategy by successfully preparing 24 kinds of single-atom catalysts $\text{M}_1-\text{N-C}$ ($\text{M} = \text{Pd}, \text{Pt}, \text{Ti}, \text{V}, \text{Cr}, \text{Mn}, \text{Fe}, \text{Co}, \text{Ni}, \text{Cu}, \text{Ga}, \text{Zr}, \text{Mo}, \text{Ru}, \text{Rh}, \text{Ag}, \text{Cd}, \text{In}, \text{Sn}, \text{Er}, \text{W}, \text{Ir}, \text{Au}, \text{and Bi}$).

Photochemical method

The photochemical reduction method has been demonstrated as a facile strategy to precisely control the location of single atoms under mild synthetic conditions [71, 72]. The absorption of photons and electronically excited states are two key steps in the photochemical synthesis process. During the process, it is important to ensure the well diffusion of the metal ions in the solution. Liu *et al.* [73] employed ultrathin TiO₂ nanosheets as a support to synthesize a single-atom Pd catalyst (Pd₁/TiO₂) at room temperature through a photochemical method, achieving a high loading of 1.5 wt%. The crucial step in preparing Pd₁/TiO₂ involves the introduction of ultraviolet (UV) light to generate ethylene glycolate (EG) radicals. This light irradiation process not only reduce and stabilize the Pd atoms on TiO₂ nanosheets, but also remove Cl⁻ ligands under mild conditions. The Pd₁/TiO₂ catalyst exhibited high photo-reactivity and stability in the hydrogenation of C=C and C=O bonds. Moreover, Ge *et al.* [74] reported the synthesis of a single-atom Pd catalyst anchored on TiO₂ (Pd SA/TiO₂) using an *in situ* photocatalytic reduction method with K₂PdCl₄ as the metal precursor. Before photoreduction, the TiO₂/K₂PdCl₄ solution mixture was frozen using liquid nitrogen to form a solid ice. Then, the solid ice was illuminated by a 500 W Xenon lamp for 5 min to generate photoexcited electrons from TiO₂, followed by the reduction of PdCl₄²⁻ to form isolated Pd species.

Atomic layer deposition method

Atomic layer deposition (ALD) is another powerful technique for fabricating desired isolated metal catalysts because of its advantageous capability to precisely control the deposition of metal atoms onto a support [75]. Huang *et al.* [76, 77] demonstrated the successful preparation of atomically dispersed Pd species on both graphene and g-C₃N₄ support by the ALD method using palladium hexafluoroacetylacetate (Pd(hfac)₂) and formalin as precursors. The ALD cycle was performed at 150 °C using a viscous flow reactor with ultrahigh purity N₂ (99.999%) as the carrier gas (200 sccm). The timing sequence was 120, 120, 60, and 120 s for Pd(hfac)₂ exposure, N₂ purge, formalin exposure, and N₂ purge, respectively. One ALD cycle was used for both Pd₁/C₃N₄ and Pd₁/graphene. The Pd loadings in Pd₁/graphene and Pd₁/g-C₃N₄ were 0.25 wt% and 0.5 wt%, respectively. In addition, Piernavieja-Hermida *et al.* [78] successfully fabricated thin film-stabilized single-atom Pd₁ catalysts by precisely controlling the ALD conditions. During the ALD cycle, the Al₂O₃ substrate surface was first exposed to gaseous Pd(II) hexafluoroacetylacetonate (Pd(hfac)₂) at 100 °C with a time sequence (300 s - 300 s). Afterward, ALD deposition of TiO₂ was performed using alternating exposures of titanium tetrachloride (TiCl₄) and deionized water at 150 °C with a time sequence 80 s - 160 s - 80 s -

160 s. 1-cycle, 7-cycle, and 14-cycle were used for the TiO₂ overcoat, respectively. Notably, TiO₂ selectively grows on the substrate instead of on the chemisorbed Pd(hfac)₂. Finally, the hfac ligands are removed by using formalin (HCHO) to form TiO₂ nanocavity-stabilized isolated Pd sites.

Ball milling method

During the ball milling process, the covalent and coordinative bonds on the support are broken by the mechanochemical force. This generates defect sites on the support, which can be utilized to stabilize metal atoms [79, 80]. Guo *et al.* [81] reported single-atom Pd catalysts supported on TiO₂ by a ball-milling method based on the “precursor-dilution” strategy. The authors first mixed titanyl phthalocyanine with palladium phthalocyanine in a weight ratio of 1:800 and milled the mixture for 20 min under 400 rpm. Then, 10 mL of ethanol was added to the chamber, and the mixture was ground for another 12 h. After drying overnight at 60 °C, the sample powder was calcined at 600 °C in air for 2 h. This process converted the two precursor salts into PdO_x and TiO₂, respectively. The Pd species were then anchored onto the TiO₂ support in the form of single atoms, along with a small amount of Pd nanoparticles. Furthermore, Zhang *et al.* [82] reported the kilogram-scale production of FeO_x supported isolated Pd catalysts through a scalable ball milling method using commercial iron(III) oxide as the raw material. They first mixed commercial iron(III) oxide and tetraamminepalladium(II) nitrate precursors, and then ground at 400 rpm for 10 h. The resulting mixture was pyrolyzed at 400 °C in air for 2 h to obtain the atom-dispersed Pd₁/FeO_x catalyst.

Microwave-assisted method

The microwave (MW) heating method is well-known for its efficiency in synthesizing organic compounds and nanoscale materials, and it is a time-saving method that also reduces the occurrence of side reactions [83, 84]. Chen *et al.* [85-87] reported a simple method for depositing Pd atoms onto carbon nitride materials using microwave irradiation. The carrier materials were first dispersed in H₂O under sonication to form a homogeneous suspension. Then, an aqueous solution of Pd(NH₃)₄(NO₃)₂ was added dropwise and stirred overnight for further microwave processing. The microwave heating process was adopted as a cyclic program of 15 s of irradiation and 3 min of cooling with 20 repetitions, using a power of 100 W. The fast microwave process leads to the uniform distribution of Pd species on carriers, effectively preventing the diffusion and agglomeration of Pd species.

Strong electrostatic adsorption

Oxide surfaces can be charged differently in an aqueous solution, depending on the isoelectric point of the oxide and the pH values of the solution [23]. For instance, the surface hydroxyl groups are deprotonated if the pH of the solution is above the isoelectric point of the oxide. Through the Coulomb force, the negatively charged oxide can strongly adsorb the metal cation [88]. Nelson *et al.* [89] synthesized atomically dispersed Pd on P25 titania (TiO₂) using a strong electrostatic adsorption method, followed by calcination at 400 °C in air. Still, a low Pd weight loading (0.1 wt%) and the addition of NH₃·H₂O are the key factors in forming isolated Pd species on TiO₂. The strong electrostatic adsorption between the surface oxygen anion (O⁻) and the cationic precursor [(NH₃)₄Pd]²⁺ promotes the deposition of isolated Pd species. By contrast, Chu *et al.* [90] reported the synthesis of a surface-modified SiC-supported Pd single atom catalyst through the electrostatic interaction between the negatively charged Pd precursor (PdCl₄²⁻) and amine species on SiC. The SiC support was first treated by the addition of aminopropyltrimethoxysilane and ultrasonication to form surface amines. The Pd precursor (i.e., PdCl₄²⁻) was bound to the amine groups on the SiC surface. Subsequently, the Pd precursors were reduced through moderate ultraviolet C (UV-C) irradiation to obtain stable Pd single-atom catalysts.

Freezing-assisted method

To prevent the random diffusion of metal precursors in the aqueous solution, some researchers suggested freezing the aqueous solution at low temperature to immobilize the metal precursors and inhibit their tendency to aggregate [91-93]. Specifically, the formed ice lattices can confine the dispersed metal precursors within a limited space, thereby preventing the formation of metal nanoparticles. Zhang *et al.* [94] reported the freeze-drying-assisted method for synthesizing atomically dispersed Pd atoms on nitrogen-doped graphene (Pd₁/N-graphene). Dicyandiamide was used as the nitrogen source, glucose as the carbon source, Na₂PdCl₄ as the Pd source, and deionized water as the solvent. All reagents are first mixed together in an aqueous solution and then freeze-dried to remove the water, followed by annealing at 800 °C to form a stable Pd–N₄ coordination geometry. The authors point out that the freeze-assisted step was crucial for achieving atomically dispersed Pd species.

1.4 Characterization of isolated Pd catalysts

Considering the interactions of the isolated Pd atoms with the supports, it is important to carefully identify the presence of isolated Pd sites, as well as their local geometric and electronic

structures. In other words, more powerful experimental techniques are highly desired to investigate the active Pd sites, thus gaining deep insight into the metal-support interaction and structure-reactivity relationship. Currently, there are some routine characterizations, including transmission electron microscopy (TEM), X-ray absorption spectroscopy (XAS), and probe molecule Fourier transform infrared (IR) spectroscopy. Several other important techniques were also employed to study the isolated metal centers, such as Raman spectroscopy, electron paramagnetic resonance (EPR), nuclear magnetic resonance (NMR), near-ambient pressure X-ray photoelectron spectroscopy (NAP-XPS), and so on. In addition to advanced microscopic and spectroscopic characterization, density functional theory (DFT), a computational method, has been widely used to characterize isolated Pd catalysts.

Scanning transmission electron microscopy

Scanning transmission electron microscopy (STEM) is a straightforward technique for characterizing the structure and morphology of isolated metal species on heterogeneous catalysts. It is no doubt that atomic-resolution STEM has significantly promoted the development of the field of single-atom catalysts [95]. Moreover, the maturation of aberration-corrected electron microscopy with sub-angstrom resolution offers a further possibility to obtain more accurate and convincing images for identifying the presence and spatial distribution of isolated metal species [96].

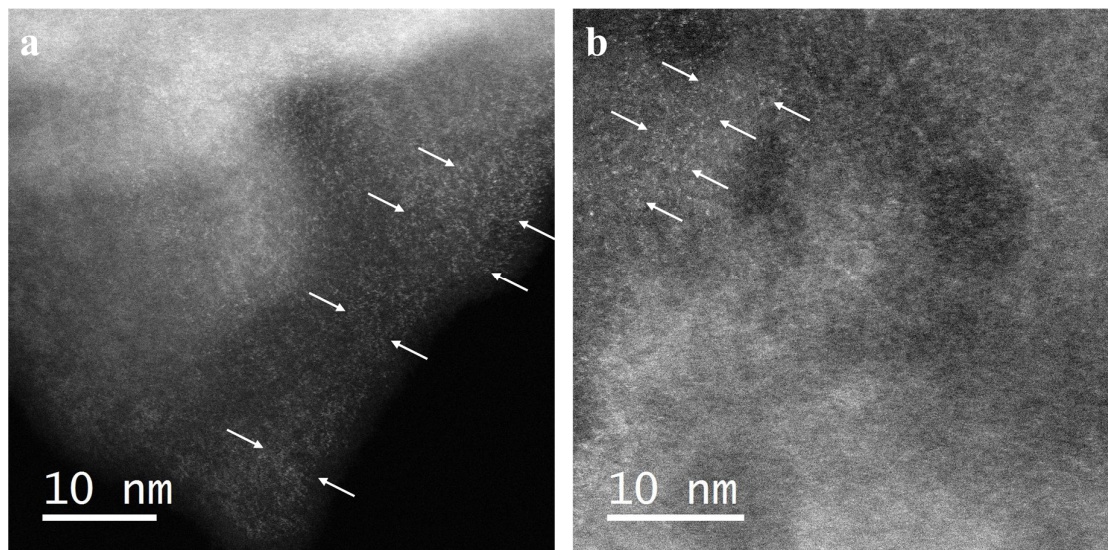


Figure 1. HAADF-STEM images of isolated Pd atoms on PCN; arrows indicate location of single atoms.

The high-angle annular dark field (HAADF), as a powerful imaging mode, can record strong signals from elastically backscattered electrons used to create dark-field atomic resolution

images [97, 98]. The provided images with the projected atomic columns can be identified by bright spots (Figure 1, example of self-synthesized 2 wt% Pd/PCN catalyst). Peng *et al.* [99] detected well-dispersed Pd atoms on a hybridized core-shell structure diamond@graphene support through high-angle annular detector STEM. Zhong *et al.* [53] found that the sizes of Pd particles in the Pd/nanodiamond catalysts varied, ranging from large nanoparticles (0.4 wt%) to nanoclusters (0.25 wt%), and finally to single atoms (0.07 wt%), as the Pd loading decreased based on the observation of HAADF-STEM. Furthermore, electron energy-loss spectroscopy (EELS), as an alternative method of elemental analysis in HAADF-STEM, is a sensitive techniques to obtain element and electronic states information, particularly suitable for elements with low atomic numbers [100-102]. Liu *et al.* [103] successfully applied atomic-resolution STEM-EELS to identify the presence of Ti^{3+} species vicinal to the isolated Pd sites on TiO_2 . Such chemical identification is crucial for understanding how the Pd atoms alter the electronic structures of the neighboring Ti atoms in the TiO_2 support. Moreover, Ru *et al.* [104] demonstrated the successful characterization of EELS spectroscopy for isolated Pd species supported by UIO-66- NH_2 without causing large-scale structural disruption. In recent years, the *in situ* or *operando* environmental TEM (ETEM) has been developed to monitor the dynamics changes of single atoms during reactions and gain a deep understanding of the catalytic mechanism at the atomic level [105, 106]. Wei *et al.* [107] used *in situ* ETEM to record the dynamic process of the transformation of large Pd nanoparticles into thermally stable Pd single-atom on the nitrogen-doped carbon support above 900 °C in an inert atmosphere, which showed competing sintering and atomization processes during this conversion.

The quality of acquired STEM images generally correlates with the relative atomic number Z of the elements in the sample [108]. Therefore, it is often easy to image the heavy-element metal atoms dispersed on low-electron density materials, but it is difficult to visualize the light metal atoms on heavy supports, like metal oxides or metallic supports [109]. Moreover, high-resolution STEM images often sacrifice information about the overall distribution of metal species in the catalyst due to the limited measurement area [95]. Inevitably, beam damage also occurs during measurements. Rice *et al.* [110] and Liu *et al.* [111] both observed the phenomenon of collapse of the zeolite crystallite framework caused by electron beam damage during STEM image acquisition.

Infrared spectroscopy

Infrared (IR) spectroscopy is one of the most common and powerful methods for characterizing supported metal-based catalysts due to its wide accessibility, surface sensitivity, and affordable

instrumentation [112]. Both diffuse reflectance spectroscopy with powder samples and transmission spectroscopy with pressed wafer samples are routine methods [113, 114]. In combination with the probe molecules, *in situ* or *operando* IR spectroscopy is able to monitor the dynamic change of the electronic and coordination information on the metal centers under reaction conditions [115-118]. The probe molecules commonly employed in research include CO, H₂, NO, and C₂H₄, with CO being the most frequently utilized [119]. The coordinative unsaturation degree of the adsorption site (on-top, bridge, three- and four-fold hollow), the chemical states, the coordination environment of catalytic centers, and its electronic environments would cause the shift of CO vibration frequency that can be recorded, allowing to assess the existence of atomically dispersed metal atoms, based on their distinct shift compared to nanoparticles [115, 120-122].

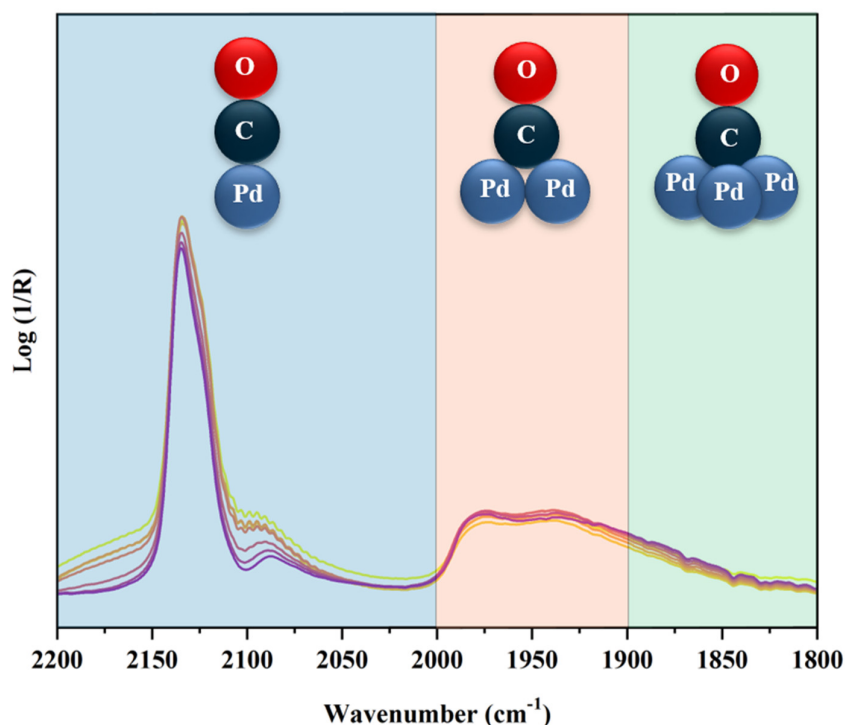


Figure 2. Schematic illustration of regions of different CO adsorption modes in FT-IR spectroscopy.

For example, the adsorption of carbon monoxide (CO) on Pd exhibits three distinct adsorption modes (Figure 2): atop mode on Pd single sites or nanoparticles with a vibration frequency of 2200–2000 cm⁻¹, bridge mode on 2-fold Pd with a vibration frequency of 2000–1900 cm⁻¹, and hollow mode on 3-fold Pd sites with a vibration frequency of 1900–1800 cm⁻¹ [123, 124]. The presence of the IR band of bridged CO adsorption is a sign of the presence of Pd nanoclusters or nanoparticle species. Muravev *et al.* [125] performed infrared spectroscopy to directly distinguish and quantify Pd single atoms from nanoparticles. The authors assigned the infrared

bands centered at 2143 and 2096 cm^{-1} to CO bonded to Pd_1O_2 (Pd atom bound to CeO_2 via two bridged oxygen) and Pd_1O_1 (Pd atom bound to CeO_2 via one oxygen atom), respectively. The carbonyl bands at 2060 and 1900 cm^{-1} were assigned to CO adsorbed on large semi-oxidized and metallic Pd nanoparticles, respectively. Furthermore, the degree of uniformity of metal sites on a support can be determined by the sharpness full width at half-maximum (FWHM) of the ν_{CO} bands. Nelson *et al.* [89] reported that the FWHM values for the primary carbonyl bands trend toward smaller values as the Pd loading decreases. The FWHM for $\text{Pd}/\text{TiO}_2\text{-0.1}$, $\text{Pd}/\text{TiO}_2\text{-0.05}$, $\text{Pd}/\text{TiO}_2\text{-0.02}$, and $\text{Pd}/\text{TiO}_2\text{-0.01}$ were 22, 15, 14, and 12 cm^{-1} , respectively. The magnitude of FWHM reflects the uniformity of CO adsorption sites, suggesting that $\text{Pd}/\text{TiO}_2\text{-0.01}$ contains the most uniform sites. Moreover, the binding strength of CO on isolated metal atoms is usually different from that on nanoclusters/nanoparticles, which can be examined by different desorption rates/degrees after purging with an inert gas or heating up. It is noteworthy that CO may react with supported metal species, leading to distortion in the coordination structure of the metal species. Hulva *et al.* [126] found that the sintering of Pd or Pt atoms was caused by CO-induced distortion. This distortion occurs because of the formation of a stable carbonyl, which weakens the interaction between the Pd atom and the support, making diffusion becomes facile even at room temperature.

X-ray absorption spectroscopy

X-ray absorption spectroscopy (XAS) plays a crucial role in characterizing single-atom catalysts, as it is element-specific and can offer the average information of absorbing atoms and their surroundings, including atomic coordination, elemental composition, and oxidation state [127-130]. According to the recording energy range, a typical XAS spectroscopy can be divided into two regions: the X-ray absorption near edge structure (XANES) region and the extended X-ray absorption fine structure (EXAFS) region, as depicted in Figure 3.

The XANES, which occurs when core electrons are excited to the valence and conduction bands, can provide valuable information about the oxidation state and coordination environment of the probed element by comparison with reference samples [24, 128, 131-134]. Moreover, high-energy-resolution fluorescence detection (HERFD) XANES, as a newly emerging technique, is highly sensitive and capable for the samples with low loading, providing substantially more structural information than conventional XANES [135, 136]. Maurer *et al.* [137] applied *operando* HERFD-XANES analysis to track the variation of the active state of Pd single sites during the CO oxidation reaction. The EXAFS, originating from the scattering interactions of photoelectrons with the neighboring atoms, can provide valuable information on the local

geometric structure and coordination environment of individual metal atom, such as coordination numbers, bond lengths in different coordination shells, and neighbors species of the absorbing atom, by Fourier/wavelet transform analysis and EXAFS fitting [95, 138, 139].

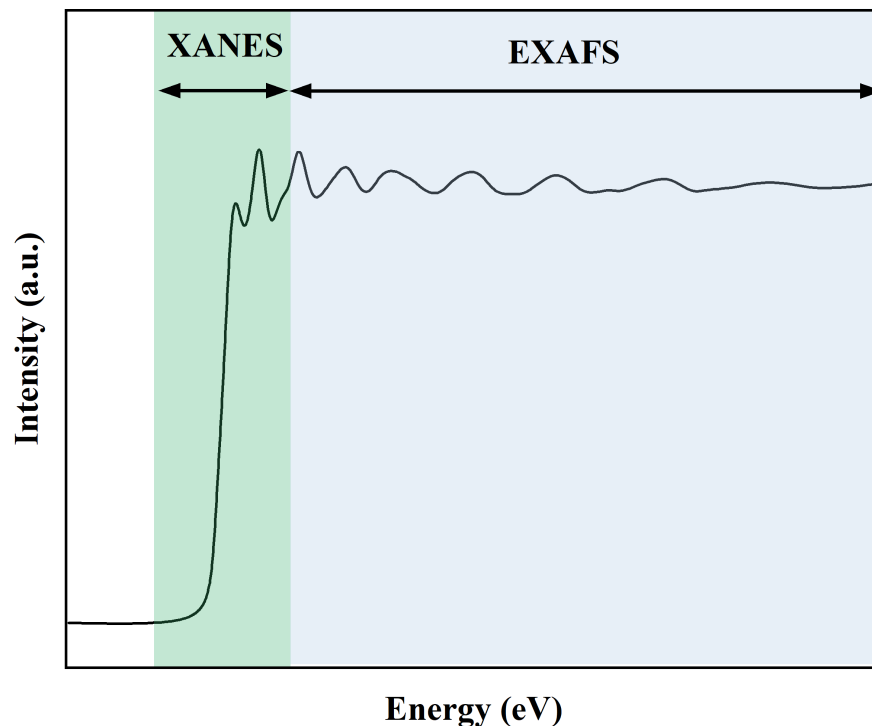


Figure 3. Schematic illustration of the regions in XAS

Furthermore, due to its high sensitivity and rapid response characteristics, *in situ* and *operando* XAS measurements can be employed to monitor the dynamic changes in the geometric structure and chemical state of the catalytic center under reactive atmospheres and conditions [122]. Peterson *et al.* [140] carried out the *operando* XAS to identify the active site of the Pd/La-alumina catalyst for the CO oxidation reaction. The authors found that the presence of intermingled atomically dispersed Pd and La ions on the γ -alumina supports plays a vital role during catalysis. Specifically, the atomically dispersed La ions can stabilize isolated Pd on the alumina surface, and these isolated Pd ions serve as the active center for CO oxidation. The *in situ* and *operando* XAS measurements can describe the stability of isolated atoms on supports and further contribute to the in-depth understanding of chemical state and structure as well as the catalytic mechanisms [137].

Notably, as a non-spatially resolved bulk technique, the structure information obtained by XAS is an average result of the detected element [128]. If there are non-uniform coordination structures in the same sample, the XAS results may lead to misleading structural information.

This issue becomes more significant when atomically dispersed species and nanoclusters coexist in the same sample. In this case, the fitted coordination number cannot accurately reflect the coordination structure. Moreover, the EXAFS fitting cannot distinguish between light scattering atoms that have nearly the same atomic number and similar electron density, such as C/N/O. Therefore, to specify the defined structures, XAS is frequently supplemented with density functional theory (DFT) calculations. However, it is crucial to exercise caution when assigning fitted results, especially when the obtained structures are only hypothetical.

Density functional theory (DFT) calculation

Density functional theory (DFT) is a computational modeling method based on quantum mechanics that is used in the fields of chemistry and physics to calculate the electronic structure of atoms, molecules, and solids [141]. It has become a powerful tool for gaining atomic-level insight into active sites and the electronic structure of isolated Pd catalysts as well as predicting reaction mechanisms, which can provide valuable complements to experimental results. Specifically, DFT calculations can be used to investigate the transition state of the reaction pathway, density of states, Bader charge, and vibration frequency, and so on. For example, Chen *et al.* [85] applied DFT to study the coordination structure of an isolated Pd/PCN catalyst, as well as the mechanism for the Suzuki-Miyaura reaction. The authors selected the ideal crystalline structure of graphitic carbon nitride as the model for the support and identified two preferred Pd sites. One site has the Pd atom located near the surface layer, while the other site has the Pd atom situated in the subsurface layer. The authors further used the optimized model to investigate the path of the Suzuki-Miyaura reaction through transition state calculation. They found that there is an alternative $\text{Pd}^{2+}/\text{Pd}^{4+}$ cycle in the oxidative addition step, instead of the $\text{Pd}^0/\text{Pd}^{2+}$ cycle in the homogeneous system. The oxidative addition step is also the rate-determining step in this reaction. Yu *et al.* [142] performed DFT to investigate the dissociation of O_2 and H_2O_2 over single Pd atom (Pd_1/TiO_2) and PdO clusters ($\text{Pd}_8\text{O}_8/\text{TiO}_2$) structure models. They found that the dissociation energy barrier of O_2 on $\text{Pd}_8\text{O}_8/\text{TiO}_2$ is lower than that on Pd_1/TiO_2 , suggesting that the breaking of O–O bonds is significantly inhibited on Pd_1/TiO_2 . Furthermore, when comparing the $\text{Pd}_8\text{O}_8/\text{TiO}_2$ model to the Pd_1/TiO_2 model, it is observed that the activation of H_2 and O_2 to form $^*\text{OOH}$ is easier on Pd_1/TiO_2 . This $^*\text{OOH}$ is a crucial intermediate in the production of H_2O_2 . Additionally, the degradation of the formed H_2O_2 is more challenging on Pd_1/TiO_2 compared to $\text{Pd}_8\text{O}_8/\text{TiO}_2$.

Density of state (DOS) calculation is a method for gaining insightful understanding of the electronic structure of isolated Pd catalysts. Generally, the density of states (DOS) refers to the

number of electronic states available at a given energy level that electrons are allowed to occupy [143]. It can be used to determine the location and width of energy bands, as well as the position of the Fermi level, providing valuable insights into the band structure and electronic properties of the material [144]. For instance, Ma *et al.* [145] optimized the Pd sites on a Mo-vacancy enriched α -MoC (200) surface and found that the preferred sites are where Pd interacts with 2 carbons (2C) and 4 carbons (4C), respectively. DOS calculations exhibited the decreased hybridization between the d-orbital of Pd and the p orbital of C as the number of Pd atoms increased, indicating the strongest orbital interaction occurs when Pd exists as a single atom. Moreover, the authors demonstrated that there is a charge transfer from the Pd atom to the neighboring C atoms, indicating that the Pd atoms were stabilized at the Mo vacancies of the α -MoC surface through orbital interaction and charge transfer between Pd and the neighboring C atoms. Zhao *et al.* [146] conducted DOS calculations to study the electronic structure of the isolated Pd₁-mpg-C₃N₄ catalysts. The DOS results showed that the valence band (VB) states are contributed by the N-2p and Pd-4d orbitals, while the conduction band (CB) states are dominated by the C-2p and N-2p orbitals. Moreover, the hybridization between the N-2p and Pd-4d orbitals at the Fermi level suggests the formation of strong Pd-N covalent bonds. But for the carbon nitride-supported Pd nanoparticle catalyst (Pd_{NP}-mpg-C₃N₄), there is a more significant contribution from the 4d orbital of Pd to the total density of states at the Fermi level compared to Pd₁-mpg-C₃N₄. The electronic structure of Pd_{NP}-mpg-C₃N₄ resulted in a stronger bond strength with the surface styrene/ethylbenzene adsorbates, thereby leading to a decrease in activity of the styrene hydrogenation reaction.

Bader charge analysis can be employed to evaluate the effective charge of the Pd sites. In 1985, Richard Bader proposed a theory called the Quantum Theory of Atoms in Molecules, which provided an intuitive way for dividing molecules into atoms [147]. He defined an atom purely based on the electronic charge density and used zero-flux surfaces to divide atoms. Based on Bader's theory of atoms in molecules, Graeme Henkelman *et al.* [148] developed a fast algorithm for doing Bader's analysis on a charge density grid. With this program, it is possible to compute the total charge associated with each atom by post-processing the charge density data. Kim *et al.* [149] conducted DFT calculations to identify the stable Pd structure on the (100) facet of CeO₂ in the form of [PdO₄] sites. The authors then performed Bader charge analysis to investigate the electron and spin density around each atom in and surrounding the [PdO₄] sites. They calibrated the Bader charge of Pd and Ce against the oxidation state of known metal complexes and derived an equation to describe their relationship. With the obtained equation, the authors were able to assign formal charges to the Pd and Ce based on the calculated charges.

For example, they determined that Pd was in an overoxidized state greater than +2, which is consistent with their XANES result. Chen *et al.* [87] employed DFT to investigate the preferred Pd sites in different carbon nitride scaffolds, including graphitic carbon nitride (GCN), linear melem oligomers (LMO), poly(triazine imide) (PTI), and poly(heptazine imide) (PHI). The Pd speciation was further studied by Bader charge analysis. It is observed that the Pd atoms are more oxidized in the subsurface layer than in the surface layer. In the presence of chlorine, Pd can coordinate with to form PdN_2Cl_2 , which is also more oxidized than their surface counterparts. Besides, Bader charge analysis provided valuable information for their further experimental and computational XPS study.

Furthermore, calculating of the vibrational frequencies of the CO molecule adsorbed on an isolated Pd atom could provide reference information to test the validity of the proposed model and compare it with the experimental CO-DRIFTS results. Notably, there is a fixed difference of 9 cm^{-1} between the calculated and experimental CO frequency. In the gas phase, the calculated CO stretching frequency is 2134 cm^{-1} (computed at the PBE level), while the experimental CO stretching frequency is 2143 cm^{-1} (obtained from DRIFTS measurement). Thus, a fixed difference of 9 cm^{-1} should be taken into account for all calculated CO frequencies when comparing them to the experimental frequencies.

However, it is also worth noting that there are always gaps between theoretical and experimental investigations of isolated Pd catalysts. For example, only when the Pd species are highly uniform and DFT calculations are performed using multiple candidate models, with the assistance of experimental structural data, can the resulting Pd model be closer to the actual structure. Moreover, the commonly used DFT methods, such as the local density approximation (LDA) and the generalized gradient approximation (GGA), contain approximations that may lead to inaccuracies [150]. To achieve the desired chemical accuracy, the methods at higher theoretical levels are required, such as the Meta-generalized gradient approximation (meta-GGA) and the hybrid functionals [151]. Of course, as the precision of the function increases, the computational expense usually goes higher.

Other characterization methods

Raman spectroscopy is another powerful technique used to investigate the adsorbed intermediates on the active metal center during reactions [152]. Due to the absence of an H_2O signal, Raman spectroscopy is a suitable method for investigating the reaction mechanism in aqueous solutions [153, 154]. Besides, compared to IR spectroscopy, Raman spectroscopy shows high sensitivity in the low frequency region of $1100\text{--}100\text{ cm}^{-1}$, which is typically

associated to the metal-ligand bonds, providing valuable coordination structural information about the metal sites [155]. To enhance the sensitivity for trace chemical species, researchers have developed surface-enhanced Raman spectroscopy (SERS), especially the shell-isolated nanoparticle-enhanced Raman spectroscopy (SHINERS), which can be employed for *in situ* studies [156]. Wei *et al.* [157] carried out the *in situ* SHINERS to monitor the Pd nucleation process from single atoms to nanoparticles, using phenyl isocyanide (PIC) as a probe molecule. Moreover, the catalytic process of hydrogenation of nitro compounds on an isolated Pd catalyst was monitored *in situ* to reveal the unique catalytic properties of SACs at the molecular level.

Electron paramagnetic resonance (EPR) spectroscopy is a powerful technique used to analyze the oxidation states and environment of paramagnetic centers, as well as their interactions with reactants [158]. The *in situ* EPR measurement allows for the collection of information on the changes in active sites under reaction conditions and can be performed under specific atmospheres and pressures [159]. Additionally, low-temperature EPR measurements using liquid nitrogen or helium can be beneficial in enhancing spectral resolution [160]. EPR spectroscopy also offer a possibility to gain insight into unsaturated coordination centers [161]. For example, oxygen vacancies on metal oxides can be detected using EPR, and these sites are usually capable of anchoring single atoms [162]. Cha *et al.* [163] performed EPR measurements to investigate the oxygen defects in TiO₂, which was employed for trapping Pd, Pt, and Au atoms. Two types of oxygen defects were observed: a signal at a g value of 2.0 is attributed to the oxygen vacancies presented in the sheets at regular lattice positions, while the additional broad response at a g value of 1.93 is assigned to the surface-exposed oxygen vacancies. Still, the limitation of this technique is that it can only be used to detect paramagnetic species.

Magic angle spinning NMR (MAS NMR) can be employed to monitor the synthesis process of single-atom catalysts [164-167]. Specifically, it can confirm the successful adsorption of organometallic precursors on the support and verify the anchoring site of isolated metal atoms through changes in the precursors [168, 169]. For example, Ren *et al.* [170] used ³¹P NMR solid-state nuclear magnetic resonance to demonstrate the coordination of monoatomic Pd with the P atoms in the porous organophosphine ligand. The role of P atoms is to serve as anchoring sites for isolated Pd atoms.

As a complementary method for characterizing single atom catalysts, X-ray photoelectron spectroscopy (XPS) is effective in investigating the chemical composition and oxidation state of surface metal species, and near-ambient pressure X-ray photoelectron spectroscopy (NAP-XPS) has been recently developed to study the thermal stability and cationic states of isolated

metal species under realistic conditions [49, 125, 171-173]. Muravev *et al.* [125] performed NAP-XPS to study the dynamic change in the oxidation state of Pd during the CO oxidation reaction. The results demonstrated that half of the atomically dispersed Pd species (337.8 eV) on CeO₂ nanorods transformed into metallic (335.4 eV) and semi-oxidized (336 eV) Pd species at a reaction temperature of 300 °C. In contrast, the Pd speciation in the flame-spray-pyrolysis developed catalyst maintained the same Pd 3d binding energy under the same reaction condition.

1.5 Nitride supported isolated Pd catalysts

One popular nitride support for preparing isolated Pd catalysts is polymeric carbon nitride (PCN). With its characteristic heptazine building units, PCN offers a unique potential for the stabilization of Pd atoms due to the presence of abundant N/C-coordinating sites within the framework intrinsic to its structure [174, 175]. The controllable nanostructure, band structure, and functionalization of PCN offers a wide possibility for tailoring the properties of isolated Pd catalysts [176-178]. Vilé *et al.* [179] anchored atomically dispersed Pd species into the cavities of mesoporous carbon nitride (mpg-C₃N₄) through a NaBH₄ reduction method. The atomic dispersion of Pd was confirmed through STEM, XAS, and XPS characterization. In comparison to Pd nanoparticle catalysts, the isolated Pd catalyst exhibited higher reactivity and selectivity for the continuous-flow three-phase hydrogenation of alkynes and nitroarenes. The authors demonstrated that this is due to the facile activation of hydrogen and adsorption of alkynes on the atomically dispersed Pd sites. Moreover, Vorobyeva *et al.* [180] introduced isolated Pd species on mesoporous carbon-doped g-C₃N₄ using a postsynthetic microwave irradiation-assisted method. Their experimental and theoretical results demonstrated that the higher C/N ratio in mesoporous carbon-doped g-C₃N₄ can greatly improve its surface area, crystal size, and thermal stability, resulting in more sites to adsorb and stabilize the Pd atoms. The Pd species existed in the form of Pd⁴⁺ (338.5 eV) and Pd²⁺ (336.9 eV) in all samples. The catalysts with a higher Pd²⁺/Pd⁴⁺ ratio exhibited better catalytic efficiency in the three-phase semi-hydrogenation of 2-methyl-3-butyl-2-ol in a continuous-flow reactor. Likewise, through a microwave irradiation assisted deposition method, Chen *et al.* [85] incorporated Pd atoms into exfoliated graphitic carbon nitride (Pd-ECN) with a Pd loading of 0.66 wt%. The presence of isolated Pd atoms was confirmed by AC-STEM and XAS, and the Pd 3d_{5/2} spectra exhibited two positively charged Pd species, tentatively assigned to Pd²⁺ at 336.5 eV and Pd⁴⁺ at 338.3 eV. The Pd-ECN catalyst exhibited excellent activity and stability for the continuous Suzuki-Miyaura coupling of aryl bromides with phenylboronic acid pinacol ester derivatives. This catalyst outperformed both homogeneous Pd complexes and heterogeneous Pd nanoparticles.

DFT calculations revealed that the macroheterocycles of ECN play a crucial role in enhancing the structural properties and stability of single Pd atoms. This not only endows the isolated Pd species with adaptive coordination, but also allows them to participate in and facilitate each catalytic step.

Two-dimensional hexagonal boron nitride (h-BN) has a planar structure, consisting of alternating boron and nitrogen atoms linked to one another via covalent B–N bonds. The lone-pair dangling bonds of the boron and nitrogen vacancies can offer anchoring sites for individual metal atoms. Li *et al.* [181] reported the deposition of atomically dispersed Pd atoms on defect-containing h-BN nanosheets (Pd₁/h-BN) using a low-temperature photochemical strategy. The combination of the HAADF-STEM image, CO-DRIFTS spectrum, and XAFS measurements confirmed the presence of isolated Pd atoms on the defective h-BN. DFT calculations suggested that the nitrogen-containing boron vacancy can provide stable anchoring sites for Pd atoms. This catalyst exhibited exceptional efficiency in the chemoselective hydrogenation of cinnamaldehyde, along with excellent stability and selectivity over eight cycles. Similarly, Büchele *et al.* [182] reported the synthesis of a porous boron nitride-supported isolated Pd catalyst through an incipient wetness impregnation method, with a Pd loading of 0.09 wt%. The HAADF-STEM confirmed the presence of atomically dispersed Pd species, and EXAFS verified the existence of Pd–N bonds with a bond length of 1.58 Å. Further XPS analysis identified a high contribution of Pd⁴⁺ in the atomically dispersed Pd catalyst. However, the authors found that the isolated Pd catalyst was virtually inactive for the batch semi-hydrogenation of 1-hexyne due to its highly oxidized nature. Deng *et al.* [183] used density functional theory (DFT) calculations to study single Pd atoms supported on defective two-dimensional boron nitride materials (2D-BN) with a boron vacancy. The authors mentioned that the stability of Pd/2D-BN was higher than that of bulk Pd. The performance of the oxygen reduction reaction (ORR) was predicted using the volcano plot. The Pd/2D-BN catalysts, with a moderate binding energy to *OH species, exhibited high ORR activity. This high activity is attributed to the precise Pd–N₃ coordination in the Pd/2D-BN catalysts. Moreover, Pd/BN catalyzed ORR via a direct 4e[−] pathway with a small reaction barrier of 0.42 eV, which was lower than that achieved by Pt-based catalysts (0.79 eV).

1.6 Oxide supported isolated Pd catalysts

Oxide supports exhibit distinct and variable properties, such as surface acidity/basicity and redox features (especially for reducible metals), which contribute to their unique catalytic properties [184, 185]. The abundant defect sites (steps, corners, and vacancies) and surface

–OH groups on the oxide supports can serve as anchor sites for individual metal atoms [186]. Moreover, the robustness of oxides at high temperatures can enhance the thermal stability of isolated Pd catalysts, preventing Pd aggregation [187]. More importantly, for oxide-supported isolated Pd catalysts, the interaction of the Pd atom to oxide supports can greatly affect its electronic and geometric structures, thereby affecting overall stability, reactivity, and selectivity [188].

Hackett *et al.* [189] reported the synthesis of mesoporous alumina-supported isolated Pd catalysts (Pd/meso- Al_2O_3) using an incipient wetness impregnation method, with Pd loadings of 0.03 wt%. EXAFS analysis and high-resolution HAADF-STEM provided unambiguous evidence that Pd mainly exists as individual atoms on Al_2O_3 at a low Pd loading (0.03 wt%) but aggregated into Pd nanoparticles at a high Pd loading (4.7 wt%). XANES analysis and XPS measurements confirmed that mesoporous alumina stabilizes Pd in the +2 oxidation state. The isolated Pd/meso- Al_2O_3 catalyst with a Pd loading of 0.03 wt% is the most effective catalyst for the oxidation of cinnamyl alcohol. Operando EXAFS measurements confirmed that the Pd(II) centers remained unchanged over the course of the reaction for periods of days.

Jin *et al.* [190] reported an isolated Pd catalyst ($\text{Pd}_1\text{-Ti}_{0.87}\text{O}_2$) supported on a monolayered cation-deficient $\text{Ti}_{0.87}\text{O}_2$ nanosheet. This catalyst was prepared through a strong electrostatic interaction between Pd cations and Ti vacancies. The Pd loading was controlled at 0.1 wt% to achieve a uniform dispersion of isolated Pd atoms on the surface of $\text{Ti}_{0.87}\text{O}_2$ nanosheets. STEM confirmed the presence of atomic Pd species, and further EXAFS analysis showed that the Pd_1 was medially bonded to four oxygen atoms from the $\text{Ti}_{0.87}\text{O}_2$ support. Further DFT calculations revealed that Pd_1 in the Pd_1O_4 slab maintained an enriched charge distribution, which was caused by charge transfer from the support. $\text{Pd}_1\text{-Ti}_{0.87}\text{O}_2$ exhibited superior activity in the room-temperature Suzuki reaction, with TOF of 11110 h^{-1} . This TOF value was over 200 times higher than that of homogeneous PdCl_2 and $\text{Pd}(\text{OAc})_2$ catalysts. *In situ* FTIR measurements and XAFS analysis demonstrated that the extraordinary activity was attributed to the efficient dissociation of bromobenzene by Pd_1 , particularly the cleavage of the C–Br bond.

Jiang *et al.* [123] employed an incipient wetness impregnation followed by a high-temperature atom trapping strategy to fabricate a 1 wt% single-atom Pd catalyst supported on CeO_2 (Pd_1/CeO_2). CO-DRIFTS and synchrotron-based XAS measurements confirmed the atomic dispersion of cationic Pd^{2+} on the CeO_2 surface. Additionally, Raman spectroscopy revealed an increased amount of oxygen vacancies on the CeO_2 surface induced by 800 °C air calcination, resulting in the unsaturated coordination of Pd^{2+} on CeO_2 . The combination of light-on and

light-off experiments, coupled with CO-DRIFTS and XAS measurements, elucidated that the unsaturated coordination of Pd^{2+} exhibited better performance for low-temperature CO oxidation compared to the fully coordinated Pd^{2+} .

He *et al.* [191] reported the kilogram-scale synthesis of an atomically dispersed Pd species on zinc oxide (Pd_1/ZnO) catalyst through ball-milling and calcination treatment of commercial $\text{Pd}(\text{acac})_2$ and $\text{Zn}(\text{acac})_2$. HAADF-STEM and EXAFS measurements confirmed the presence of atomically dispersed Pd species and the absence of Pd nanoparticles. The ball-milling process had a significant impact on the microstructures of the milled substrates. XPS revealed that Pd was present on the ZnO surface in the +2 oxidation state. The Pd_1/ZnO catalyst exhibited exceptional performance and stability in phenylacetylene semi-hydrogenation and CO oxidation reactions.

Chen *et al.* [192] reported a FeO_x -supported single-atom Pd bifunctional catalyst stabilized through a coprecipitation method. The Pd/FeO_x catalyst demonstrated higher atomic efficiency for the water-gas shift reaction compared to its nanoparticle counterpart. It also exhibited good stability, even in the presence of CO_2 and H_2 . Through HRTEM, *in situ* DRIFTS, and TPSR-MS measurements, the authors discovered that individual Pd atoms significantly enhance the reducibility of FeO_x and facilitate the formation of oxygen vacancies, thereby promoting the dissociation of H_2O to form H_2 and atomic O. The atomic oxygen could further react with the linearly adsorbed CO species on isolated Pd sites through a redox mechanism, leading to increased CO conversion on Pd/FeO_x .

2. Objectives and strategies of this thesis

Isolated Pd catalysts are excellent candidates for thermocatalysis, photocatalysis, and electrocatalysis due to their unique electronic and coordination structures, as well as their high atomic utilization efficiency. Considering these advantages, this thesis is aiming at the creation of high-loading isolated Pd catalysts on PCN support. The abundant multidentate sites in PCN can stabilize Pd atoms through covalent bonds, effectively preventing aggregation during the synthesis and reaction processes. Furthermore, by extending the support from nitride to oxide, the charge state of Pd is expected to be different since the surrounding atoms being oxygen instead of nitrogen. Therefore, in this thesis, isolated Pd sites were achieved on both nitride (PCN, hBN, Si₃N₄, and TiN) and oxide supports (TiO₂, B₂O₃, SiO₂, ZnO, and Al₂O₃). The effects of surrounding nitrogen or oxygen atoms on the coordination and electronic structures of the Pd center were thoroughly investigated using various experimental and theoretical techniques.

2.1 Modification of PCN support through four different exfoliation strategies

Heptazine-based polymeric carbon nitride (PCN) has attracted extensive attention due to its easy preparation with the abundance of raw materials and its suitable optical bandgap of 2.7 eV. The structure of PCN (Figure 4a) is based on the building block of a heptazine core. The in-plane structure (Figure 4b) has discernible basal planes of individual polymer strands connected by hydrogen bonds between the nitrogen in the rings of one strand and NH or NH₂ groups of an adjacent strand [193]. The out-of-plane structure (Figure 4c) is that the heptazine ring from one layer eclipses the next layer through van der Waals forces.

The combination structure of in-plane hydrogen bonds and out-of-plane weak van der Waals forces allows for the exfoliation into a 2D nanosheet structure. This could result in enhanced surface activity, as well as unique optical and electronic properties [194, 195]. Thus, various exfoliation approaches have been developed to prepare ultrathin PCN nanosheets, like thermal oxidation etching [196-199], chemical oxidation method [200, 201], liquid-assisted ultrasonic method [176, 202, 203], and hydrothermal oxidation method [204-206]. Several special methods have also been reported to effectively delaminate bulk PCN into 2D nanosheets, such as melamine-assisted method [207, 208], liquid ammonia-assisted lithiation, steam reforming method [209-211], and mechanical grinding method [212].

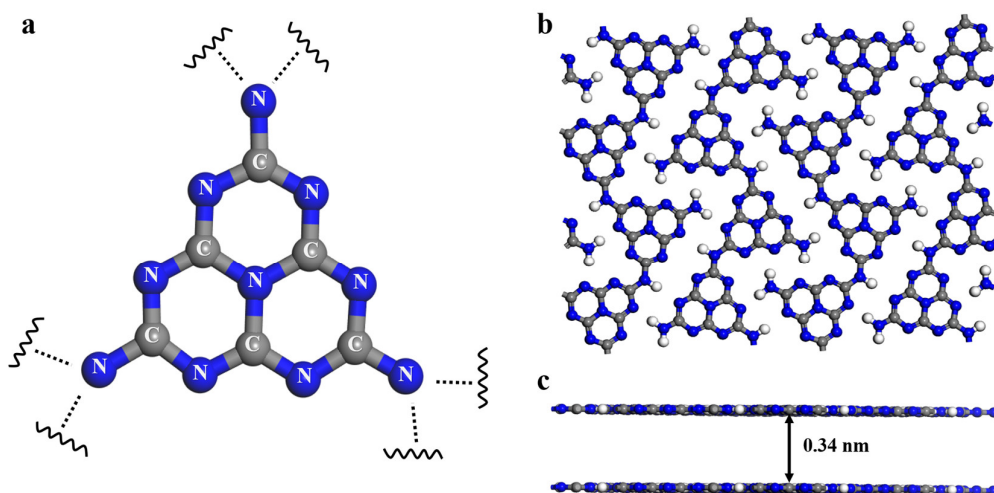


Figure 4. (a) Heptazine structures of PCN, (b) in-plane repeats between heptazine units, and (c) out of plane π - π stacking motif of the same heptazines on top of each other

Notably, the morphology and electronic structure of PCN nanosheets prepared by different methods are not identical. In the case of PCN treated by the thermal oxidation etching method, the in-plane hydrogen bonds between the adjacent strands of heptazine subunits are destroyed during the oxidation process in air. This leads to a reduction in thickness through layer-by-layer thermal etching [196]. Besides, motivated by the development of graphene oxide (GO), the treatment of PCN with oxidizers, such as H_2SO_4 , followed by the addition of deionized water, results in the addition of surface hydroxyl and epoxide groups [201]. The exfoliation mechanism in concentrated H_2SO_4 is due to its oxidation and protonation effects, as well as the heating effect that occurs after mixing with H_2O . These effects facilitate the cleavage of weak hydrogen bonds and structural defects in PCN, leading to the formation of smaller fragments. For liquid-assisted ultrasonic exfoliation, the ultrasonic wave's acoustic energy is transmitted to overcome the van der Waals forces between the layers to produce nanosheets [203]. Thus, PCN nanosheets can be prepared using various methods, which are believed to result in a range of physicochemical properties, such as surface area, optical/electronic properties, surface groups, and structural defects, *etc.*

Here, four common exfoliation strategies (liquid ultrasonication, thermal oxidation, hydrothermal oxidation, and chemical oxidation) were employed to fabricate 2D thin-layered PCN. Detailed investigations of differently exfoliated PCN were carried out to understand the relationship between the exfoliation mechanism and the structural/optical properties. The findings allow conclusions on the properties of the differently exfoliated PCN to determine appropriate support for the deposition of Pd.

2.2 Investigation of the role of nitride and oxide supports for the charge state of isolated Pd catalysts

Isolated Pd catalysts have gained great attention due to exclusively high activity and selectivity brought by their unsaturated coordination sites and unique electronic structures. However, understanding how the support influences the electronic structure of isolated Pd catalysts remains a challenge. Often, the isolated Pd atoms are stabilized by chemical bonds to the support and are charged. The support, to some extent, resembles the organic ligand of homogeneous catalysts, and the ligand plays an important role in activating and stabilizing intermediates [213]. Thus, modulating the coordination between the Pd atoms and the supports can significantly alter the oxidation state, electronic structure, and steric configuration of isolated Pd catalysts, thereby regulating their catalytic properties. Among various types of supported isolated Pd catalysts, those based on nitride and oxide supports have attracted particular attention [47, 214, 215]. The abundant defective sites (oxygen and titanium vacancies) as well as hydroxyls groups on the oxide surface can provide plenty of anchoring sites for single metal atoms [23]. Besides, numerous nitride materials, as well as carbon-nitrogen materials derived from MOFs and polymers, have also been used as supports to prepare Pd single-atom catalyst [216-219]. Therefore, considering nitrides and oxides as supports remains of continued interest for Pd single-atom catalysts, it is vital to understand how the binding environment of the Pd sites on these supports affects their electronic structure.

Herein, two types of supports were used for the synthesis of isolated Pd catalysts: nitride supports (PCN, hBN, Si₃N₄, and TiN) and oxide supports (TiO₂, B₂O₃, SiO₂, ZnO, and Al₂O₃). Upon depositing Pd using the same procedure, it was assumed that the supports were the only factor influencing the electronic and coordination structure of the synthesized Pd catalysts. Various characterization methods, including XPS, XAS, STEM, CO-DRIFTS, and Bader charge analysis, were performed to study the electronic and coordination structure of the as-synthesized Pd catalysts. Besides, based on the periodic trend in electronegativity, the relationship between the experimental oxidation state and computational Bader charge was investigated. Furthermore, the relationship between the vibrational frequency of carbonyl species and the experimental oxidation state of Pd was studied as well. In the end, the influence of Pd loading and Pd particle size on the Pd/PCN catalysts was evaluated by the Suzuki-Miyaura coupling reaction.

3. Experiments and methods

3.1 Catalyst synthesis

3.1.1 Synthesis of PCN nanosheet through four exfoliation strategies

Materials. Urea (99.0–100.5%) was purchased from Sigma-Aldrich. Sulfuric acid (H_2SO_4 , 95%) was purchased from Fisher Scientific. All the chemicals were used as received without any purification.

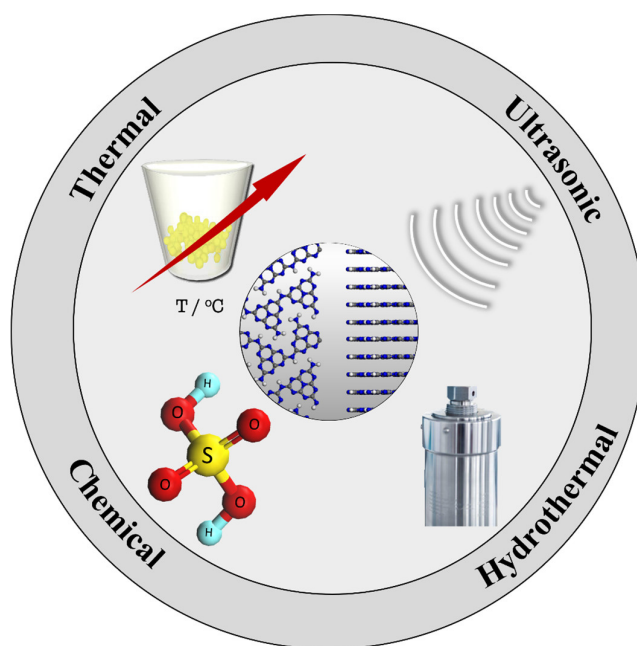


Figure 5. Schematic illustration of different exfoliation processes for synthesizing nanolayered PCN.

Synthesis of pristine PCN. 15 g of urea was packed into a 60 mL ceramic crucible with a cover and then heated at 550 °C for 4 h in a muffle furnace in air at a heating rate of 2 °C min⁻¹.

Synthesis of t-CN. The catalysts were prepared according to a reported thermal oxidation etching method [196]. 200 mg of pristine PCN was packed into a 30 mL ceramic crucible without a cover and heated at 500 °C in a muffle furnace in air with a ramping rate of 5 °C min⁻¹ for either 3 h or 6 h.

Synthesis of c-CN. c-CN was synthesized according to a reported chemical oxidation method with slight modifications [200]. 200 mg of pristine PCN were mixed with 5 mL of H_2SO_4 (95%) in a 25 mL flask and stirred for either 8 h or 16 h at room temperature. Then, the dispersion was slowly poured into 200 mL of deionized water, and the color of the dispersion changed from yellow to white. After stirring for 10 min, the white product was separated by filtration using a

0.1 μm PTFE membrane filter (Millipore JVWP04700) and dried at 80 $^{\circ}\text{C}$ for 16 h in air. The dry product turned a bright yellow color. The product was further washed twice with deionized water at 80 $^{\circ}\text{C}$ to remove the remaining H_2SO_4 . The final product collection followed the same filtration procedure as described above.

Synthesis of u-CN. u-CN was prepared using a liquid-ultrasonic exfoliation method. The synthesis was conducted in a self-constructed device based on a UIP1000hd ultrasonic processor (Hielscher Ultrasonics GmbH), which consisted of a generator, a transducer, a sonotrode (BS2D50F), and a stainless-steel pressure vessel (10 L) [220]. 100 mg of pristine PCN was dispersed in 20 mL of deionized water and stirred at room temperature for 1 h. The prepared suspension was then transferred into a 45 mL Parr autoclave (series 4700) and placed on a grid inside the pressure vessel, maintaining a distance of 35 mm from the sonotrode. The vessel was sealed and filled with water as a transfer medium. The pressure was adjusted to 5 bar. The ultrasonic processor maintained a constant frequency of 20 kHz. The amplitude of the generator was adjusted to 80%. The ultrasonic experiments were performed for either 8 or 16 h. Notably, the pressure and temperature gradually increased over time to about 5.5 bar and 69 $^{\circ}\text{C}$ after 8 h, respectively. The yellow powder was collected by filtration with a 0.1 μm PTFE membrane filter and then washed with distilled water. The product was finally dried in an oven in air at 80 $^{\circ}\text{C}$ for 16 h.

Synthesis of h-CN. The preparation of h-CN followed a hydrothermal exfoliation method, as reported in [204], with slightly modified procedures. 500 mg of PCN powder was dispersed into 100 mL of deionized water and stirred at room temperature for 1 hour. Then, the suspension was transferred into a Teflon-sealed autoclave (with a volume of 150 mL, manufactured by Berghof Products + Instruments GmbH) and maintained at 180 $^{\circ}\text{C}$ for either 12 or 24 h. The resulting product was collected by filtration using a 0.1 μm PTFE membrane filter. The filtrate solution and the insoluble solids were dried at 80 $^{\circ}\text{C}$ for 16 h in air.

3.1.2 Synthesis of nitride and oxide supported isolated Pd catalysts

Materials. Palladium(II) trifluoroacetate ($\text{Pd}(\text{TFA})_2$, 97%, Sigma-Aldrich), Palladium(II) acetylacetonate ($\text{Pd}(\text{acac})_2$, $\geq 99.8\%$, Sigma-Aldrich), Palladium(II) acetate ($\text{Pd}(\text{OAc})_2$, 98%, Sigma-Aldrich), Acetone ($\geq 99.8\%$, Fisher Chemical), Urea (99.0–100.5%, Alfa Aesar), TiN (10–20 nm, IOLITEC GmbH), hBN (99.5%, Alfa Aesar), Si_3N_4 (15–30 nm, Alfa Aesar), TiO_2 (Aeroxide P25, Evonik Industries), ZnO (20 nm, IOLITEC GmbH), Al_2O_3 (gamma-phase, 99.9%, Alfa Aesar), B_2O_3 (99.98%, Alfa Aesar), SiO_2 (10–20 nm, IOLITEC GmbH) were used as received without further purification.

Synthesis of the PCN supports

The PCN support was synthesized using the same method as described above for t-CN-3, with the only difference being that the amount of bulk PCN was increased to 500 mg instead of 200 mg.

Synthesis of the supported Pd catalysts

500 mg powders of support materials (PCN, TiN, hBN, Si₃N₄, TiO₂, Al₂O₃, ZnO, B₂O₃, and SiO₂) were dispersed in 25 mL of acetone and stirred for 20 min. Pd(TFA)₂ (or Pd(acac)₂ or Pd(OAc)₂) was dissolved in acetone to form a 10 mM solution. Then, 4.84 mL of the above solution was added dropwise, with stirring, to the catalyst slurry to achieve the desired 1 wt% loading. The slurry was stirred for another 24 h, and the solvent acetone was gradually removed by evacuation. The powder was then dried at 80 °C for 24 h in Ar flow (100 sccm). The Pd/PCN catalysts with different Pd loadings (0.5 wt%, 2 wt%, 4 wt%, 8 wt%, and 16 wt%) were synthesized using the same procedure, with the only variation being the volume of the Pd precursor solution.

To avoid the influence of remaining Pd precursor on the Suzuki-Miyaura cross-coupling reaction, the as-synthesized Pd/PCN samples were washed with acetone for six times, and details are as follows: the Pd/PCN samples was first stirred in a 300 mL acetone for 30 min at room temperature and repeated this procedure for three times; After that, the Pd/PCN sample was washed with a 300 mL acetone for 3 h at room temperature and repeated that three times. For samples with Pd loading above 4 wt%, 900 mL of acetone was used for further washing at room temperature for 3 h and repeated seven times. Sample collection was achieved by filtration with a 0.1 µm PTFE membrane filter. Both the washing and filtering processes are carried out under argon protection. The resultant samples were dried in a tube furnace at 80 °C for 12 h in argon flow.

3.2 Experimental characterization

Electron microscope

Scanning electron microscopy (SEM) was used to characterize the morphology and microstructure of the materials. The SEM micrographs were recorded using a MERLIN® VP Compact (Zeiss, Oberkochen, Germany) equipped with a high-efficiency secondary electron detector (HE-SE2), an In-lens Duo detector, and an energy-dispersive X-ray (EDX) detector (xFlash 6-30, Co. Bruker, Berlin). The images were recorded with accelerating voltages of 2.0

and 5.0 kV, respectively. Representative areas of the samples were analyzed by QUANTAX ESPRIT Microanalysis software (version 2.0). The samples were mounted on an Al-SEM-carrier with adhesive conductive carbon tape (co. PLANO, Wetzlar) and coated with carbon under vacuum (EM SCD 500, Co. Leica, Bensheim). Note: The measurement was carried out by Tim Peppel (LIKAT) and Armin Springer (EMZ, University of Rostock).

Atomic Force Microscopy (AFM) was used to evaluate the morphologies and thickness of the samples. The measurements were conducted on a Shimadzu SPM-9700 in tapping mode. The materials were deposited on the surface of a freshly cleaved mica by a method of drop-casting the corresponding suspension. The results were analyzed using Gwyddion software.

Scanning transmission electron microscopy (STEM) was carried out to visualize individual Pd atoms in the as-synthesized samples. The 0.5 wt%, 2 wt%, 4 wt%, and 16 wt% Pd/PCN samples were measured at LIKAT Analytical Services Group by Nils Rockstroh. The measurement was performed at 200 kV with an aberration-corrected JEM-ARM200F (JEOL, Corrector: CEOS). The microscope was further equipped with a JED-2300 energy-dispersive X-ray spectrometer (JEOL) featuring a silicon drift detector (dry SD60GV). High-angle annular dark field (HAADF) and annular bright field (ABF) detectors were used for general imaging. The solid powders were deposited onto a holey carbon-supported Cu grid (mesh 300) without any pretreatment. The grid was then transferred into the microscope. The washed 2 wt% Pd/PCN sample was measured at the University of Rostock by Kevin Oldenburg. The measurement was conducted at 200 kV with an aberration-corrected ARM200CF NeoARM (JEOL, Corrector: CEOS). The measurement of the 1 wt% Pd/TiO₂ sample was contributed by Song Hong and Zhenyu Sun from Beijing University of Chemical Technology, which was recorded using a JEOL ARM200 microscope with a 200 kV accelerating voltage.

Electron paramagnetic resonance

Electron paramagnetic resonance (EPR) spectroscopy was performed to monitor the separation and transfer of charge carriers under visible light irradiation. The measurements were conducted on a Bruker EMX CW-micro X-band EPR spectrometer (microwave frequency \approx 9.8 GHz) using an ER4119HS-WI optical resonator and a flat quartz cell (Starna) with an inner distance of 0.5 mm. The spectra were recorded with a microwave power of 6.6 mW, a modulation frequency of 100 kHz, and a modulation amplitude of 5 G. The measurements were conducted at room temperature. The light source is a 300 W Xe-arc lamp (LOT-Quantum Design GmbH) equipped with a cutoff filter ($>$ 420 nm). For spin-trapping experiments, 10 μ L of the commercial 5,5-dimethyl-1-pyrroline N-oxide (DMPO) was mixed with 500 μ L of

deoxygenated water and then injected into the flat cell containing a 30 mg sample. O₂ was directly bubbled into the aqueous suspension of the flat cell. The first two spectra were recorded in the absence of light. The spectra for spin-trap experiments were recorded at room temperature with a microwave power of 6.7 mW, a modulation frequency of 100 kHz, and a modulation amplitude of 1 G, respectively. *g* values were calculated using equation (1):

$$g = \frac{h\nu}{\beta B_0} \quad (1)$$

In which, *h* is the Planck constant (6.626×10^{-34} J·s), *ν* is the frequency, *β* is the Bohr magneton (9.27×10^{-27} J·mT⁻¹), and *B*₀ is the resonance field. Calibration of the *g* values was performed with a DPPH (2,2-diphenyl-1-picrylhydrazyl) standard (*g* = 2.0036 ± 0.0004). Note: The measurement was performed by Xinchao Dai and Jabor Rabeah from LIKAT.

Electrochemical measurements.

Mott-Schottky plots were performed to study the flat band potential (versus Ag/AgCl at pH = 6.6) of the as-obtained samples. The measurements were carried out on an electrochemical workstation (ZAHNER PP211) equipped with a standard three-electrode system. The prepared samples (10% Nafion solution as the binder) coated on FTO sheet glass was used as the working electrode. The platinum wire and Ag/AgCl (3 mol L⁻¹ NaCl) were used as the counter and reference electrodes, respectively. The electrolyte solution was a 0.5 mol L⁻¹ Na₂SO₄ solution. Transient photocurrents (TPC) were measured in the same three-electrode system to evaluate the behavior of charge carrier transfer. The 375 nm UV light was produced by a 60 W LED lamp. The working electrodes were prepared as follows: 10 mg of the sample was dispersed in a solution containing 0.1 mL of Nafion and 0.9 mL of isopropanol (99.8%). The mixture was then subjected to ultrasonic treatment for 20 min to form a homogeneous slurry. Then, 0.2 mL of slurry was dropped onto the pre-cleaned 2.5 cm × 2.5 cm FTO glass, followed by air-drying before measurement.

Elemental analysis

Elemental analysis was conducted on a Leco TruSpec Micro CHNS Elemental analyzer. The samples were burned at 1100 °C with pure oxygen in a helium stream. The quantitative analysis of carbon (C), hydrogen (H), nitrogen (N), and sulfur (S) was accomplished through high-temperature digestion coupled with dynamic gas component separation. Carbon, hydrogen, and sulfur were detected by IR detectors. Nitrogen was detected by a TCD detector. Note: The measurement was performed at the LIKAT Analytical Services Group by Astrid Lehmann.

Inductively coupled plasma optical emission spectroscopy

Inductively coupled plasma-optical emission spectroscopy (ICP-OES) was used to evaluate the Pd composition of as-synthesized catalysts. The measurements were performed on a Varian 715-ES ICP emission spectrometer. 20–30 mg of the sample was dissolved in 6 mL of aqua regia and 2 mL of hydrofluoric acid. The mixture was digested in a microwave-assisted sample preparation system “Multiwave Pro” (Anton Paar/Perkin-Elmer) at a temperature of 200 °C and a pressure of 50 bar. The prepared solution was filled up to 100 mL with deionized water and then measured. The analysis was done by ICP Expert software. Note: The measurement was performed at the LIKAT Analytical Services Group by Anja Simmola.

Infrared spectroscopy

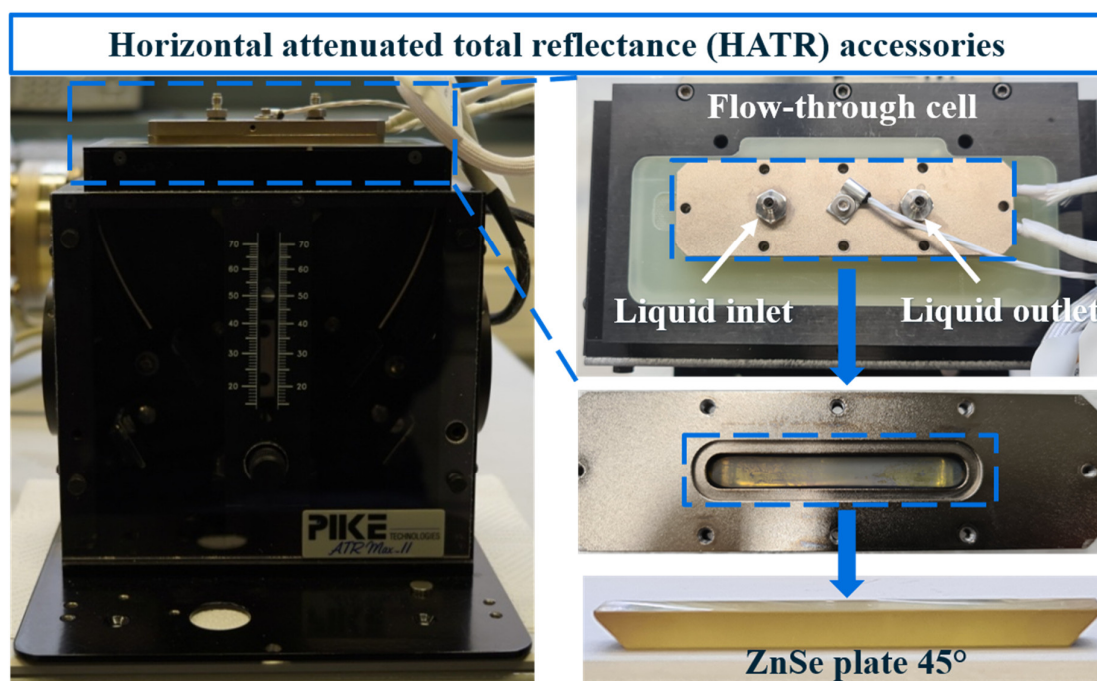


Figure 6. Horizontal Attenuated Total Reflectance (HATR) accessories with flow-through cell and ZnSe plate, implemented in a Nicolet iS50 FT-IR spectrometer.

In situ attenuated total reflectance (ATR) measurements were used to monitor the dynamic changes of the substrate and product in the liquid phase during the Suzuki coupling experiments. The experiments were recorded using a setup consisting of a commercial high throughput and variable angle horizontal ATR accessory (Pike Technologies, ATRMAX II™, see Figure 6), which was mounted in a sample chamber of a Nicolet™ iS50 FTIR Spectrometer equipped with a liquid-nitrogen cooled MCT detector. The attached ATR crystal is a trapezoidal ZnSe internal reflection element (45°, 56×10×4 mm³, Pike Technologies). All ATR-IR spectra were obtained

by averaging 100 scans at 4 cm^{-1} resolution. All experiments were carried out at room temperature ($25\text{ }^{\circ}\text{C}$) in air. The solution flow was regulated by a compact dual piston pump (Knauer, Azura P4.1S), and the flow rates used in the all experiments were 2 mL min^{-1} .

For the substrate calibration experiments, the background spectrum was collected with the solvent ethanol/ H_2O ($v/v = 2/1$). Then, the solvent was changed to a solution containing one or two substrates [either bromobenzene (1 mmol, 99%, Alfa Aesar), iodobenzene (1 mmol, 98%, Alfa Aesar), phenylboronic acid (2 mmol, 98+%, Alfa Aesar), or K_2CO_3 (2 mmol, $\geq 99\%$, Carl Roth)] in a 15 mL solvent ethanol/ H_2O ($v/v = 2/1$) and recording the spectrum. No catalysts are required for the substrate calibration experiments.

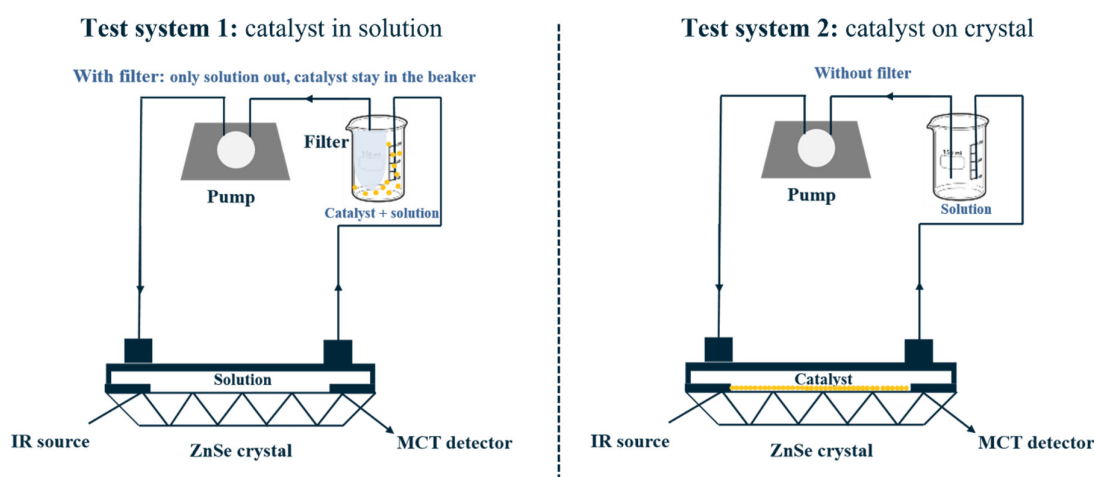


Figure 7. Schematic representation of the ATR set-up used to monitor the Suzuki-Miyaura reaction.

Test system 1 (catalyst in solution, see Figure 7) was performed to monitor the dynamic changes in substrate and product during the reaction. First, the background spectrum was collected with the reaction solution [bromobenzene (1 mmol), phenylboronic acid (2 mmol), and K_2CO_3 (2 mmol) in a 15 mL ethanol/ H_2O solvent ($v/v = 2/1$)]. Then, the catalyst was added to the beaker, and a filter was used to separate the catalyst from the solution. With the filter, only the reaction solution is able to pass through the ZnSe crystal surface, while the Pd catalyst stays in the beaker. This allows for recording the changing spectra of the reaction solution.

Test system 2 (catalyst on ATR crystal) was used to collect information about the absorbing intermediate on the catalyst surface. The catalysts were coated onto a ZnSe crystal using a drop-drying method. First, collect the background spectrum using the solvent ethanol/ H_2O ($v/v = 2/1$). Afterward, the solvent was changed to the reaction solution containing a mixture of bromobenzene (1 mmol), phenylboronic acid (2 mmol), and K_2CO_3 (2 mmol) in a 15 mL solvent of ethanol/ H_2O ($v/v = 2/1$). The procedure for catalyst coating is as follows: The catalyst

slurry (5 mg in 2 mL of acetone) was first sonicated for 5 min. Then, a drop-coating method was used to deposit it onto the ZnSe crystal, followed by air-drying before measurement.

Ex situ diffuse reflectance infrared Fourier transform spectroscopy (DRIFTS) was applied to analyze the molecular structure of the as-synthesized catalysts. The measurements were recorded on a Thermo Scientific Nicolet iS50 spectrometer, which was equipped with a mercury-cadmium-telluride (MCT) detector, a mirror system (Praying Mantis™, Harrick), and a high temperature *in situ* DRIFT cell (Harrick), as depicted in Figure 8. Each spectrum was collected by averaging 200 scans at a resolution of 4 cm⁻¹ in the 4000–400 cm⁻¹ range. The samples were pretreated at 150°C in Ar (30 sccm) for 30 min and then cooled down to room temperature.

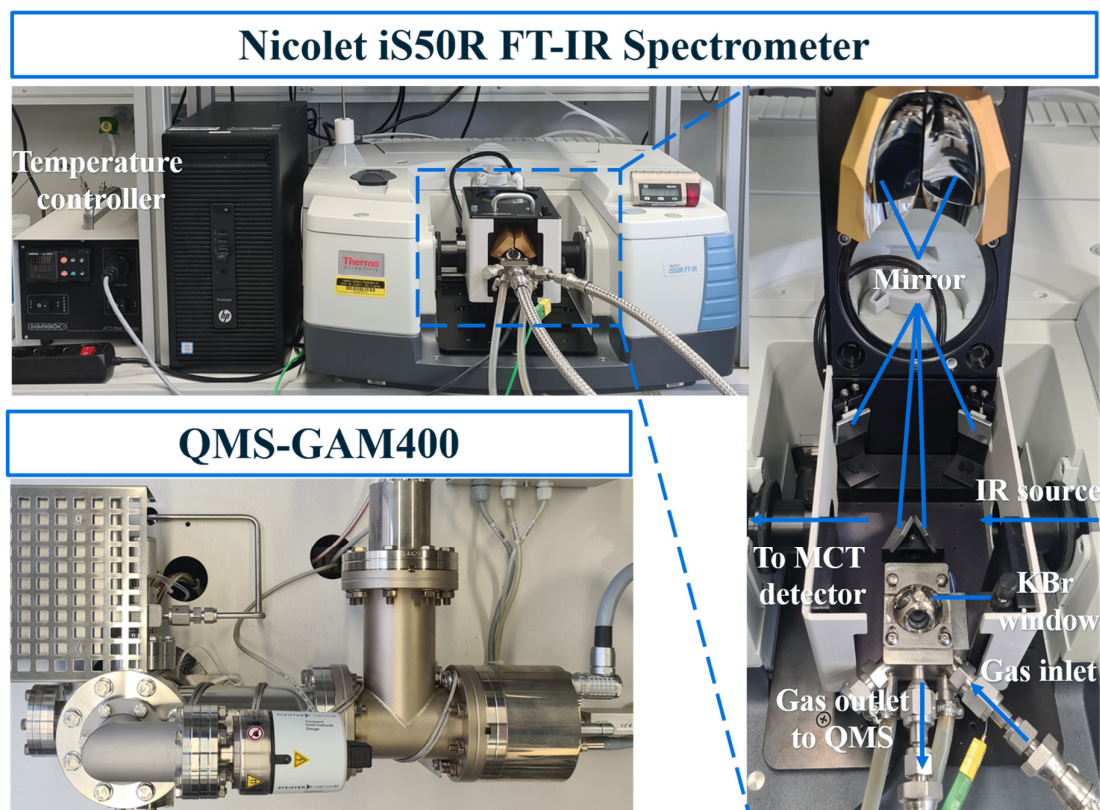


Figure 8. DRIFTS cell with Praying Manti accessory, implemented in a Nicolet iS50 FT-IR spectrometer; the outlet is connected to QMS GAM400.

In situ DRIFTS spectra of CO adsorption and CO oxidation measurements were used to monitor the bonding and reactivity of CO molecules adsorbed on the surface of Pd. The spectra were acquired using the same set-up and parameters as mentioned above. Moreover, the outlet was connected to an InProcess Instruments GAM 400 Quadrupole Mass Spectrometer (QMS) equipped with a Secondary Electron Multiplier to monitor the composition of the flow.

Materials were initially pretreated at 80 °C under a flow of Ar (30 sccm) for 30 min and then cooled to 25 °C. The following tests were maintained at 25 °C in steady-state mode. Next, the sample was exposed to 1% CO in Ar (30 sccm) for 30 min to reach the CO saturation coverage. The gas flow was then switched to pure Ar (2 sccm) to purge the sample for 1 h to remove the gas phase CO from the cell. The spectra were collected during both the CO-adsorption and the Ar-purge processes. The spectra were obtained by subtracting the background from the first spectra of the sample. For the CO oxidation experiments, the sample was first exposed to 2% CO in Ar (30 sccm) for 30 min. Subsequently, 10% O₂ balanced with Ar was introduced into the cell at a flow rate of 30 sccm at 25 °C for 30 min in order to react with the CO molecules adsorbed on Pd. Afterward, keeping the same gas atmosphere, the temperature was increased from 25 °C to 200 °C at a rate of 2 °C min⁻¹.

Near-ambient pressure X-ray photoelectron spectroscopy

Near-ambient pressure X-ray photoelectron spectroscopy (NAP-XPS) was used to probe the nature of Pd sites during the CO adsorption experiments. *Operando* NAP-XPS studies were carried out using a laboratory NAP-XPS instrument (Surface Nano Analysis GmbH, Germany). The setup was equipped with a differentially pumped Phoibos 150 electron energy analyzer with a nozzle of 500 µm diameter, a monochromated Al K α radiation source ($E = 1486.6$ eV), and a laser system for sample heating. The gases were fed to the reaction cell by mass flow controllers (Brooks, GF40) at a total pressure of 2 mbar. Reactants and products were monitored by a quadrupole mass spectrometer (QMS, MKS e-vision 2) connected to the lens system of the spectrometer. The powder samples were pressed into tablets with a diameter of 5 mm on a stainless-steel sample plate using a laboratory press and a load of about 1 ton. Temperature was monitored by a thermocouple that was attached to a sample plate and pressed onto the sample surface. The electron binding energies were referenced to the C 1s core level of native carbon species (C–C and C–H bonds) at an energy of 284.8 eV. For analysis, the peaks were deconvoluted using Gaussian Lorentzian curves with the software Unifit 2023. Note: The measurement was performed at the LIKAT Analytical Services Group by Stephan Bartling.

Nitrogen adsorption isotherm

N₂ adsorption-desorption isotherms were used to evaluate the Brunauer-Emmett-Teller (BET) surface area. The measurements were performed on an ASAP 2020 instrument (Micromeritics, USA). The samples were pretreated at 200 °C under vacuum condition (0.001 mbar) and then analyzed using N₂ physisorption with the Brunauer-Emmett-Teller (BET) method at liquid nitrogen temperature. Note: The measurement was performed by Reinhard Eckelt from LIKAT.

Nuclear magnetic resonance

^1H , ^{13}C , and ^{11}B NMR spectra were recorded on a Bruker AVANCE AV 400 instrument. The solvents are deuterium oxide (D_2O , 99.9 atom% D, Sigma-Aldrich) and Ethanol-OD (99 atom% D, Sigma-Aldrich). Note: The measurement was performed at the LIKAT Analytical Services Group by Susann Buchholz.

Photoluminescence spectroscopy

Photoluminescence (PL) spectroscopy was used to investigate the separation efficiency of photogenerated charge carriers. The PL emission spectra were recorded on a Cary Eclipse Fluorescence Spectrometer (Varian) with an excitation wavelength of 365 nm at room temperature.

Solid-state nuclear magnetic resonance

Solid-state nuclear magnetic resonance (NMR) was used to study the composition and chemical structure of the synthesized samples. All MAS NMR measurements were recorded on a Bruker AVANCE III HD spectrometer operating at a 400.2 MHz ^1H frequency, using a Bruker ASCEND DNP 9.4 T widebore (89 mm) magnet. All measurements were performed at room temperature. For ^{13}C multiple-CP (multiCP) experiments, the samples were loaded into ZrO_2 rotors (4 mm, Bruker) and spun in a Bruker triple-channel (HXY) probe with a MAS frequency of 8 kHz. ^{13}C quantitative spectra were measured using the MultiCP excitation method described by Johnson & Schmidt-Rohr [221]. The radio frequency (RF) pulse powers for ^1H and ^{13}C were 83 kHz and 50 kHz, respectively. ^1H power was matched to ^{13}C during Hartmann-Hahn cross polarization (CP) with a contact time of 5 ms and 1 s delay between the 3 CP blocks for ^1H magnetization recovery. SPINAL-64 at 83 kHz was applied for broadband decoupling of ^1H [222]. The recycle delay was 5 s. For ^1H spectra, a rotor-synchronized Hahn echo with an interpulse delay of one rotor period was applied. The samples were loaded into ZrO_2 rotors (1.3 mm, Bruker) and spun in a Bruker double channel (HX) high-speed probe with a MAS frequency of 60 kHz. The radio frequency (RF) pulse power was 125 kHz. The recycle delay was 0.6 s. Note: The measurement was conducted in collaboration with Victoria Aladin and Björn Corzilius from the University of Rostock.

Temperature-programmed decomposition

Temperature-programmed decomposition (TPDE) measurements were performed on a Microtrac BELCAT instrument equipped with a thermal conductivity detector (TCD) and an

InProcess Instruments GAM 400 quadrupole mass spectrometer (QMS). Before the measurements, the catalyst was pretreated in Ar (50 sccm) at 80 °C for 6 h and then cooled to -100 °C with liquid nitrogen. After purging with He (50 sccm), the temperature was increased to 400 °C at a ramping rate of 5 °C min⁻¹ while monitoring the released gas components.

Thermogravimetry and mass spectrometry

Thermogravimetry-mass spectrometry (TGA-MS) was used to study the thermal behavior of the samples. The experiments were performed using a SENSYS evo TG-DSC instrument (SETARAM) coupled with a mass spectrometer (OmniStar, Pfeiffer Vacuum GmbH). 10 mg of the sample was heated from room temperature to 800 °C at a rate of 10 °C min⁻¹ in air. Note: The measurement was carried out by Christine Rautenberg from LIKAT.

UV-Vis diffuse reflectance spectra

Ultraviolet-visible diffuse reflectance spectroscopy (UV-Vis DRS) was carried out to study the optical properties of as-synthesized catalysts. The spectra were collected on a Perkin Elmer Lambda 365 UV/Vis spectrometer with a photometric range of 190–1100 nm. The BaSO₄ was used as a white standard reference material. Powders were mounted onto a sample holder with a quartz glass window. The measurements were performed at room temperature.

X-ray absorption spectroscopy

X-ray absorption spectroscopy (XAS) was used to investigate the electronic structure and local coordination environment of Pd sites in the as-synthesized catalyst. *Ex situ* XAS measurements were performed at the CAT-ACT beamline at the KIT Light Source [223]. For *ex situ* measurements, all samples were prepared in the form of pellets, suitable for XAS measurements at the Pd K edge (24350 eV). XANES spectra and EXAFS data at the Pd K-edge (DCM Si(311), collimated mirror Pt, focusing mirror Rh, beam size 2×2 mm²) were recorded in transmission mode (using ionization chambers filled with Ar, OKEN, Japan). EXAFS data up to $k = 16 \text{ \AA}^{-1}$ was recorded at room temperature. All data were processed using the IFEFFIT package for background correction and normalization [224]. The k^3 -weighted EXAFS data at the Pd K-absorption-edges were Fourier-transformed in the range of 3 to 12 \AA^{-1} with the use of a Hanning window with a sill width of 1 \AA^{-1} . The EXAFS data for oxide supports were fitted to PdO reference structures (ICSD database, icsd.fiz-karlsruhe.de) and to PdN_x models for nitride supports using the Artemis package of IFEFFIT. For determining the structural parameters (coordination number and distances), fittings were performed in R-space in the range from 1 to 4 \AA , the amplitude (S_0^2) was set to 0.70 for all the samples, based on the analysis of the PdO

sample. Note: The measurement was planned in collaboration with Jan-Dierk Grunwaldt and Anna Zimina from KIT, who measured the samples at the storage ring in Karlsruhe.

Another set of absorption measurements was performed at the BAMline@BESSY II. The beamline layout includes a double crystal Si(111) monochromator and a double multilayer monochromator with a new 3-stripe multilayer, which can be used to suppress harmonics if required. Measurements were performed with the standard absorption setup, consisting of two ionization chambers filled with air. The beam size was $2 \times 2 \text{ mm}^2$. The recorded energy range was between 24150 and 25350 eV. To minimize the influence of statistical noise, the data has been fitted with a Gaussian process using a Matern kernel. Data evaluation has been done in the same manner as for the KIT data. Note: The measurement was conducted in the BAMline by Martin Radtke.

X-ray diffraction

X-ray powder diffraction (XRD) was used to characterize the crystal structure and phase compositions of the developed catalysts. The experiments were carried out on a Panalytical X'Pert diffractometer using an Xcelerator detector with Cu $K\alpha_1/\alpha_2$ radiation (40 kV, 40 mA; $\lambda = 0.15406 \text{ nm}, 0.154443 \text{ nm}$) by step-scanning method ($0.087^\circ \text{s}^{-1}$). Ni foil was used to suppress the Cu β -radiation, and the powder was mounted onto a silicon zero-background sample holder. Conversion of the obtained intensities from automatic to fixed divergence slits of 0.25° for further analysis. The software HighScore Plus (Panalytical, Pseudo-Voigt function) was used to fit the peak positions and profiles. Identification of the phases according to the PDF-2 database of the International Centre for Diffraction Data (ICDD). Note: The measurement was performed at the LIKAT Analytical Services Group by Henrik Lund.

X-ray photoelectron spectroscopy

X-ray photoelectron spectroscopy (XPS) was performed to investigate the elemental compositions and chemical states of the surface elements. The measurements were collected on an ESCALAB 220iXL (Thermo Fisher Scientific) using a monochromated Al $K\alpha$ source ($E = 1486.6 \text{ eV}$, 125 W, spot size $400 \text{ }\mu\text{m}$). A conductive, double-sided adhesive carbon tape was used for sampling powder onto a stainless-steel holder. The electron binding energies were measured with charge compensation using a flood electron source. The adventitious C 1s at 284.8 eV (C–C and C–H bonds) was used for charge reference. Deconvolution of the peaks was performed using the Unifit 2023 software package, employing Gaussian-Lorentzian curves for quantitative analysis. Normalization of the peak areas was performed using the spectrometer

transmission function and the Scofield element-specific sensitivity factor [225]. Note: The measurement was performed at the LIKAT Analytical Services Group by Stephan Bartling.

3.3 Theoretical calculation

All calculations were based on density functional theory using the Vienna Ab Initio Simulation Package (VASP) [226, 227]. The generalized gradient approximation (GGA) with the Perdew-Burke-Ernzerhof (PBE) functional was adopted in the DFT calculations [228, 229]. The core electrons were described using the projector augmented wave (PAW) method [230, 231]. The structure was optimized until the force tolerance and energy difference became smaller than 0.001 eV/Å and 10^{-5} eV, respectively. A plane wave basis set was used with a kinetic energy cutoff of 450 eV. The vacuum layer between the periodically repeated slabs was set at 30 Å to avoid significant interactions between the slabs. The empirical correction in Grimme's scheme (DFT-D3) was used for describing the long-range van der Waals interactions [232, 233]. Geometry optimization and total energy calculations were performed with a $3 \times 3 \times 1$ Γ -centred k -point sampling.

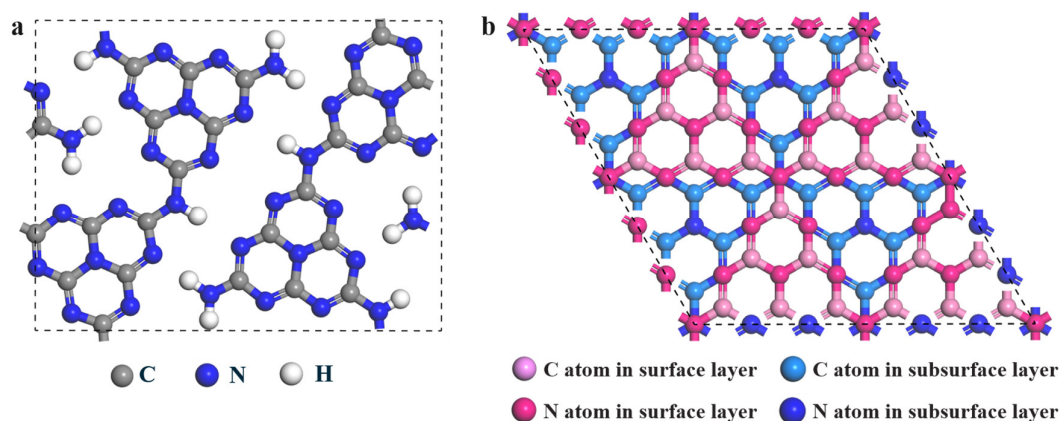


Figure 9. (a) Hydrogen-bonded PCN model, and (b) the sheet staggered arrangement of ideal PCN model with AB stacking with P63/mmc space group.

Regarding the PCN model, the lattice constants for the hydrogen-bonded model are $a = 12.654$ Å, $b = 16.589$ Å, and $c = 43.800$ Å, with $\alpha = 90^\circ$, $\beta = 90^\circ$, $\gamma = 90^\circ$, see Figure 9a. The heptazine units in the hydrogen-bonded model were connected by covalent C–N bonds to form strands aligned in a zigzag manner, and the adjacent heptazine strands are bridged by hydrogen bonds between the ring-nitrogen atoms and the NH and NH₂ groups, respectively [175, 234]. Heptazine rings in one layer overlap with the rings in the next layer, and there are van der Waals interactions between the layers. For reference, a perfect ABAB-stacking model ($a = 7.125$ Å, $b = 7.125$ Å, and $c = 43.800$ Å, with $\alpha = 90^\circ$, $\beta = 90^\circ$, $\gamma = 120^\circ$, see Figure 9b) was constructed.

The heptazine-based structure with an ABAB-type staggered arrangement (space group P63/mmc) is considered to be a relatively stable pristine PCN, and its heptazine units of the second layer are almost fully located on the open hollow site of the first layer [235, 236]. The Γ -centred $7 \times 7 \times 1$ k -point grid was used for sampling the Brillouin zone in density of states (DOS) calculations.

Regarding the Pd/PCN models, the monolayer hydrogen-bonded PCN models was used as support to hold the Pd atom and Pd nanocluster (0.5 nm). The schematic illustration of the preferential sites in the surface PCN layer is depicted in Figure 10. Besides, Pd atoms were also anchored at different positions within the two uppermost PCN layers, and the preferential site is illustrated in Figure A.28.

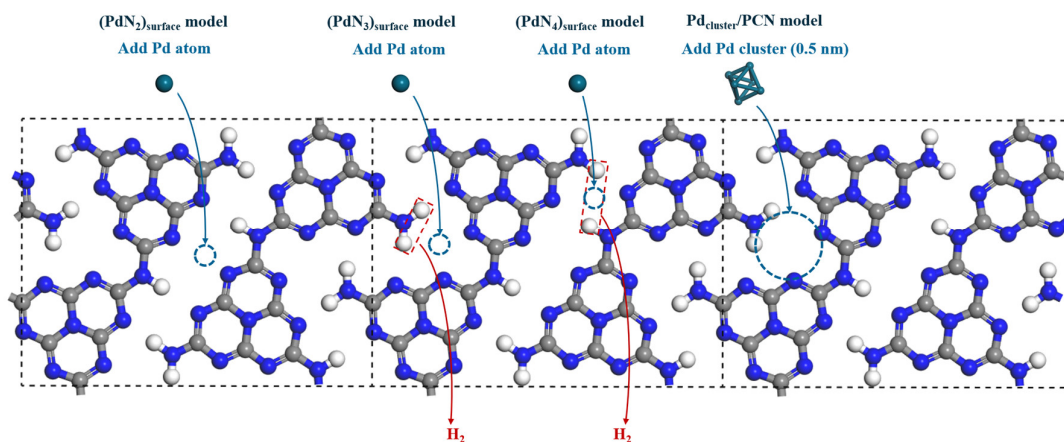


Figure 10. Schematic illustration of Pd atom and Pd nanocluster (0.5 nm) anchored on hydrogen-bonded PCN model.

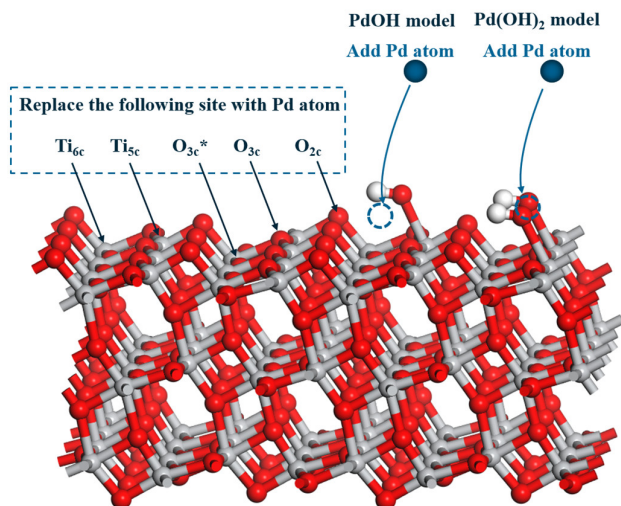


Figure 11. Candidate binding sites for Pd atoms on a TiO_2 anatase (101) surface.

Regarding the Pd/TiO₂ models, a model of (3 × 1) supercell slabs including six-atomic layers for the anatase TiO₂ (101) surfaces was adopted. The corresponding formulas are Ti₁₃₆O₇₂. A vacuum of more than 30 Å is used to avoid the interaction between slabs. The TiO₂ (101) surface terminates with two types of Ti cations, 5-fold coordinated Ti (Ti_{5c}) and 6-fold coordinated Ti (Ti_{6c}), located lower than Ti_{5c}, and three types of O anions, 2-fold coordinated O sites (O_{2c}), 3-fold coordinated O sites (O_{3c}), and another 3-fold coordinated O sites (O_{3c}*), located lower than O_{3c} [237, 238]. Anatase TiO₂ (101) surface can offer four types of anchoring sites for single Pd atoms, including the Atop site, Ti-vacancy sites, O-vacancy sites, and various models of hydrogenated Pd(OH)_x complex, see Figure 11.

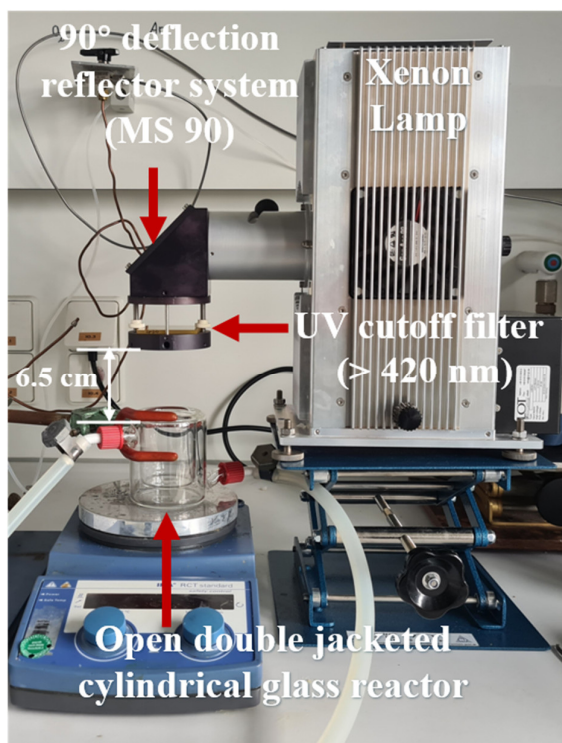
Regarding the bulk Pd model, a Pd(111) slab was modeled using a 4 × 2 supercell with three layers of thickness. All three layers of the slab were allowed to relax, and the slabs were separated by 15 Å of vacuum. The **k**-point sampling was a Γ -centred 2 × 2 × 1 grid.

All the Pd–C, Pd–N, Pd–O, and Pd–F models are obtained from the Materials Project database as well as the algorithms and parameters for the DFT calculation [239]. Materials Projects Database ID for the Pd models: Pd₄C (Fe₄C-mp-1078579), Pd₂C (Mo₂C-mp-1221498), Pd₄C₃ (mp-1216474), PdC (mp-1009538), Pd₃N (mp-1079760), Pd₃N₂ (mp-1080191), PdN (mp-999293), Pd₃N₄ (mp-1080192), Pd₂O (mp-10729), PdO (mp-1336), Pd₂O₃ (mp-510080), PdO₂ (mp-1018886), PdF (PdO-mp-1336), PdF₂ (mp-1058), PdF₃ (mp-13679), PdF₄ (mp-13868). All the model structures were optimized before performing Bader charge analysis. Additional Pd²⁺ models are obtained from the Cambridge Crystallographic Data Centre (CCDC). Database ID: bis(1,1'-Methylenebis(3-ethylimidazol-2-ylidene))-palladium(II) bis(hexafluorophosphate) (CCDC-894018), bis(2,2,6,6-Tetramethyl-3,5-heptanedithionato-S, S')-palladium(II) (CCDC-233613), bis(2,2'-Bipyridyl)-palladium(II) dinitrate monohydrate (CCDC-1100240), bis(2,4-Pentanedionato)-palladium(II) (CCDC-289749). The effective charge of Pd was evaluated by Bader charge analysis, which is proposed by Henkelman *et al.* [148, 240, 241].

CO adsorption properties were used as a tool to assess the accuracy of proposed structures in relation to experimental CO-DRIFTS measurements. The CO vibrational frequencies were calculated using the harmonic approximation method, in which CO and its nearest neighboring atoms were considered in the calculation. In the gas phase, the CO bond length (1.144 Å) and stretching frequency (2134 cm⁻¹) were determined at the PBE level. A difference of 9 cm⁻¹ was taken into account with respect to the experimental CO frequency in the gas phase (2143 cm⁻¹). The CO adsorption energies were calculated as the difference between isolated species and the adsorption complexes. Positive values indicate stable adsorbed species.

3.4 Catalytic testing

3.4.1 Photocatalytic phenol degradation



The performance of the differently exfoliated PCN was evaluated by studying the photodegradation of phenol under visible light. 10 mg of the sample was dispersed in a phenol aqueous solution (20 mL, 2 mg L⁻¹). The light irradiation system is through a 300 W Xenon lamp containing a UV cutoff filter (> 420 nm) and a 90° deflection reflector system (MS 90) with a dichroic mirror (Figure 12). The distance between the reflector system and the reactor was 6.5 cm. The temperature was maintained at 25 °C with a thermostat. The mixture was stirred for 30 min to reach the adsorption-desorption equilibrium before

Figure 12. Photocatalytic reaction set-up for the light irradiation. During the phenol degradation.

photocatalytic tests, 0.2 mL of the sample was collected every 1 h and filtered by a 0.22 µm PTFE filter for further high-performance liquid chromatography (HPLC) analysis. HPLC analysis was carried out on an Agilent Technologies 1260 Infinity containing a G4225A vacuum degasser, G1312B binary pump, G1329B autosampler, G1315D diode array detector, and G1316A tempered column compartment. A Phenomenex C18 column (Kinetex. 2.6 µm, 150 *3 mm) with pre-column was used for product separation, and the column temperature was maintained at 40 °C. The wavelength for UV detection was set at 270 nm. The isocratic mobile phase was made up of 80% water and 20% acetonitrile (with 0.5% trifluoroacetic acid). A volume of 20 µL was injected by the autosampler into the mobile phase flowing at 0.6 mL min⁻¹.

3.4.2 Suzuki-Miyaura coupling reaction

Batch reaction

Batch reactions for the coupling of bromobenzene with phenylboronic acid were carried out in a 60 mL double-jacketed glass reactor. Before dissolving the substrates, ethanol and deionized

aqueous solutions were degassed using a thermal gassing method in an argon stream to remove dissolved oxygen as much as possible. In a typical reaction, the reactor was filled with 40 mL of an ethanol/H₂O solution (v/v = 5/3) containing bromobenzene (1 mmol, 99%, Alfa Aesar), phenylboronic acid (2 mmol, 98+%, Alfa Aesar), and K₂CO₃ (2 mmol, ≥99%, Carl Roth). The reactor was then evacuated and filled with argon through the Schlenk line, and this procedure was repeated three times to ensure the complete removal of air. Next, 2 mg of catalyst was dispersed into the reaction mixture. The reaction temperature was maintained at 25 °C using a thermostat. The total reaction time was 1 hour, and 1 mL samples were withdrawn from the reactor at specific time intervals and filtered through a 0.22 µm PTFE filter. The products were analyzed using an Agilent 6890N gas chromatography (GC) with toluene (99.99%, Fisher Chemical) as the internal standard. For the photocatalytic test, the reaction solution stays the same while being irradiated by a LUMATEC Superlite S04 lamp with visible light ranging from 400–700 nm and an intensity of 225 mW/cm², as illustrated in Figure 13.

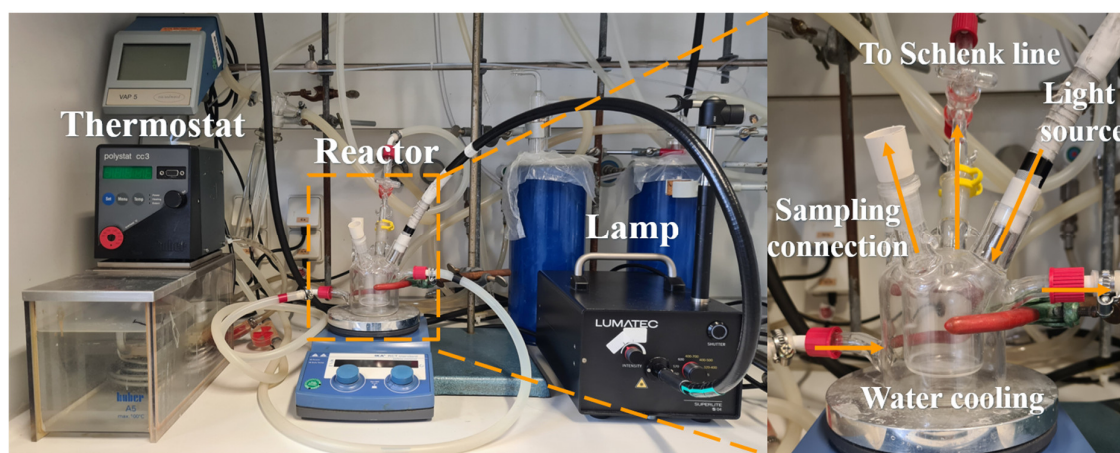


Figure 13. Batch reaction set-up for Suzuki-Miyaura reaction.

Continuous flow reaction

Continuous flow experiments for the coupling of bromobenzene with phenylboronic acid were performed on a modular Ehrfeld microreaction system equipped with a cartridge reactor 240 (length = 63 mm, internal Ø = 10 mm, V = 5 mL). The experimental setup is shown in Figure 14 and 15. The catalyst (500 mg, particle size between 315 µm and 800 µm) was loaded into the cartridge (bed length = 1.20 cm) and filled with glass wool and glass beads (d = 0.75 mm). The reaction solution (same concentration as the batch reaction) was pumped through the column at a flow speed of 0.1 mL min⁻¹ regulated by a Knauer K-501 HPLC pump. The gas flow rate was set to 0.2 sccm through a Bronkhorst mass flow controller (MFC). Gas and liquid phases were mixed in a slit-plate micro mixer (model LH2) before feeding the reaction mixture

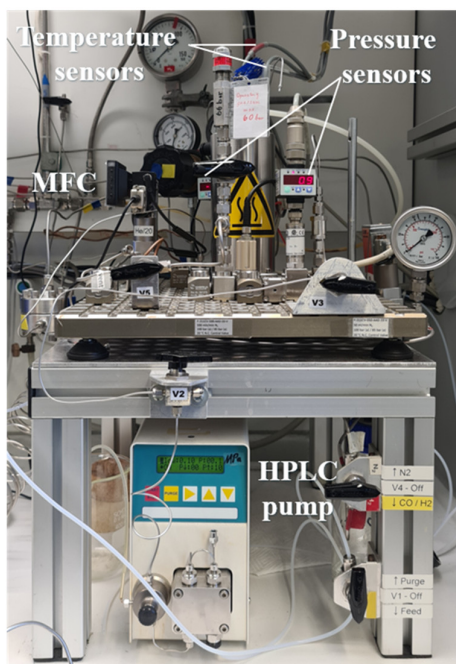


Figure 14. Continuous flow reactor for Suzuki-Miyaura reaction.

into the cartridge reactor. A temperature sensor was measured inside the cartridge reactor directly before the gas liquid mixture enters the cartridge, and the reaction temperature was maintained at 30 °C. A pressure sensor was placed in front of the slit-plate mixer to monitor changes in pressure. Samples were taken every 1 hour for GC analysis.

The spent catalysts were recovered for characterization. Prior to characterization, the spent catalyst was washed with 400 mL of an ethanol/H₂O solution (v/v = 5/3) for 3 h under an argon atmosphere to remove residual substrate from the surface. The washing procedure was repeated twice. The samples were collected by filtration using a 0.1 µm PTFE membrane filter and then dried in a tube furnace at 80 °C for 12 h in Ar.

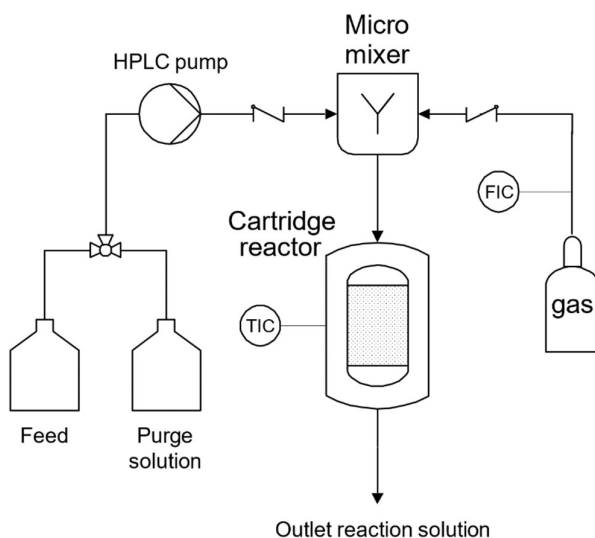


Figure 15. Schematic representation of the continuous flow reactor set-up used for Suzuki-Miyaura reaction.

Please note: The personal contribution and other collaborators' contribution are detailed explicitly in the chapter “List of Writing/Experiments/Calculations to Highlight Own Work and Contributions by Other Researchers” (Page 152-153).

4. Results and discussion

4.1 Catalyst characterization

4.1.1 Experimental characterization for exfoliated PCN catalysts

4.1.1.1 Production yield and apparent density

The production yields for differently exfoliated PCN were compared. As shown in Table 1, the yields of t-CN-3 and t-CN-6 are approximately 40% and 31%, respectively, indicating a decrease in yield as the exfoliation time increases. TGA-MS measurement was performed to assess the weight changes and thermal stability of PCN. As shown in Figure 16a, there are two stages of weight loss in air. The first stage starts at 120 °C and is attributed to the loss of adsorbed water molecules and/or surface hydroxyl groups, as confirmed by *in situ* DRIFTS measurement (Figure 16b). The second stage starts at 500 °C and is caused by the pyrolysis of the PCN framework into CO₂, NH₃, NO, and NO₂, resulting in a complete weight loss at 700 °C.

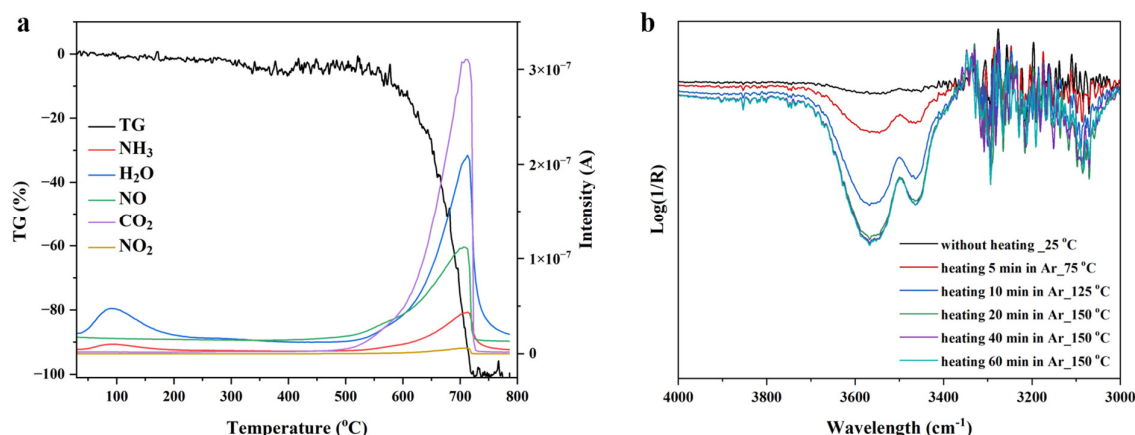


Figure 16. (a) TGA-MS of pristine PCN. (b) *In situ* DRIFTS spectra of PCN heated to 150 °C for 60 min (10 °C min⁻¹) in Ar atmosphere.

Notably, the yields for c-CN-8 and c-CN-16 are calculated as 105% and 106%, respectively. Both yields beyond 100% are due to the formation of a significant number of oxygen-containing groups on the surface, consistent with the observation from their DRIFTS spectra (Figure 24b). Elemental analysis further confirmed the increased oxygen content in c-CN-3 (11.23 wt% oxygen) and c-CN-6 (13.22 wt% oxygen) in comparison to pristine PCN (5.82 wt% oxygen). For the samples u-CN-8 and u-CN-16, the yield is both close to 100%, indicating that the mass remains unchanged after the ultrasonic treatment. The negligible mass loss results from the transfer process of the u-CN. Pristine PCN, treated by hydrothermal exfoliation, produced a

mixture consisting of two types of products: a water-soluble one and an insoluble solid. Besides, the yield of h-CN decreased slightly as the exfoliation time increased. To sum up, the analysis of production yield showed that the thermal and hydrothermal oxidation method lead to a significant mass loss of PCN, and a high yield of exfoliated PCN can be achieved through liquid ultrasonication method and chemical oxidation method.

Table 1. Production yield of differently exfoliated PCN^a

Sample	Method	Time (h)	Precursor (g)	Property	Yield (%)
t-CN-3	Thermal oxidation exfoliation	3	0.2	—	40
t-CN-6		6	0.2	—	31
c-CN-8	Chemical oxidation exfoliation	8	0.2	—	105
c-CN-16		16	0.2	—	106
u-CN-8	Liquid-ultrasonic exfoliation	8	0.1	—	98
u-CN-16		16	0.1	—	97
h-CN-12	Hydrothermal oxidation exfoliation	12	0.5	Insoluble	29
h-CN-S12				Soluble	28
h-CN-24		24	0.5	Insoluble	21
h-CN-S24				Soluble	12

^a All the yield data are the average values of three independent experiments.

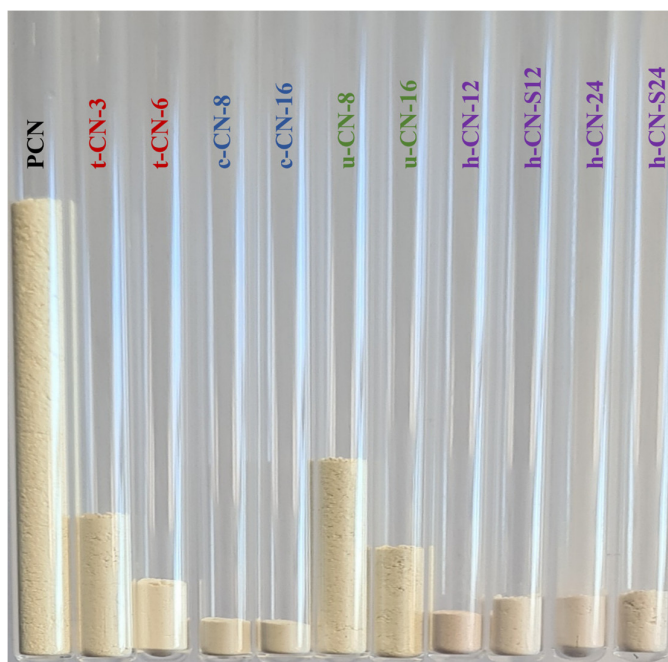


Figure 17. Density comparison of differently exfoliated PCN. Each sample is 50 mg.

The apparent density of differently exfoliated PCN was further evaluated. In brief, 50 mg samples were placed in quartz containers of equal volume, and the apparent densities were compared based on their height. As shown in Figure 17, the height of t-CN and u-CN decreased with the exfoliation time, indicating an increase in the freely settled density over time. In general, a low apparent density indicates fine particles, and a high apparent density suggests large particles. For example, the t-CN-3 with lower density is a light and fine powder, while the t-CN-6 with higher density is a coarse and hard powder. Moreover, apparent density is directly proportional to porosity, including the volume of internal pores and voids. Therefore, it is easier to achieve close packing if the shape of the sample is regular. In comparison to the amorphous structure of PCN, c-CN exhibited a block structure, and h-CN formed a rod-like structure, as confirmed by SEM (Figure 18). The above analysis of apparent density demonstrates that different exfoliation methods can result in different apparent densities of the final products. It is worth mentioning here that quantitative intensity analysis is unreliable in spectral characterization due to significant differences in density.

4.1.1.2 Morphology and surface area

As presented in Figure 18a and Figure 19, the pristine PCN displays an irregular wrinkled structure with already a thin thickness of 3.9 nm. Considering that the interlayer distance in the pristine PCN is around 0.320 nm, it is equivalent to 13 single monolayers [193]. The u-CN (Figure 18d and Figure 20) exhibits a same morphology as the pristine PCN, but with a significantly reduced thickness of 2.4 nm (equivalent to 9 layers). This indicates that sonication can efficiently exfoliate the bulk structure into few-layered nanosheets and retaining the original structure. After thermal oxidation exfoliation, the resulting t-CN transformed into a soft, sheet-like structure (Figure 18b and Figure A.1b). The average thicknesses of t-CN-3 and t-CN-6 (Figure A.3 and Figure 21) are evaluated to be 3.2 nm (equivalent to 11 layers) and 2.8 nm (equivalent to 10 layers), respectively, suggesting a decrease in thickness with longer thermal treatment time.

In contrast, after chemical oxidation treatment, the wrinkled and porous structure of PCN was destroyed and transformed into a dense block-like structure (Figure 18c and Figure A.2). Further AFM image (Figure 22) of c-CN-16 shows flakes with much smaller sizes of around 0.7 μm but a slightly increased thickness of 4.2 nm (equivalent to 14 layers), suggesting that the chemical treatment could destroy the in-plane hydrogen-bonded network and result in agglomeration to form a block structure, inconsistent with the SEM results. The h-CN (Figure 18e, f and Figure A.1 e, f) exhibits a rod-like structure after hydrothermal treatment of PCN.

Therefore, thermal, chemical, and hydrothermal exfoliation strongly affect the morphology of PCN, while ultrasonic exfoliation preserves the original structure of PCN. More importantly, it is certain that a thinner structure can be obtained after thermal and ultrasonic treatments.

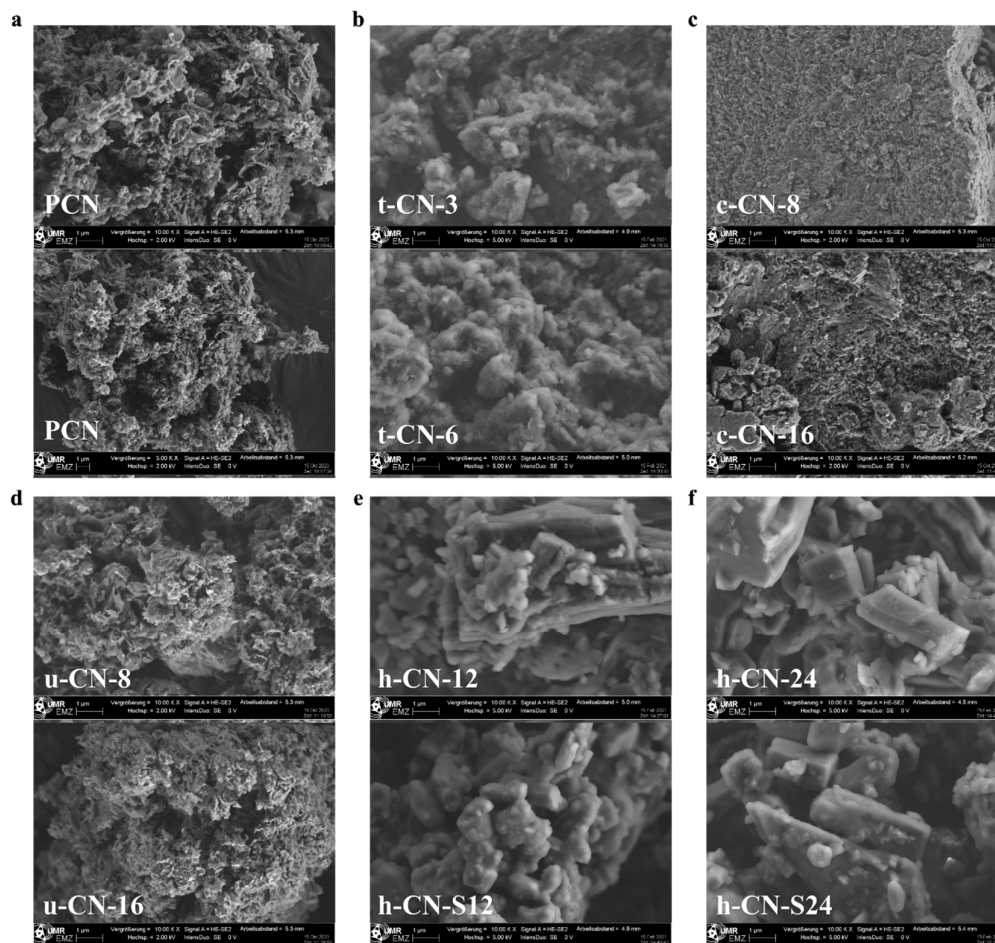


Figure 18. SEM images of (a) PCN, (b) t-CN, (c) c-CN, (d) u-CN and (e, f) h-CN. Scale bar, 1 μm .

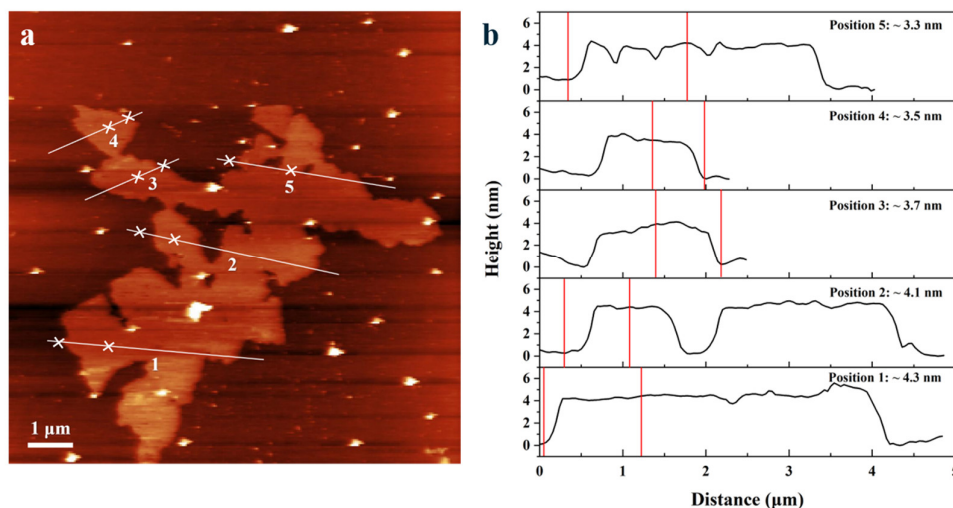


Figure 19. AFM images and the corresponding height profiles of pristine PCN

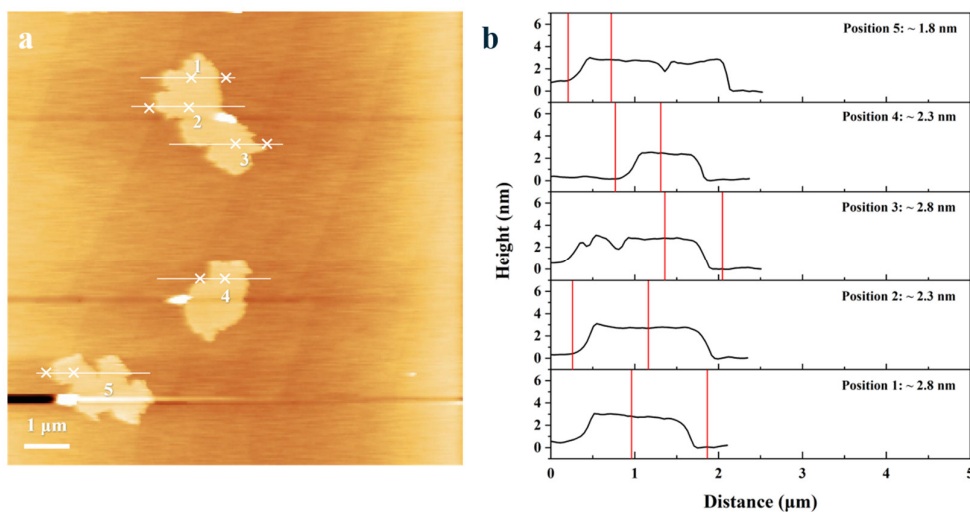


Figure 20. AFM images and the corresponding height profiles of u-CN-16.

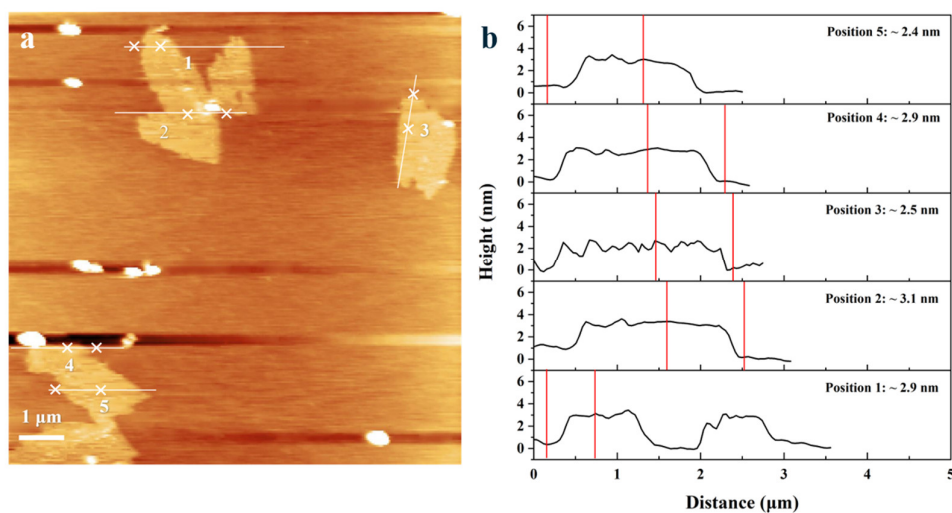


Figure 21. AFM images and the corresponding height profiles of t-CN-6.

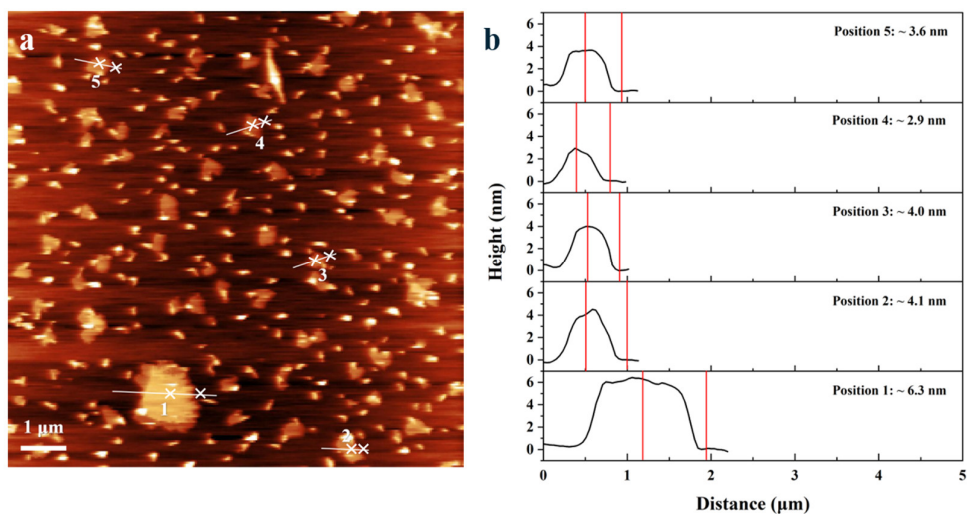


Figure 22. AFM images and the corresponding height profiles of c-CN-16.

The Brunauer-Emmett-Teller (BET) surface areas of the differently exfoliated PCN were measured using N_2 adsorption-desorption isotherms. As shown in Figure 23, the surface area of pristine PCN is $103 \text{ m}^2 \text{ g}^{-1}$. After thermal oxidation exfoliation, the BET surface area of the resulting t-CN-3 and t-CN-6 was measured to be $134 \text{ m}^2 \text{ g}^{-1}$ and $92 \text{ m}^2 \text{ g}^{-1}$, respectively. The decrease in surface area over exfoliation time is attributed to the denser packing of the interlayer structure, pointing out the influence of excessive thermal exfoliation. The same trend was found in u-CN samples. The BET surface areas of u-CN-8 and u-CN-16 are determined as $107 \text{ m}^2 \text{ g}^{-1}$ and $91 \text{ m}^2 \text{ g}^{-1}$, respectively, which further emphasizes that the importance of timing control to avoid the excessive exfoliation.

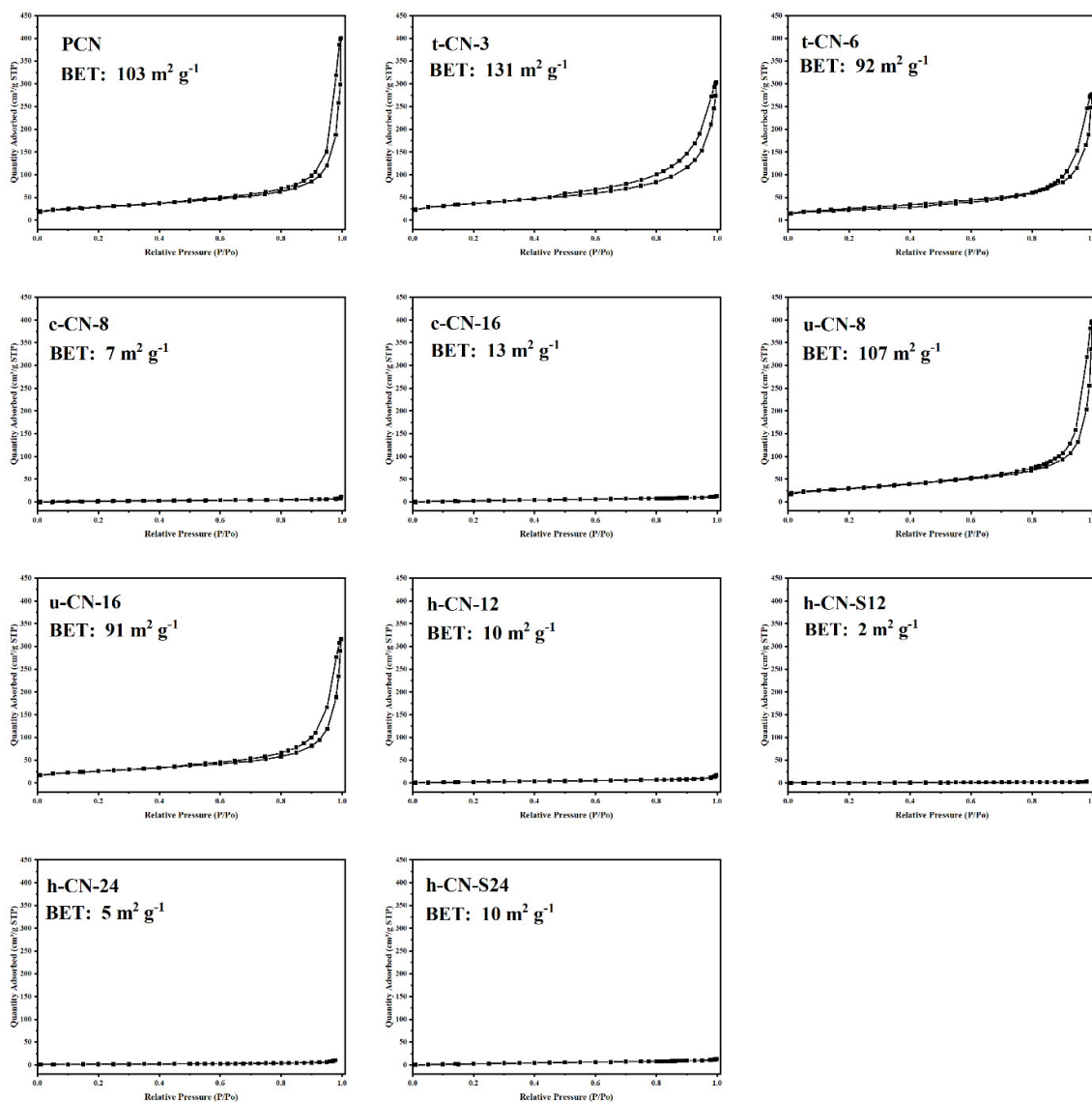


Figure 23. Nitrogen adsorption-desorption isotherms of differently exfoliated PCN.

Surprisingly, the surface areas of c-CN-8 and c-CN-16 dropped to 7 and 13 m² g⁻¹, respectively. This is due to the destruction of the porous nanostructure caused by the oxidation effect of concentrated H₂SO₄, in agreement with the observation from SEM. Therefore, except for t-CN-3 that shows a higher surface area than pristine PCN, the surface areas of all other exfoliated samples are severely decreased.

4.1.1.3 Crystal structure, molecule structure and structural defects

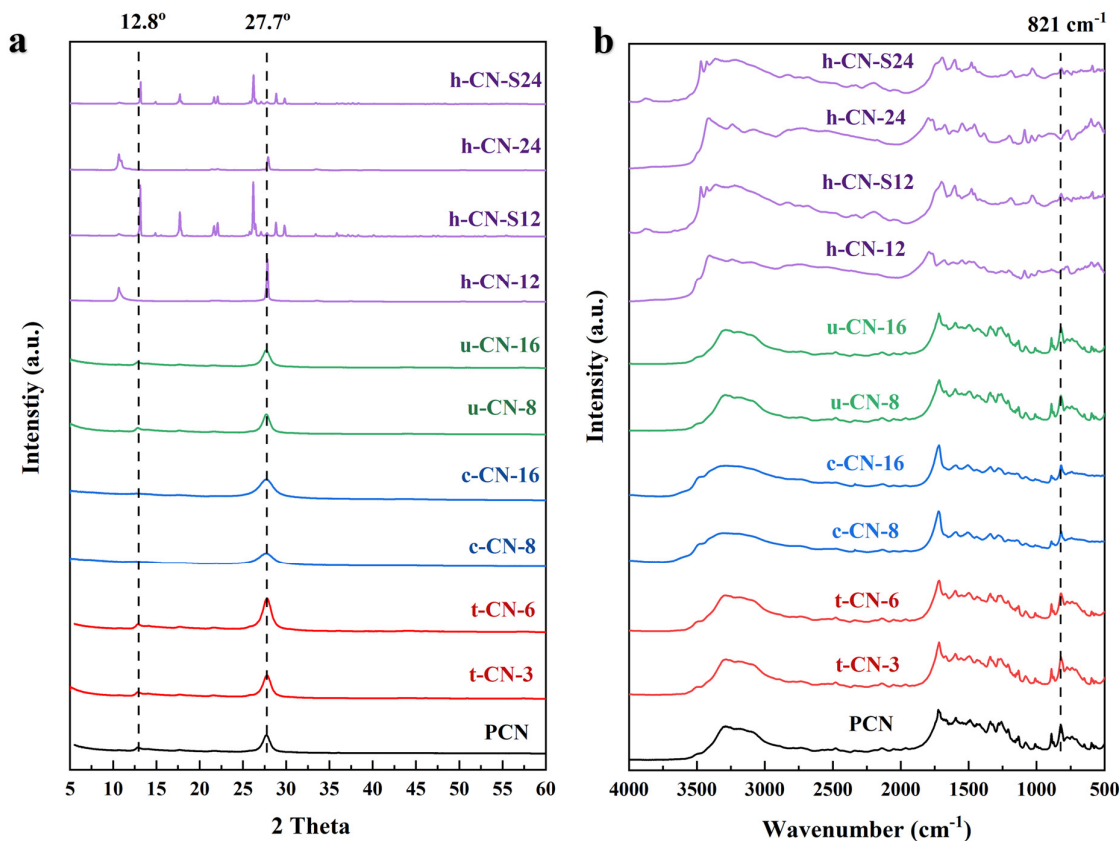


Figure 24. (a) XRD patterns and (b) DRIFTS spectra of differently exfoliated PCN.

Powder X-ray diffraction (XRD) was carried out to characterize the crystal structures. As shown in Figure 24a, pristine PCN exhibits two diffraction reflexes: the strong (002) reflex at 27.7° is known as the interlayer π - π stacking structure of conjugated aromatic rings, and the weak (210) reflex at 12.8° is assigned to the in-planar repeats between heptazine units [242]. The u-CN exhibits similar reflex positions and intensities as the pristine PCN, suggesting that the crystal structure is largely maintained after ultrasonic treatment. The relative intensities of the (002) reflex for t-CN are significantly higher in comparison to pristine PCN, suggesting the enhanced crystallinity after thermal treatment, consistent with the literature [243]. In contrast, the (002) reflex of c-CN becomes weaker and broader, and its (210) reflex even almost disappears. All

the changes in c-CN indicate the crystallite size along the (002) direction is reducing, and the lattice-like structure along the (210) direction is disappearing, which are also evidence of exfoliation. For h-CN, the diffraction reflexes for the soluble samples h-CN-S12 and h-CN-S24 are assigned to melamine rather than PCN [244]. For the insoluble samples h-CN-12 and h-CN-24, the intensities of the (002) reflex decrease over time, the (210) reflex at 12.8° disappears and is replaced by a new and sharp reflex at 10.7° , indicating that the original crystal structure of PCN is destroyed and transformed into a new compound. This compound is indexed as a cyanuric acid-melamine complex, consisting of hydrogen bonds [245, 246]. Based on the above XRD analysis, it can be concluded that the PCN crystal structures were largely retained after ultrasonic exfoliation, whereas thermal and chemical exfoliation did not. Certainly, hydrothermal exfoliation is the most destructive method, leading to the destruction of the π -delocalized electronic system, thereby likely affecting its photocatalytic performance.

The molecular structure was investigated using DRIFTS. As shown in Figure 24b, the t-CN and u-CN exhibit similar DRIFTS spectra to the pristine PCN, indicating that the original PCN backbone remained the same after thermal exfoliation and ultrasonic exfoliation. The broad bands at $3500\text{--}3000\text{ cm}^{-1}$ are attributed to the N-H, N-H₂, and O-H stretching modes [247, 248]. The strong bands at $1700\text{--}1200\text{ cm}^{-1}$ are ascribed to the aromatic C-N stretching bonds and aromatic ring modes [249]. The sharper band at 821 cm^{-1} corresponds to the breathing mode of heptazine units [250]. In comparison to pristine PCN, the band at $3500\text{--}3000\text{ cm}^{-1}$ in c-CN becomes broader, indicating the introduction of more oxygen-containing groups after chemical oxidation treatment, consistent with the findings from CHNS and XPS elemental analysis (Table 2). Besides, the IR bands of c-CN in the region of $1700\text{--}1200\text{ cm}^{-1}$ and 821 cm^{-1} become much weaker, implying that chemical treatment strongly affects the in-plane structural packing motif and makes it less ordered. For the insoluble samples h-CN-12 and h-CN-24, the molecular structures are no longer identical to PCN, indicating the destruction of the original structure after hydrothermal treatment. The band at 1794 cm^{-1} is attributed to a newly formed carbonyl group. For the soluble samples h-CN-S12 and h-CN-S24, their DRIFTS spectra exhibit discernible and additional absorption bands as melamine, in accordance with the above XRD assignment. The new bands at 3471 and 3426 cm^{-1} are characteristic of the terminal N-H stretching mode. The new band at 782 cm^{-1} is ascribed to the bending and stretching modes of the C-N heterocycles, which are characteristic absorptions of the melamine structure [244].

The chemical states of the exfoliated samples were investigated by XPS. Compared to pristine PCN, the higher intensity of O 1s in c-CN and h-CN suggests that more oxygen-containing

groups were introduced to the material (Figure 25a). Figure 25b depicts the high-resolution C 1s XPS spectra. The C1s peak, ranging from 281.8 eV to 298.1 eV, was deconvoluted into four peaks at 289.8, 288.3, 286.4, and 284.6 eV [251, 252]. The peak at 289.8 eV is assigned to the sp^2 -hybridized carbon of $N=C-O$. The peak at 288.3 eV is assigned to sp^2 -bonded carbon of $N=C=N$. The peak at 286.4 eV is attributed to the sp^2 carbon atoms bonded to N inside the aromatic structure ($N-(C)_3$). The lowest energy at 284.6 eV is typically related to graphitic $C=C$ bonds. The h-CN-12 and h-CN-24 exhibit a noticeable positive shift in the $N=C-N$ species due to the introduction of highly electronegative O atoms (Allen electronegativity: O = 3.6, N = 3.0, C = 2.6) into the aromatic CN heterocycle. Besides, as depicted in Table A.1, the area ratios of $N=C-O$ for t-CN-3 and c-CN-8 are significantly higher than that of pristine PCN, whereas $N=C=N$ are lower. This finding again points out the oxidation of $N=C-N$ to $N=C-O$, indicating that the aromatic CN heterocycles in PCN were oxidized during thermal and chemical oxidation treatments.

A comparison of surface C/N atomic ratios before and after exfoliation is also helpful in confirming the loss of nitrogen atoms in the pristine PCN framework. As depicted in Table 2, the atomic ratios of surface C/N are 0.79 and 0.82 for c-CN-8 and c-CN-16, respectively, which are higher than that of pristine PCN of 0.70. Similarly, the atomic ratios of surface C/N for the t-CN-6 increased to 0.80, confirming the loss of nitrogen atoms after thermal treatment.

The high-resolution N 1s spectrum (Figure 25c) of pristine PCN, ranging from 396.4 eV to 402.7 eV, has been resolved into three main peaks at 398.7 eV, 400.1 eV, and 401.2 eV, corresponding to the sp^2 $C=N-C$ bonds in the tri-s-triazine (pyridinic N), sp^3 tertiary nitrogen $N-(C)_3$ groups, and amino functions carrying hydrogen ($C-N-H$), respectively [211, 247]. The 404.6 eV peak is weak and is attributed to charging effects or π electron delocalization in heterocycles [253, 254]. Besides, the decreased area ratios of $C=N-C$ in t-CN-3 and c-CN-8 (Table A.2) indicate the loss of nitrogen. This finding is consistent with the above C 1s spectrum. For h-CN-12, the binding energies of $C-N-H$ and $N-(C)_3$ species show a positive shift of 0.5 eV, while the binding energy of $C=N-C$ shows a negative shift of 0.4 eV. For h-CN-S12, all three $C-N-H$, $N-(C)_3$, and $C=N-C$ species are negatively shifted. The shifts in the N 1s core electron as well as the above C 1s core electron in h-CN-12 and h-CN-S12 indicate that their structures are no longer identical to the pristine PCN. The reason for that is the decomposition of the heptazine structures and the introduction of oxygen-containing groups.

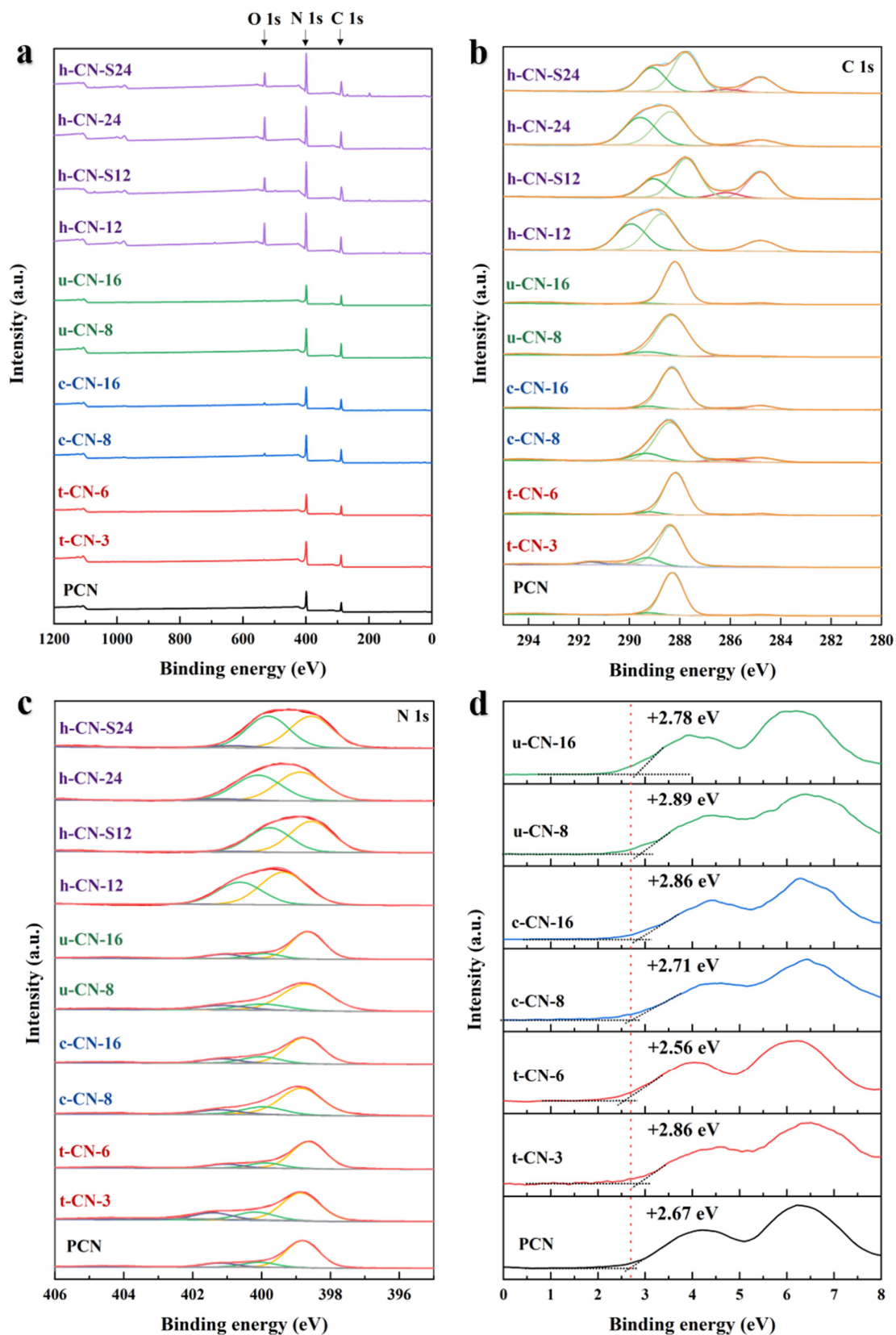


Figure 25. (a) XPS survey spectra, high-resolution XPS spectra of C1s (b) and N1s (c), and (d) VB XPS spectra of differently synthesized PCN.

Table 2. Characterization data of differently exfoliated PCN.

Sample	Formular*	O* (wt%)	C/N* (at.%)	Surface O* (at.%)	Surface C/N* (at.%)
PCN	$C_3N_{4.73}H_{1.59}O_{0.40}$	5.82	0.63	0.76	0.70
t-CN-3	$C_3N_{4.72}H_{1.98}O_{0.31}$	4.50	0.64	0.67	0.67
t-CN-6	$C_3N_{4.52}H_{2.22}O_{0.37}$	5.46	0.66	1.40	0.80
c-CN-8	$C_3N_{4.70}H_{3.57}O_{0.83}$	11.23	0.64	3.23	0.79
c-CN-16	$C_3N_{4.77}H_{2.58}O_{1.0}$	13.22	0.63	3.11	0.82
u-CN-8	$C_3N_{4.93}H_{2.65}O_{0.44}$	6.12	0.61	0.65	0.71
u-CN-16	$C_3N_{4.61}H_{1.48}O_{0.24}$	3.62	0.65	1.12	0.73
h-CN-12	$C_3N_{4.74}H_{2.93}O_{1.84}$	21.83	0.63	16.56	0.79
h-CN-S12	$C_3N_{4.90}H_{5.90}O_{1.40}$	16.85	0.61	11.32	0.87
h-CN-24	$C_3N_{4.24}H_{5.10}O_{1.47}$	18.95	0.71	17.04	0.70
h-CN-S24	$C_3N_{4.94}H_{6.01}O_{0.94}$	11.97	0.61	11.29	0.65

* Molecular formular, O weight percentage and C/N atomic ratios are determined by elemental analysis.

※ Surface O atomic quantity and surface C/N atomic ratios are determined by XPS.

Solid-state NMR spectroscopy was performed to understand the nature of the building blocks in differently exfoliated samples in relation to the bulk PCN networks. The ^{13}C CP MAS NMR spectra of PCN exhibits two distinctive chemical shifts at 165 (C1/C1') and 157 (C2) ppm (Figure 26a, c), which are attributed to heptazine units [255]. The signal at 163–165 ppm can be divided into two major carbon species: the signal at 165 ppm originates from the carbon atom C1' closer to the protons of non-polymerized NH_2 , and the peak at 163 ppm is assigned to the carbon atom C1 closer to the protons of partially polymerized NH species. The signal at 157 ppm is attributed to the carbon atom C2 bonded to three nitrogen atoms. The ^{13}C NMR spectral profile remained the same in the t-CN-6 and u-CN-16, confirming the maintenance of the aromatic system. However, in c-CN-16, a slight shift of the center of weight of the C1/C1' peak was observed, caused by the increased contribution of the C1, which suggest the destruction of terminal $-\text{NH}_2$ species. The spectral profiles of h-CN-24 and h-CN-S24 are not identical to PCN, pointing out that the destruction of the heptazine structure resulted in downfield shift. Specifically, in h-CN-S24, two new chemical shifts at 167.6 and 169.3 ppm correspond to the carbon species in the melamine structure [256]. Additional features in the ^1H NMR spectra are assigned as follows (Figure 26b). The signal at 9.2 ppm is attributed to the hydrogen-bonded NH_2 group, and the signal at 4.2 ppm is assigned to the non-hydrogen-bonded

NH₂ group. The shoulder appearing at around 10 ppm is ascribed to H on the bridging N (–NH–) group with additional hydrogen bonds. The more intense signal at 5 ppm in c-CN-16 is attributed to the OH groups caused by the oxidation of heptazine units, and the less intense signal at 9 ppm is due to the destruction of the edge –NH₂ group, in agreement with the observation from the ¹³C MAS NMR observation. For h-CN-S24, the signal appearing at 15 ppm suggests the presence of keto-imines derived from the oxidation of melamine. This signal was also found in h-CN-24, providing additional evidence for the formation of supramolecular complexes. The new signal at about 7 ppm in h-CN-S24 pointed to the NH₃⁺, which could explain its water solubility.

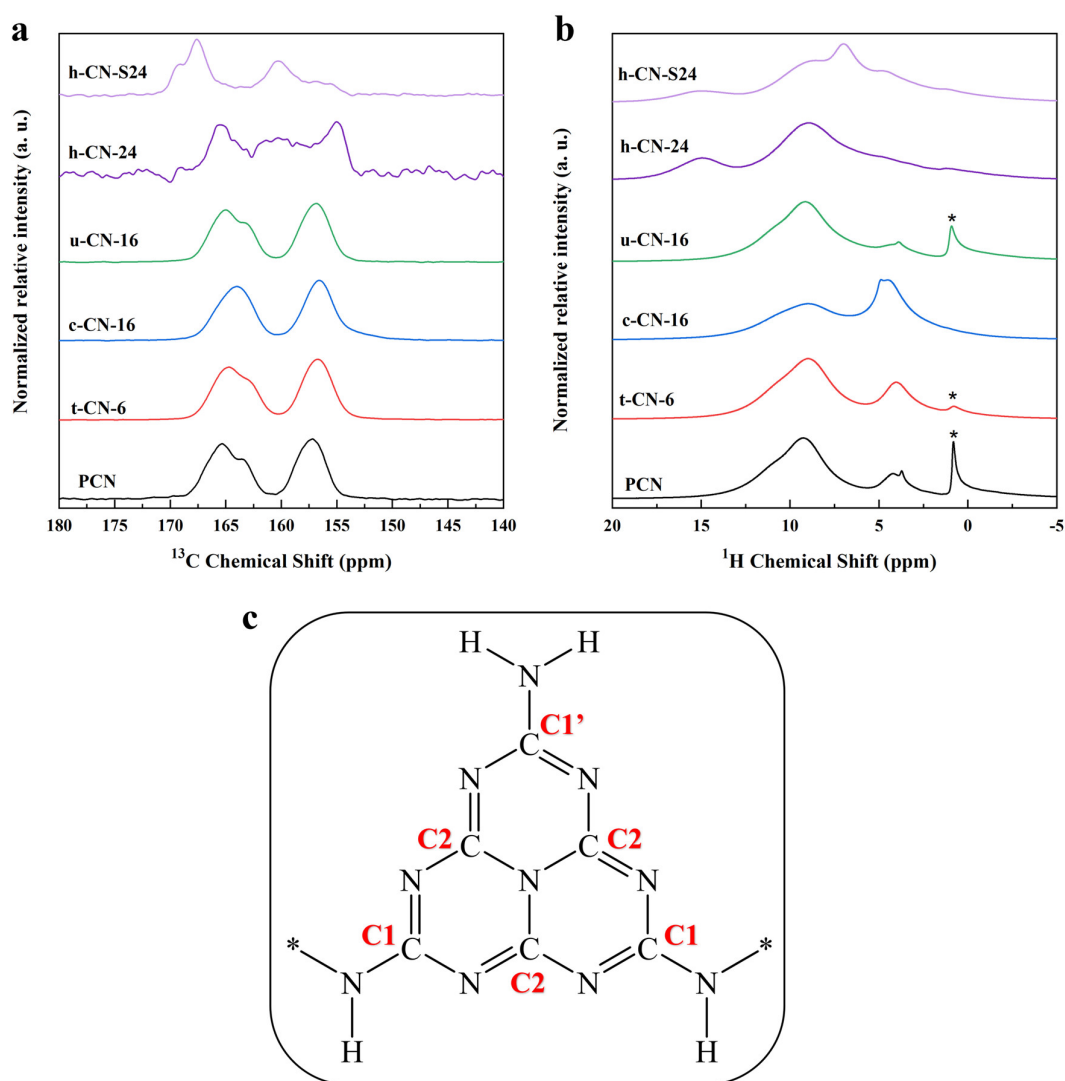


Figure 26. (a) ¹³C CPMAS NMR spectra at 8 kHz, recorded with the near-quantitative Multi-CP sequence,[221] and (b) ¹H MAS NMR at 60 kHz rotational frequency of differently exfoliated PCN. * mark a impurity signal from isopropanol. (c) Chemical structures of heptazine unit. * represent atomic connectivity to the next heptazine unit.

In situ EPR spectroscopy was employed to monitor the process of electron photoexcitation and capture. As shown in Figure 27, the pristine PCN shows a single Lorentzian line at $g = 2.0038$, which is attributed to unpaired electrons on the sp^2 -carbon atoms inside the π -conjugated C_3N_4 network [257, 258]. The same EPR signal is observed in t-CN-6, c-CN-16, and u-CN-16. However, in h-CN-24 and h-CN-S24, the signal is missing, suggesting no free charge carrier. This is due to the destruction of the π -conjugated C_3N_4 network, thereby the photocatalytic activity might be lost. Under light irradiation, the enhanced EPR intensities are found in PCN, t-CN-6, c-CN-16, and u-CN-16, indicating the increased photoexcited electron transfer from the VB to the CB [259].

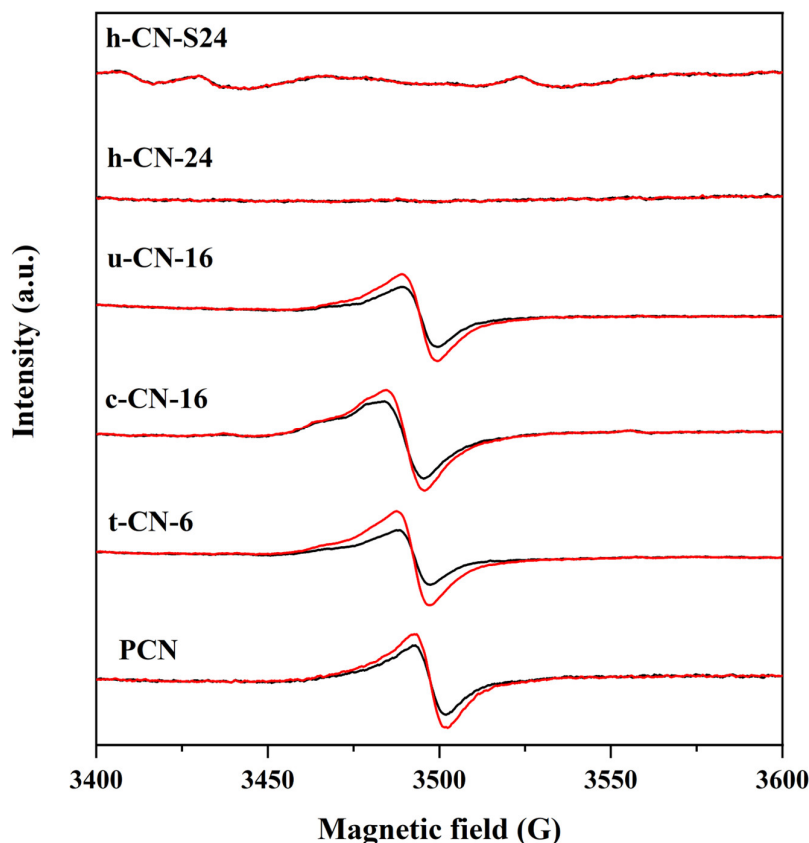


Figure 27. EPR spectra of differently exfoliated PCN with (Red line) and without (Black line) the light (> 420 nm) irradiation.

4.1.1.4 Optical properties and electronic band structure

UV-Vis DRS measurements were performed to study the optical absorption properties of differently exfoliated PCN. As shown in Figure 28, compared to pristine PCN, no clear shift of absorption edges was observed in t-CN, c-CN, and u-CN.

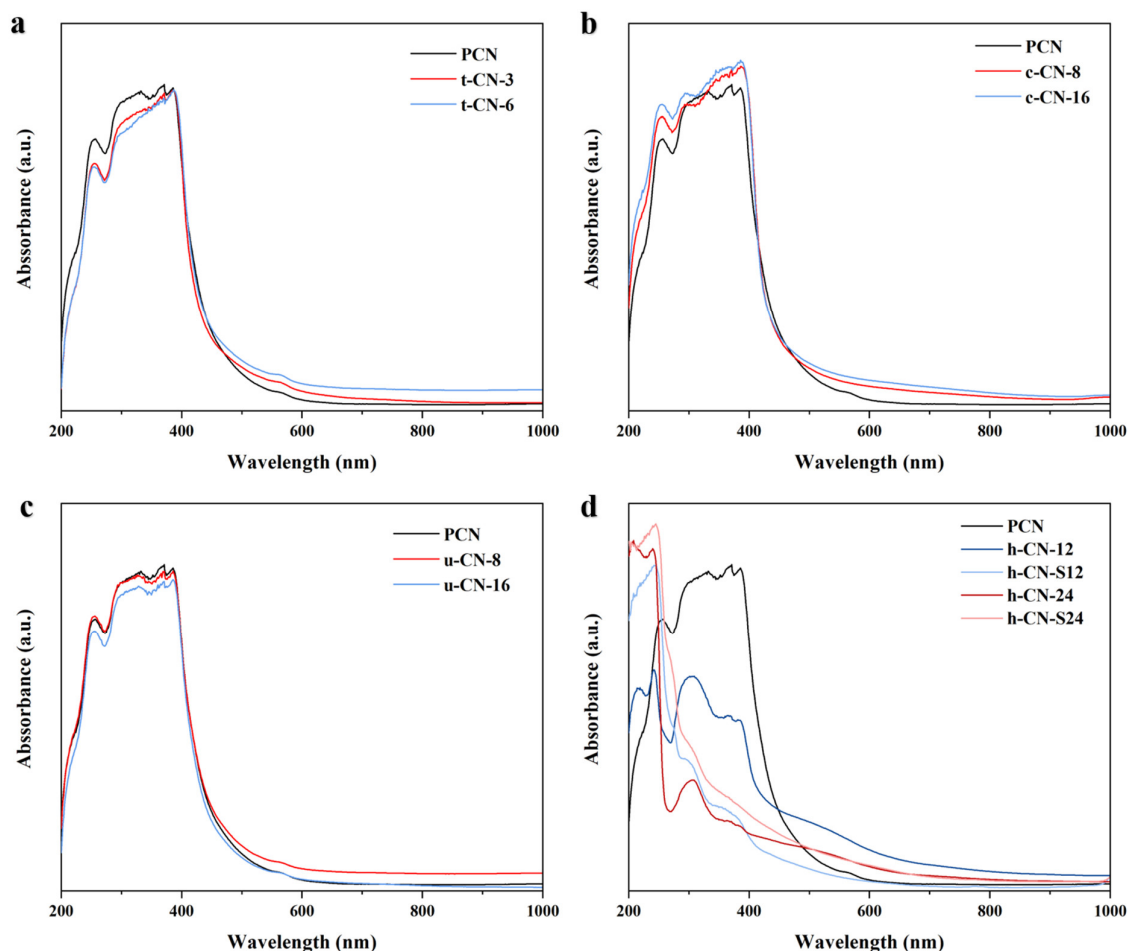


Figure 28. UV-vis absorption spectra of t-CN (a), c-CN (b), u-CN (c) and h-CN (d), which were calculated from the reflectance data with the Kubelka-Munk function.

Their optical bandgaps were further evaluated by the Tauc plots converted from Kubelka-Munk function [i.e., curve of converted $(ah\nu)^{1/2}$ versus $h\nu$ from the UV-vis spectrum, in which a , h , and ν are the absorption coefficient, Planck constant, and light frequency, respectively, a constant of $1/2$ is applied for an indirect band gap material] [260]. As shown in Figure 29, no significant changes in bandgap were observed in t-CN, c-CN, and u-CN. In contrast, a blue shift in the absorption edge and an apparent decrease in the absorbance were found in all h-CN samples. However, due to the lack of free charge carriers (confirmed by EPR) in h-CN, their bandgap is not discussed here. It is known that the color of a sample directly corresponds to its light absorption capacity. The pristine PCN sample is pale yellow, pointing to blue-violet light with a wavelength ranging from 400 nm to 500 nm. For t-CN-3 and t-CN-6, it was observed that the samples appeared white when they were initially taken out of the muffle furnace, but after grinding, their color turns back to yellow (Figure A.4).

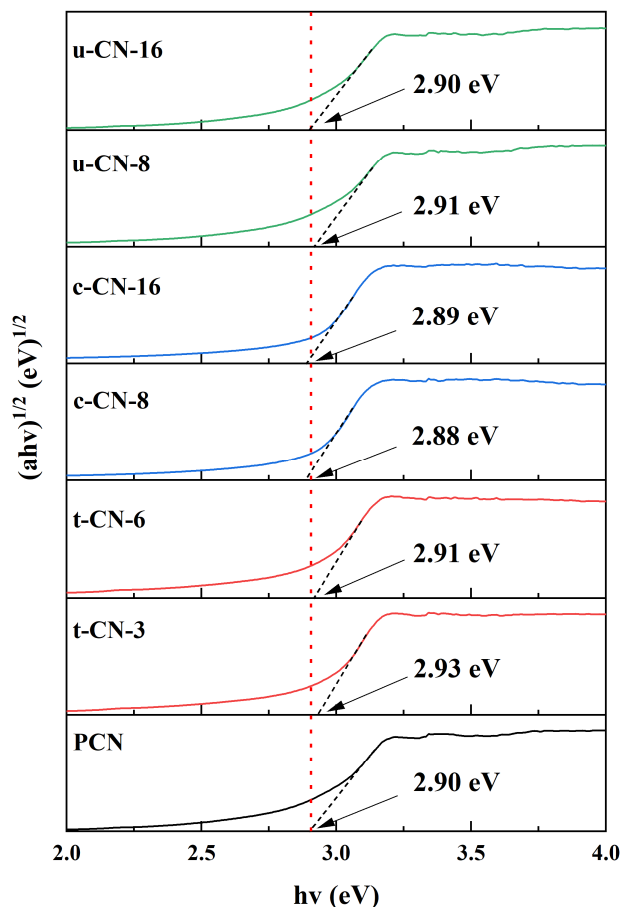


Figure 29. Bandgap calculation of differently exfoliated PCN according to Tauc's method.

Mott-Schottky plots were employed to study the flat band potential (versus Ag/AgCl at pH=6.6) of differently exfoliated PCN (Figure A.5). In combination with the above optical bandgap, the electronic band structures of differently exfoliated PCN were calculated and illustrated in Figure 30. Compared to the pristine PCN, the HOMO energy levels of t-CN-3 and t-CN-6 exhibited an up-shift trend over the exfoliation time. Conversely, the HOMO potentials of c-CN-8 and c-CN-16 were shifted downwards. Further valence band XPS spectra (VB-XPS) measurements confirmed this shift trends of valence band (VB) edge for t-CN and c-CN (Figure 25d). The VB edge of t-CN-6 shifted upwards to 2.56 eV compared to pristine PCN (2.67 eV). On the contrary, the VB potential of c-CN showed a progressive downshift over exfoliation time. Based on the band structure analysis, it can be concluded that thermal exfoliation can cause a shift upwards in the position of the VB and CB, thereby possessing a higher thermodynamic driving force for the photoreduction ability of electrons, while weakening the photooxidation ability of holes. By contrast, chemical exfoliation and ultrasonic exfoliation can shift the potentials of VB and CB edge of PCN downward, thus strengthening the photooxidation ability of holes while weakening the photoreduction ability of electrons.

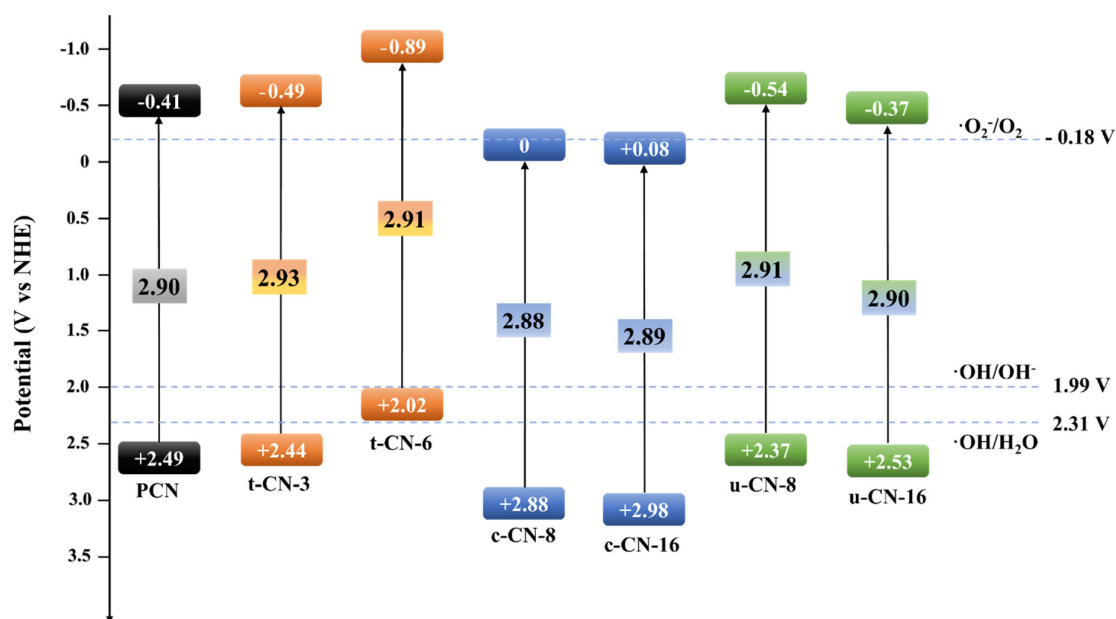


Figure 30. Electronic band structure of differently exfoliated PCN.

4.1.1.5 Charge-carrier separation and transport

The charge transfer behaviors of the samples were evaluated by photocurrent response. As illustrated in Figure 31a, u-CN retains the same photocurrent intensity as pristine PCN. An enhanced photocurrent density is generated in t-CN, which is nearly two times higher than that of the pristine PCN. This strongly illustrates that the mobility of the photoexcited charge carriers is promoted. The significant decreases in photocurrent density in c-CN and h-CN indicate inefficient photoelectron generation and low transfer efficiency in PCN after chemical and hydrothermal treatments.

Steady-state photoluminescence (PL) spectra were employed to further study the transfer and separation efficiency of charge carriers. With respect to the pristine PCN, the PL peak intensities for all t-CN, c-CN, and u-CN go higher and increases further with the exfoliation time increasing (Figure 31b). This suggests a decrease in charge-carrier separation efficiency after exfoliation, in agreement with the reported work [196, 200]. Particularly, the t-CN-6 exhibits a significantly greater intensity, indicating a higher recombination of charge-carrier as a result of its enhanced crystallinity [196]. This demonstrates that thermal exfoliation can promote the generation of photoexcited electrons but can also result in high charge-carrier recombination. As for c-CN, it shows a blue shift of 30 nm due to the quantum confinement effect of the reduced particle size of PCN [212]. The lowest intensities and blue shift of the PL peak were observed in h-CN samples, which were caused by the low charge generation, as confirmed by the above photocurrent analysis.

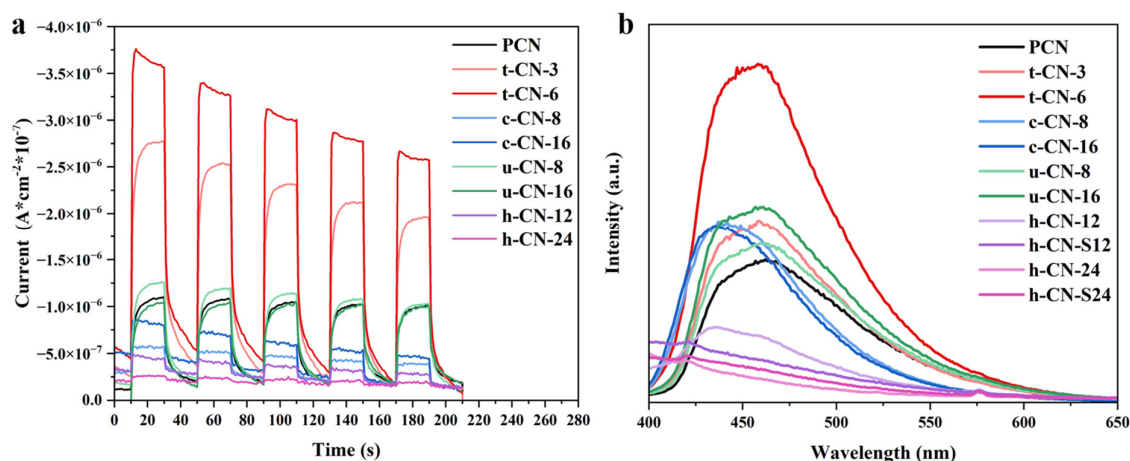


Figure 31. (a) Transient photocurrent (I–T) curves and (b) photoluminescence (emission) spectra of differently exfoliated PCN.

4.1.2 Experimental characterization for isolated Pd catalysts

4.1.2.1 Pd loading, BET surface area, and crystal and molecule structure

The samples were prepared using a wet impregnation method, in which organometallic palladium salts [$\text{Pd}(\text{TFA})_2$, $\text{Pd}(\text{acac})_2$, and $\text{Pd}(\text{OAc})_2$] in acetone for 24 h. The acetone was gradually removed by evacuation, and the samples were dried at 80 °C in an argon atmosphere for 24 h without undergoing further calcination (see chapter 3.1.2). Several organic solvents were tested in this study, considering their boiling points and polarity, as well as the solubility of $\text{Pd}(\text{TFA})_2$ in these solvents. As shown in Figure A.6, in addition to toluene, $\text{Pd}(\text{TFA})_2$ is highly soluble in these organic solvents. However, after standing for 24 h, a formation of Pd black was observed in ethanol, 2-propanol, and methanol, which might be due to the β -H elimination followed by the reductive elimination pathway [139]. Furthermore, considering that higher drying temperatures could lead to the aggregation of Pd atoms, acetone was decided to use as the solvent to prepare the isolated Pd catalysts. The low-boiling-point and low-polarity of the solvent acetone can effectively prevent Pd aggregation and result in the atomic dispersion of cationic Pd species [52]. The desired Pd loading on different supports is ca. 1 wt%, as confirmed by ICP-OES (Table A.3).

The BET surface area of all supports was characterized through nitrogen adsorption-desorption measurements. As shown in Figure A.7, the range of BET surface area for nitride supports varies from 8 $\text{m}^2 \text{g}^{-1}$ to 68 $\text{m}^2 \text{g}^{-1}$, and the BET surface area for oxide supports varies from 9 $\text{m}^2 \text{g}^{-1}$ to 168 $\text{m}^2 \text{g}^{-1}$. Therefore, the BET surface area of all supports is relatively random, and no high surface area is pursued.

After the deposition of 1 wt% Pd, all samples show enhanced intensities in their UV-Vis DRS spectra (Figure 32). The intensities of the absorbance spectra are further increased in higher loadings of 4 wt% Pd/TiO₂ and 4 wt% Pd/Al₂O₃ samples. Similarly, the absorbance spectra of Pd/PCN catalysts increase with the Pd loading increasing (Figure A.8). Furthermore, for the Pd/PCN samples with Pd loadings below 2 wt%, the DRS spectra suggest no difference before and after washing, while for the samples with higher Pd loading (4 wt%, 8 wt%, and 16 wt%), the absorbance spectra of the washed samples are significantly enhanced, even though the Pd loading was reduced to half of the original amount after washing. The reason for that is the removal of ligands letting more Pd atoms or clusters to be exposed. An exception here is the TiN support, which is a black material on which almost no diffuse reflection occurs. Therefore, it is hard to study the Pd/TiN sample by UV-Vis DRS and DRIFTS measurements.

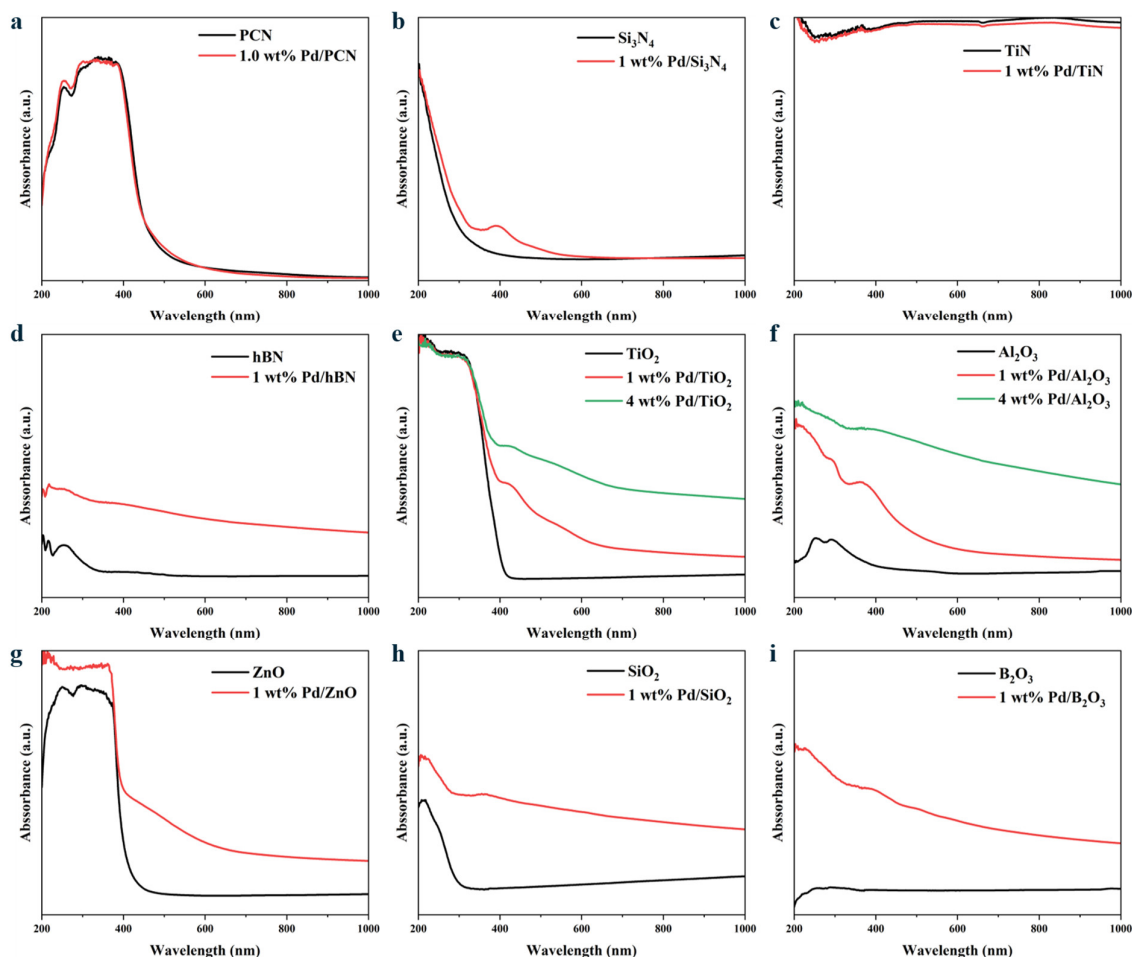


Figure 32. UV-Vis absorption spectra of various Pd samples and their corresponding pure supports.

The crystal structure and phase compositions were characterized by powder XRD. As shown in Figure 33, all Pd deposited samples show similar XRD patterns to their pure supports, and no

reflections associated with metallic Pd nanoparticles were observed, suggesting the high dispersion of the Pd. An additional reflex at 14.9° related to the TFA ligand was found in Pd/TiN and Pd/Si₃N₄, while in Pd/Al₂O₃ and Pd/B₂O₃ samples, an additional reflex at 18.1° associated with the TFA ligand was observed. Moreover, with an increasing Pd loading in the Pd/PCN samples (Figure A.9), the reflex (210) at 13.3° and the (002) at 27.7° attributed to the PCN are not as pronounced as before. The new emerging reflexes in the 2θ range of $5 - 25^\circ$, related to the precursor Pd(TFA)₂, were found in the unwashed 8 wt% and 16 wt% Pd/PCN samples, and these reflexes disappeared after washing, suggesting successful removal of the TFA ligand.

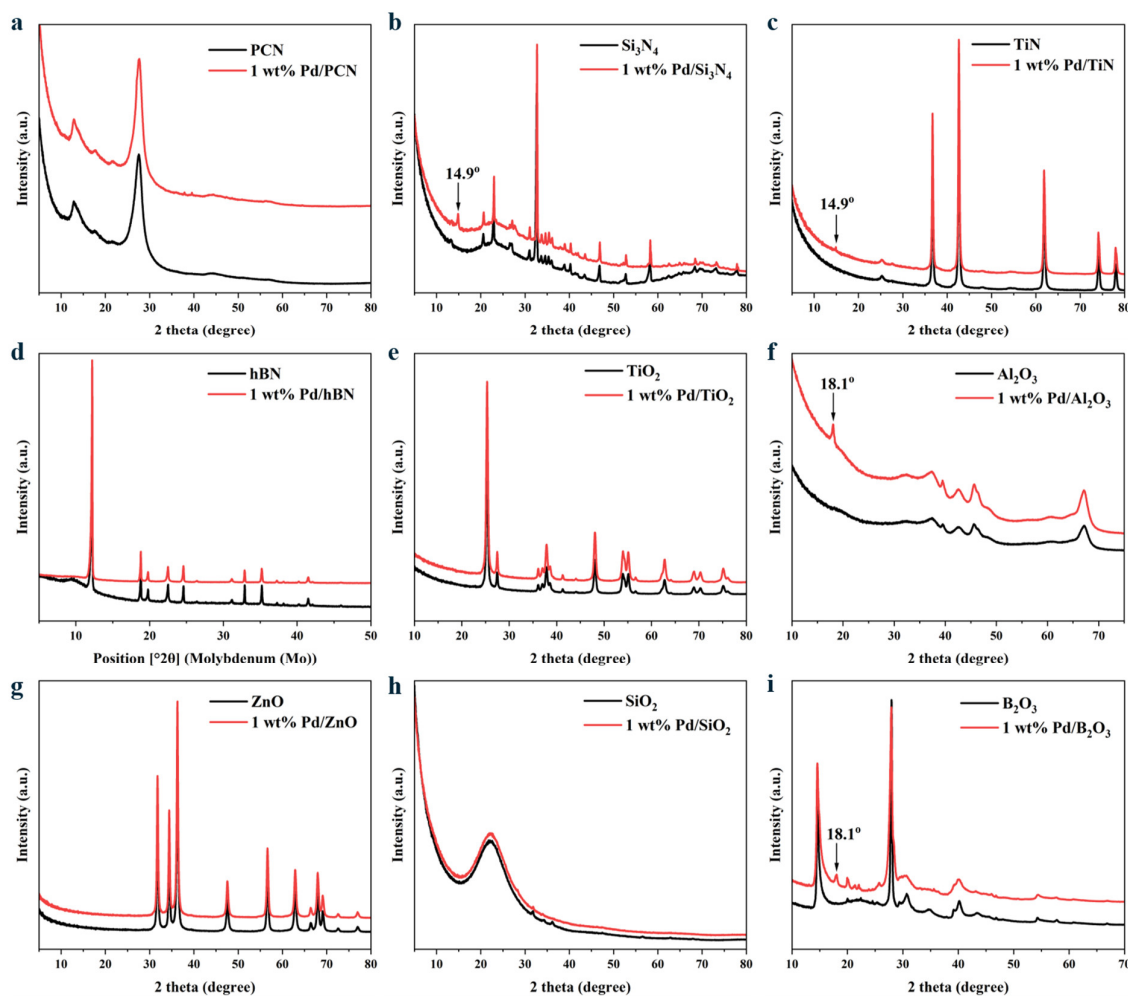


Figure 33. XRD pattern of various Pd samples and their corresponding pure supports.

The molecular structures of the Pd samples were characterized by DRIFTS. As illustrated in Figure A.10 and A.11, the characteristic DRIFTS spectra of all Pd catalysts are similar to those of the corresponding support, indicating that the molecular structure maintains the same after the deposition of the Pd. The IR bands at 1254 and 1181 cm^{-1} associated with Pd(TFA)₂ were observed in metal oxides (TiO₂, Al₂O₃, and ZnO) supported Pd samples, whereas they do not

appeared in the non-metal oxide (SiO_2 and B_2O_3) or nitrides (hBN and Si_3N_4) supported Pd samples. Besides, all Pd/PCN samples show similar DRIFTS spectra to bulk PCN, and no IR band related to $\text{Pd}(\text{TFA})_2$ was observed. The above XRD and DRIFTS analysis prove that the crystal structure and molecular structure of all supports stay the same after Pd deposition.

4.1.2.2 Evaluation of residual organic ligands on support surface

To investigate the fate of residual TFA ligand, a series of Pd/PCN catalysts with Pd loadings ranging from 0.5 to 16 wt% were prepared and then washed with acetone. For samples with Pd loading below 2 wt%, there is no loss of Pd after washing (Table A.5). Meanwhile, the relative amount of F significantly decreased (Table A.6), suggesting that the organic ligands are mostly not or not strongly attached to Pd.

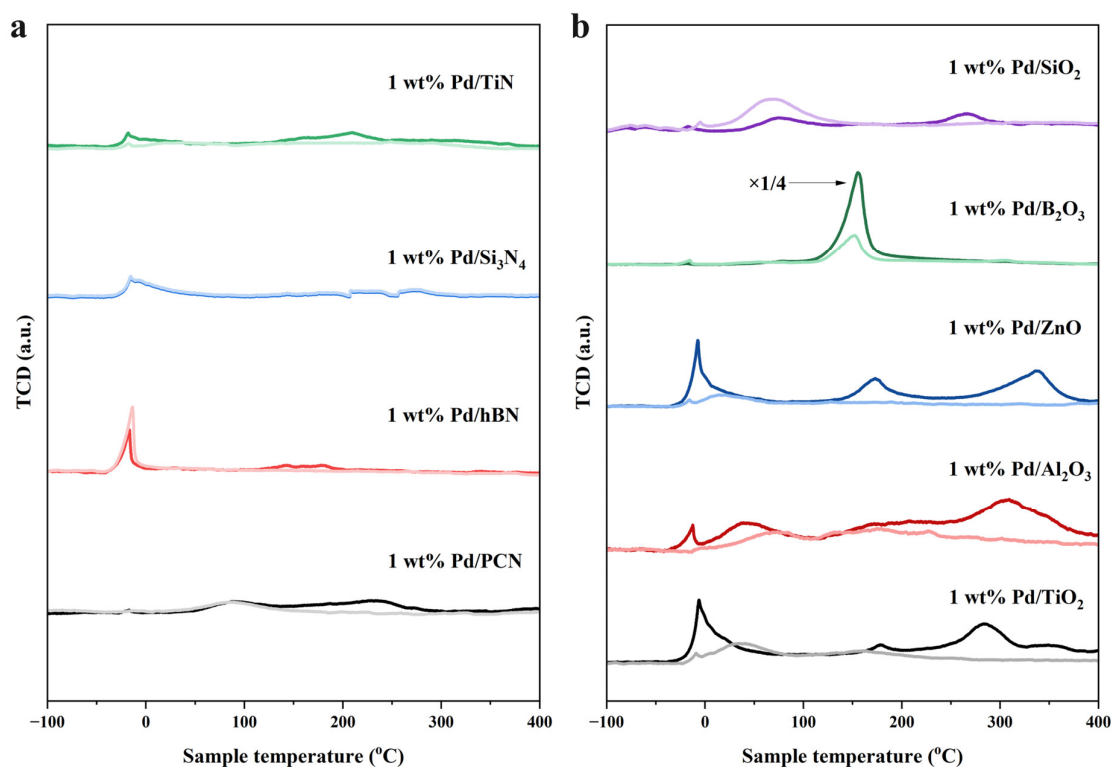


Figure 34. TPDE patterns of various Pd samples (intensely colored line) and their corresponding pure supports (pale line) in helium atmosphere.

Moreover, temperature-programmed decomposition (TPDE) measurements, coupled with quadrupole mass spectrometry (QMS), were performed to evaluate the remaining ligand in the catalysts. As shown in Figure 34, for Pd/oxide catalysts, two big shoulders are present on the high-temperature (150 °C – 400 °C) side of the main temperature-programmed decomposition peak. These shoulders result from the decomposition of the organic ligand from the Pd precursor. For Pd/nitrides samples, however, no such significant signal was observed in the

same temperature range. Further QMS measurements (Figure A.12 and A.13) confirmed that the Pd/oxide samples released a large amount of CO and CO₂, especially for metal oxide supported Pd samples, while nitride supported Pd samples did not. The combination of TPDE and QMS results suggests that there is a significant amount of Pd precursor remaining on the oxide surface while not on the nitride surface. This result was further confirmed by elemental analysis, where less F element was found in Pd/nitride catalysts compared to Pd/oxide catalysts (Table A.4).

4.1.2.3 Oxidation state analysis by XPS

XPS was performed to investigate the chemical nature of surface Pd species. Two types of Pd species were observed on nitride supports (Figure 35a): one peak is at ca. 338.3 eV, and the other one is at ca. 336.3 eV. To gain more insight on parameters influencing the oxidation state of Pd on different nitride supports, further studies were conducted. The Pd/PCN was selected as an example, and three different Pd(II) salts were deposited on PCN to investigate the Pd species in more detail. Notably, the Pd 3d binding energies of the pure Pd(II) salts are slightly different: the Pd 3d_{5/2} peaks for Pd(TFA)₂, Pd(acac)₂, and Pd(OAc)₂ are found at 339.1, 338.6, and 338.8 eV, respectively (Figure 35b). However, after depositing these three different Pd salts on PCN with the same procedure, the resulting Pd species exhibit similar Pd 3d binding energies (Figure 35c). This indicates the same electronic structure and excludes the influence of the different ligands (TFA, acac, and OAc).

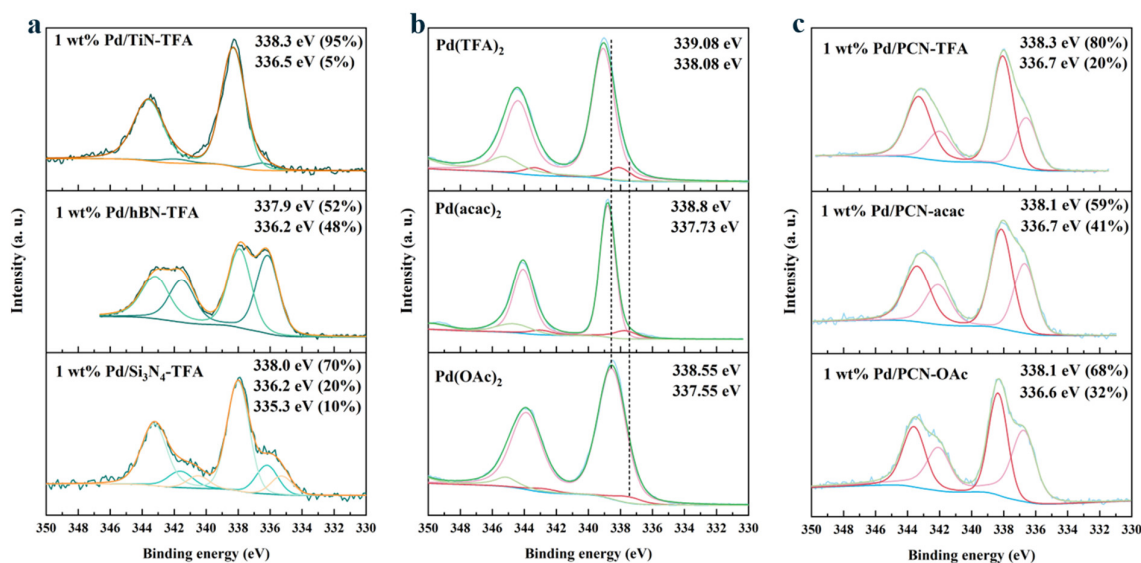


Figure 35. Pd 3d photoemission spectra of (a) different Pd/nitride samples, (b) different Pd salts, and (c) Pd/PCN samples prepared with different Pd salts.

The influence of Pd loading on the binding energy in Pd/PCN samples (ranging from 0.5 wt% to 16 wt%) was studied as well: the samples with Pd loadings of 0.5, 1, 2, 4, and 8 wt% all exhibit similar Pd 3d binding energies (Figure 36a). The negative shift of the Pd 3d binding energy of -0.3 eV was only observed in the highest loading of 16 wt% sample. However, there is no obvious shift trend from the Pd 3d XPS spectra of the washed Pd/PCN samples (Figure 36b). One additional binding energy at 335.4 eV was observed in the 400 °C calcined Pd/PCN samples, which was attributed to the formation of large Pd nanoparticles or metallic Pd (Figure 37). Overall, three different Pd species appeared in the Pd/PCN samples: (1) Pd species with a binding energy at ca. 338.3 eV corresponds to the atomically dispersed Pd species, (2) Pd species with a binding energy at ca. 336.3 eV is attributed to the Pd nanoclusters, and (3) Pd species with a binding energy at ca. 335.4 eV is assigned to the large Pd nanoparticles or metallic Pd.

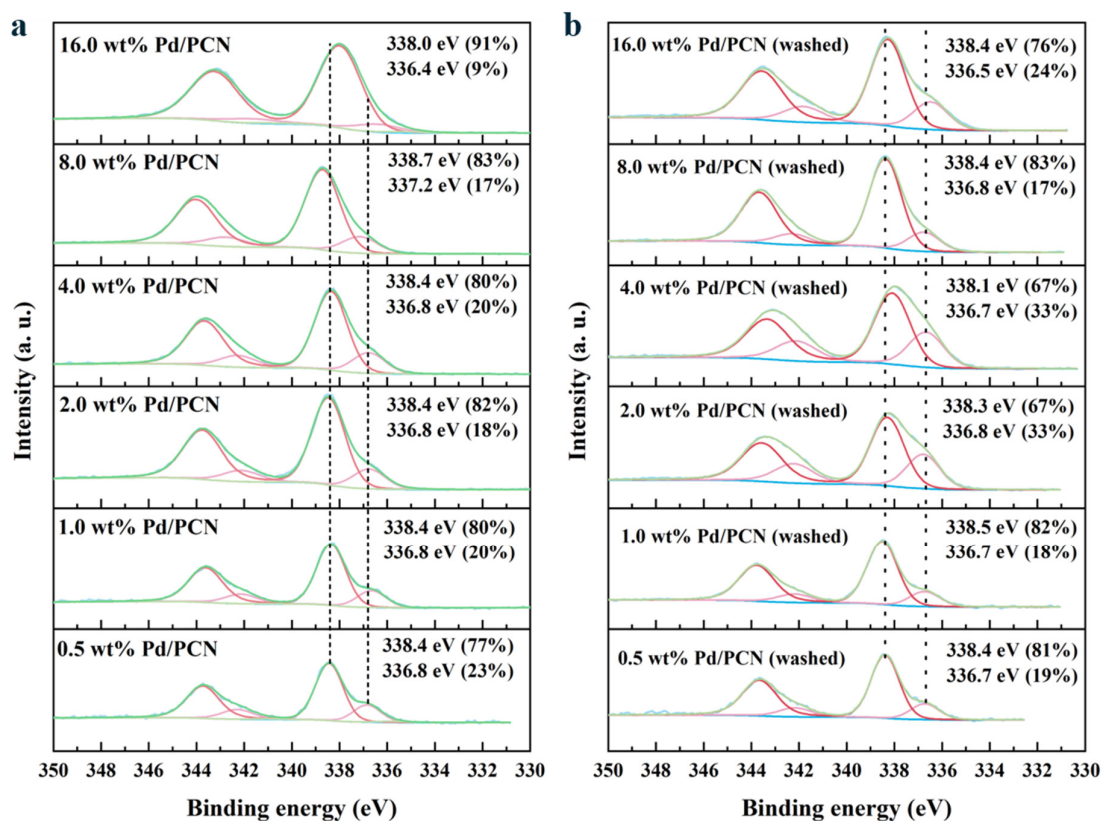


Figure 36. Pd 3d photoemission spectra of Pd/PCN samples before and after washing.

It is noteworthy that without any calcination, the lowest Pd 3d binding energy of 335.3 eV was observed in Pd/Si₃N₄. This binding energy could originate from the formation of large Pd nanoparticles or the formation of Pd–O–Si species, which is supported by its FT-EXAFS

analysis (Figure 52). A similar binding energy at ca. 335.5 eV was further observed in the XPS spectra for the Pd/SiO₂ sample.

However, although the binding energies on different nitride supports are similar, the ratios of species with higher and lower binding energies are different. For example, in 1 wt% Pd/hBN, the Pd species with a lower binding energy at 336.2 eV accounts for approximately 48% of the total Pd species, while in 1 wt% Pd/TiN, the Pd species with a lower binding energy at 336.5 eV represents only about 5% of the total Pd species.

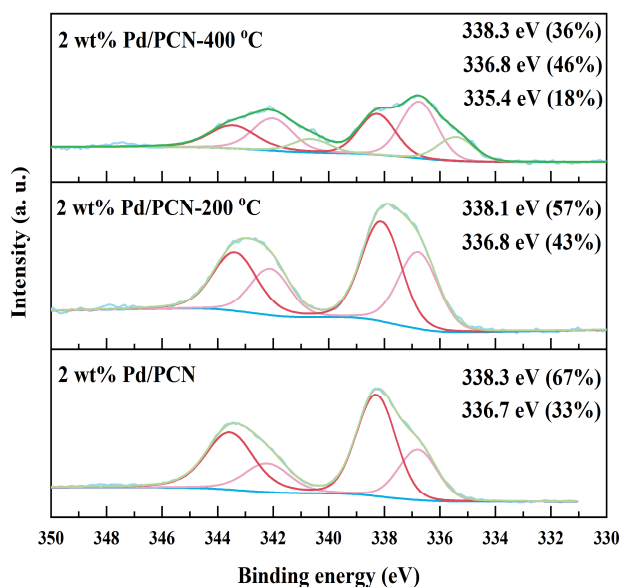


Figure 37. Pd 3d photoemission spectra of 2 wt% Pd/PCN-200 °C and 2 wt% Pd/PCN-400 °C.

For the Pd/oxide samples, there are also two types of Pd species: one is at ca. 337.3 eV, and the second one is at ca. 335.8 eV (Figure 38). Pd/TiO₂ is discussed here as an example. When increasing the Pd loading from 1 wt% to 4 wt%, the binding energy positions remain unchanged, but the relative ratio of Pd species with a low valence state (ca. 335.8 eV) significantly increases (Figure A.14a). A similar trend was observed in the XPS spectra of high-loading 4 wt% Pd/Al₂O₃ (Figure A.14c). Therefore, the broad peak centered at 337 eV is associated with the atomic Pd species, and the component at ca. 335.8 eV is assigned to the nanometer Pd clusters. One additional binding energy at ca. 334.3 eV was observed in the 400 °C calcined Pd/TiO₂ samples, which could be assigned to the formation of large nanoparticles or metallic Pd (Figure 39). The ratios of Pd species with high and low binding energies also differ in Pd/oxide samples. For example, in 1 wt% Pd/ZnO sample, the Pd species with a lower binding energy at 335.8 eV is around 48% of the total Pd species, but in 1 wt% Pd/B₂O₃ sample, the Pd species with a lower binding energy at 335.8 eV only comprises 16% of the total Pd species. This phenomenon is similar to the observation for Pd/nitride samples.

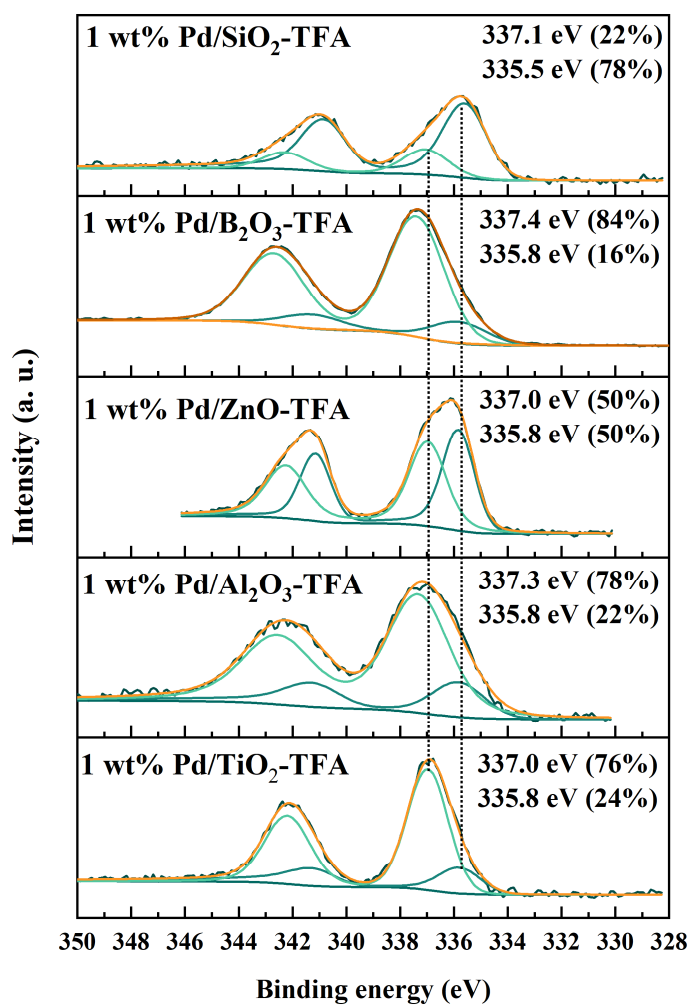


Figure 38. Pd 3d photoemission spectra of Pd/oxide samples.

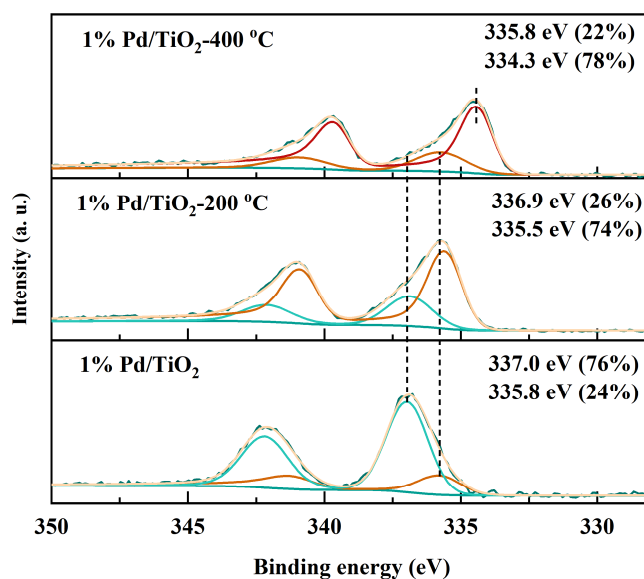


Figure 39. Pd 3d photoemission spectra of 1 wt% Pd/PCN-200 °C and 1 wt% Pd/PCN-400 °C.

To summarize, the above XPS analysis demonstrates that the Pd species on different nitride supports (PCN, TiN, hBN, and Si₃N₄) exhibit similar Pd 3d binding energies (Figure 40). Likewise, the Pd species on different oxide supports also show similar Pd 3d binding energies. The difference is that the Pd 3d binding energies of Pd species on nitride supports are more positive than those of Pd species on oxide supports.

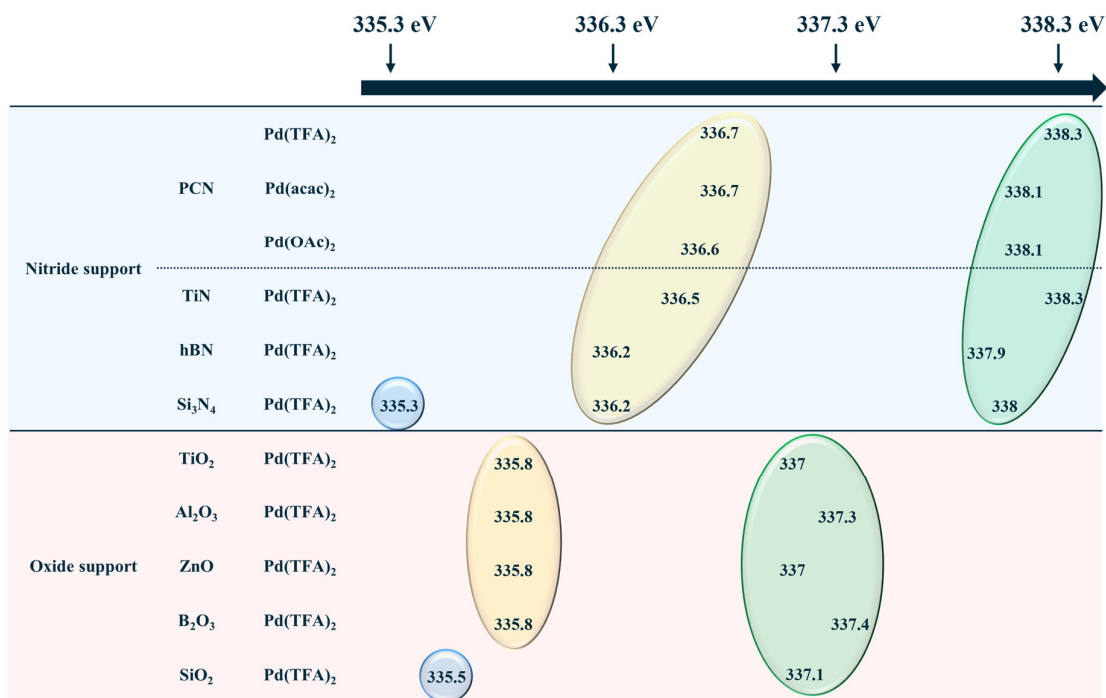


Figure 40. Binding energy of Pd 3d_{5/2} peaks obtained from X-ray photoelectron spectra of various Pd catalysts.

4.1.2.4 Atomic site analysis by STEM

In Figure 41, the high-angle annular dark-field scanning transmission electron microscopy (HAADF-STEM) images of the Pd/PCN samples show that the Pd speciation is predominantly atomically dispersed in the samples with Pd loading of 0.5 wt% and 2 wt%, with very few nanoparticles being observed. Besides, the 2 wt% Pd/PCN sample shows additional Pd clusters, which are unstable under the electron beam (Figure 42a, b). These unstable Pd clusters are derived from the residual salts during synthesis, which can be effectively removed by further acetone washing (Figure 42c, d). After removing the Pd nanoclusters, the washed 2 wt% Pd/PCN sample remained the isolated Pd atoms and a few large Pd nanoparticles on the surface (Figure A.15). It is worth noting that the PCN material was not stable under high doses of the electron beam, as can be seen in the red region highlighted in Figure 41b. The same effect was observed in Figure 41a, rendering the Pd atoms visible.

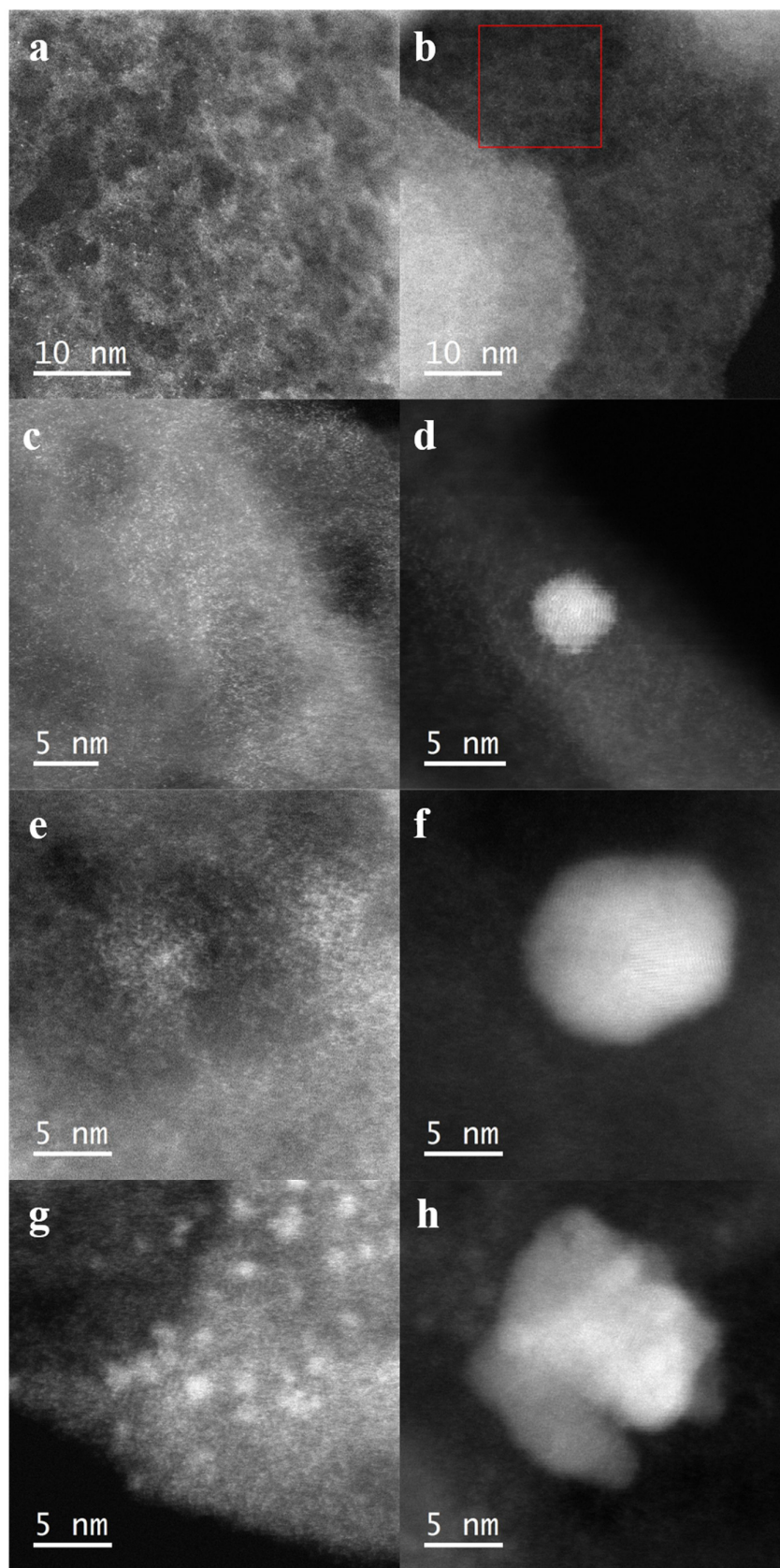


Figure 41. Representative HAADF-STEM images of 0.5 wt% (a and b), 2 wt% (c and d), 4 wt% (e and f), and 16 wt% Pd/PCN samples (g and h).

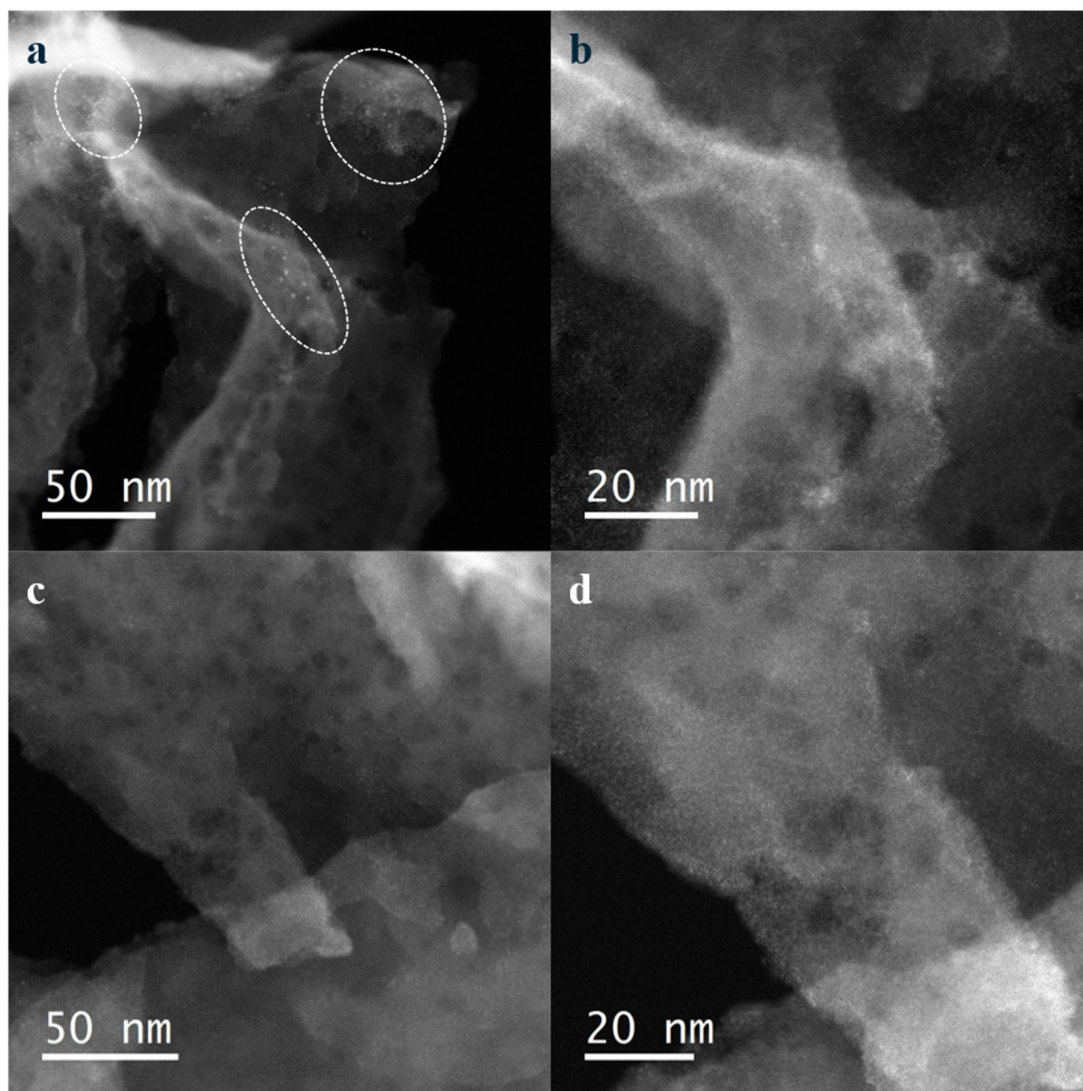


Figure 42. Representative HAADF-STEM images of 2 wt% Pd/PCN sample before (a and b) and after washing (c and d). Unstable Pd nanoclusters highlighted by the white ellipses.

Furthermore, in the 4 wt% Pd/PCN sample, the Pd atoms tend to aggregate together, and as the Pd loading increases, the formed Pd particle size also grows. The 16 wt% Pd/PCN sample exhibits that the nanoclusters (~2 nm diameter) are already the dominant species. The HAADF-STEM (Figure 43) of 1 wt% Pd/TiO₂ shows the presence of atomic Pd species on the TiO₂ support, while a large amount of Pd nanoclusters (~2 nm diameter) and Pd nanoparticle (5–10 nm diameter) were also observed due to the aggregation of the unbonded Pd precursor. Additional SEM images confirm that the morphologies of the TiO₂ and PCN support retained the same before and after Pd deposition, as illustrated in Figure A.16.

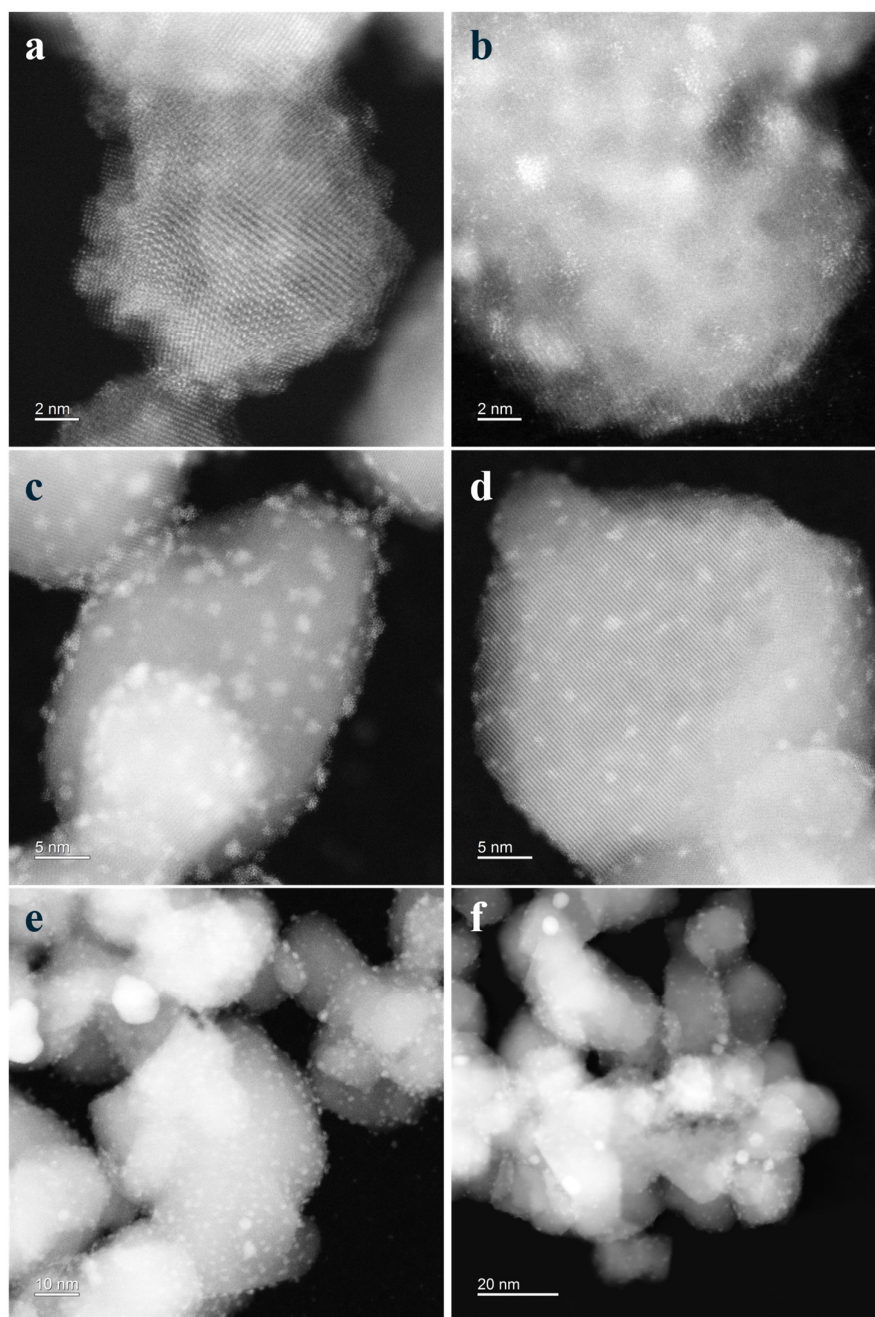


Figure 43. Representative HAADF-STEM images of 1 wt% Pd/TiO₂ sample.

4.1.2.5 Chemical state analysis by CO-DRIFTS

The influence of the support on the oxidation state of Pd was further investigated by CO-DRIFTS. Three Pd/oxide samples (Figure 44) generally showed two types of carbonyl bands, which are related to linear CO on isolated Pd cations and bridged CO on Pd nanoclusters, respectively. The presence of CO binds in bridged configurations in all Pd catalysts based on oxidic supports, indicating the coexistence of Pd single atoms and nanoparticles [125]. No adsorbed CO was present on the bare oxide supports under the experimental conditions.

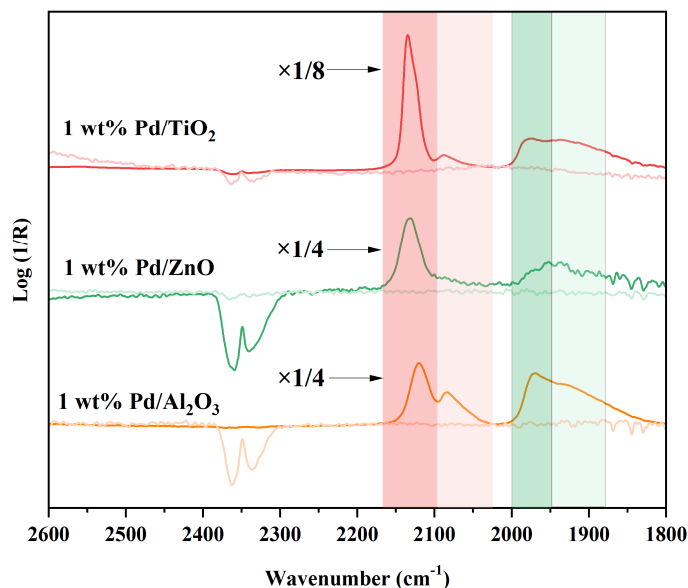


Figure 44. CO-DRIFTS spectra of Pd/TiO₂, Pd/ZnO, and Pd/Al₂O₃ samples, marked with intensely colored line, and CO-DRIFTS spectra of their corresponding pure supports, marked with pale line.

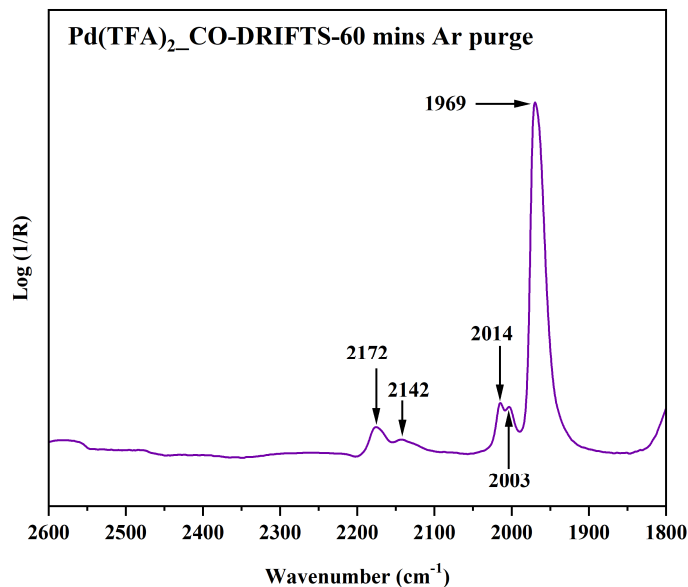


Figure 45. CO-DRIFTS spectrum of Pd (TFA)₂.

For Pd/TiO₂, the infrared bands centered at 2135 and 2126 cm⁻¹ are attributed to CO adsorbed on the isolated Pd species with different oxidation states, whereas the band centered at 2088 cm⁻¹ is attributed to the CO adsorbed on either the Pd nanoclusters or Pd-Ti species from EXAFS fitting. The broad bands centered at 1969 and 1938 cm⁻¹ are assigned to bridged CO adsorbed on Pd nanoclusters or Pd nanoparticles, which result from the aggregation of unbonded Pd precursors. This assignment was further confirmed by the CO-DRIFTS spectrum of Pd(TFA)₂ (Figure 45), which exhibits a pronounced bridge carbonyl band centered at 1969

cm^{-1} . Moreover, the $\text{Pd}(\text{TFA})_2$ did not present any carbonyl bands in the region of $2130 - 2050 \text{ cm}^{-1}$, suggesting the emerged bands for Pd/TiO_2 at 2135 , 2126 , and 2088 cm^{-1} derived from CO adsorbed on anchored Pd sites, rather than from the Pd precursor.

With increasing the Pd loading to 4 wt%, the band intensities for CO linearly adsorbed on Pd at 2135 and 2126 cm^{-1} remain unchanged, while the intensity of the bridge carbonyl band at 1938 cm^{-1} is significantly enhanced, indicating the formation of more Pd nanoclusters (Figure A.14b). Similarly, in comparison to the 1 wt% $\text{Pd}/\text{Al}_2\text{O}_3$, the enhanced intensities of bridge carbonyl bands were found in the CO-DRIFT spectrum of 4 wt% $\text{Pd}/\text{Al}_2\text{O}_3$ (Figure A.14d). The increase in the number of Pd nanoclusters in 4 wt% Pd/TiO_2 and 4 wt% $\text{Pd}/\text{Al}_2\text{O}_3$ agrees well with the observation from their Pd 3d XPS spectra. After calcination of Pd/TiO_2 at 200°C and 400°C , both CO-DRIFTS spectra still show three linear CO infrared bands. However, increasing the temperature (Figure 46) did lead to a downshift in frequencies and a drop in intensities of linear carbonyl bands, and conversely, the enhanced intensities of bridge carbonyl bands were observed.

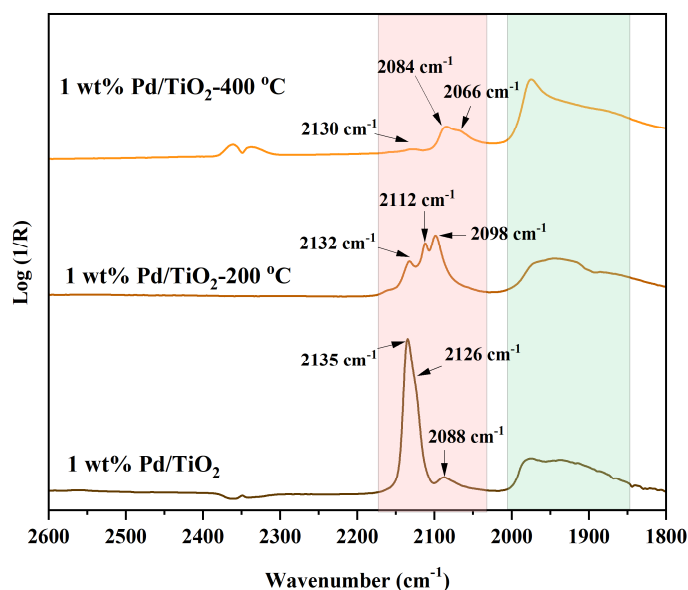


Figure 46. CO-DRIFTS spectra of 1 wt% Pd/TiO_2 - 200°C and 1 wt% Pd/TiO_2 - 400°C .

Furthermore, over Pd/TiO_2 , an oxidation sequence of different carbonyl species was observed: the CO molecules adsorbed on Pd nanoclusters were quickly oxidized and removed upon O_2 exposure at 25°C (Figure 47a), as indicated by the rapid drop in the major CO bands at 1974 and 1938 cm^{-1} ; afterward, the bands related to CO linearly adsorbed on Pd with the signal at 2088 , 2126 , and 2135 cm^{-1} were oxidized in this order with the increased temperature to 200°C (Figure 47b) [261, 262]. A similar oxidation sequence was also observed in $\text{Pd}/\text{Al}_2\text{O}_3$ (Figure

A.17) and Pd/ZnO (Figure A.18). Besides, the NAP-XPS analysis revealed a CO-induced Pd sintering in the Pd/TiO₂ sample. The spectrum of the Pd 3d core line, shown in Figure 48, shows that the isolated Pd species (~ 337.4 eV) turned into near-neutral Pd $^{\delta+}$ species (~ 336.2 eV) after adsorption of CO, which is due to the formation of a stable carbonyl leading to a weakened interaction between the Pd atom and the TiO₂ support.

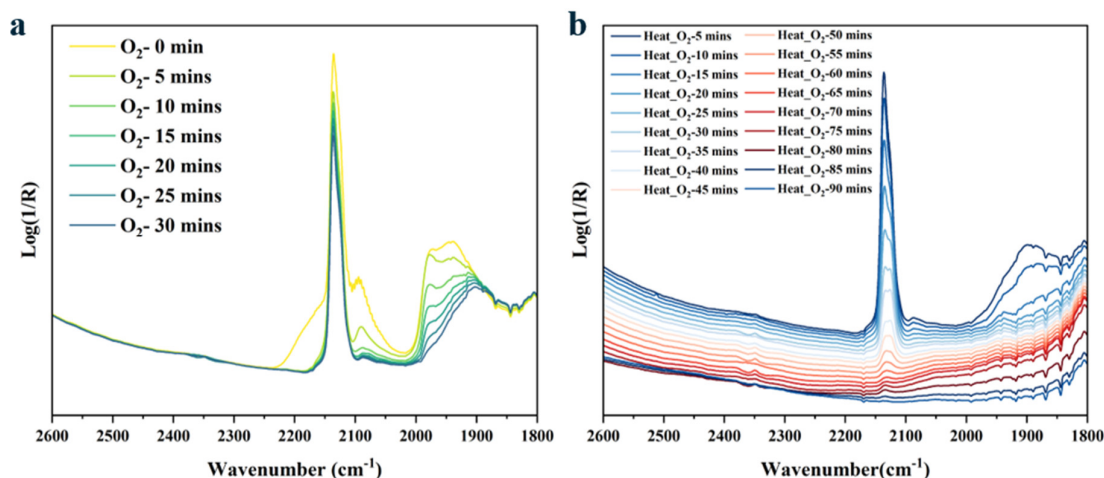


Figure 47. DRIFTS spectra of CO removed from Pd/TiO₂ upon O₂ exposure at 25 °C (a) and during heating process to 200 °C (b).

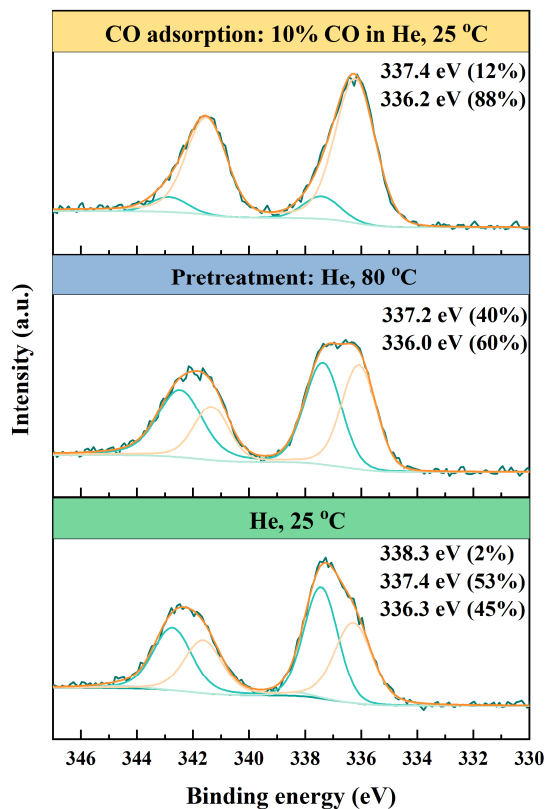


Figure 48. NAP-XPS of the Pd 3d core line of Pd/TiO₂ during the CO adsorption process.

In comparison to Pd/oxide catalysts, the CO adsorption bands for the Pd/nitride samples are significantly weaker (Figure 49). No signal is even observed in 1 wt% Pd/Si₃N₄. To obtain a better IR response signal, the CO-DRIFTS spectra of Pd/PCN samples with higher loadings were measured (Figure 50). There are four sets of CO adsorption bands centered at 2123, 2090, 1987, and 1933 cm⁻¹. The IR bands at 2123 and 2090 cm⁻¹ correspond to linear adsorption of CO molecules on isolated Pd atoms. The IR bands at 1987 and 1933 cm⁻¹ are assigned to the bridge adsorption of CO molecules on the Pd nanoclusters or Pd nanoparticles. The relative intensity of the IR bands at 1987 and 1933 cm⁻¹ increases with the Pd loading, which is consistent with the presence of more Pd nanoclusters on the PCN support, as observed from the HAADF-STEM images (Figure 41). Further evidence comes from the CO-DRIFTS spectra of the washed Pd/PCN catalysts. As shown in Figure 42, the bridge carbonyl bands at 1987 and 1947 cm⁻¹ are significantly decreased, indicating the removal of the Pd nanoclusters, confirmed by the STEM results (Figure 42).

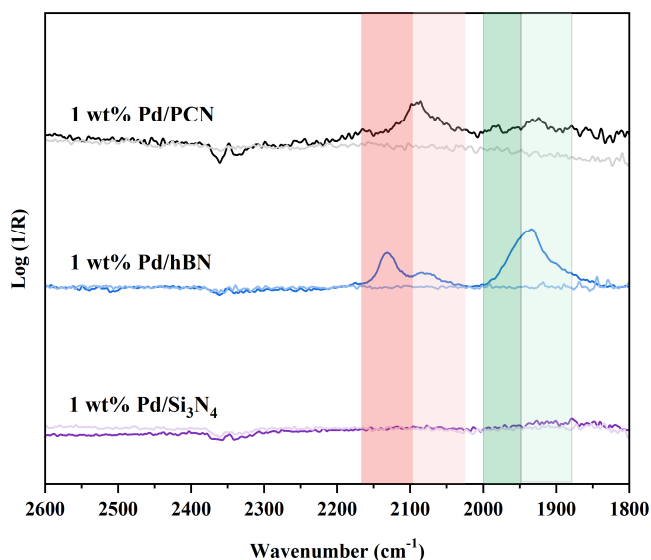


Figure 49. CO-DRIFTS spectra of Pd/PCN, Pd/hBN, and Pd/Si₃N₄ samples, marked with intensely colored line, and CO-DRIFTS spectra of their corresponding pure supports, marked with pale line.

Besides, it is observed that the intensity of linear carbonyl bands changes as the Pd loading increases. Pd/PCN samples below 1 wt% loading exhibit only one linear CO adsorption band centered at 2090 cm⁻¹, which is assigned to the Pd species with a low Pd 3d binding energy. With the Pd loading increased to 2 wt%, the intensity of the IR band centered at 2090 cm⁻¹ remains the same, suggesting the saturation of this type of Pd species. At the same time, a new linearly adsorbed CO band centered at 2123 cm⁻¹ emerges, indicating the presence of another Pd species, and its intensity rises to saturation when the Pd loading is 4 wt%. Further increasing

the Pd loading will only contribute to the bridge CO adsorption, suggesting the formation of more Pd nanoclusters.

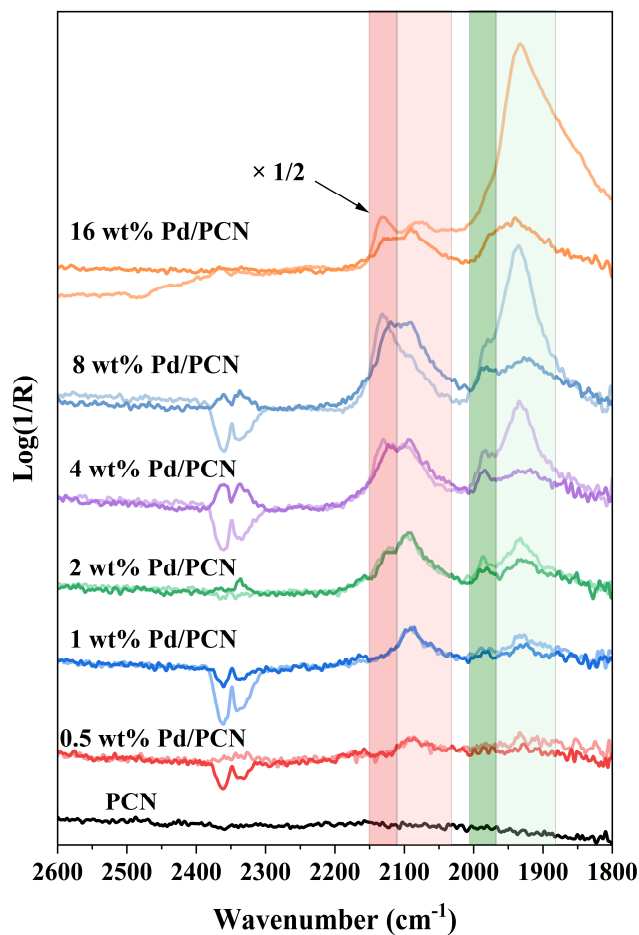


Figure 50. CO-DRIFTS spectra of various Pd/PCN samples, marked with pale line, and CO-DRIFTS spectra of the washed Pd/PCN catalysts, marked with intensely colored line.

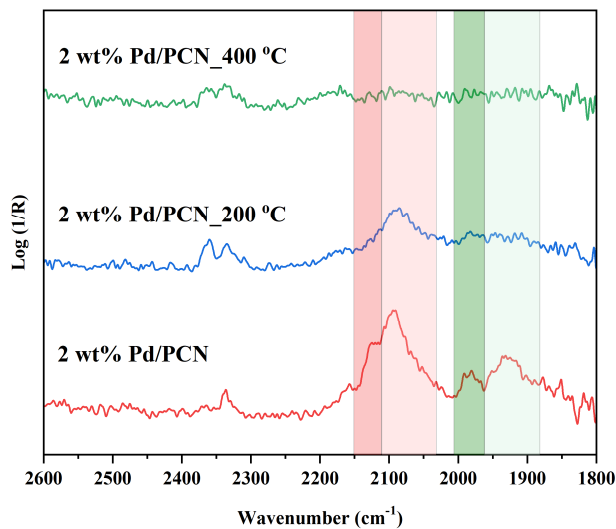


Figure 51. CO-DRIFTS spectra of 2 wt% Pd/PCN-200 °C and 2 wt% Pd/PCN-400 °C.

To sum up, through the above CO-DRIFTS analysis, a Pd deposition sequence on PCN was observed: (1) cationic Pd with a low oxidation state, exhibiting a linearly adsorbed CO stretching frequency of 2090 cm^{-1} , (2) cationic Pd with a high oxidation state, displaying a linearly adsorbed CO stretching frequency of 2123 cm^{-1} , and (3) semi-oxidized Pd sites with two stretching frequencies of bridge-adsorbed CO, centered at 1987 and 1947 cm^{-1} , respectively. From Pd 3d XPS spectra, however, only two types of Pd species were observed, so that the binding energy peak centered at 338.3 eV may contain at least two types of Pd species: one is Pd species bonded to the PCN support, and the other comprises unbonded Pd species, i.e., Pd salts. The CO-DRIFTS spectra for the 2 wt% Pd/PCN calcined at 400°C shows no CO adsorption band (Figure 51), which is due to the formation of large Pd nanoparticle or metallic Pd after calcination, as confirmed by XRD (Figure A.20).

4.1.2.6 Atomic structure analysis by XAS

Pd K-edge X-ray absorption data were recorded *ex situ* for all samples. XANES spectroscopy is highly sensitive to the 3D arrangement of atoms around the photo-absorber and has been applied to identify the atomic-site structures. The shapes of the XANES spectra (Figure 52a) for the Pd/TiO₂, Pd/Al₂O₃, and Pd/ZnO are close to the bulk PdO in contrast to the samples Pd/hBN, Pd/Si₃N₄, and Pd/PCN, which hint to different coordination environment for Pd on different supports. Also, the modification of the spectral shape on different nitride supports was observed.

The EXAFS data is shown in Figure 52b, and the results of the fitting are summarized in Table 3. In Pd/Al₂O₃ and Pd/ZnO, the averaged Pd–O coordination number for both is 3.6, and the corresponding bond lengths are 2.04 and 2.02 Å , respectively. For Pd/TiO₂, in addition to the peak corresponding to the Pd–O shell at a distance of 2.07 Å , a weak peak, which might be attributed to the Pd–O–Ti species at a distance of 2.73 Å (CN < 0.2), was found in the FT-EXAFS spectra. The EXAFS analysis revealed that in Pd/hBN, the Pd atom is bonded to the hBN surface through three nitrogen atoms at a distance of 2.05 Å , and an additional shell with a distance of 2.80 Å is associated with the Pd–N–Pd shell, indicating the presence of Pd nanoparticles. Notably, the coexistence of Pd atoms and Pd nanoparticles limits the determination of the oxidation state through XANES spectra. For Pd/Si₃N₄, in addition to the Pd–N shell at a distance of 1.98 Å , a peak at a distance of 2.34 Å was found, which might be attributed to Pd–O–Si species. The FT-EXAFS data for 1 wt% Pd/PCN showed only the contribution of Pd–N scattering paths with an average coordination number of 4. No Pd–Pd characteristic distances were detected.

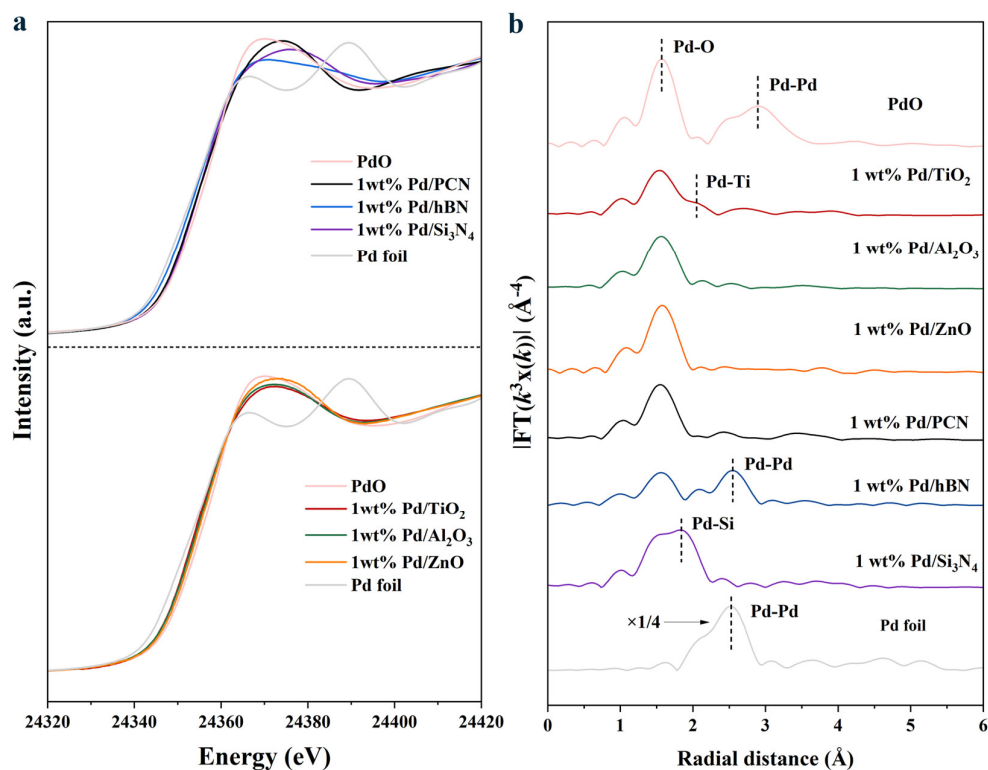


Figure 52. (a) Pd K-edge XANES spectra and (b) EXAFS magnitude of the Fourier transform (FT) for various Pd samples.

Table 3. EXAFS fitting parameters at the Pd K-edge for various Pd samples ($S_{O_2}=0.7$)

Sample	Shell	N	R (Å)	$\sigma^2 (*10^{-3} \text{ Å}^2)$	ΔE (eV)	R-factor
Pd foil	Pd-Pd	12*	2.74 ± 0.01	4.6 ± 0.1	2.1 ± 0.4	0.0044
	Pd-O	4*	2.01 ± 0.01	0.8 ± 0.5		
PdO	Pd-Pd	4*	3.04 ± 0.01	8.2 ± 1.3	4.7 ± 0.9	0.0122
	Pd-Pd	8*	3.42 ± 0.01	13.0 ± 1.9		
1 wt% Pd/TiO ₂	Pd-O	3.9 ± 0.6	2.07 ± 0.02	7	7.7	0.0580
	Pd-Ti	< 0.2	2.73	7		
1 wt% Pd/Al ₂ O ₃	Pd-O	3.6 ± 0.3	2.04 ± 0.01	3.8 ± 1.3	5.0 ± 1.1	0.0182
1 wt% Pd/ZnO	Pd-O	3.6 ± 0.4	2.02 ± 0.01	2.0 ± 1.3	4.6 ± 1.4	0.0281
1 wt% Pd/hBN	Pd-N	3.3 ± 0.3	2.05 ± 0.01	6.3 ± 1.6	0.5 ± 0.8	0.0225
	Pd-Pd	4.0 ± 0.5	2.80 ± 0.01	10.3 ± 1.9		
1 wt% Pd/Si ₃ N ₄	Pd-N	2.5 ± 1.8	2.03 ± 0.05	5.0 ± 3.3	-2.15 ± 6.46	0.0334
	Pd-Si	4.4 ± 2.1	2.35 ± 0.04	6.7 ± 5.0		
1 wt% Pd/PCN	Pd-N	4.0 ± 0.4	2.03 ± 0.01	2.6 ± 1.3	0.5 ± 1.5	0.0261

S_{02} is the amplitude reduction factor, and S_{02} was fixed to 0.7 as determined from PdO fitting; N is the coordination number; R is interatomic distance (the bond length between central atoms and surrounding coordination atoms); σ^2 is Debye–Waller factor (a measure of thermal and static disorder in absorber-scatterer distances); ΔE is edge-energy shift (the difference between the zero kinetic energy value of the sample and that of the theoretical model). R -factor is used to value the goodness of the fitting. * These values were fixed during EXAFS fitting, based on the known structure.

Moreover, the white line intensities of all Pd/PCN samples are higher than that of the Pd foil reference and are similar to the PdO reference. But the intensities of the white lines decreased as the Pd loading increased. Meanwhile, the position of the "white line" (dotted area) gradually shifted downward by 2 eV (Figure 53a). The shift in positions and decrease in intensities of the white line suggest a reduction in the oxidation state of Pd as the Pd loading increases. Further FT-EXAFS data (Figure 53b) reveals the presence of a Pd–Pd first shell in the highest loading (16 wt% Pd/PCN) sample, confirming the formation of metallic Pd, in agreement with the observation from the HAADF-STEM (Figure 41). The detailed coordination information of Pd/PCN samples is listed in Table 4.

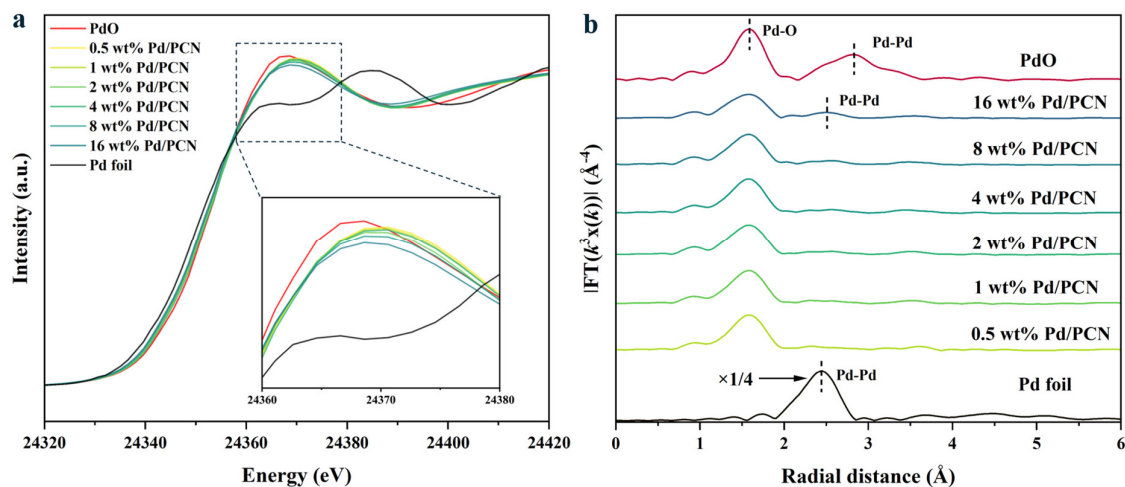


Figure 53. (a) Pd K-edge XANES spectra and (b) EXAFS magnitude of the Fourier transform (FT) for various Pd/PCN samples.

To more clearly present the atomic dispersion of Pd throughout the Pd/PCN samples, wavelet transform (WT) of Pd K-edge EXAFS oscillations was carried out. Wavelet analysis is known for its powerful resolution in both k and R spaces. From the WT contour plots of Pd foil and PdO standards (Figure 54), the intensity maxima at 2.5 and 2.8 Å are associated with the Pd–Pd and Pd–O–Pd contributions, respectively. The WT contour plot of 0.5 wt% Pd/PCN displays only one intensity maximum at 1.5 Å, which can be ascribed to the Pd–N bonds. The Pd–Pd peak at 2.5 Å was detected in the 16 wt% Pd/PCN sample. Therefore, based on FT- and WT-

EXAFS analysis, it is sure that Pd is atomically dispersed in 0.5 wt% Pd/PCN, and Pd nanoparticles are present in 16 wt% Pd/PCN.

Table 4. EXAFS fitting parameters at the Pd K-edge for various Pd/PCN samples ($S_0 = 0.7$).

Sample	Shell	N	R (Å)	$\sigma^2 (*10^{-3} \text{ Å}^2)$	ΔE (eV)	R-factor
Pd foil	Pd-Pd	12*	2.74 ± 0.01	4.5 ± 0.2	-5.3 ± 0.5	0.0130
	Pd-O	4*	2.02 ± 0.01	1.8 ± 0.4		
PdO	Pd-Pd	4*	3.05 ± 0.01	7.8 ± 0.7	2.0 ± 0.8	0.0193
	Pd-Pd	8*	3.43 ± 0.02	15.7 ± 1.9		
0.5 wt% Pd/PCN	Pd-N	3.8 ± 0.4	2.04 ± 0.01	2.4 ± 1.4	0.5 ± 1.7	0.0229
1.0 wt% Pd/PCN	Pd-N	3.9 ± 0.4	2.04 ± 0.01	2.7 ± 1.4	0.1 ± 1.7	0.0225
2.0 wt% Pd/PCN	Pd-N	3.8 ± 0.4	2.05 ± 0.01	3.1 ± 1.4	-0.2 ± 1.7	0.0221
4.0 wt% Pd/PCN	Pd-N	3.8 ± 0.4	2.04 ± 0.01	2.6 ± 1.2	-0.2 ± 1.6	0.0199
8.0 wt% Pd/PCN	Pd-N	3.8 ± 0.3	2.04 ± 0.01	3.2 ± 1.1	-0.7 ± 1.3	0.0154
16.0 wt% Pd/PCN	Pd-N	3.5 ± 0.3	2.06 ± 0.01	4.0 ± 1.1	-0.8 ± 1.3	0.0265
	Pd-Pd	0.4 ± 0.3	2.79 ± 0.03	4.7 ± 5.2		

S_0 is the amplitude reduction factor, and S_0 was fixed to 0.7 as determined from PdO fitting; N is the coordination number; R is interatomic distance (the bond length between central atoms and surrounding coordination atoms); σ^2 is Debye-Waller factor (a measure of thermal and static disorder in absorber-scatterer distances); ΔE is edge-energy shift (the difference between the zero kinetic energy value of the sample and that of the theoretical model). R-factor is used to value the goodness of the fitting. * These values were fixed during EXAFS fitting, based on the known structure.

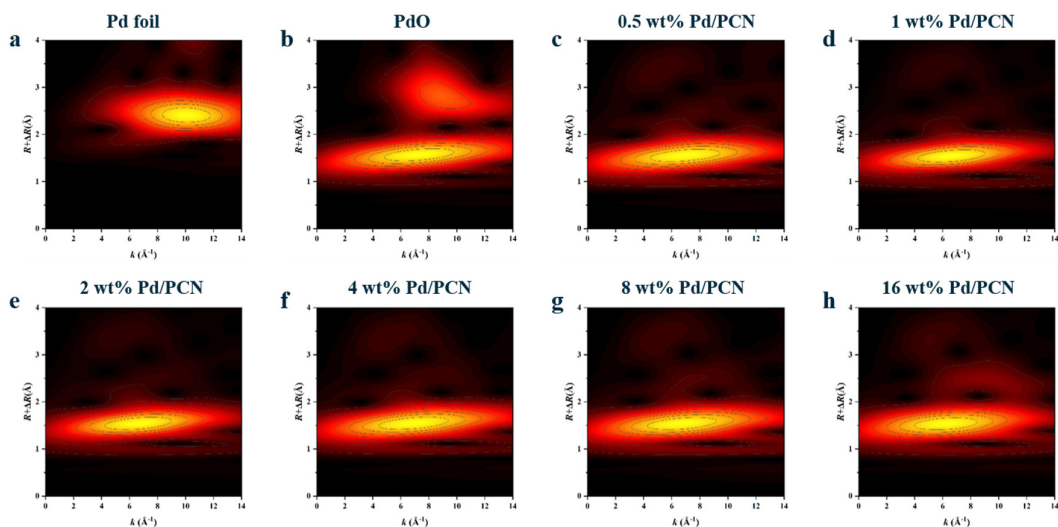


Figure 54. Wavelet transform analysis of Pd K-edge EXAFS oscillations of various Pd/PCN samples.

4.2 Theoretical investigation

4.2.1 Structural investigation for exfoliated PCN catalysts

4.2.1.1 Process of exfoliation of pristine PCN

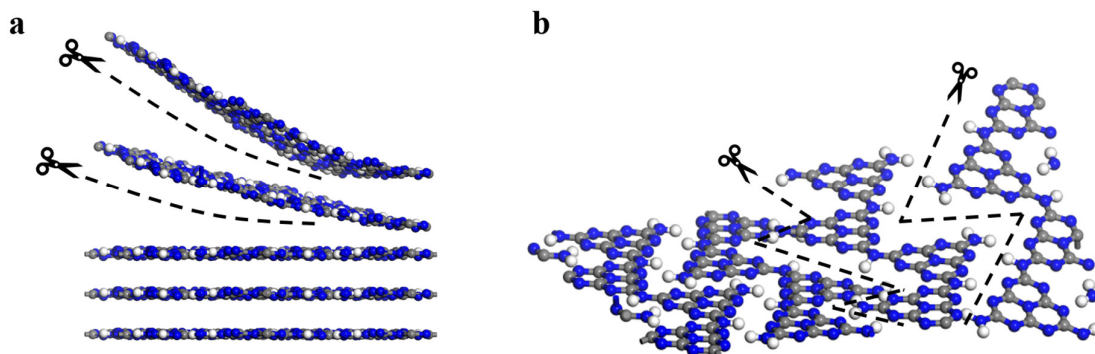


Figure 55. Two exfoliation process of PCN: (a) interlayer exfoliation, (b) in-plane structure fragmentation.

Ideally, the PCN exfoliation is to disrupt the interlayer van der Waals interactions between the layers without generating any fragments. Such exfoliation requires in-plane covalent C–N bonds, which are optimized with an ideal C/N ratio of 0.75. In fact, PCN usually contains a hydrogen content of 1.5 wt% or more, and the hydrogen atom exists in the form of an in-plane N–H···N bond [193]. In this case, both the in-plane hydrogen bonds and the interlayer van der Waals interactions are likely to be destroyed during the exfoliation process (Figure 55). Here, DFT calculations were performed to study the respective energies required to break in-plane hydrogen bonds and interlayer van der Waals interactions. As shown in Figure A.21, the interlayer π – π interactions were calculated by performing a layer-by-layer exfoliation of a ten-layer hydrogen-bonded PCN model. The interlayer energy per atom (72 atoms: C₂₄H₁₂N₃₆) in the unit cell, E_a , was determined using equation (2):

$$E_a = \left(\frac{E_n - n \times E_1}{n - 1} \right) / 72 \quad (2)$$

Where n denotes the number of layers in the model (*i.e.*, 10), E_n represents the corresponding energy of the n -layer model, and E_1 represents the energy of the monolayer model. The average interlayer energy E_a is calculated as -0.03 eV/atom. The value is derived assuming that the interaction energy is equally shared among all species. Furthermore, as displayed in Figure A.22, the calculation of the energy for in-plane hydrogen bonds ($E_{\text{N-H}\cdots\text{N}}$) in the monolayer model shows that it is -0.30 eV per interaction, which is significantly higher than the energy of

interlayer van der Waals forces. In this case, by keeping the input energy within the range of -0.03 to -0.30 eV, exfoliation will only occur between the layers. If the input energy is sustained above -0.30 eV, exfoliation will disrupt the interlayer interactions, as well as the in-plane hydrogen bonds. However, in the current level of exfoliation, the input energy transmitted through the medium to the material is hard to measure and control. To ensure that exfoliation occurs, the input energy is usually significantly greater than the minimum energy required to disrupt interlayer interactions. Thus, two processes are expected to occur during exfoliation: (1) the disruption of weaker π - π interactions between the layers, and (2) the disruption of stronger in-plane hydrogen bonds between strands of heptazine units.

4.2.1.2 Density of states analysis for exfoliated PCN

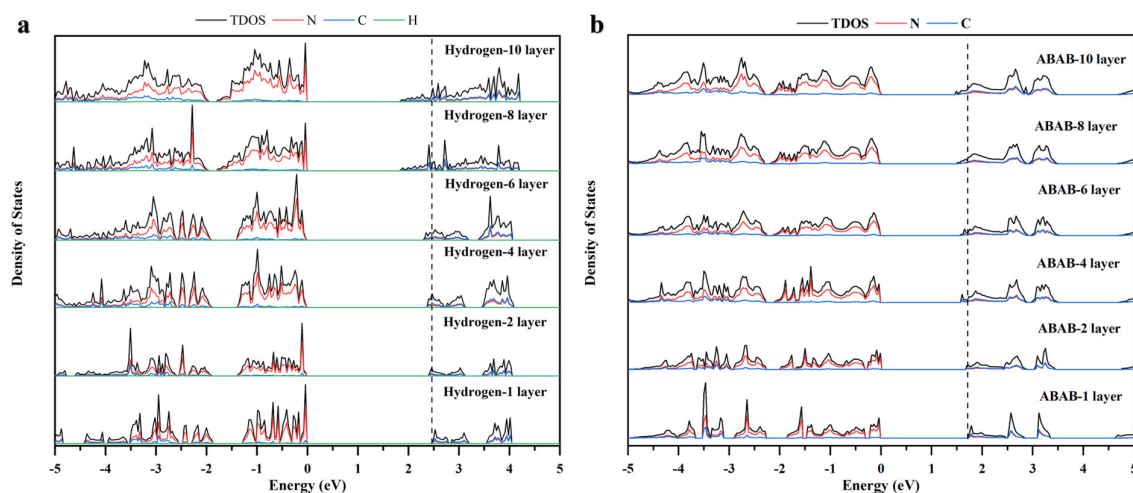


Figure 56. The total density of states and projected orbital density of states (DOS) images of hydrogen-bonded model (a) and ABAB-stacking ideal model (b).

Density of states (DOS) calculation was further performed to understand the electronic structure. For the hydrogen-bonded PCN model, the CB edges are contributed by the p orbitals of carbon and nitrogen, and the VB edges are derived from the p orbitals of nitrogen (Figure 56a and Figure A.23). There is a significant hybridization between the carbon 2p states (C_p) and the nitrogen 2p states (N_p), and the C_p - N_p hybridization is the main bonding source in the pristine PCN, deriving from the combination of sp^2 - sp^2 σ bonds and p - p π bonds. The calculated DOS images suggest that the bandgaps decrease as the layer number increases. An ABAB-stacking ideal PCN model (C/N ratio of 0.75) was further constructed to confirm this trend. As shown in Figure 56b, the resulting DOS images exhibited the same trend as the observations from hydrogen-bonded PCN models, which also correlate well with the literature [196, 235, 236]. However, the experimental results did not match with this conclusion, since the experimental

bandgap of the exfoliated samples did not increase with layer number. The reason why no increase in bandgap appeared in the experiment is that the bandgaps are affected not only by the layer number but also by factors such as particle size, surface groups, vacancies, *etc* [211, 263-265].

4.2.2 Structural investigation for isolated Pd catalysts

4.2.2.1 Bader charge analysis

Bader charge analysis is a meaningful theoretical calculation method that can be a valuable complement to experimental characterization in understanding the electronic structure of surface metal sites. The experimentally gained information was used to benchmark the theoretical calculations. Pd/PCN and Pd/TiO₂ were chosen as examples of nitride supports and oxide supports, respectively. For PCN support, the hydrogen-bonded network provides plenty of sites or defects to stabilize Pd atoms. With respect to the TiO₂ support, the anatase (101) surface can provide four types of anchoring sites for single Pd atoms, including Ti rows, O rows, Ti-vacancy, and O-vacancy sites. Next, the Bader charge analysis was applied to the possible sites to determine the effective charge of Pd (Table 5 and 6). Although the Bader charge generally underestimates the formal oxidation state, it is a useful scheme to correlate effective and ionic charges [126]. However, it is still unclear how to assign the models to different experimental oxidation states. For example, the Bader charge of the (PdN₄)_{surface} model (Figure A.27) is +0.82 e, while the value for the (PdN₄)_{interlayer} model (Figure A.28) is +0.51 e, which is far away from the formal oxidation state. Nevertheless, both models are fitted with a coordination number of 4 in the FT-EXAFS fitting. In this case, relying solely on the EXAFS-fitted coordination number may lead to misleading model assignments. Therefore, the oxidation state should be considered as another calibration standard.

To investigate the correlation between the experimental oxidation state and the calculated Bader charge, a series of Pd–C, Pd–N, Pd–O, and Pd–F models (see chapter 3.3) with different oxidation states (+1, +2, +3, and +4) were selected to calculate their Bader charge. Since the Bader charge is greatly influenced by electronegativity, a correlation analysis was performed between the Bader charge of Pd and the corresponding Allen electronegativity of the coordinated anions (C, N, O, and F). Four linear equations were obtained (Figure 57a). These linear relationships are reasonable because the electronegativity of anions increase from carbon to fluorine across the periodic table, and large electronegativity values indicate a stronger attraction of electrons than small electronegativity values. This is reflected in the changes in the Bader charge of Pd. To confirm the obtained relationship, four additional Pd(II) models (Pd–4C,

Pd-4S, Pd-4N, and Pd-4O, Figure A.24) were studied, and a similar equation was obtained, well confirming the above relationship between Bader charge and electronegativity. Then, the Bader charge and oxidation state were further correlated (Figure 57b). For all models, however, the tendency is more like a parabolic relationship rather than a linear one. The closest linear relationship was found for Pd-C models. Notably, by using the above equations for Pd-N and Pd-O models, the oxidation state of different Pd sites in the Pd/PCN and Pd/TiO₂ models was able to obtain according to their Bader charges, as listed in Tables 5 and 6, respectively.

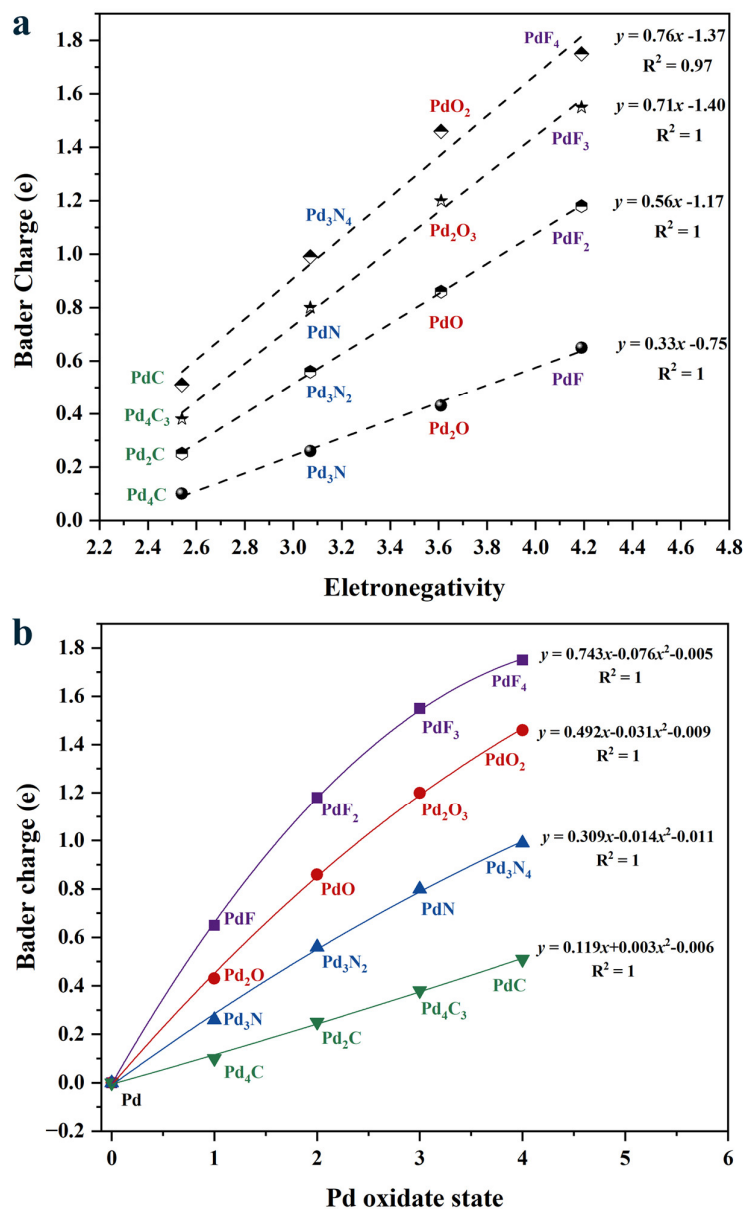


Figure 57. (a) Bader charge for Pd models with different oxidation state (+1, +2, +3, and +4), plotted against the electronegativity of different type of bonding atom (C, N, O, and F). (b) Bader charge-oxidation state plots for different Pd models.

4.2.2.2 CO stretching frequency calculation

The relationship between the CO stretching frequencies and the Pd oxidation state was also studied. As shown in Figure 58, the stretching frequencies of CO are proportional to the oxidation state of isolated Pd species in either Pd/PCN models or Pd/TiO₂ models.

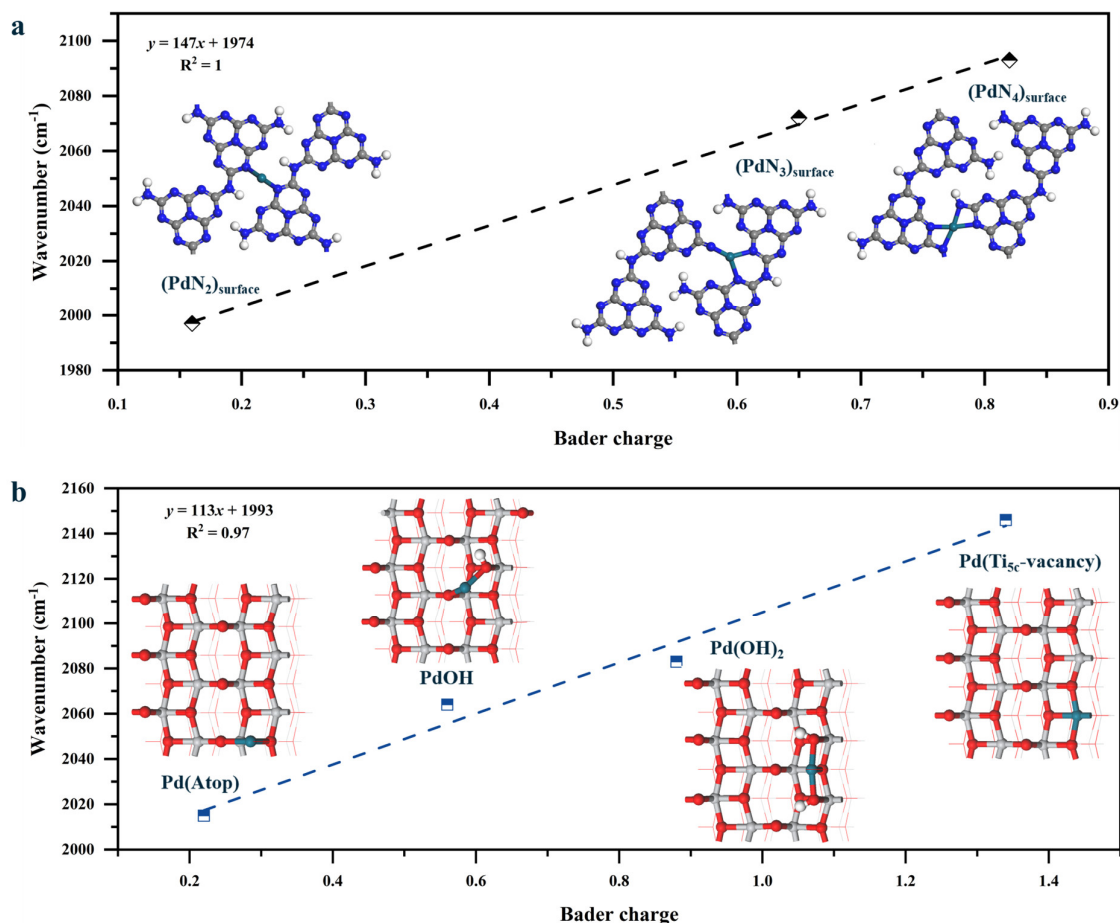


Figure 58. Plots of Bader charge and CO stretching frequencies for Pd/PCN (a) and Pd/TiO₂(101) (b), respectively.

Combining the relationships between Bader charge and oxidation state (Figure 57) with the relationships between Bader charge and CO stretching frequency (Figure 58), two separate equations

$$y = 1981 + 45.4x - 2.06x^2 \quad (3)$$

$$y = 2001 + 55.6x - 3.50x^2 \quad (4)$$

were introduced for Pd/PCN and Pd/TiO₂, respectively. y (cm⁻¹) represents the experimental CO stretching frequency, and x denotes the corresponding oxidation state of Pd. Notably, a 9 cm⁻¹ difference between the experimental (2143 cm⁻¹) and computational (2134 cm⁻¹) CO

stretching frequencies was taken into account in the equations. With the CO stretching frequency known from the experiment, equations (3) and (4) were used to estimate the oxidation state of Pd on PCN and TiO₂ supports, respectively. As shown in Table 7, the calculated oxidation state of Pd on the PCN is higher than that on the TiO₂, in agreement with the their XPS results (Figure 40).

For Pd/PCN, based on the calculated oxidation state of 3.77 and the measured coordination number of 4, it was proposed that Pd bonds to four surface nitrogen atoms, as shown in the (PdN₄)_{surface} model (Figure A.27). The Pd species with a calculated oxidation state of 2.84 was assigned to the (PdN₃)_{surface} model (Figure A.26), where the Pd atom is bound to three N atoms on the surface. However, due to the presence of a large amount of unbonded Pd salts on TiO₂, the coordination number cannot be used as a reference in the model assignment. Notably, what cannot be ignored on the oxide surface is the hydroxyl group [266-268]. The excess hydroxyl group would coordinate with Pd atoms through M–O(OH) (metal–hydroxyl group) interactions. For Pd/TiO₂, the Pd species with a calculated oxidation state of 2.99 was assigned to the Pd(OH)₂ model (Figure A.36), where the Pd atom is bound to one lattice O and two extra –OH groups on the surface. The Pd species with a calculated oxidation state of 1.75 was attributed to the PdOH model (Figure A.35), where the Pd atom is bound to one lattice O and one extra –OH group on the surface. The proposed Pd structures have calculated oxidation states of +2.09 for the Pd(OH)₂ model and +1.22 for the PdOH model. The calculated oxidation states of the assigned model agree with the experimental Pd 3d XPS results.

However, unambiguous determination of the Pd oxidation state on the basis of adsorbed CO stretching frequency alone is not possible, the influence of the support must also be taken into consideration. Because there are different CO frequencies on either PCN or TiO₂ support, depending on the adsorption sites on the support (Table A. 7). Besides, even for the Pd species with the same valence state, while supported on different materials, the CO frequencies were not the same (Table A. 8). Additionally, the effect of the size of Pd particles on the CO frequency was also investigated. As shown in Table A. 9, CO adsorption energies on small Pd particles (0.5 nm) and bulk Pd were calculated as 182 kJ mol^{−1} and 175 kJ mol^{−1}, respectively. The slightly stronger binding of CO to small Pd clusters results in a lower vibrational frequency of 1990 cm^{−1} compared to that of bulk Pd (2049 cm^{−1}).

Table 5. Bader charge of Pd (Q |e|), calculated Pd oxidation state, CO adsorption energy (E_{ads} , eV), C–Pd distance (R_{PdC} , Å), C–O bond length (R_{CO} , Å), and CO stretching frequency (ω_{e} , cm^{-1}) for CO adsorption on Pd atom on a hydrogen-bonded PCN. The corresponding structure is shown in Figure A.25 – A.27.

Model	Q e	Calculated oxidation state	E_{ads} (kJ mol ⁻¹)	R_{PdC} (Å)	R_{CO} (Å)	ω_{e} (cm ⁻¹)
(PdN ₂) _{surface}	0.16	0.57	252	1.833	1.152	1997
(PdN ₃) _{surface}	0.65	2.40	17	2.737	1.137	2072
(PdN ₄) _{surface}	0.82	3.13	12	3.035	1.143	2093

Table 6. Bader charge of Pd (Q |e|), calculated Pd oxidation state, CO adsorption energy (E_{ads} , eV), C–Pd distance (R_{PdC} , Å), C–O bond length (R_{CO} , Å), and CO stretching frequency (ω_{e} , cm^{-1}) for CO adsorption on Pd moieties on a TiO₂ (101) terrace sites. The corresponding structure is shown in Figure A.29– A.36.

Model	Q e	Calculated oxidation state	E_{ads} (kJ mol ⁻¹)	R_{PdC} (Å)	R_{CO} (Å)	ω_{e} (cm ⁻¹)
Pd (Atop)	0.22	0.45	228	1.856	1.175	2015
Pd(O _{2c} -vacancy)	-0.47	-0.68	134	1.922	1.171	2027
Pd(O _{3c} -vacancy)	-0.53	-0.75	120	1.974	1.165	2057
Pd(O _{3c} *-vacancy)	-0.34	-0.50	63	3.624	1.153	2120
Pd(Ti _{5c} -vacancy)	1.34	3.54	144	1.941	1.153	2146
Pd(Ti _{6c} -vacancy)	1.41	3.79	34	3.673	1.155	2104
PdOH	0.56	1.22	211	1.844	1.168	2064
Pd(OH) ₂	0.88	2.09	225	1.831	1.167	2083

Table 7. Conversion of experimental CO stretching frequencies to the Bader charge and oxidation state of Pd for 2 wt% Pd/PCN and 1 wt% Pd/TiO₂, respectively.

Model	Linear CO frequency from DRIFTS experiments (cm ⁻¹)	Q e	Calculated oxidation state
2 wt% Pd/PCN	2123	0.95	3.77
	2093	0.75	2.84
1 wt% Pd/TiO ₂	2135	1.18	2.99
	2126	1.10	2.74
	2088	0.76	1.75

4.3 Catalytic activity

4.3.1 Exfoliated PCN catalysts for phenol photodegradation

The performance of differently exfoliated PCN samples were evaluated by phenol photodegradation. As shown in Figure 59, the blank experiment demonstrates that the photolysis of phenol without a photocatalyst can be ignored. The pristine PCN is highly active for the phenol photodegradation under visible light at 25 °C. The reaction kinetics were further illustrated using basic pseudo-first-order kinetics through the equation (5):

$$\ln \frac{c}{c_0} = -kt \quad (5)$$

Where c_0 (mg L⁻¹) and c (mg L⁻¹) are the initial concentration and remaining concentration at reaction time t , and k is the apparent rate constant, which is equal to the corresponding slope of the fitting line. The rate constants for t-CN-3 and t-CN-6 are 0.0088 and 0.0037 min⁻¹, respectively, which indicate a decrease in activity over thermal exfoliation time. This decrease is due to the high electron-hole recombination rate, as confirmed by the photocurrent and PL analysis. Notably, the t-CN-3 is the only sample that exhibits better activity than the pristine PCN (0.0085 min⁻¹). The u-CN-8 and u-CN-16 show the photocatalytic activities of 0.068 and 0.054 min⁻¹, respectively, which again emphasizes that excessive exfoliation can lead to decrease. Moreover, c-CN-8 and c-CN-16 exhibit very low-rate constants of 0.0004 and 0.0002 min⁻¹, respectively, about 95% less compared to pristine PCN. The reasons for this are their lower surface area and lower generation rate of photoexcited electrons. Due to the destruction of heptazine units, the rate constant for h-CN-12 is only 0.0007 min⁻¹, about 92% less than pristine PCN, and the other h-CN samples exhibit almost no activity.

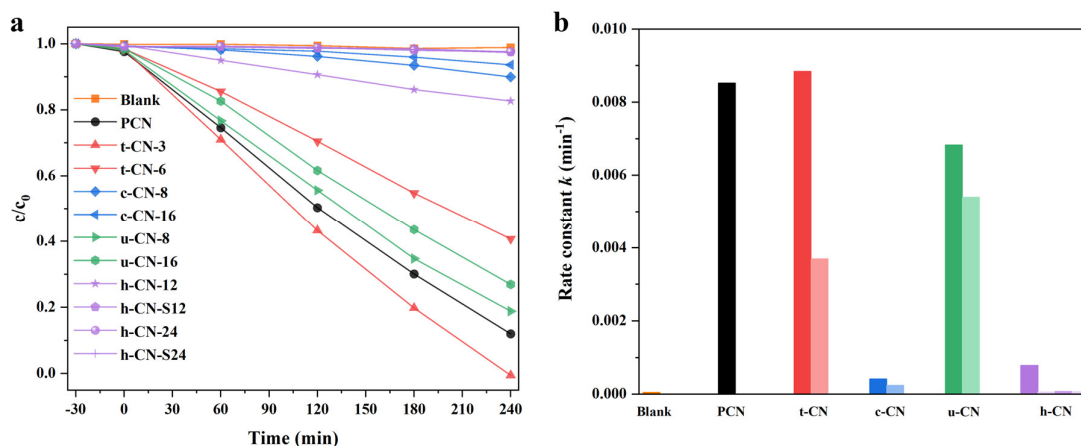


Figure 59. (a) Photocatalytic activity and (b) pseudo first-order rate constants of phenol degradation with differently exfoliated PCN.

4.3.2 Isolated Pd/PCN catalysts for Suzuki-Miyaura reaction

Here, the washed Pd/PCN catalysts were tested with the Suzuki-Miyaura reaction to compare their performance (Figure 60). The Pd catalysts (2 mg) were dispersed into an EtOH/H₂O solution (40 mL) containing bromobenzene (1 mmol) and phenylboronic acid (2 mmol). K₂CO₃ (2 mmol) is used as a base. The reaction temperature is 25 °C. The reaction atmosphere is argon. The coupling of bromobenzene and phenylboronic acid converts into the corresponding product, biphenyl. The yields of biphenyl were determined by gas chromatography (GC) with toluene as the internal standard.

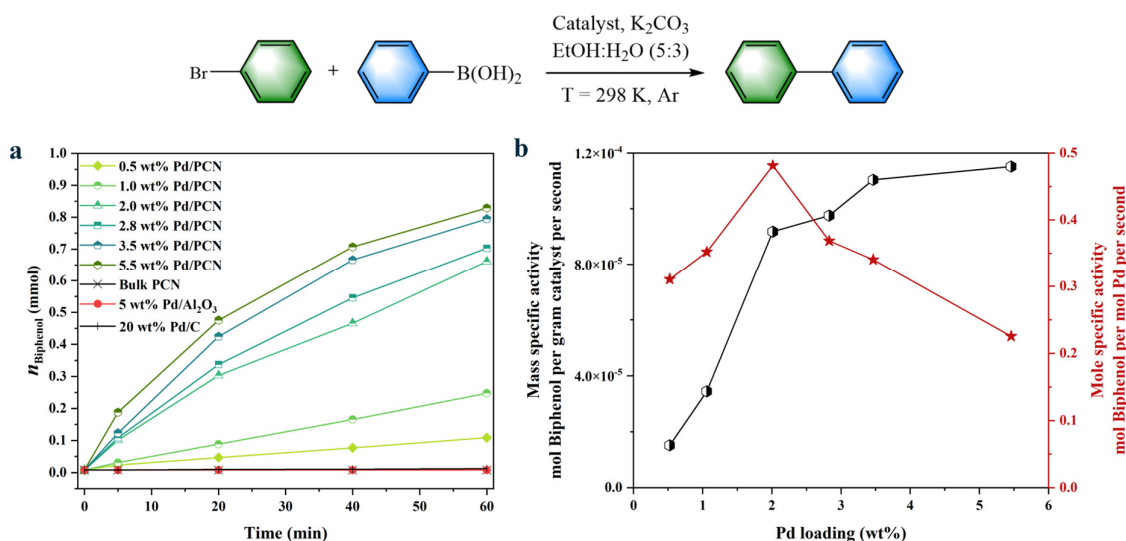


Figure 60. (a) Biphenyl formation over bulk PCN, Pd/PCN catalysts, commercial 5% Pd/Al₂O₃, and commercial 20 wt% Pd/C. (b) The mole specific activity (mol Biphenyl per mol Pd per second, left axis, black) and mass specific activity (mol Biphenyl per unit mass of the catalyst per second, right axis, red) of the different Pd/PCN catalysts.

As shown in Figure 60a, the pure PCN, commercial 5% Pd/Al₂O₃, and commercial 20% Pd/C catalysts were all inactive for the coupling reaction at 25 °C. Mass-specific activity is an important indicator describing the catalyst activity, as it reflects the total power of the catalyst to convert the reactant. Figure 60b reveals that the mass-specific activity increases as Pd loading increases. Then, the mole-specific activity was further used to compare their intrinsic activity. The 2 wt% Pd/PCN exhibited the highest mole specific activity. With samples containing Pd higher than 2wt%, a decline in activity was observed, which is due to the Pd atoms in the interior of the clusters and particles are not accessible to reactant molecules and cannot directly participate in the catalytic process.

The best performance 2 wt% Pd/PCN sample was further evaluated in the continuous flow reactor. The concentration of the reaction solution in flow test was the same as in the batch

mode. The reaction temperature was 30 °C. It was found that this catalyst behaved differently in a pure Ar or pure O₂ atmosphere (Figure 61): the cross-coupling reaction of bromobenzene and phenylboronic acid occurred in Ar, while the self-coupling reaction of phenylboronic acid took place in O₂ (Table A.10). However, the deactivation of catalyst was observed over time on stream in both atmospheres. The Ar-spent sample came to a dark grey (Figure A.50). In the CO-DRIFTS analysis of spent catalysts, the intensities of the bands corresponding to linear carbonyl and bridge carbonyl are not as pronounced as in fresh catalysts, while the ICP analysis shows that the Pd content stays the same in the spent catalysts. Pd 3d XPS spectra are shifted to lower binding energies in both Ar- and O₂-spent catalysts, while Ar-spent shift even more than O₂-spent. Likewise, XRD reflexes associated with Pd were observed in the Ar-spent sample, indicating the formation of Pd nanoparticle. Moreover, a high concentration of potassium (K) was observed in the spent catalysts, as confirmed by XPS and ICP (Table A.11). Thus, the reasons for the deactivation might be the sintering of Pd, the aggregation of Pd and K, or both.

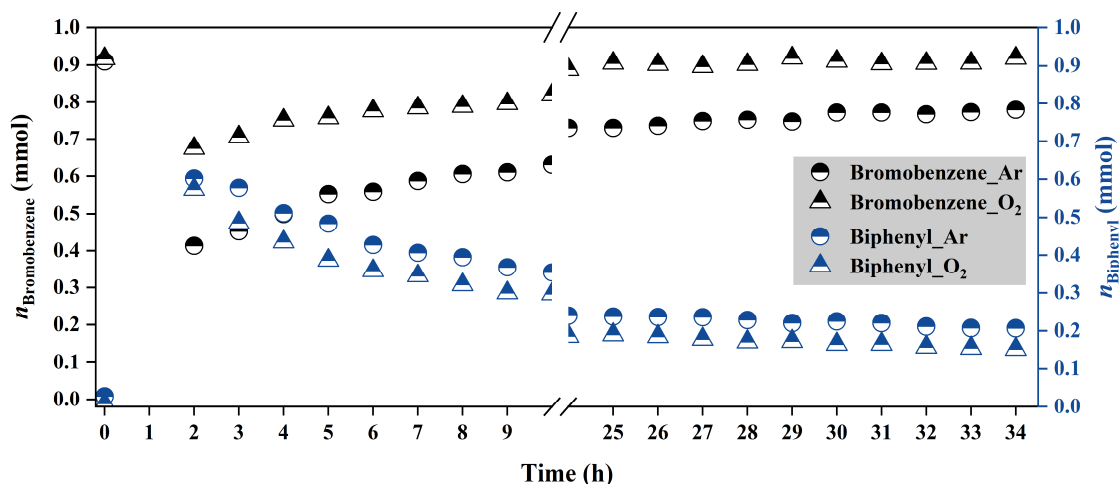


Figure 61. Continuous flow experiments of Suzuki coupling of bromobenzene with phenylboronic acid over 2 wt% Pd/PCN in Ar and O₂.

In order to study the influence of Pd particle size, the 2 wt% Pd/PCN was calcined at 200 °C and 400 °C, respectively, and then evaluated their performance. The test is performed in batch mode, and the reaction atmosphere is either Ar or air. However, the results revealed that the calcined samples were no longer active no matter in an Ar or air. Considering that the support PCN is a semiconductor photocatalyst, the reaction mixture was further irradiated with visible light (> 420 nm). After that, the product biphenyl appeared, and a decreasing trend in activity over calcination temperature was observed, suggesting the increase of particle size as reason for activity decay (Figure 62). Notably, for all three samples, there is always a better

performance in air than in Ar. This might be due to the simultaneous occurrence of cross- and self-coupling reactions in air, as observed in the continuous flow reaction.

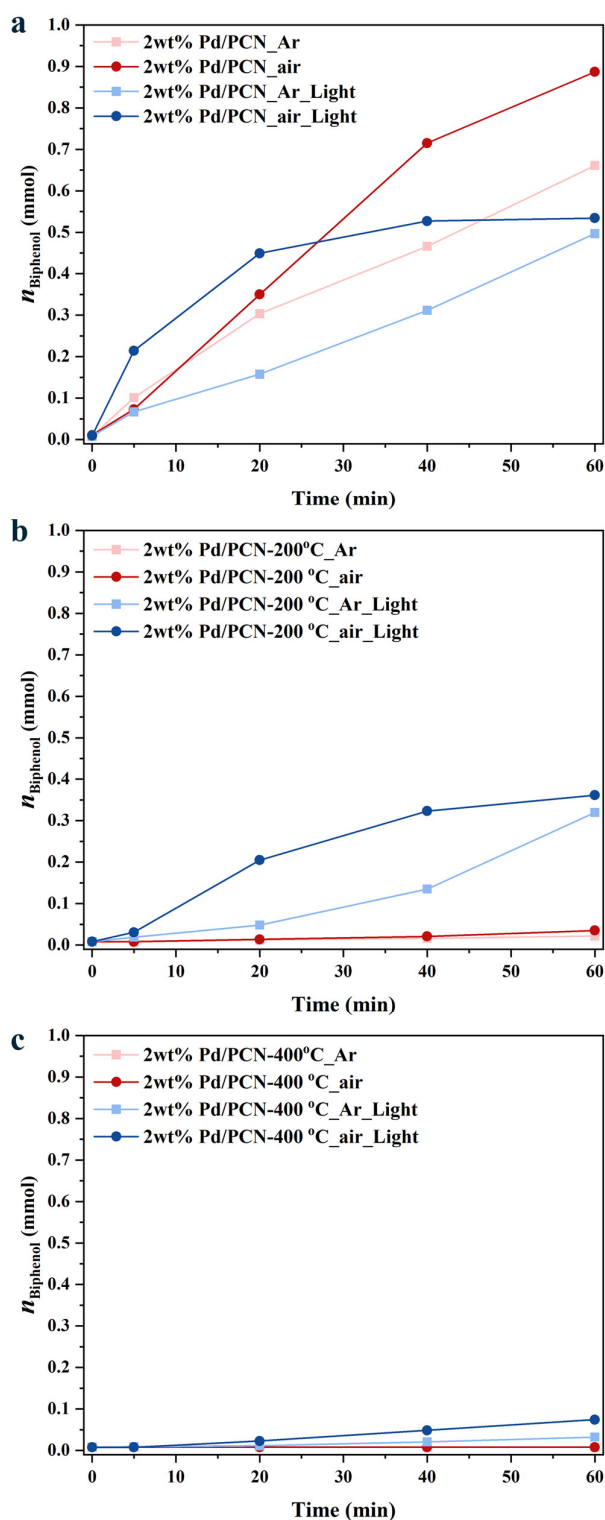


Figure 62. Biphenyl formation over different Pd catalysts with and without light: (a) 2 wt% Pd/PCN, (b) 2 wt% Pd/PCN-200 °C, and (c) 2 wt% Pd/PCN-400 °C.

4.4 Catalytic mechanism

4.4.1 Mechanism of exfoliated PCN catalysts for phenol photodegradation

To detect the main reactive species during the photodegradation process, a series of electron paramagnetic resonance (EPR) measurements were conducted using 5,5-dimethyl-1-pyrroline N-oxide (DMPO) as a spin trap. Notably, photoelectrons can be trapped by the spin-trapping process involving the addition of $\cdot\text{OH}$ and $\cdot\text{O}_2^-$ to the double bond of DMPO, forming stable DMPO-OH and DMPO-OOH adducts, which provide distinguishable EPR signals [257]. Upon visible-light irradiation, the DMPO-OH signals were detected in the pristine PCN (Figure 63). The HOMO level of PCN (2.49 V vs NHE) is more positive than that of $\cdot\text{OH}/\text{OH}^-$ (1.99 V vs NHE) and $\cdot\text{OH}/\text{H}_2\text{O}$ (2.31 V vs NHE), thereby $\cdot\text{OH}$ can be thermodynamically generated. However, the c-CN-16 and u-CN-16 show much weaker DMPO-OH signals, indicating worse $\cdot\text{OH}$ radical generation ability after chemical and ultrasonic treatments. Meanwhile, the signal of photoexcited electrons from VB to CB was observed in both c-CN-16 and u-CN-16, suggesting that photoelectrons are mostly recombined in the bulk instead of reaching the surface to react with H_2O to produce $\cdot\text{OH}$ radicals. Similarly, the intensity of the $\cdot\text{OH}$ signal in t-CN-6 slightly decreased compared to pristine PCN due to the rapid recombination of charge carriers in the bulk. For the best performing sample t-CN-3, except $\cdot\text{OH}$ radical, an additional $\cdot\text{O}_2^-$ radical signal was detected (Figure A.51). Accordingly, the related flat band potential of t-CN-3 is -0.49 V (vs NHE), which is more negative than the standard potential of $\text{O}_2/\cdot\text{O}_2^-$ (-0.18 V vs NHE), thereby allowing the production of $\cdot\text{O}_2^-$.

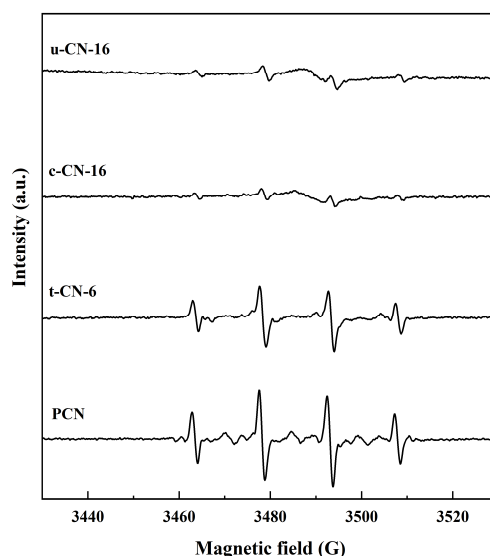


Figure 63. Representative DMPO spin trapping EPR spectra of PCN, t-CN-6, c-CN-16 and u-CN-16 suspension under successive treatment of O_2 during the visible-light irradiation.

4.4.2 Mechanism of isolated Pd/PCN catalysts for Suzuki-Miyaura reaction

Attenuated total reflectance-Fourier transform infrared spectroscopy (ATR-FTIR) was performed to monitor the reaction. During substrate calibration, after mixing phenylboronic acid with K_2CO_3 , two new bands at 1304 and 753 cm^{-1} attributed to the boron-related functional group were observed (Figure 64b). The presence of new infrared bands suggests the interaction between phenylboronic acid and K_2CO_3 . However, the functional group with an IR signal at 1304 cm^{-1} did not participate in the subsequent reaction (Figure 64a), indicating that it belonged to a stable boron intermediate.

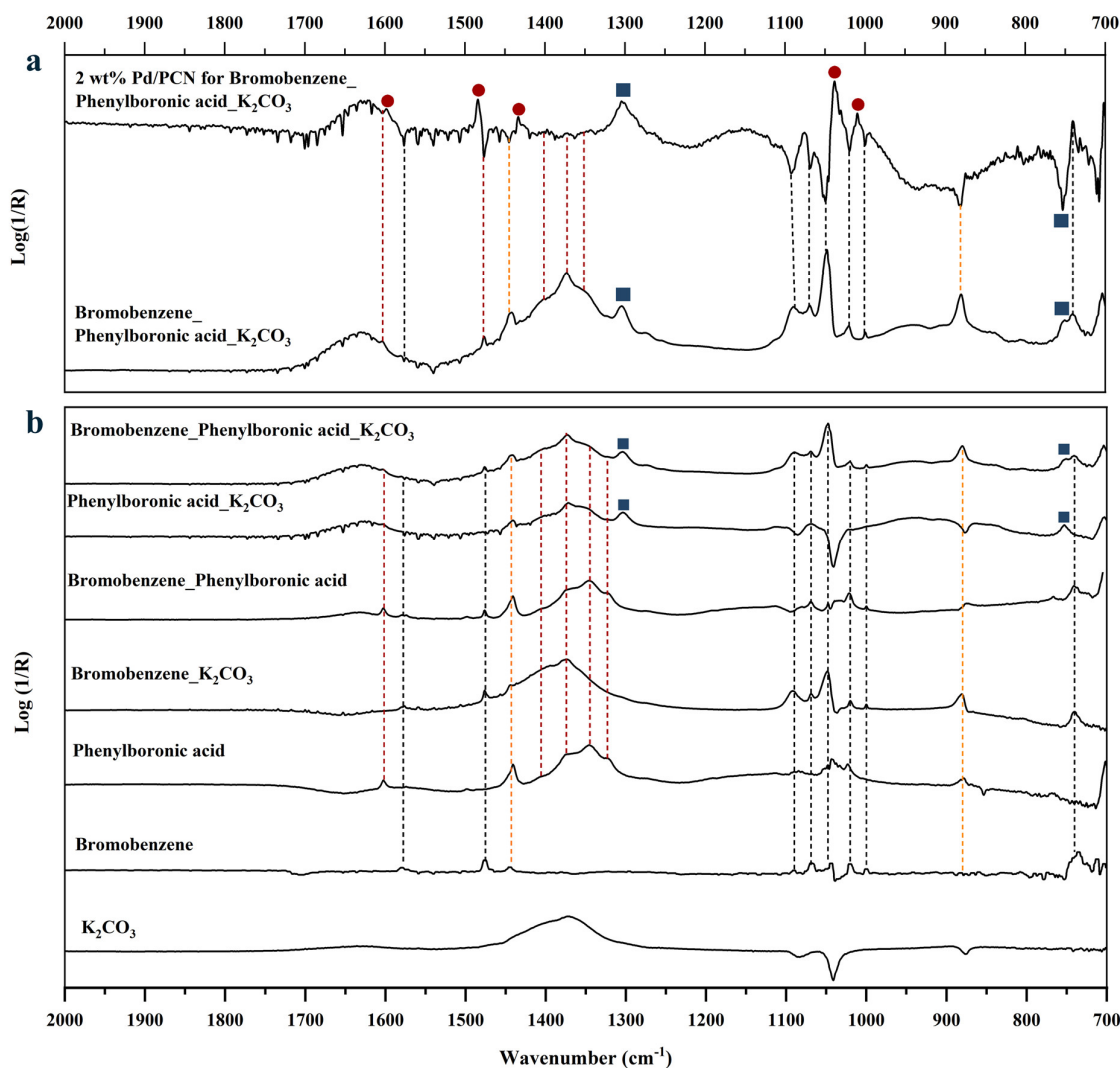


Figure 64. (a) *In situ* ATR-IR spectra of 2 wt% Pd/PCN for the coupling reaction of bromobenzene and phenylboronic acid. (b) *In situ* ATR-IR spectra of the substrate calibration (bromobenzene, phenylboronic acid, and K_2CO_3). The bands related to the functional groups from bromobenzene and phenylboronic acid are marked with black and red dashed lines, respectively. The yellow dashed lines mark the IR bands present in both substrates. New bands derived from boron-related group are marked with dark blue square, and new bands related to biphenyl is marked with dark red spheres.

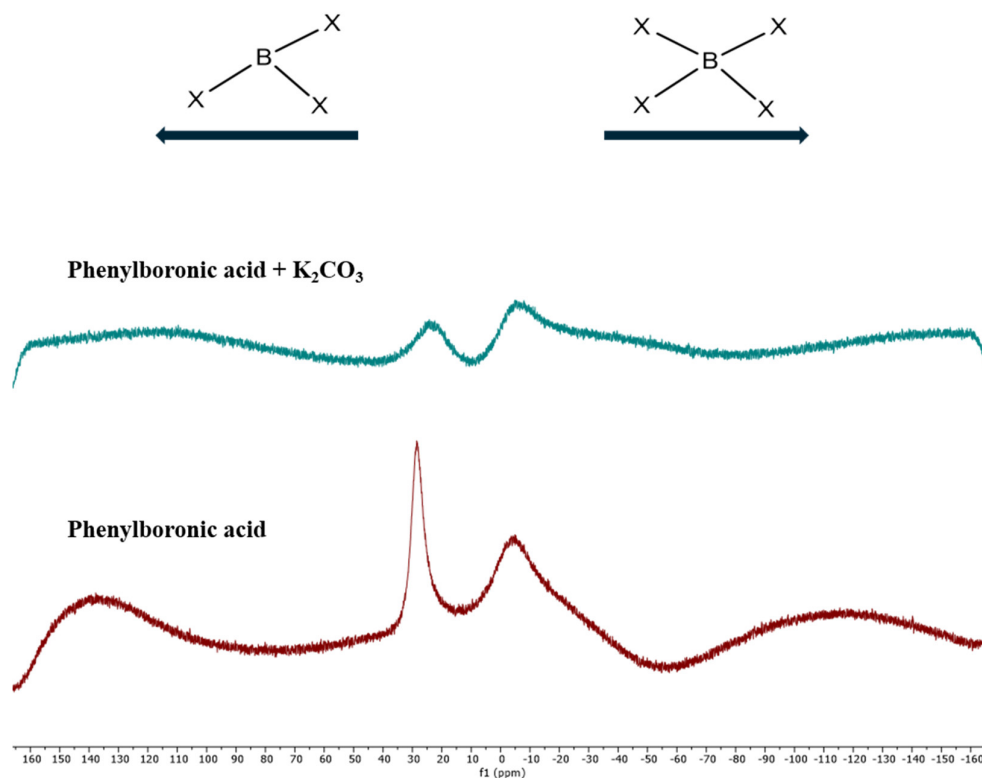


Figure 65. ^{11}B NMR spectra of phenylboronic acid with (green line) and without (red line) K_2CO_3 .

Further evidence was obtained from ^{11}B and ^{13}C NMR. The ^{11}B NMR signal of phenylboronic acid at 28 ppm shifted slightly downfield to 24 ppm and became broad after being mixed with K_2CO_3 (Figure 65). At the same time, the ^{13}C NMR signals also shifted slightly downfield (+0.2 to +0.7 ppm), and the signal at 131 ppm, attributed to the carbon bonded to boron, was missing (Figure A.52). Furthermore, after the catalyst was present, the infrared bands at 1090, 1067, 1050, 1020, and 1000 cm^{-1} belonging to the C–Br bond in bromobenzene turned negative, and the infrared bands in the region of 1310–1440 cm^{-1} associated with boron in phenylboronic acid dropped significantly, suggesting the breakage of C–Br bond and the involvement of boron-related group in the cross-coupling reaction. The new infrared bands at 1598, 1484, and 1433 cm^{-1} are attributed to biphenyl [269]. A similar result was observed with another aryl halide, iodobenzene, which again demonstrated the cross-coupling reaction (Figure A.54).

5. Summary

In this thesis, the charge states of Pd on nitride and oxide supports were systematically investigated. The main conclusions are briefly summarized as below:

First, to obtain larger specific surface area and provide more sites for anchoring Pd atoms, the polymeric carbon nitride support was modified by four different exfoliation methods, including liquid ultrasonication method, thermal oxidation method, hydrothermal oxidation method, and chemical oxidation method. Depending on the employed exfoliation method, the morphology, surface area and functionalization, band edge positions, charge carrier generation, and mobility can be influenced differently, up to the point where semiconducting behavior is entirely lost. In addition, two processes occur during the exfoliation process which affects the PCN structure, one is overcoming the interlayer van der Waals forces, and the other is the in-plane hydrogen bonds rupture, therefore the preparation of PCN nanosheets without any fragmentation remains a significant challenge. The analysis results demonstrated that the ultrasonic method effectively reduced the number of layers in PCN while retaining its crystal and molecular structure without sample loss. Chemical and hydrothermal oxidation methods greatly affect the structure, morphology, and reactivity of PCN. The hydrothermal oxidation method even resulted in inactivation due to fully destruction of the heptazine units of PCN. Only the sample prepared by the thermal exfoliation method exhibited better performance than the pristine PCN in phenol photodegradation. Therefore, the thermally exfoliated PCN was used as a support for the synthesis of isolated Pd catalysts.

Through a simple wet chemical method, a series of Pd/PCN (0.5, 1, 2, 4, 8, and 16 wt%) catalysts were prepared using $\text{Pd}(\text{TFA})_2$ as the Pd precursor. STEM demonstrated that Pd exists in the form of single atoms on the surface of PCN when the Pd loading amount is less than 2 wt%, and the binding of the Pd atoms to the PCN support was found to be very stable. When the Pd loading exceeds 2 wt%, there will be a massive aggregation of Pd atoms during synthesis, leading to the formation of unstable Pd nanoclusters and stable Pd nanoparticles. The XANES results showed that the average oxidation state of Pd tends to decrease as the Pd loading increases. EXAFS also found that Pd–Pd bonds appeared in the 16 wt% loaded Pd/PCN sample.

XPS results revealed that there were two Pd species in Pd/PCN samples, and similar Pd 3d binding energies were found on another three Pd/nitride samples (using hBN, TiN, and Si_3N_4 as supports). Moreover, the Pd/PCN synthesized by another two Pd precursors ($\text{Pd}(\text{acac})_2$ and $\text{Pd}(\text{OAc})_2$) also exhibited similar Pd 3d XPS binding energies. Therefore, the Pd 3d XPS binding

energies on different nitride supports remain consistent, even with varying Pd precursors. Similarly, the binding energies of Pd on the different oxide supports (TiO_2 , ZnO , Al_2O_3 , B_2O_3 , and SiO_2) are always consistent. More importantly, the Pd 3d binding energies were consistently higher on nitride supports than on oxide supports, which suggests that the charge states of Pd strongly depend on the type of support used.

DFT calculations were used to investigate the possible Pd anchor sites on PCN and TiO_2 , respectively. Bader charge analysis was further performed to determine the effective charge of Pd. Based on electronegativity, the relation equations between the experimental oxidation state and the calculated Bader charge were successfully obtained (Figure 66). By utilizing the equations, the calculated Bader charge of Pd in the Pd/PCN and Pd/ TiO_2 models can be converted to its corresponding experimental oxidation state. This allows for a further comparison with the assigned oxidation state derived from XPS and XANES analysis. Additionally, by combining the converted oxidation state with the coordination information derived from EXAFS, the determination of the closest DFT-proposed model to the actual structure of the catalyst can be achieved.

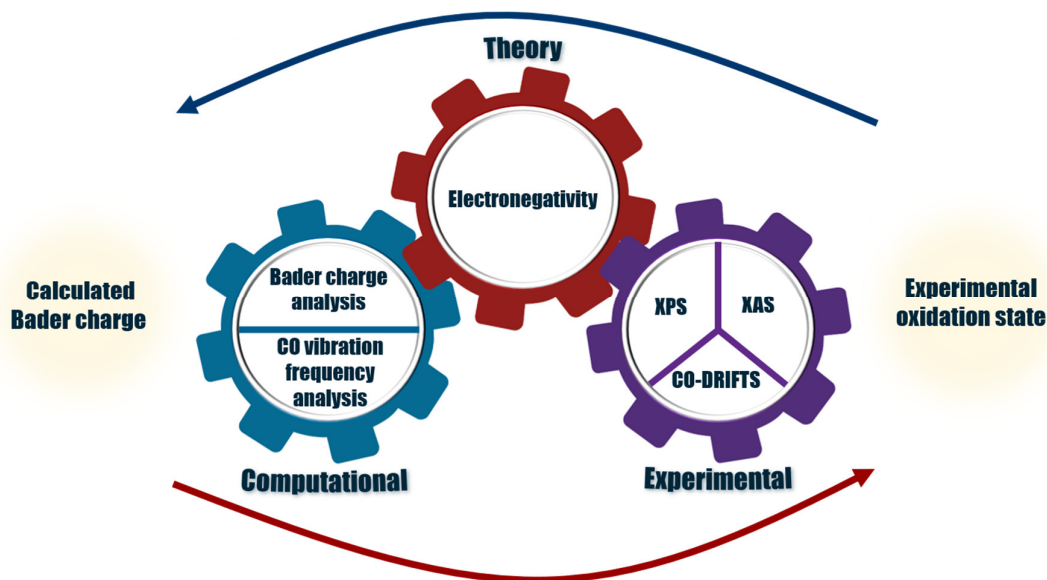


Figure 66. The connection between computation, theory, and experiment.

The relationship between Bader charge and CO vibrational frequency was also concluded. Specifically, using the obtained relation equations, the experimental CO frequency measured by CO-DRIFTS can be used to determine the Bader charge of the Pd species, which can then be further converted into the experimental oxidation state. It is found the DFT calculation reproduced the experimental data very well and confirmed that Pd atoms prefer to interact with

surface hydroxyl groups to form $\text{Pd}(\text{OH})_x$ species on oxide supports, whereas on nitride supports, Pd atoms are incorporated into the surface structure in the form of Pd–N bonds. However, two points need to be emphasized here: First, there is a fixed 9 cm^{-1} difference between the experimentally measured CO frequency and the theoretically calculated CO frequency. Second, in addition to the adsorption of CO molecules by Pd, the influence of support on the CO frequency cannot be ignored.

The synthesized Pd/PCN catalysts are highly active for the Suzuki-Miyaura cross-coupling reaction at $25\text{ }^\circ\text{C}$. The 2 wt% Pd/PCN sample exhibited the highest mole-specific activity. The calcined 2 wt% Pd/PCN samples were only active under visible light irradiation. This is because the PCN can be excited by visible light, and the photoexcited electrons can be transferred to the surface Pd species to promote the reaction. Moreover, a considerable decline in activity was observed with the increased calcination temperature, pointing out the influence of particle size on activity decay. The presence of O_2 significantly promotes this reaction since it enables the simultaneous cross- and self-coupling reactions to occur on the active Pd sites. Further continuous flow measurements demonstrated that the Pd/PCN catalysts behaved differently in Ar and O_2 : cross-coupling of bromobenzene and phenylboronic acid occurred in Ar, and self-coupling of phenylboronic acid occurred in O_2 . *In situ* ATR-IR measurements confirmed the interaction between the substrate phenylboronic acid and the base K_2CO_3 . Upon addition of Pd/PCN catalyst, the cleavage of the C–Br bond in bromobenzene and the transfer of boron-related groups in phenylboronic acid were observed, proving the cross-coupling reaction between bromobenzene and phenylboronic acid.

The above studies on isolated palladium catalysts and the resulting correlations are anticipated to contribute to a better understanding of isolated transition-metal catalysts and bridge the gap between experimental characterization and theoretical computation for studying supported metal catalysts, finally contributing to the understanding of the structure-reactivity relationship of heterogeneous catalysts.

6. Outlook

Further research can expand the support type from nitrides and oxides to include carbides, phosphides, and sulfides to see how the other coordinated atoms (C, P, and S) influence the charge state of Pd sites in isolated Pd catalysts.

Moreover, from an experimental standpoint, it is vital to combine various techniques and establish a set of standardized methods to study the charge state of the metal center in single-atom catalysts. This is because the determination of oxidation state based on experimental techniques has limitations that depend on the method and material system used. For example, direct assignment of formal oxidation state based on the CO vibration frequency from CO-DRIFTS measurements is not possible, as the frequency can be impacted by the support, as has been confirmed. Therefore, in addition to developing advanced techniques and related theories, it is also important to integrate various techniques and take advantage of their strengths to jointly study the electronic structure of isolated metal catalysts.

From a theoretical perspective, more potential Pd anchoring sites should be taken into consideration. For example, in this thesis, the DFT-proposed Pd/TiO₂ models are all based on the anatase TiO₂ (101) terrace sites since the (101) planes are thermodynamically more stable. It would be interesting to explore the coordination environment and the electronic structure of Pd anchoring sites on other exposed TiO₂ facets (i.e., (001) and (010) facets) as well as different surface structures (i.e., step-edge and kink sites). Future work should also emphasize the importance of unpaired electrons in the modeling of PCN. Specifically, if spin polarized DFT is used, it would be beneficial for discussing the spin density of the PCN, since this allows for a detailed analysis of the nature of the charge carriers and the structure of the anchoring sites for Pd atoms. Additionally, applying machine learning techniques to discover the influence of the support on the electronic structure of the metal center in single atom catalysts would be interesting. It could help build an extensive and curated database for mapping between the types of coordinated atoms and their corresponding charge states.

Future research will also focus on improving the integration of experimental characterization and theoretical calculations to investigate the structure of single-atom catalysts based on common properties (i.e., periodic trends of electronegativity, ionization energy, and atomic radius). In this thesis, two correlations were successfully established: one between the experimental oxidation state and the calculated Bader charge, based on the periodic trend in electronegativity, and the other between the experimental oxidation state and the CO vibration

frequency, connected by the Bader charge. Further efforts can be made to gain a deeper understanding of the fundamental physics behind and beyond the correlations. For example, how the CO orbital interaction with Pd affects its vibrational frequency, what the similarities and differences are in computed charges, atomistic structure, and spectroscopy results, and how to establish connections between the core-level binding energies, bond distances, occupancy numbers, and charge densities on the basis of common principles. Future work will also extend these correlations to explore other transition metal atoms, such as Pt, Ru, and Ir, *etc.*

List of Reference

- [1] F. Zaera, *The Journal of Physical Chemistry Letters*, 1 (2010) 621-627.
- [2] C.R. Catlow, M. Davidson, C. Hardacre, G.J. Hutchings, *Philosophical Transactions of the Royal Society A*, 374 (2016) 20150089.
- [3] X. Zhang, E.A. Davidson, D.L. Mauzerall, T.D. Searchinger, P. Dumas, Y. Shen, *Nature*, 528 (2015) 51-59.
- [4] V. Kyriakou, I. Garagounis, A. Vourros, E. Vasileiou, M. Stoukides, *Joule*, 4 (2020) 142-158.
- [5] H. Sinn, W. Kaminsky, *Ziegler-Natta Catalysis, Advances in Organometallic Chemistry*, Elsevier, 1980, 99-149.
- [6] P. Cossee, *Journal of Catalysis*, 3 (1964) 80-88.
- [7] S. Rood, S. Eslava, A. Manigrasso, C. Bannister, *Proceedings of the Institution of Mechanical Engineers, Part D: Journal of Automobile Engineering*, 234 (2019) 936-949.
- [8] A.S.-M. F. D. Manchester, J. M. Pitre *Journal of Phase Equilibria* 15 (1994) 62–83.
- [9] W. Brown, C. Foote, B. Iverson, E. Anslyn, *Organic Chemistry*, Cengage Learning, 2008.
- [10] J. Tsuji, *Palladium Reagents and Catalysts: New Perspectives for the 21st Century*, John Wiley & Son, 2004.
- [11] J.X. Liu, Y. Su, I.A.W. Filot, E.J.M. Hensen, *Journal of the American Chemical Society*, 140 (2018) 4580-4587.
- [12] T.Y. T. Kobayashi, K. Kayano, *Applied Catalysis B: Environmental*, 30 (2001) 287-292.
- [13] A.A. Thomas, S.E. Denmark, *Science*, 352 (2016) 329-332.
- [14] A. Suzuki, *Angewandte Chemie International Edition*, 50 (2011) 6722-6737.
- [15] E. Antolini, *Energy & Environmental Science*, 2 (2009) 915–931.
- [16] A. Chen, C. Ostrom, *Chemical Reviews*, 115 (2015) 11999-12044.
- [17] S. Zhang, L. Li, A. Kumar, *Materials Characterization Techniques*, CRC Press, 2008.
- [18] B. Qiao, A. Wang, X. Yang, L.F. Allard, Z. Jiang, Y. Cui, J. Liu, J. Li, T. Zhang, *Nature Chemistry*, 3 (2011) 634-641.
- [19] J. Yang, W. Li, D. Wang, Y. Li, *Advanced Materials*, 32 (2020) e2003300.
- [20] Z. Xu, Y. Zhang, L. Qin, Q. Meng, Z. Xue, L. Qiu, G. Zhang, X. Guo, Q. Li, *Small*, 16 (2020) e2002071.
- [21] X.F. Yang, A. Wang, B. Qiao, J. Li, J. Liu, T. Zhang, *Accounts of Chemical Research*, 46 (2013) 1740-1748.
- [22] C. Gao, J. Low, R. Long, T. Kong, J. Zhu, Y. Xiong, *Chemical Reviews*, 120 (2020) 12175–12216.
- [23] R. Lang, X. Du, Y. Huang, X. Jiang, Q. Zhang, Y. Guo, K. Liu, B. Qiao, A. Wang, T. Zhang, *Chemical Reviews*, 120 (2020) 11986–12043.

- [24] J. Timoshenko, B. Roldan Cuenya, *Chemical Reviews*, 121 (2021) 882-961.
- [25] X. Li, X. Yang, J. Zhang, Y. Huang, B. Liu, *ACS Catalysis*, 9 (2019) 2521-2531.
- [26] F.M. Mueller, A.J. Freeman, J.O. Dimmock, A.M. Furdyna, *Physical Review B*, 1 (1970) 4617-4635.
- [27] W.M. Haynes, *CRC Handbook of Chemistry and Physics*, CRC Press, 2014.
- [28] Z. Li, S. Ji, Y. Liu, X. Cao, S. Tian, Y. Chen, Z. Niu, Y. Li, *Chemical Reviews*, 120 (2020) 623-682.
- [29] N.N. Greenwood, A. Earnshaw, *Chemistry of the Elements*, Elsevier Science & Technology, 1984.
- [30] D.C. Powers, T. Ritter, Palladium(III) in Synthesis and Catalysis, in: A.J. Canty (Ed.) *Higher Oxidation State Organopalladium and Platinum Chemistry*, Springer Berlin Heidelberg, Berlin, Heidelberg, 2011, 129-156.
- [31] C.A. Salazar, K.N. Flesch, B.E. Haines, P.S. Zhou, D.G. Musaev, S.S. Stahl, *Science*, 370 (2020) 1454-1460.
- [32] X. Hu, A.C.K. Yip, *Frontiers in Catalysis*, 1 (2021) 667675.
- [33] N.Y. M Haruta, T Kobayashi, S Iijima, *Journal of Catalysis*, 115 (1989) 301-309.
- [34] G. Sitja, S. Le Moal, M. Marsault, G. Hamm, F. Leroy, C.R. Henry, *Nano Letters*, 13 (2013) 1977-1982.
- [35] I.V. Yudanov, A. Genest, S. Schauermaun, H.J. Freund, N. Rosch, *Nano Letters*, 12 (2012) 2134-2139.
- [36] Z.J. Wang, S. Ghasimi, K. Landfester, K.A.I. Zhang, *Chemistry of Materials*, 27 (2015) 1921-1924.
- [37] L. Liu, A. Corma, *Chemical Reviews*, 118 (2018) 4981-5079.
- [38] X. Bai, X. Zhao, Y. Zhang, C. Ling, Y. Zhou, J. Wang, Y. Liu, *Journal of the American Chemical Society*, 144 (2022) 17140-17148.
- [39] W. Guo, X. Tan, J. Bi, L. Xu, D. Yang, C. Chen, Q. Zhu, J. Ma, A. Tayal, J. Ma, Y. Huang, X. Sun, S. Liu, B. Han, *Journal of the American Chemical Society*, 143 (2021) 6877-6885.
- [40] H. Zhao, R. Yu, S. Ma, K. Xu, Y. Chen, K. Jiang, Y. Fang, C. Zhu, X. Liu, Y. Tang, L. Wu, Y. Wu, Q. Jiang, P. He, Z. Liu, L. Tan, *Nature Catalysis*, 5 (2022) 818-831.
- [41] Y. Deng, Y. Guo, Z. Jia, J.C. Liu, J. Guo, X. Cai, C. Dong, M. Wang, C. Li, J. Diao, Z. Jiang, J. Xie, N. Wang, H. Xiao, B. Xu, H. Zhang, H. Liu, J. Li, D. Ma, *Journal of the American Chemical Society*, 144 (2022) 3535-3542.
- [42] L. Qi, M. Babucci, Y. Zhang, A. Lund, L. Liu, J. Li, Y. Chen, A.S. Hoffman, S.R. Bare, Y. Han, B.C. Gates, A.T. Bell, *Journal of the American Chemical Society*, 143 (2021) 21364-21378.
- [43] Z. Li, W. Niu, Z. Yang, N. Zaman, W. Samarakoon, M. Wang, A. Kara, M. Lucero, M.V. Vyas, H. Cao, H. Zhou, G.E. Sterbinsky, Z. Feng, Y. Du, Y. Yang, *Energy & Environmental Science*, 13 (2020) 884-895.

- [44] X. Ao, W. Zhang, B. Zhao, y. ding, G. Nam, L. Soule, A.A. Abdelhafiz, C. Wang, M. Liu, *Energy & Environmental Science*, 13 (2020) 3032-3040.
- [45] M.G. Farpon, W. Henao, P.N. Plessow, E. Andres, R. Arenal, C. Marini, G. Agostini, F. Studt, G. Prieto, *Angewandte Chemie International Edition*, 62 (2023) e202214048.
- [46] Z. Li, D. He, X. Yan, S. Dai, S. Younan, Z. Ke, X. Pan, X. Xiao, H. Wu, J. Gu, *Angewandte Chemie International Edition*, 59 (2020) 18572-18577.
- [47] S. Ji, Y. Chen, X. Wang, Z. Zhang, D. Wang, Y. Li, *Chemical Reviews*, 120 (2020) 11900–11955.
- [48] M. Moliner, J.E. Gabay, C.E. Kliwer, R.T. Carr, J. Guzman, G.L. Casty, P. Serna, A. Corma, *Journal of the American Chemical Society*, 138 (2016) 15743-15750.
- [49] B. Hu, K. Sun, Z. Zhuang, Z. Chen, S. Liu, W.C. Cheong, C. Chen, M. Hu, X. Cao, J. Ma, R. Tu, X. Zheng, H. Xiao, X. Chen, Y. Cui, Q. Peng, C. Chen, Y. Li, *Advanced Materials*, 34 (2022) e2107721.
- [50] G. Malta, S.A. Kondrat, S.J. Freakley, C.J. Davies, L. Lu, S. Dawson, A. Thetford, E.K. Gibson, D.J. Morgan, W. Jones, P.P. Wells, P. Johnston, C.R. Catlow, C.J. Kiely, G.J. Hutchings, *Science*, 355 (2017) 1399-1403.
- [51] L. Lin, W. Zhou, R. Gao, S. Yao, X. Zhang, W. Xu, S. Zheng, Z. Jiang, Q. Yu, Y.W. Li, C. Shi, X.D. Wen, D. Ma, *Nature*, 544 (2017) 80-83.
- [52] X. Sun, S.R. Dawson, T.E. Parmentier, G. Malta, T.E. Davies, Q. He, L. Lu, D.J. Morgan, N. Carthey, P. Johnston, S.A. Kondrat, S.J. Freakley, C.J. Kiely, G.J. Hutchings, *Nature Chemistry*, 12 (2020) 560–567.
- [53] C. Dong, Z. Gao, Y. Li, M. Peng, M. Wang, Y. Xu, C. Li, M. Xu, Y. Deng, X. Qin, F. Huang, X. Wei, Y.-G. Wang, H. Liu, W. Zhou, D. Ma, *Nature Catalysis*, 5 (2022) 485–493.
- [54] N. Stock, S. Biswas, *Chemical Reviews*, 112 (2012) 933-969.
- [55] H. Furukawa, K.E. Cordova, M. O'Keeffe, O.M. Yaghi, *Science*, 341 (2013) 1230444.
- [56] H. Zhang, J. Wei, J. Dong, G. Liu, L. Shi, P. An, G. Zhao, J. Kong, X. Wang, X. Meng, J. Zhang, J. Ye, *Angewandte Chemie International Edition*, 55 (2016) 14310-14314.
- [57] D. Saliba, M. Ammar, M. Rammal, M. Al-Ghoul, M. Hmadeh, *Journal of the American Chemical Society*, 140 (2018) 1812-1823.
- [58] D. Fairen-Jimenez, S.A. Moggach, M.T. Wharmby, P.A. Wright, S. Parsons, T. Duren, *Journal of the American Chemical Society*, 133 (2011) 8900-8902.
- [59] Y.S. Wei, M. Zhang, R. Zou, Q. Xu, *Chemical Reviews*, 120 (2020) 12089-12174.
- [60] Y. Zhao, H. Zhou, X. Zhu, Y. Qu, C. Xiong, Z. Xue, Q. Zhang, X. Liu, F. Zhou, X. Mou, W. Wang, M. Chen, Y. Xiong, X. Lin, Y. Lin, W. Chen, H.-J. Wang, Z. Jiang, L. Zheng, T. Yao, J. Dong, S. Wei, W. Huang, L. Gu, J. Luo, Y. Li, Y. Wu, *Nature Catalysis*, 4 (2021) 134-143.
- [61] N. Wang, X. Zhao, R. Zhang, S. Yu, Z.H. Levell, C. Wang, S. Ma, P. Zou, L. Han, J. Qin, L. Ma, Y. Liu, H.L. Xin, *ACS Catalysis*, (2022) 4156-4164.
- [62] Y.N. Gong, L. Jiao, Y. Qian, C.Y. Pan, L. Zheng, X. Cai, B. Liu, S.H. Yu, H.L. Jiang, *Angewandte Chemie International Edition*, 132 (2020) 1-6.

- [63] Z. Li, Y. Chen, S. Ji, Y. Tang, W. Chen, A. Li, J. Zhao, Y. Xiong, Y. Wu, Y. Gong, T. Yao, W. Liu, L. Zheng, J. Dong, Y. Wang, Z. Zhuang, W. Xing, C.-T. He, C. Peng, W.-C. Cheong, Q. Li, M. Zhang, Z. Chen, N. Fu, X. Gao, W. Zhu, J. Wan, J. Zhang, L. Gu, S. Wei, P. Hu, J. Luo, J. Li, C. Chen, Q. Peng, X. Duan, Y. Huang, X.-M. Chen, D. Wang, Y. Li, *Nature Chemistry*, 12 (2020) 764–772.
- [64] Z. Li, F. Liu, Y. Jiang, P. Ni, C. Zhang, B. Wang, C. Chen, Y. Lu, *Nano Research*, 15 (2022) 4411–4420.
- [65] C. Gao, S. Chen, Y. Wang, J. Wang, X. Zheng, J. Zhu, L. Song, W. Zhang, Y. Xiong, *Advanced Materials*, 30 (2018) e1704624.
- [66] Y. Pan, S. Liu, K. Sun, X. Chen, B. Wang, K. Wu, X. Cao, W.C. Cheong, R. Shen, A. Han, Z. Chen, L. Zheng, J. Luo, Y. Lin, Y. Liu, D. Wang, Q. Peng, Q. Zhang, C. Chen, Y. Li, *Angewandte Chemie International Edition*, 57 (2018) 8614–8618.
- [67] H. Wu, H. Li, X. Zhao, Q. Liu, J. Wang, J. Xiao, S. Xie, R. Si, F. Yang, S. Miao, X. Guo, G. Wang, X. Bao, *Energy & Environmental Science*, 9 (2016) 3736–3745.
- [68] Y. Chen, S. Ji, S. Zhao, W. Chen, J. Dong, W.C. Cheong, R. Shen, X. Wen, L. Zheng, A.I. Rykov, S. Cai, H. Tang, Z. Zhuang, C. Chen, Q. Peng, D. Wang, Y. Li, *Nature Communications*, 9 (2018) 5422.
- [69] Q. Li, W. Chen, H. Xiao, Y. Gong, Z. Li, L. Zheng, X. Zheng, W. Yan, W.C. Cheong, R. Shen, N. Fu, L. Gu, Z. Zhuang, C. Chen, D. Wang, Q. Peng, J. Li, Y. Li, *Advanced Materials*, 30 (2018) e1800588.
- [70] X. He, Q. He, Y. Deng, M. Peng, H. Chen, Y. Zhang, S. Yao, M. Zhang, D. Xiao, D. Ma, B. Ge, H. Ji, *Nature Communications*, 10 (2019) 3663.
- [71] X. Wang, J. Chen, J. Zeng, Q. Wang, Z. Li, R. Qin, C. Wu, Z. Xie, L. Zheng, *Nanoscale*, 9 (2017) 6643–6648.
- [72] M. Yang, L.F. Allard, M. Flytzani-Stephanopoulos, *Journal of the American Chemical Society*, 135 (2013) 3768–3771.
- [73] P. Liu, Y. Zhao, R. Qin, S. Mo, G. Chen, L. Gu, D.M. Chevrier, P. Zhang, Q. Guo, D. Zang, B. Wu, G. Fu, N. Zheng, *Science*, 352 (2016) 797–801.
- [74] X. Ge, P. Zhou, Q. Zhang, Z. Xia, S. Chen, P. Gao, Z. Zhang, L. Gu, S. Guo, *Angewandte Chemie International Edition*, 59 (2020) 232–236.
- [75] J. Fonseca, J. Lu, *ACS Catalysis*, (2021) 7018–7059.
- [76] X. Huang, H. Yan, L. Huang, X. Zhang, Y. Lin, J. Li, Y. Xia, Y. Ma, Z. Sun, S. Wei, J. Lu, *The Journal of Physical Chemistry C*, 123 (2018) 7922–7930.
- [77] X. Huang, Y. Xia, Y. Cao, X. Zheng, H. Pan, J. Zhu, C. Ma, H. Wang, J. Li, R. You, S. Wei, W. Huang, J. Lu, *Nano Research*, 10 (2017) 1302–1312.
- [78] M. Piernawieja-Hermida, Z. Lu, A. White, K.B. Low, T. Wu, J.W. Elam, Z. Wu, Y. Lei, *Nanoscale*, 8 (2016) 15348–15356.
- [79] H. Xu, Z. Zhang, J. Liu, C.L. Do-Thanh, H. Chen, S. Xu, Q. Lin, Y. Jiao, J. Wang, Y. Wang, Y. Chen, S. Dai, *Nature Communications*, 11 (2020) 3908.

- [80] G.F. Han, F. Li, A.I. Rykov, Y.K. Im, S.Y. Yu, J.P. Jeon, S.J. Kim, W. Zhou, R. Ge, Z. Ao, T.J. Shin, J. Wang, H.Y. Jeong, J.B. Baek, *Nature Nanotechnology*, 17 (2022) 403-407.
- [81] Y. Guo, Y. Huang, B. Zeng, B. Han, M. Akri, M. Shi, Y. Zhao, Q. Li, Y. Su, L. Li, Q. Jiang, Y.T. Cui, L. Li, R. Li, B. Qiao, T. Zhang, *Nature Communications*, 13 (2022) 2648.
- [82] H. Zhang, X. Zhang, S. Shi, Q. He, X. He, T. Gan, H. Ji, *ACS Appl Mater Interfaces*, 14 (2022) 53755-53760.
- [83] I. Bilecka, M. Niederberger, *Nanoscale*, 2 (2010) 1358-1374.
- [84] H. Fei, J. Dong, C. Wan, Z. Zhao, X. Xu, Z. Lin, Y. Wang, H. Liu, K. Zang, J. Luo, S. Zhao, W. Hu, W. Yan, I. Shakir, Y. Huang, X. Duan, *Advanced Materials*, 30 (2018) e1802146.
- [85] Z. Chen, E. Vorobyeva, S. Mitchell, E. Fako, M.A. Ortuno, N. Lopez, S.M. Collins, P.A. Midgley, S. Richard, G. Vile, J. Perez-Ramirez, *Nature Nanotechnology*, 13 (2018) 702-707.
- [86] Z. Chen, S. Mitchell, F. Krumeich, R. Hauert, S. Yakunin, M.V. Kovalenko, J. Pérez-Ramírez, *ACS Sustainable Chemistry & Engineering*, 7 (2019) 5223-5230.
- [87] Z. Chen, E. Vorobyeva, S. Mitchell, E. Fako, N. López, S.M. Collins, R.K. Leary, P.A. Midgley, R. Hauert, J. Pérez-Ramírez, *National Science Review*, 5 (2018) 642-652.
- [88] L. Jiao, J.R. Regalbuto, *Journal of Catalysis*, 260 (2008) 329-341.
- [89] N.C. Nelson, L. Chen, D. Meira, L. Kovarik, J. Szanyi, *Angewandte Chemie International Edition*, 59 (2020) 17657-17663.
- [90] C. Chu, D. Huang, S. Gupta, S. Weon, J. Niu, E. Stavitski, C. Muhich, J.H. Kim, *Nature Communications*, 12 (2021) 5179.
- [91] J. Liu, M. Jiao, B. Mei, Y. Tong, Y. Li, M. Ruan, P. Song, G. Sun, L. Jiang, Y. Wang, Z. Jiang, L. Gu, Z. Zhou, W. Xu, *Angewandte Chemie International Edition*, 58 (2019) 1163-1167.
- [92] H. Fei, J. Dong, M.J. Arellano-Jimenez, G. Ye, N. Dong Kim, E.L. Samuel, Z. Peng, Z. Zhu, F. Qin, J. Bao, M.J. Yacaman, P.M. Ajayan, D. Chen, J.M. Tour, *Nature Communications*, 6 (2015) 8668.
- [93] Y. Li, J. Hao, H. Song, F. Zhang, X. Bai, X. Meng, H. Zhang, S. Wang, Y. Hu, J. Ye, *Nature Communications*, 10 (2019) 2359.
- [94] S. Zhou, L. Shang, Y. Zhao, R. Shi, G.I.N. Waterhouse, Y.C. Huang, L. Zheng, T. Zhang, *Advanced Materials*, 31 (2019) e1900509.
- [95] R. Qin, K. Liu, Q. Wu, N. Zheng, *Chemical Reviews*, 120 (2020) 11810-11899.
- [96] F. Krumeich, E. Muller, R.A. Wepf, *Micron*, 49 (2013) 1-14.
- [97] M.P. Oxley, A.R. Lupini, S.J. Pennycook, *Reports on Progress in Physics*, 80 (2017) 026101.
- [98] C. Dwyer, *Atomic-Resolution Core-Level Spectroscopy in the Scanning Transmission Electron Microscope*, Elsevier, 2013, 145-199.
- [99] M. Peng, Z. Jia, Z. Gao, M. Xu, D. Cheng, M. Wang, C. Li, L. Wang, X. Cai, Z. Jiang, H. Jiang, N. Wang, D. Xiao, H. Liu, D. Ma, *ACS Catalysis*, 12 (2022) 2244-2252.

- [100] O.L. Krivanek, C. Mory, M. Tence, C. Colliex, *Microscopy Microanalysis Microstructures*, 2 (1991) 257-267.
- [101] M.T. K. Suenaga, C. Mory, C. Colliex, H. Kato, T. Okazaki, H. Shinohara, K. Hirahara, S. Bandow, S. Iijima, *Science*, 290 (2000) 2280-2282.
- [102] L.F.K. D. A. Muller, M. Murfitt, J. H. Song, H. Y. Hwang, J. Silcox, N. Dellby, O. L. Krivanek, *Science*, 319 (2008) 1073-1076.
- [103] P. Liu, Y. Zhao, R. Qin, L. Gu, P. Zhang, G. Fu, N. Zheng, *Science Bulletin*, 63 (2018) 675-682.
- [104] W. Ru, Y. Liu, B. Fu, F. Fu, J. Feng, D. Li, *Small*, 18 (2022) e2103852.
- [105] P.L. Gai, E.D. Boyes, *Microscopy Research and Technique*, 72 (2009) 153-164.
- [106] L. Liu, D.N. Zakharov, R. Arenal, P. Concepcion, E.A. Stach, A. Corma, *Nature Communications*, 9 (2018) 574.
- [107] S. Wei, A. Li, J.C. Liu, Z. Li, W. Chen, Y. Gong, Q. Zhang, W.C. Cheong, Y. Wang, L. Zheng, H. Xiao, C. Chen, D. Wang, Q. Peng, L. Gu, X. Han, J. Li, Y. Li, *Nature Nanotechnology*, 13 (2018) 856-861.
- [108] J. Liu, *Chinese J Catal*, 38 (2017) 1460-1472.
- [109] M.K. Samantaray, V. D'Elia, E. Pump, L. Falivene, M. Harb, S. Ould Chikh, L. Cavallo, J.M. Basset, *Chemical Reviews*, 120 (2020) 734-813.
- [110] J.Y.K. S.B. Rice, M.M. Diskoa, M.M.J. Treacy, *Ultramicroscopy* 34 (1990) 108-118.
- [111] L. Liu, U. Diaz, R. Arenal, G. Agostini, P. Concepcion, A. Corma, *Nature Materials*, 16 (2017) 132-138.
- [112] E. Stavitski, *Infrared Spectroscopy on Powder Catalysts, In-situ Characterization of Heterogeneous Catalysts*, John Wiley & Sons, 2013, 241-265.
- [113] D. Heyl, U. Rodemerck, U. Bentrup, *ACS Catalysis*, 6 (2016) 6275-6284.
- [114] J. Jones, H. Xiong, A.T. DeLaRiva, E.J. Peterson, H. Pham, S.R. Challa, G. Qi, S. Oh, M.H. Wiebenga, X.I. Pereira Hernandez, Y. Wang, A.K. Datye, *Science*, 353 (2016) 150-154.
- [115] K. Ding, A. Gulec, A.M. Johnson, N.M. Schweitzer, G.D. Stucky, L.D. Marks, P.C. Stair, *Science*, 350 (2015) 189-192.
- [116] A.J. Therrien, A.J.R. Hensley, M.D. Marcinkowski, R. Zhang, F.R. Lucci, B. Coughlin, A.C. Schilling, J.-S. McEwen, E.C.H. Sykes, *Nature Catalysis*, 1 (2018) 192-198.
- [117] L. Nie, D. Mei, H. Xiong, B. Peng, Z. Ren, X.I.P. Hernandez, A. DeLaRiva, M. Wang, M.H. Engelhard, L. Kovarik, A.K. Datye, Y. Wang, *Science*, 358 (2017) 1419-1423.
- [118] S. Xie, L. Liu, Y. Lu, C. Wang, S. Cao, W. Diao, J. Deng, W. Tan, L. Ma, S.N. Ehrlich, Y. Li, Y. Zhang, K. Ye, H. Xin, M. Flytzani-Stephanopoulos, F. Liu, *Journal of the American Chemical Society*, 144 (2022) 21255-21266.
- [119] C. Lamberti, A. Zecchina, E. Groppo, S. Bordiga, *Chemical Society Reviews*, 39 (2010) 4951-5001.

- [120] J.T. Yates, S.D. Worley, T.M. Duncan, R.W. Vaughan, *The Journal of Chemical Physics*, 70 (1979) 1225-1230.
- [121] A.A.a.S. Davydov, N.T., *Molecular Spectroscopy of Oxide Catalyst Surfaces*, Wiley, 2003.
- [122] L. DeRita, J. Resasco, S. Dai, A. Boubnov, H.V. Thang, A.S. Hoffman, I. Ro, G.W. Graham, S.R. Bare, G. Pacchioni, X. Pan, P. Christopher, *Nature Materials*, 18 (2019) 746-751.
- [123] D. Jiang, g. Wan, C.E. Garcia Vargas, L. Li, X.I. Pereira Hernandez, C. Wang, Y. Wang, *ACS Catalysis*, (2020) 11356-11364.
- [124] D.K. Mingshu Chen, Cheol-Woo Yi, D.W. Goodman, *Science*, 310 (2005) 291-293.
- [125] V. Muravev, G. Spezzati, Y.-Q. Su, A. Parastaev, F.-K. Chiang, A. Longo, C. Escudero, N. Kosinov, E.J.M. Hensen, *Nature Catalysis*, 4 (2021) 469–478.
- [126] J. Hulva, M. Meier, R. Bliem, Z. Jakub, F. Kraushofer, M. Schmid, U. Diebold, C. Franchini, G.S. Parkinson, *Science*, 371 (2021) 375-379.
- [127] F.d. Groot, *Chemical Reviews*, 101 (2001) 1779–1808.
- [128] B.B. Sarma, F. Maurer, D.E. Doronkin, J.D. Grunwaldt, *Chemical Reviews*, 123 (2022) 379–444.
- [129] D.C. Koningsberger, D.E. Ramaker, *Applications of X-ray Absorption Spectroscopy in Heterogeneous Catalysis: EXAFS, Atomic XAFS, and Delta XANES*, *Handbook of Heterogeneous Catalysis*, John Wiley & Sons, 2008.
- [130] C. Geantet, C. Pichon, *X-Ray Absorption Spectroscopy, Characterization of Solid Materials and Heterogeneous Catalysts*, John Wiley & Sons, 2012, 511-536.
- [131] G.S. Henderson, F.M.F. de Groot, B.J.A. Moulton, *Reviews in Mineralogy and Geochemistry*, 78 (2014) 75-138.
- [132] E.D. Park, Y.-S. Hwang, C.W. Lee, J.S. Lee, *Applied Catalysis A: General*, 247 (2003) 269-281.
- [133] W.B. Kim, E.D. Park, J.S. Lee, *Applied Catalysis A: General*, 242 (2003) 335-345.
- [134] S.-J. Kim, S. Lemaux, G. Demazeau, J.-Y. Kim, J.-H. Choy, *Journal of Materials Chemistry*, 12 (2002) 995-1000.
- [135] A.S. Hoffman, D. Sokaras, S. Zhang, L.M. Debeve, C.Y. Fang, A. Gallo, T. Kroll, D.A. Dixon, S.R. Bare, B.C. Gates, *Chemistry: A European Journal*, 23 (2017) 14760-14768.
- [136] B.C. Gates, M. Flytzani-Stephanopoulos, D.A. Dixon, A. Katz, *Catalysis Science & Technology*, 7 (2017) 4259-4275.
- [137] F. Maurer, J. Jelic, J.J. Wang, A. Ganzler, P. Dolcet, C. Woll, Y.M. Wang, F. Studt, M. Casapu, J.D. Grunwaldt, *Nature Catalysis*, 3 (2020) 824–833
- [138] B. Ravel, *Quantitative EXAFS Analysis*, in: C.L. Jeroen A. Van Bokhoven (Ed.) *X-Ray Absorption and X-Ray Emission Spectroscopy*, John Wiley & Sons, 2016, 281-302.
- [139] D. Zhang, D. Yang, S. Wang, L. Zeng, J. Xin, H. Zhang, A. Lei, *Chinese Journal of Chemistry*, 39 (2021) 307-311.

- [140] E.J. Peterson, A.T. DeLaRiva, S. Lin, R.S. Johnson, H. Guo, J.T. Miller, J. Hun Kwak, C.H. Peden, B. Kiefer, L.F. Allard, F.H. Ribeiro, A.K. Datye, *Nature Communications*, 5 (2014) 4885.
- [141] F.S. Jens K. Nørskov, Frank Abild-Pedersen, and Thomas Bligaard, *Fundamental Concepts in Heterogeneous Catalysis*, John Wiley & Son, 2014.
- [142] S. Yu, X. Cheng, Y. Wang, B. Xiao, Y. Xing, J. Ren, Y. Lu, H. Li, C. Zhuang, G. Chen, *Nature Communications*, 13 (2022) 4737.
- [143] S. Hunklinger, C. Enss, *Solid State Physics*, De Gruyter, 2022.
- [144] P.M. Charles Kittel, *Introduction to solid state physics* Eighth edition, John Wiley & Sons, 2005.
- [145] Y. Ma, Y. Ren, Y. Zhou, W. Liu, W. Baaziz, O. Ersen, C. Pham-Huu, M. Greiner, W. Chu, A. Wang, T. Zhang, Y. Liu, *Angewandte Chemie International Edition*, 59 (2020) 21613-21619.
- [146] E. Zhao, M. Li, B. Xu, X.L. Wang, Y. Jing, D. Ma, S. Mitchell, J. Perez-Ramirez, Z. Chen, *Angewandte Chemie International Edition*, 61 (2022) e2022074.
- [147] R.F.W. Bader, *Accounts of Chemical Research*, 18 (1985) 9-15.
- [148] G. Henkelman, A. Arnaldsson, H. Jónsson, *Computational Materials Science*, 36 (2006) 354-360.
- [149] Y. Kim, G. Collinge, M.S. Lee, K. Khivantsev, S.J. Cho, V.A. Glezakou, R. Rousseau, J. Szanyi, J.H. Kwak, *Angewandte Chemie International Edition*, 60 (2021) 22769-22775.
- [150] E. Engel, R.M. Dreizler, *Density Functional Theory: An Advanced Course*, Springer Berlin Heidelberg, 2011.
- [151] J.A.S. David S. Sholl, *Density functional theory: a practical introduction*, John Wiley & Sons, 2009.
- [152] Y. Zhao, T. Ling, S. Chen, B. Jin, A. Vasileff, Y. Jiao, L. Song, J. Luo, S.Z. Qiao, *Angewandte Chemie International Edition*, 58 (2019) 12252-12257.
- [153] C.Y. Li, J.C. Dong, X. Jin, S. Chen, R. Panneerselvam, A.V. Rudnev, Z.L. Yang, J.F. Li, T. Wandlowski, Z.Q. Tian, *Journal of the American Chemical Society*, 137 (2015) 7648-7651.
- [154] S.S. Masango, R.A. Hackler, A.-I. Henry, M.O. McAnally, G.C. Schatz, P.C. Stair, R.P. Van Duyne, *The Journal of Physical Chemistry C*, 120 (2016) 3822-3833.
- [155] H. Kim, K.M. Kosuda, R.P. Van Duyne, P.C. Stair, *Chemical Society Reviews*, 39 (2010) 4820-4844.
- [156] J.C. Dong, M. Su, V. Briega-Martos, L. Li, J.B. Le, P. Radjenovic, X.S. Zhou, J.M. Feliu, Z.Q. Tian, J.F. Li, *Journal of the American Chemical Society*, 142 (2020) 715-719.
- [157] J. Wei, S.N. Qin, J. Yang, H.L. Ya, W.H. Huang, H. Zhang, B.J. Hwang, Z.Q. Tian, J.F. Li, *Angewandte Chemie International Edition*, 60 (2021) 9306-9310.
- [158] P. Pietrzyk, Z. Sojka, E. Giamello, *Electron Paramagnetic Resonance Spectroscopy, Characterization of Solid Materials and Heterogeneous Catalysts*, John Wiley & Sons, 2012, 343-406.
- [159] A. Bruckner, *Chemical Society Reviews*, 39 (2010) 4673-4684.

- [160] T.H. Vuong, N. Rockstroh, U. Bentrup, J. Rabeah, J. Knossalla, S. Peitz, R. Franke, A. Brückner, *ACS Catalysis*, 11 (2021) 3541-3552.
- [161] T.H. Vuong, J. Radnik, J. Rabeah, U. Bentrup, M. Schneider, H. Atia, U. Armbruster, W. Grünert, A. Brückner, *ACS Catalysis*, 7 (2017) 1693-1705.
- [162] M.C. Krystyna Dyrek, *Chemical Reviews*, 97 (1997) 305-331.
- [163] G. Cha, I. Hwang, S. Hejazi, A.S. Dobrota, I.A. Pasti, B. Osuagwu, H. Kim, J. Will, T. Yokosawa, Z. Badura, S. Kment, S. Mohajernia, A. Mazare, N.V. Skorodumova, E. Spiecker, P. Schmuki, *iScience*, 24 (2021) 102938.
- [164] P. Serna, B.C. Gates, *Accounts of Chemical Research*, 47 (2014) 2612-2620.
- [165] J.D. Pelletier, J.M. Basset, *Accounts of Chemical Research*, 49 (2016) 664-677.
- [166] S. Liu, J.M. Tan, A. Gulec, L.A. Crosby, T.L. Drake, N.M. Schweitzer, M. Delferro, L.D. Marks, T.J. Marks, P.C. Stair, *Organometallics*, 36 (2017) 818-828.
- [167] W.-Y. Huang, G.-Q. Wang, W.-H. Li, T.-T. Li, G.-J. Ji, S.-C. Ren, M. Jiang, L. Yan, H.-T. Tang, Y.-M. Pan, Y.-J. Ding, *Chem*, 6 (2020) 2300-2313.
- [168] J.H. Ja Hun Kwak, Donghai Mei, Cheol-Woo Yi, Do Heui Kim, Charles H. F. Peden, Lawrence F. Allard, Janos Szanyi, *Science*, 325 (2009) 1670-1673.
- [169] Z. Zhang, Y. Zhu, H. Asakura, B. Zhang, J. Zhang, M. Zhou, Y. Han, T. Tanaka, A. Wang, T. Zhang, N. Yan, *Nature Communications*, 8 (2017) 16100.
- [170] S. Ren, B. Ye, S. Li, L. Pang, Y. Pan, H. Tang, *Nano Research*, 15 (2021) 1500-1508.
- [171] W.F.S. Jolm F. Moulder, Peter E.'Sobol, K.D. Bomben, *Handbook of X-ray photoelectron spectroscopy*, Perkin-Elmer Corporation, 1992.
- [172] A. Walsh, A.A. Sokol, J. Buckeridge, D.O. Scanlon, C.R.A. Catlow, *Nature Materials*, 17 (2018) 958-964.
- [173] V. Muravev, J.F.M. Simons, A. Parastaev, M.A. Verheijen, J.J.C. Struijs, N. Kosinov, E.J.M. Hensen, *Angewandte Chemie International Edition*, 61 (2022) e202200434.
- [174] X. Wang, K. Maeda, A. Thomas, K. Takanabe, G. Xin, J.M. Carlsson, K. Domen, M. Antonietti, *Nature Materials*, 8 (2009) 76-80.
- [175] B.V. Lotsch, M. Dobliger, J. Sehnert, L. Seyfarth, J. Senker, O. Oeckler, W. Schnick, *Chemistry-A European Journal*, 13 (2007) 4969-4980.
- [176] X. Zhang, X. Xie, H. Wang, J. Zhang, B. Pan, Y. Xie, *Journal of the American Chemical Society*, 135 (2013) 18-21.
- [177] J. Liu, H. Wang, Z.P. Chen, H. Moehwald, S. Fiechter, R. van de Krol, L. Wen, L. Jiang, M. Antonietti, *Advanced Materials*, 27 (2015) 712-718.
- [178] J. Liu, Y. Liu, N. Liu, Y. Han, X. Zhang, H. Huang, Y. Lifshitz, S.T. Lee, J. Zhong, Z. Kang, *Science*, 347 (2015) 970-974.
- [179] G. Vile, D. Albani, M. Nachttegaal, Z. Chen, D. Dontsova, M. Antonietti, N. Lopez, J. Perez-Ramirez, *Angewandte Chemie International Edition*, 54 (2015) 11265-11269.

- [180] E. Vorobyeva, Z. Chen, S. Mitchell, R.K. Leary, P. Midgley, J.M. Thomas, R. Hauert, E. Fako, N. López, J. Pérez-Ramírez, *Journal of Materials Chemistry A*, 5 (2017) 16393-16403.
- [181] Z. Li, W. Wei, H. Li, S. Li, L. Leng, M. Zhang, J.H. Horton, D. Wang, W. Sun, C. Guo, W. Wu, J. Wang, *ACS Nano*, 15 (2021) 10175-10184.
- [182] S. Buchele, Z. Chen, E. Fako, F. Krumeich, R. Hauert, O.V. Safonova, N. Lopez, S. Mitchell, J. Perez-Ramirez, *Angewandte Chemie International Edition*, 59 (2020) 19639-19644.
- [183] C. Deng, R. He, W. Shen, M. Li, *Physical Chemistry Chemical Physics*, 21 (2019) 18589-18594.
- [184] J.C. Védrine, *Chinese J Catal*, 40 (2019) 1627-1636.
- [185] C. Wang, G. Garbarino, L.F. Allard, F. Wilson, G. Busca, M. Flytzani-Stephanopoulos, *ACS Catalysis*, 6 (2015) 210-218.
- [186] E.W. McFarland, H. Metiu, *Chemical Reviews*, 113 (2013) 4391-4427.
- [187] C. Perego, R. Revel, O. Durupthy, S. Cassaignon, J.-P. Jolivet, *Solid State Sciences*, 12 (2010) 989-995.
- [188] R.F.H. Theo H. Fleisch, Alexis T. Bell, *Journal of Catalysis*, 87 (1984) 398-413.
- [189] S.F. Hackett, R.M. Brydson, M.H. Gass, I. Harvey, A.D. Newman, K. Wilson, A.F. Lee, *Angewandte Chemie International Edition*, 46 (2007) 8593-8596.
- [190] Y. Jin, F. Lu, D. Yi, J. Li, F. Zhang, T. Sheng, F. Zhan, Y.n. Duan, G. Huang, J. Dong, B. Zhou, X. Wang, J. Yao, *CCS Chemistry*, (2020) 1453-1462.
- [191] X. He, Y. Deng, Y. Zhang, Q. He, D. Xiao, M. Peng, Y. Zhao, H. Zhang, R. Luo, T. Gan, H. Ji, D. Ma, *Cell Reports Physical Science*, 1 (2020) 100004.
- [192] X. Sun, J. Lin, Y. Zhou, L. Li, Y. Su, X. Wang, T. Zhang, *AIChE Journal*, 63 (2017) 4022-4031.
- [193] F.K. Kessler, Y. Zheng, D. Schwarz, C. Merschjann, W. Schnick, X. Wang, M.J. Bojdys, *Nature Reviews Materials*, 2 (2017) 17030.
- [194] Y. Wang, Y. Guo, Z. Wang, L. Fu, Y. Zhang, Y. Xu, S. Yuan, H. Pan, Y. Du, J. Wang, N. Tang, *ACS Nano*, 15 (2021) 12069-12076.
- [195] J.N. Coleman, M. Lotya, A. O'Neill, S.D. Bergin, P.J. King, U. Khan, K. Young, A. Gaucher, S. De, R.J. Smith, I.V. Shvets, S.K. Arora, G. Stanton, H.Y. Kim, K. Lee, G.T. Kim, G.S. Duesberg, T. Hallam, J.J. Boland, J.J. Wang, J.F. Donegan, J.C. Grunlan, G. Moriarty, A. Shmeliov, R.J. Nicholls, J.M. Perkins, E.M. Grieveson, K. Theuwissen, D.W. McComb, P.D. Nellist, V. Nicolosi, *Science*, 331 (2011) 568-571.
- [196] P. Niu, L. Zhang, G. Liu, H.-M. Cheng, *Advanced Functional Materials*, 22 (2012) 4763-4770.
- [197] J. Ran, T.Y. Ma, G. Gao, X.-W. Du, S.Z. Qiao, *Energy & Environmental Science*, 8 (2015) 3708-3717.
- [198] M. Rahman, K. Davey, S.Z. Qiao, *Small*, 13 (2017) 1700376.
- [199] Y. Li, R. Jin, Y. Xing, J. Li, S. Song, X. Liu, M. Li, R. Jin, *Advanced Energy Materials*, 6 (2016) 1601273.

- [200] J. Xu, L. Zhang, R. Shi, Y. Zhu, *Journal of Materials Chemistry A*, 1 (2013) 14766–14772.
- [201] F. Cheng, H. Wang, X. Dong, *Chem Commun (Camb)*, 51 (2015) 7176-7179.
- [202] S. Yang, Y. Gong, J. Zhang, L. Zhan, L. Ma, Z. Fang, R. Vajtai, X. Wang, P.M. Ajayan, *Advanced Materials*, 25 (2013) 2452-2456.
- [203] K. Schwinghammer, M.B. Mesch, V. Duppel, C. Ziegler, J. Senker, B.V. Lotsch, *Journal of the American Chemical Society*, 136 (2014) 1730-1733.
- [204] X. Wu, F. Chen, X. Wang, H. Yu, *Applied Surface Science*, 427 (2018) 645-653.
- [205] X. Wu, X. Wang, F. Wang, H. Yu, *Applied Catalysis B: Environmental*, 247 (2019) 70-77.
- [206] Q. Han, B. Wang, J. Gao, Z. Cheng, Y. Zhao, Z. Zhang, L. Qu, *ACS Nano*, 10 (2016) 2745-2751.
- [207] L. Ma, H. Fan, M. Li, H. Tian, J. Fang, G. Dong, *Journal of Materials Chemistry A*, 3 (2015) 22404-22412.
- [208] X. Wu, D. Gao, H. Yu, J. Yu, *Nanoscale*, 11 (2019) 9608-9616.
- [209] P. Yang, H. Ou, Y. Fang, X. Wang, *Angewandte Chemie International Edition*, 56 (2017) 3992-3996.
- [210] Q. Liang, Z. Li, Z.-H. Huang, F. Kang, Q.-H. Yang, *Advanced Functional Materials*, 25 (2015) 6885-6892.
- [211] N. Meng, J. Ren, Y. Liu, Y. Huang, T. Petit, B. Zhang, *Energy & Environmental Science*, 11 (2018) 566-571.
- [212] J. Ji, J. Wen, Y. Shen, Y. Lv, Y. Chen, S. Liu, H. Ma, Y. Zhang, *Journal of the American Chemical Society*, 139 (2017) 11698-11701.
- [213] X. Cui, W. Li, P. Ryabchuk, K. Junge, M. Beller, *Nature Catalysis*, 1 (2018) 385-397.
- [214] M.D. Marcinkowski, S.F. Yuk, N. Doudin, R.S. Smith, M.-T. Nguyen, B.D. Kay, V.-A. Glezakou, R. Rousseau, Z. Dohnálek, *ACS Catalysis*, 9 (2019) 10977-10982.
- [215] S.K. Kaiser, Z. Chen, D. Faust Akl, S. Mitchell, J. Perez-Ramirez, *Chemical Reviews*, 120 (2020) 11703–11809.
- [216] H. Fei, J. Dong, Y. Feng, C.S. Allen, C. Wan, B. Voloskiy, M. Li, Z. Zhao, Y. Wang, H. Sun, P. An, W. Chen, Z. Guo, C. Lee, D. Chen, I. Shakir, M. Liu, T. Hu, Y. Li, A.I. Kirkland, X. Duan, Y. Huang, *Nature Catalysis*, 1 (2018) 63-72.
- [217] G. Gao, Y. Jiao, E.R. Waclawik, A. Du, *Journal of the American Chemical Society*, 138 (2016) 6292-6297.
- [218] Q. He, J.H. Lee, D. Liu, Y. Liu, Z. Lin, Z. Xie, S. Hwang, S. Kattel, L. Song, J.G. Chen, *Advanced Functional Materials*, 30 (2020) 2000407.
- [219] J. Liu, Z. Chen, C. Liu, B. Zhang, Y. Du, C. Liu, L. Ma, S. Xi, R. Li, x. Zhao, j. Song, X. Sui, W. Yu, L. Miao, J. Jiang, M.J. Koh, K.P. Loh, *Journal of Materials Chemistry A*, 9 (2021) 11427-11432.

- [220] S. Hubner, S. Kressirer, D. Kralisch, C. Bludszuweit-Philipp, K. Lukow, I. Janich, A. Schilling, H. Hieronymus, C. Liebner, K. Jahnisch, *ChemSusChem*, 5 (2012) 279-288.
- [221] R.L. Johnson, K. Schmidt-Rohr, *Journal of Magnetic Resonance*, 239 (2014) 44-49.
- [222] B.M. Fung, A.K. Khitrin, K. Ermolaev, *J Magn Reson*, 142 (2000) 97-101.
- [223] A. Zimina, K. Dardenne, M.A. Denecke, D.E. Doronkin, E. Huttel, H. Lichtenberg, S. Mangold, T. Pruessmann, J. Rothe, T. Spangenberg, R. Steininger, T. Vitova, H. Geckeis, J.D. Grunwaldt, *Review of Scientific Instruments*, 88 (2017) 113113.
- [224] B. Ravel, M. Newville, *Journal of Synchrotron Radiation*, 12 (2005) 537-541.
- [225] J.H. Scofield, *Journal of Electron Spectroscopy and Related Phenomena*, 8 (1976) 129-137.
- [226] J.F. Georg Kresse, *Computational Materials Science*, 6 (1996) 15-50.
- [227] J.F. Georg Kresse, *Physical Review B*, 54 (1996) 11169-11186.
- [228] K.B. John P. Perdew, Matthias Ernzerhof, *Physical Review Letters*, 77 (1996) 3865-3868.
- [229] M. Ernzerhof, G.E. Scuseria, *The Journal of Chemical Physics*, 110 (1999) 5029-5036.
- [230] P.E. Blochl, *Physical review B*, 50 (1994) 17953-17979.
- [231] D.J. Georg Kresse, *Physical Review B*, 59 (1999) 1758-1775.
- [232] S. Grimme, J. Antony, S. Ehrlich, H. Krieg, *The Journal of Chemical Physics*, 132 (2010) 154104.
- [233] J. Wirth, R. Neumann, M. Antonietti, P. Saalfrank, *Physical Chemistry Chemical Physics*, 16 (2014) 15917-15926.
- [234] P. Niu, L.C. Yin, Y.Q. Yang, G. Liu, H.M. Cheng, *Advanced Materials*, 26 (2014) 8046-8052.
- [235] S.P. Sun, S. Gu, J.H. Sun, F.F. Xia, G.H. Chen, *Journal of Alloys and Compounds*, 735 (2018) 131-139.
- [236] H. Zhang, X. Zuo, H. Tang, G. Li, Z. Zhou, *Physical Chemistry Chemical Physics*, 17 (2015) 6280-6288.
- [237] F.H. Tian, X. Wang, W. Zhao, L. Zhao, T. Chu, S. Yu, *Surface Science*, 616 (2013) 76-84.
- [238] Y.F. Li, U. Aschauer, J. Chen, A. Selloni, *Accounts of Chemical Research*, 47 (2014) 3361-3368.
- [239] A. Jain, S.P. Ong, G. Hautier, W. Chen, W.D. Richards, S. Dacek, S. Cholia, D. Gunter, D. Skinner, G. Ceder, K.A. Persson, *APL Materials*, 1 (2013) 011002.
- [240] M. Yu, D.R. Trinkle, *The Journal of Chemical Physics*, 134 (2011) 064111.
- [241] W. Tang, E. Sanville, G. Henkelman, *Journal of Physics: Condensed Matter*, 21 (2009) 084204.
- [242] H.Y. Zhuo, X. Zhang, J.X. Liang, Q. Yu, H. Xiao, J. Li, *Chemical Reviews*, 120 (2020) 12315-12341.
- [243] M. Groenewolt, M. Antonietti, *Advanced Materials*, 17 (2005) 1789-1792.
- [244] Z. Zhou, J. Wang, J. Yu, Y. Shen, Y. Li, A. Liu, S. Liu, Y. Zhang, *Journal of the American Chemical Society*, 137 (2015) 2179-2182.

- [245] R.C. Dante, F.M. Sánchez-Arévalo, P. Chamorro-Posada, J. Vázquez-Cabo, L. Huerta, L. Lartundo-Rojas, J. Santoyo-Salazar, O. Solorza-Feria, *Journal of Solid State Chemistry*, 226 (2015) 170-178.
- [246] S. Guo, Z. Deng, M. Li, B. Jiang, C. Tian, Q. Pan, H. Fu, *Angewandte Chemie International Edition*, 55 (2016) 1830-1834.
- [247] P. Xia, B. Zhu, J. Yu, S. Cao, M. Jaroniec, *Journal of Materials Chemistry A*, 5 (2017) 3230-3238.
- [248] W. Wang, J.C. Yu, Z. Shen, D.K. Chan, T. Gu, *Chemical Communications (Camb)*, 50 (2014) 10148-10150.
- [249] J. Huang, P. Meng, X. Liu, *Journal of Alloys and Compounds*, 805 (2019) 654-662.
- [250] E. Alwin, K. Koci, R. Wojcieszak, M. Zielinski, M. Edelmanna, M. Pietrowski, *Materials (Basel)*, 13 (2020) 2756.
- [251] C. Ye, J.-X. Li, Z.-J. Li, X.-B. Li, X.-B. Fan, L.-P. Zhang, B. Chen, C.-H. Tung, L.-Z. Wu, *ACS Catalysis*, 5 (2015) 6973-6979.
- [252] L. Ye, D. Wu, K.H. Chu, B. Wang, H. Xie, H.Y. Yip, P.K. Wong, *Chemical Engineering Journal*, 304 (2016) 376-383.
- [253] D. Foy, G. Demazeau, P. Florian, D. Massiot, C. Labrugère, G. Goglio, *Journal of Solid State Chemistry*, 182 (2009) 165-171.
- [254] Y. Cui, J. Zhang, G. Zhang, J. Huang, P. Liu, M. Antonietti, X. Wang, *Journal of Materials Chemistry*, 21 (2011) 13032-13039.
- [255] X. Li, I.V. Sergeev, F. Aussenac, A.F. Masters, T. Maschmeyer, J.M. Hook, *Angewandte Chemie International Edition*, 57 (2018) 6848-6852.
- [256] B. Jurgens, E. Irran, J. Senker, P. Kroll, H. Muller, W. Schnick, *Journal of the American Chemical Society*, 125 (2003) 10288-10300.
- [257] J. Xiao, J. Rabeah, J. Yang, Y. Xie, H. Cao, A. Brückner, *ACS Catalysis*, 7 (2017) 6198-6206.
- [258] L. Yang, J. Huang, L. Shi, L. Cao, Q. Yu, Y. Jie, J. Fei, H. Ouyang, J. Ye, *Applied Catalysis B: Environmental*, 204 (2017) 335-345.
- [259] G. Zhang, G. Li, T. Heil, S. Zafeiratos, F. Lai, A. Savateev, M. Antonietti, X. Wang, *Angewandte Chemie International Edition*, 58 (2019) 3433-3437.
- [260] L. Zhang, J. Ran, S.Z. Qiao, M. Jaroniec, *Chemical Society Reviews*, 48 (2019) 5184-5206.
- [261] R. Naumann d'Alnoncourt, M. Friedrich, E. Kunkes, D. Rosenthal, F. Girgsdies, B. Zhang, L. Shao, M. Schuster, M. Behrens, R. Schlögl, *Journal of Catalysis*, 317 (2014) 220-228.
- [262] P. Kast, M. Friedrich, D. Teschner, F. Girgsdies, T. Lunkenbein, R. Naumann d'Alnoncourt, M. Behrens, R. Schlögl, *Applied Catalysis A: General*, 502 (2015) 8-17.
- [263] J. Zhang, M. Zhang, L. Lin, X. Wang, *Angewandte Chemie International Edition*, 54 (2015) 6297-6301.

- [264] J. Kröger, A. Jiménez-Solano, G. Savasci, V.W.h. Lau, V. Duppel, I. Moudrakovski, K. Küster, T. Scholz, A. Gouder, M.L. Schreiber, F. Podjaski, C. Ochsenfeld, B.V. Lotsch, *Advanced Functional Materials*, 31 (2021) 2102468.
- [265] X. Zhang, P. Ma, C. Wang, L. Gan, X. Chen, P. Zhang, Y. Wang, H. Li, L. Wang, X. Zhou, K. Zheng, *Energy & Environmental Science*, 15 (2022) 830-842.
- [266] M. Wagner, B. Meyer, M. Setvin, M. Schmid, U. Diebold, *Nature*, 592 (2021) 722-725.
- [267] J. Saavedra, H.A. Doan, C.J. Pursell, L.C. Grabow, B.D. Chandler, *Science*, 345 (2014) 1599-1602.
- [268] S. Cao, Y. Zhao, S. Lee, S. Yang, J. Liu, G. Giannakakis, M. Li, M. Ouyang, D. Wang, E.C.H. Sykes, M. Flytzani-Stephanopoulos, *Science Advances*, 6 (2020) eaba3809.
- [269] C.D. Craver, C. Society, *The Coblentz Society Desk Book of Infrared Spectra*, The Society, 1982.

Appendix

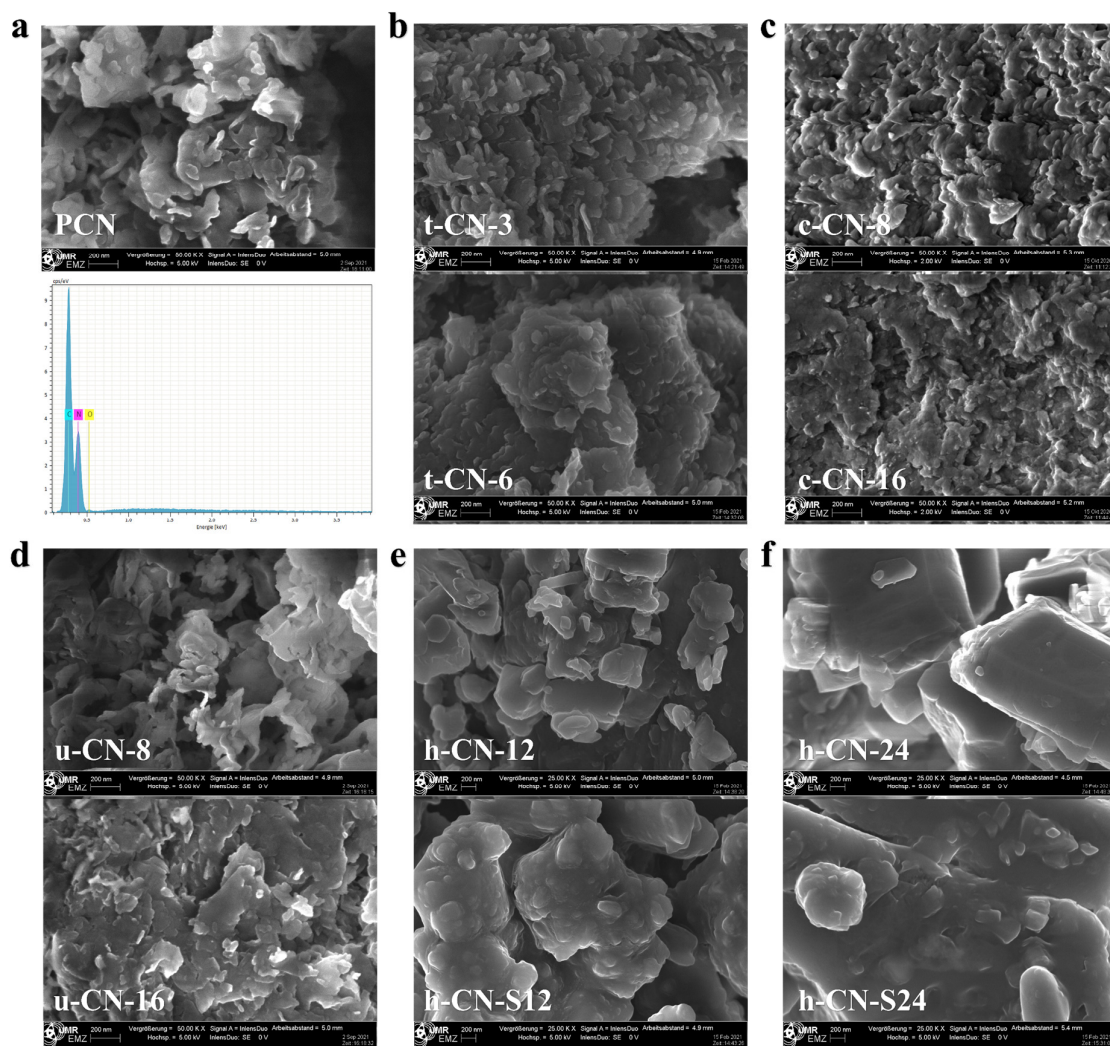


Figure A. 1. SEM images of PCN(a), t-CN (b), c-CN (c), u-CN (d) and h-CN (e, f). Scale bar, 200 nm.

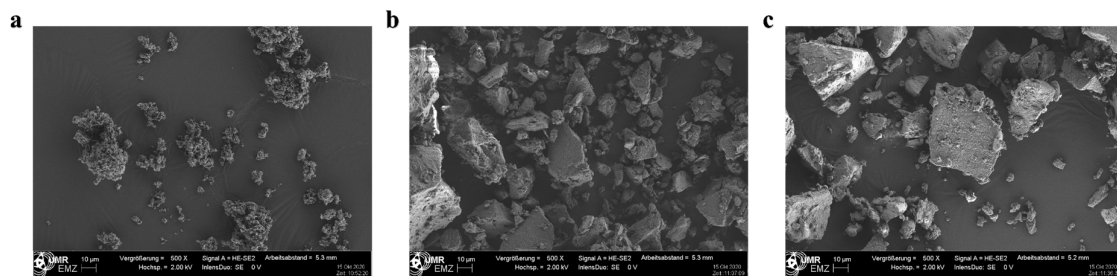


Figure A. 2. SEM images of bulk PCN (a), c-CN-8 (b) and c-CN-16 (c). Scale bar, 10 μ m.

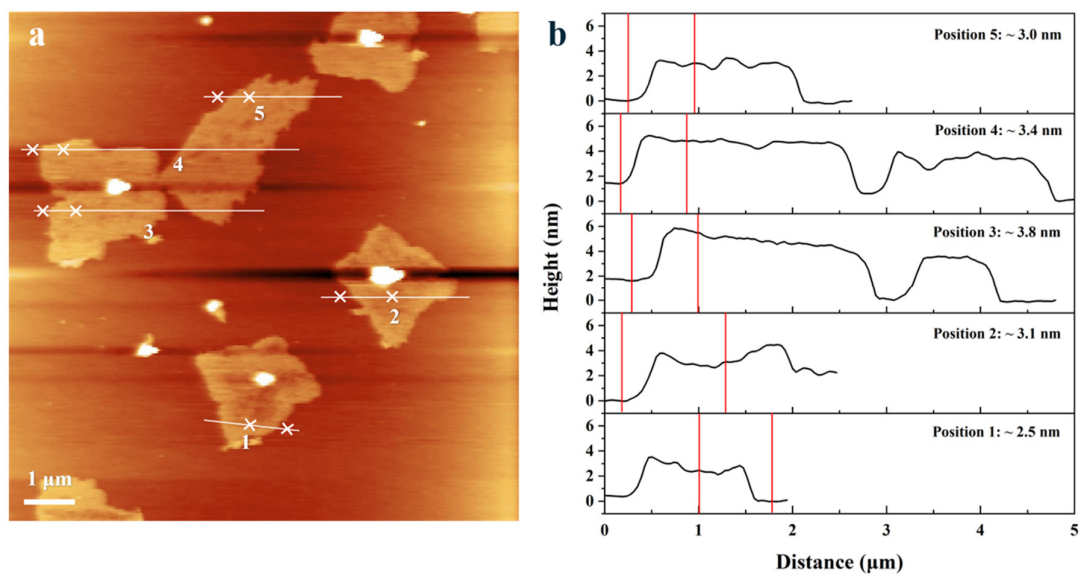


Figure A. 3. AFM image and the corresponding height profile of t-CN-3.

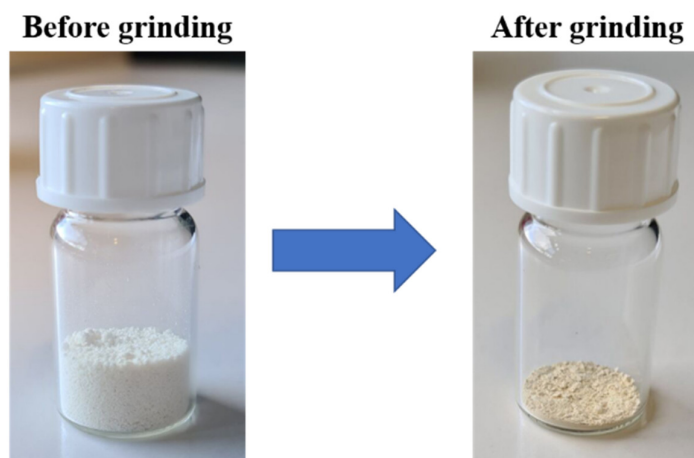


Figure A. 4. Sample picture of t-CN-3 before and after grinding.

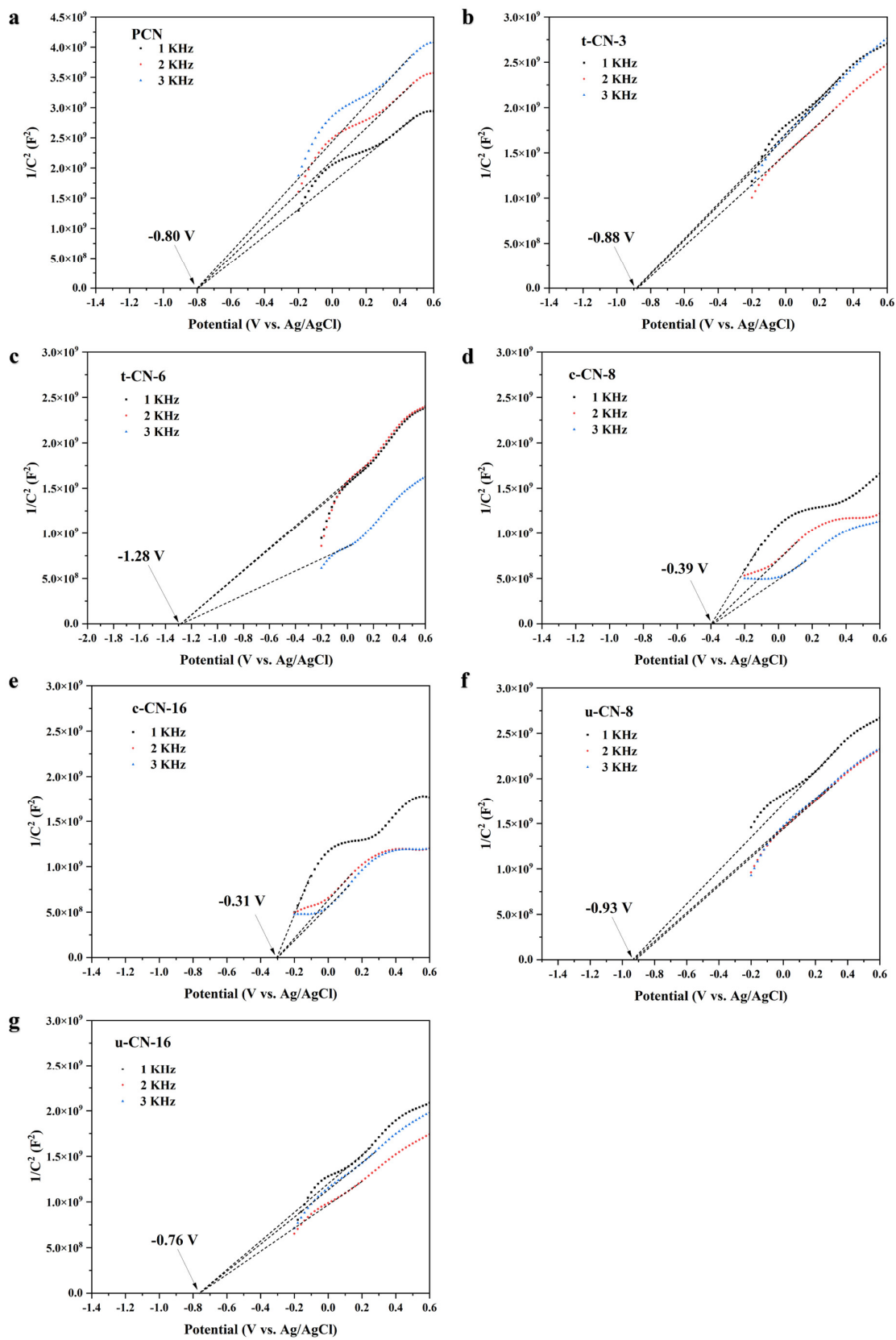
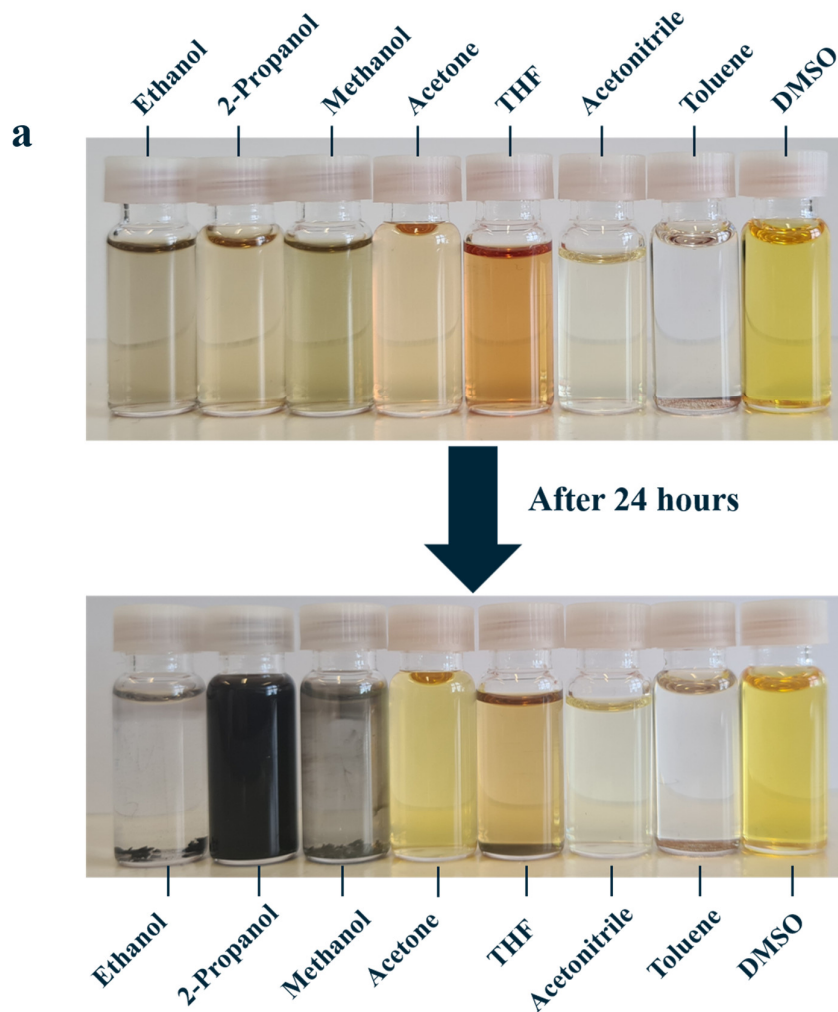


Figure A. 5. Mott-Schottky plots of differently exfoliated PCN.



b

Solvent	Boiling point (°C)	Relative polarity*
Ethanol	78.3	0.654
2-Propanol	82.3	0.546
Methanol	64.7	0.762
Acetone	56.3	0.355
THF	66	0.207
Acetonitrile	81.6	0.460
Toluene	110.6	0.099
DMSO	189.0	0.444

*The values for relative polarity are normalized from measurements of solvent shifts of absorption spectra and were extracted from Christian Reichardt, Solvents and Solvent Effects in Organic Chemistry, Wiley-VCH Publishers, 3rd ed., 2003.

Figure A. 6. (a) Color changes of $\text{Pd}(\text{TFA})_2$ before and after 24 h of standing in various organic solvents. (b) Boiling points and relative polarity of various organic solvents.

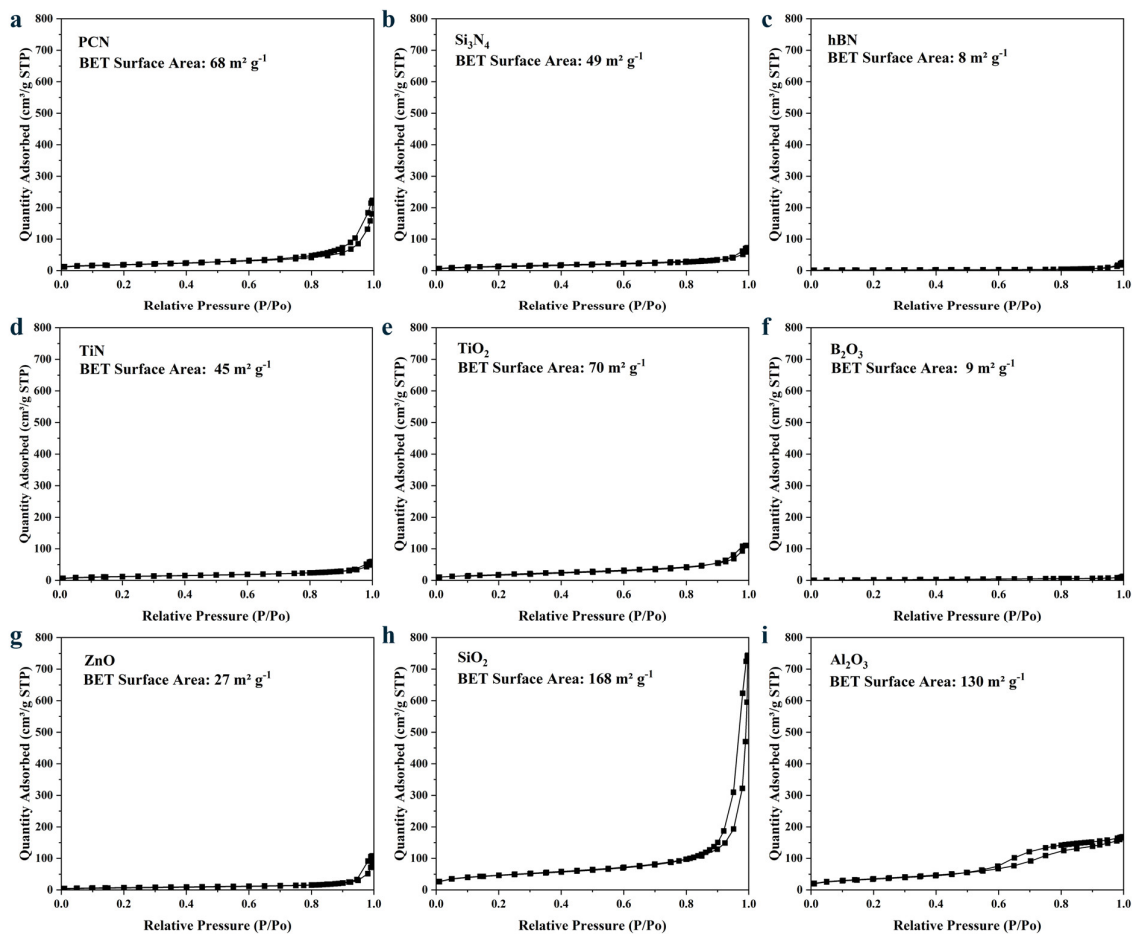


Figure A. 7. Nitrogen adsorption-desorption isotherms of nitride and oxide supports.

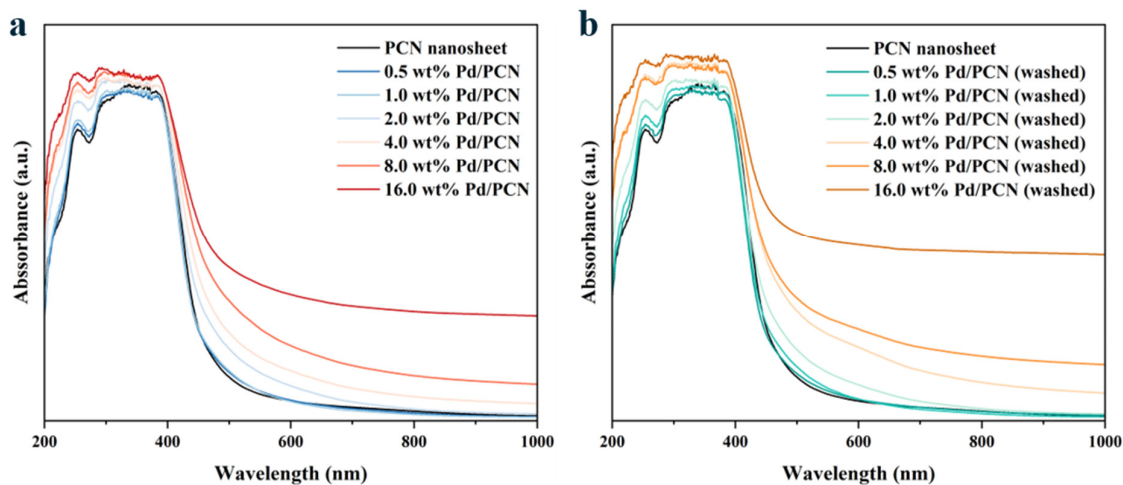


Figure A. 8. UV-Vis absorption spectra of Pd/PCN samples before (a) and after (b) washing.

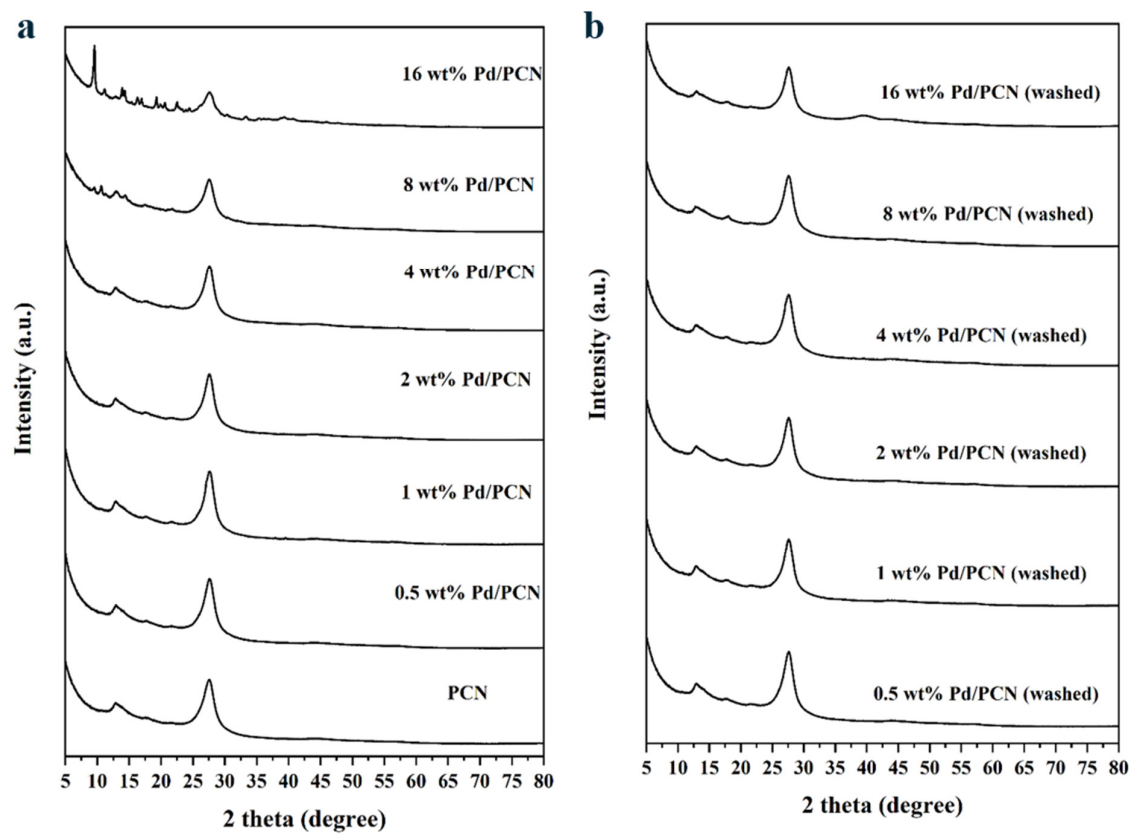


Figure A. 9. XRD patterns of Pd/PCN samples before and after washing.

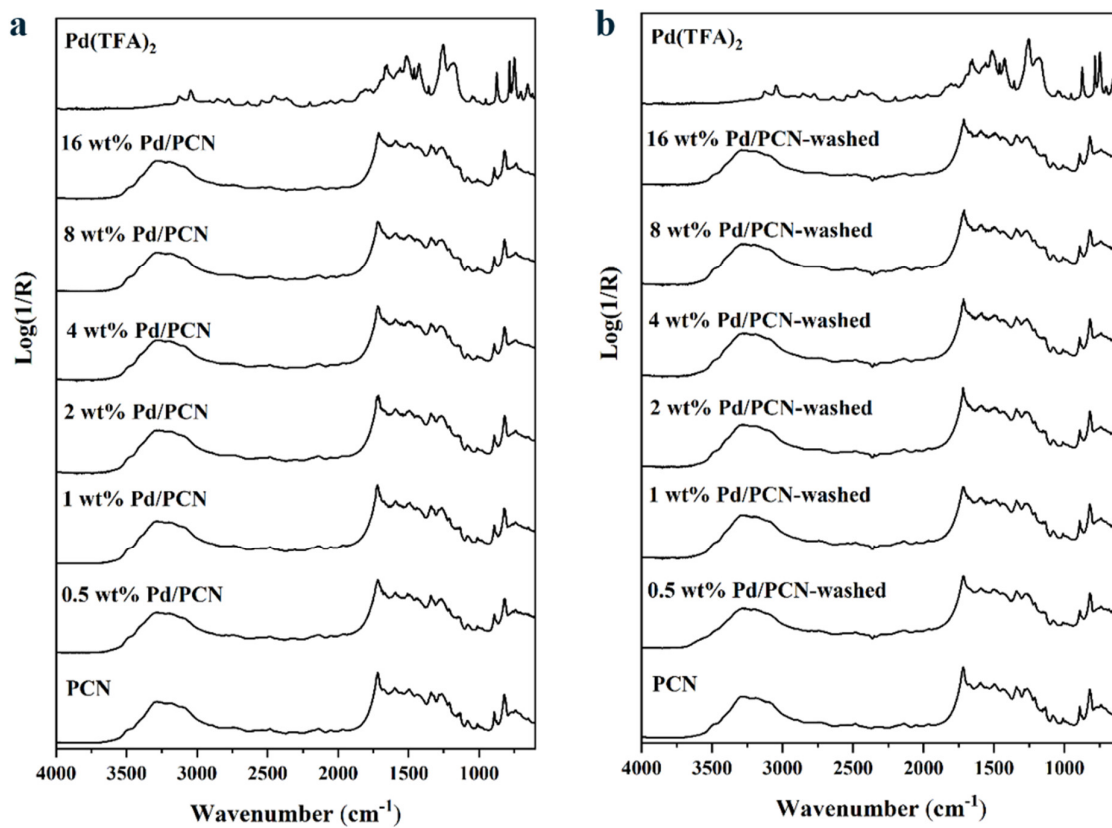


Figure A. 10. DRIFTS spectra of Pd/PCN samples before and after washing.

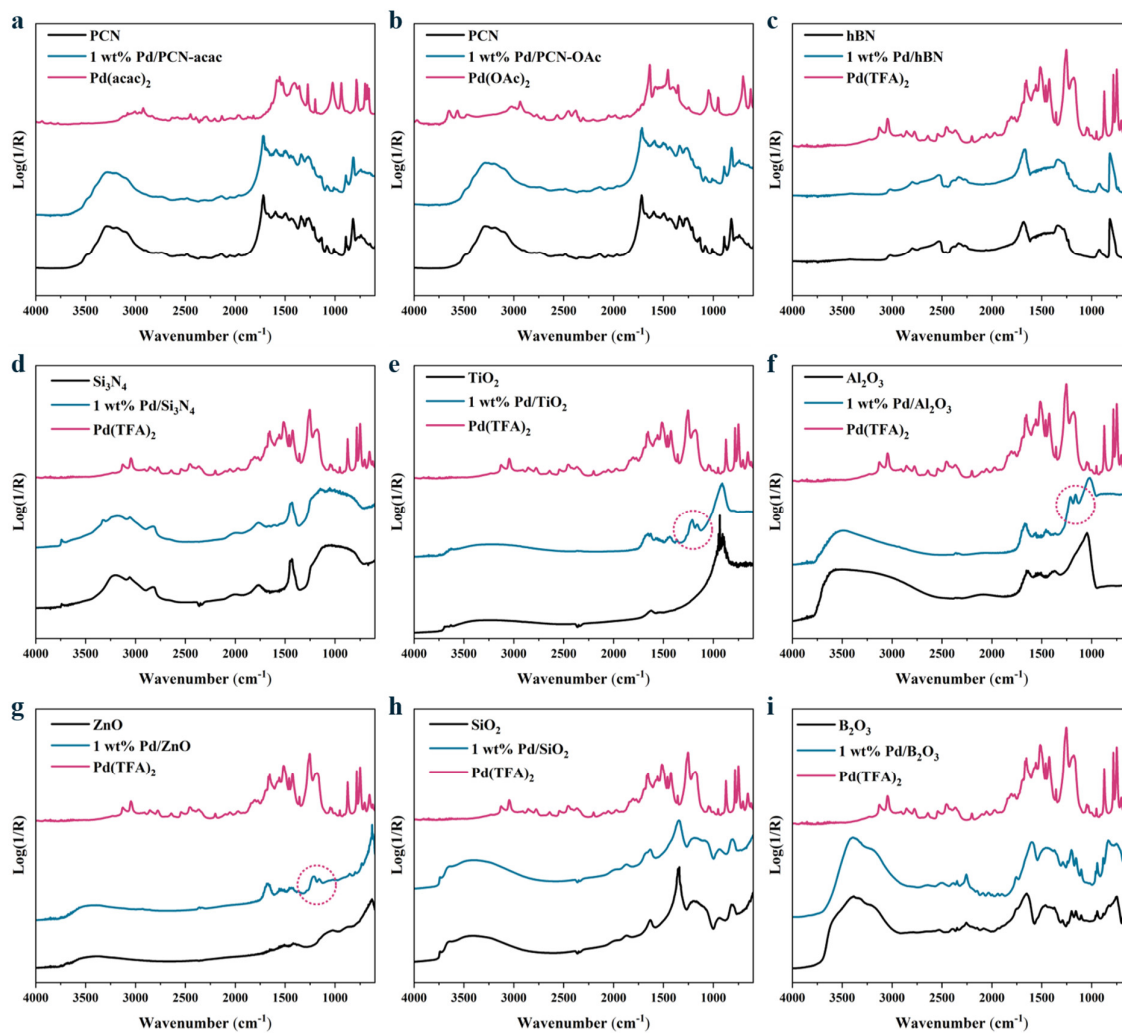


Figure A. 11. DRIFTS spectra of various Pd samples and their corresponding pure support.

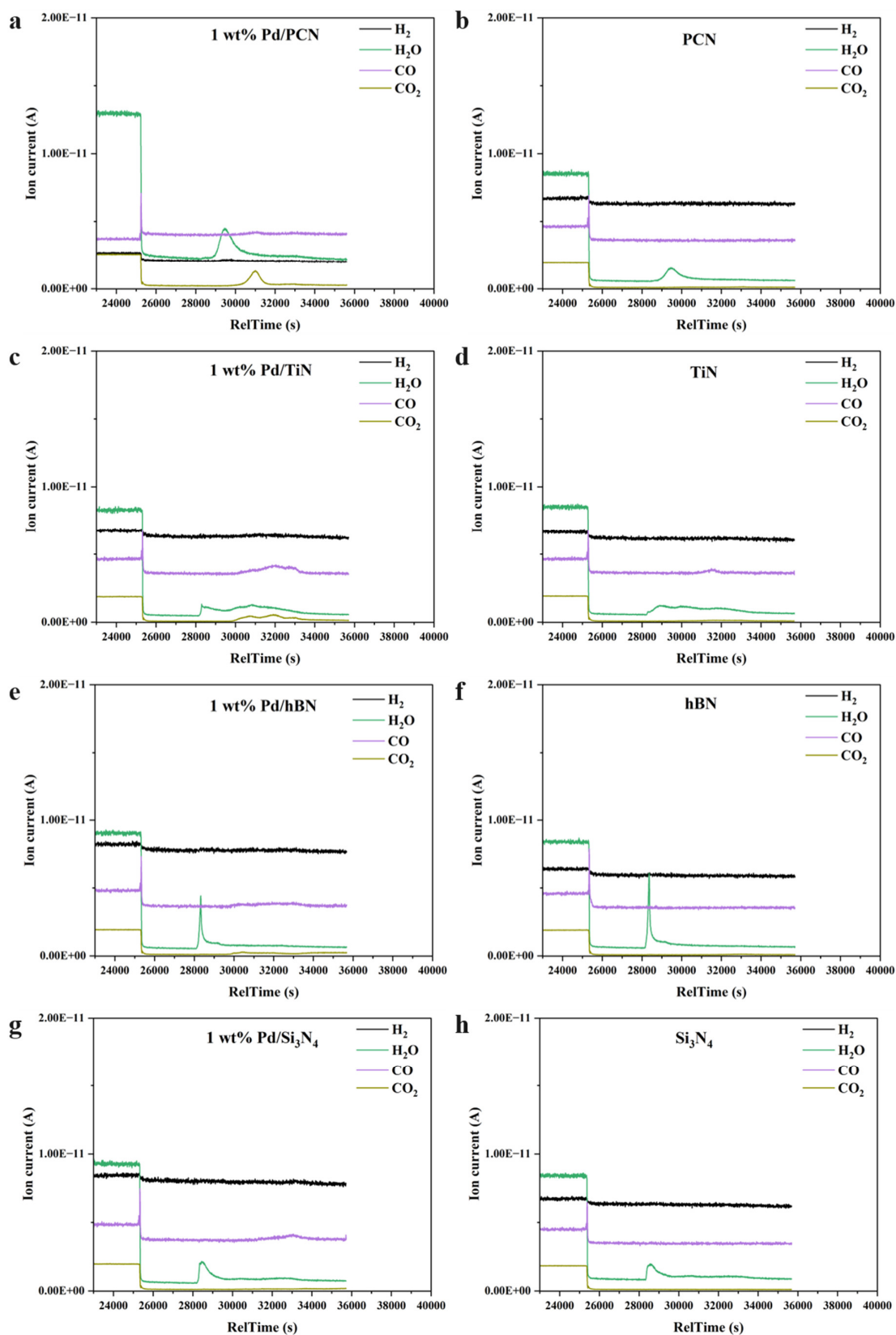


Figure A. 12. Corresponding QMS response during TPDE measurements of different Pd/nitride samples (left) and pure nitride supports (right).

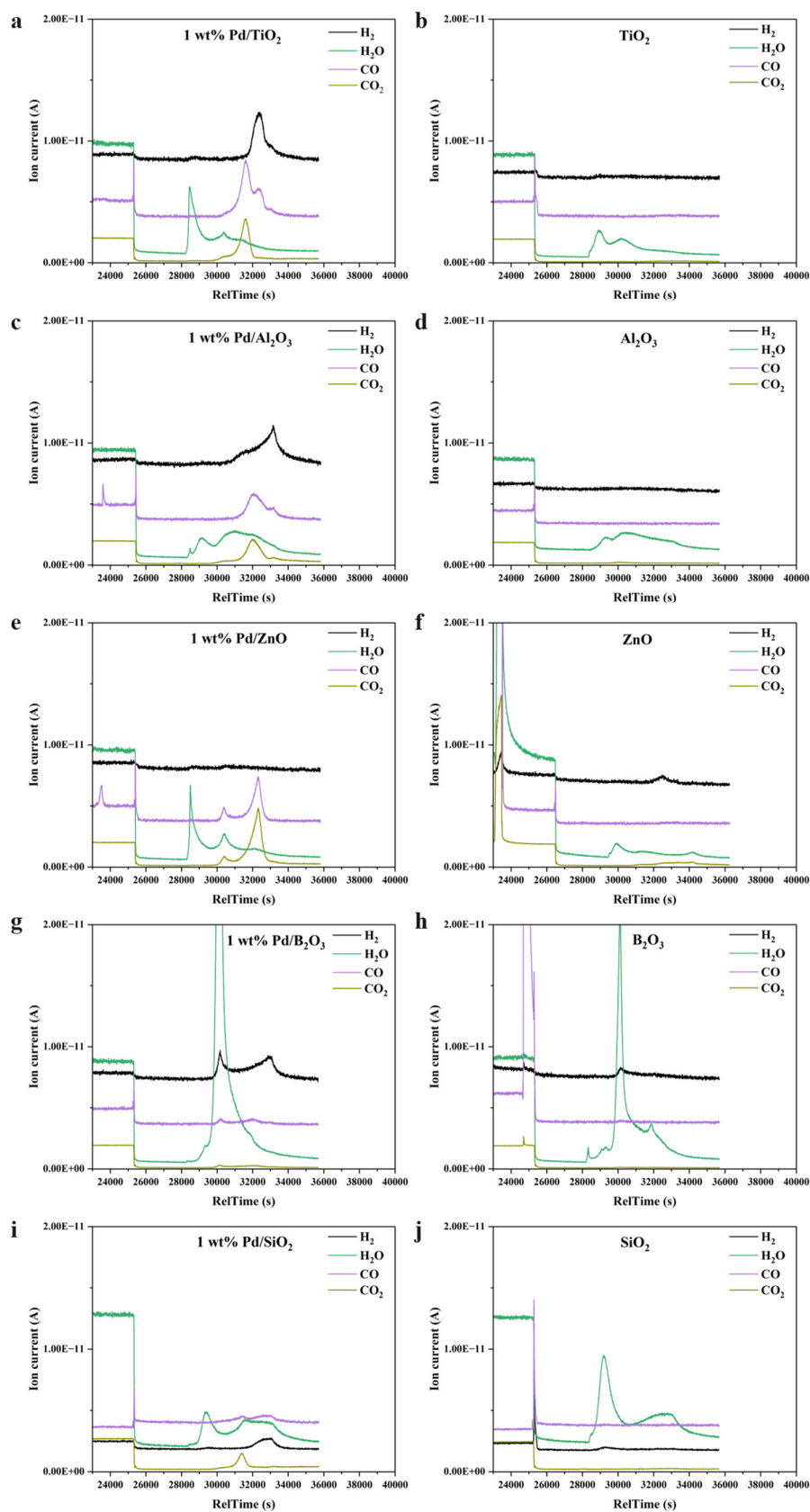


Figure A. 13. Corresponding QMS response during TPDE measurements of different Pd/oxide samples (left) and pure oxide supports (right).

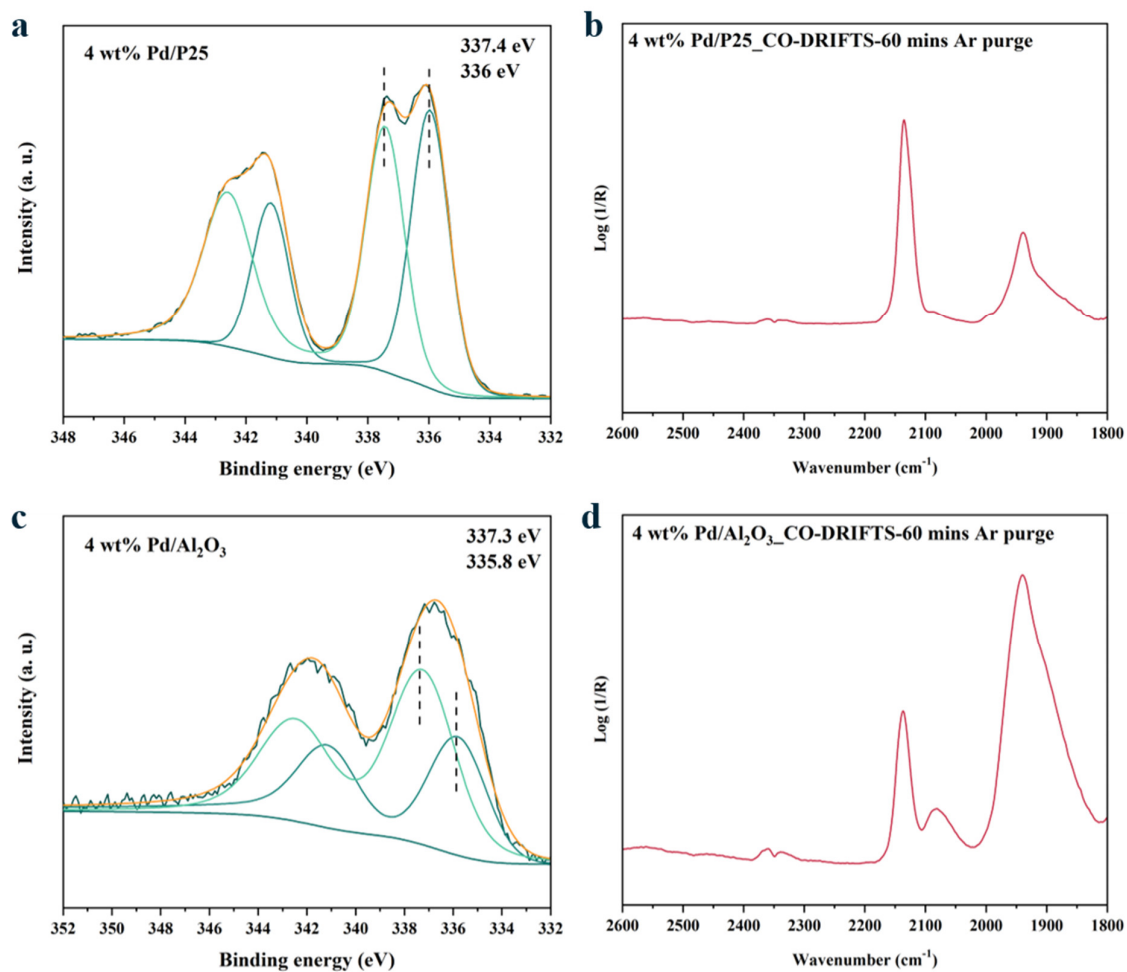


Figure A. 14. Pd 3d photoemission spectra and CO-DRIFTS spectra of 4 wt% Pd/TiO₂ (a and c) and 4 wt% Pd/Al₂O₃ (c and d).

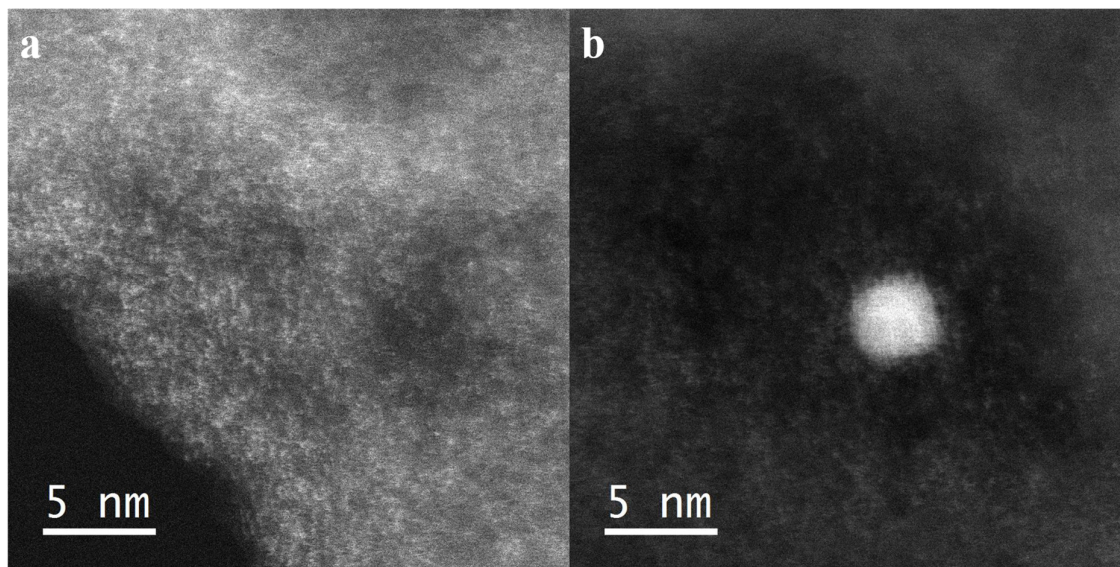


Figure A. 15. Representative HAADF-STEM images of the washed 2 wt% Pd/PCN sample.

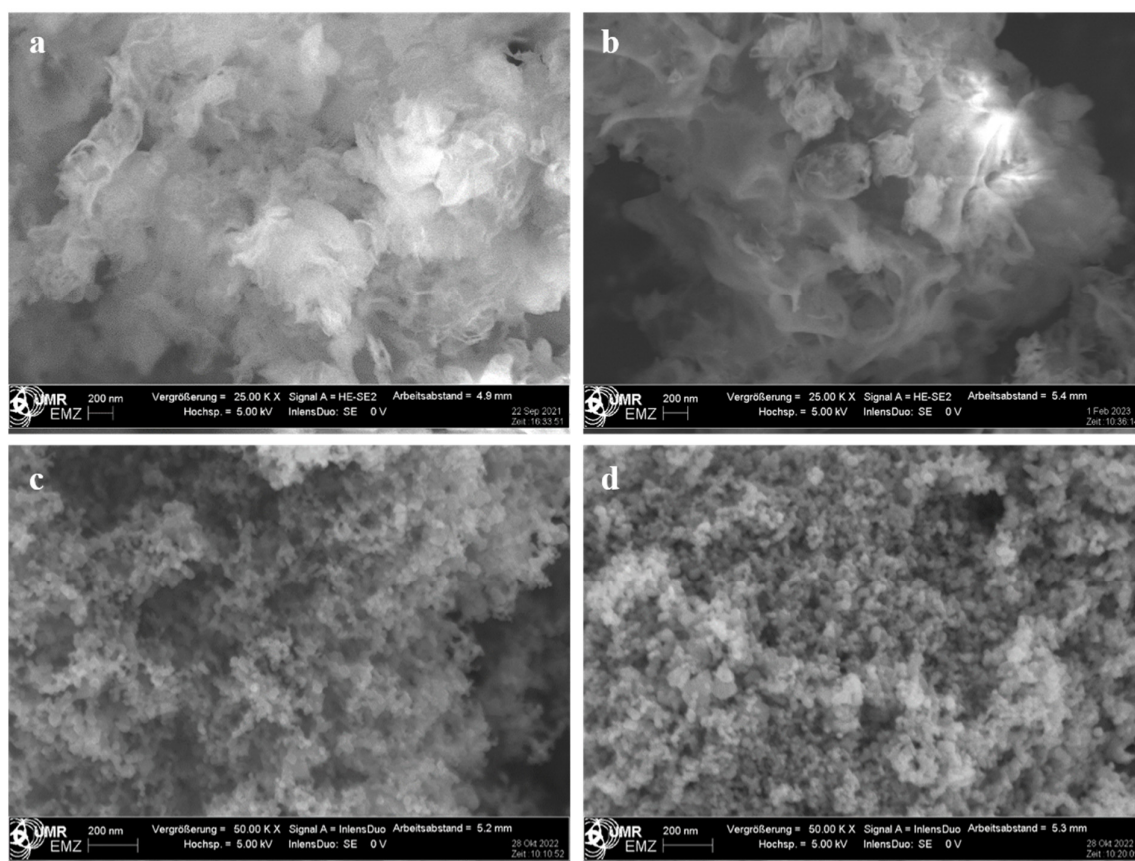


Figure A. 16. SEM images of (a) PCN, (b) 1 wt% Pd/PCN, (c) TiO_2 and (d) 1 wt% Pd/ TiO_2 .

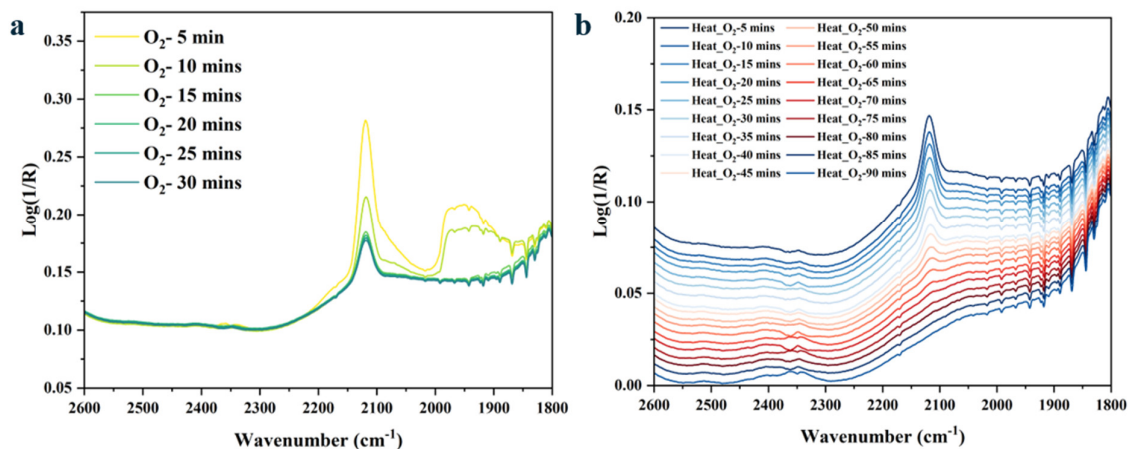


Figure A. 17. DRIFTS spectra of CO desorbed from Pd/Al₂O₃ upon O₂ exposure at 25 °C (a) and during heating process to 200 °C (b).

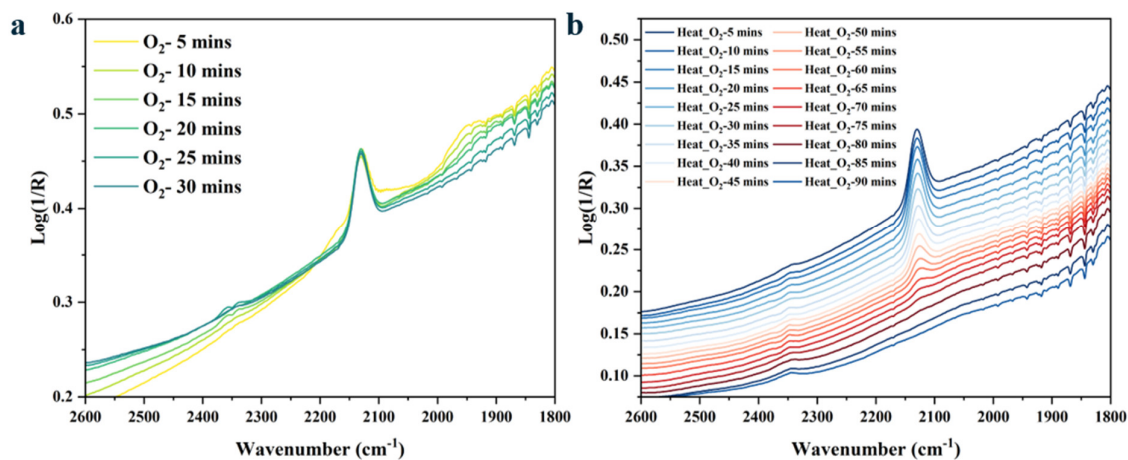


Figure A. 18. DRIFTS spectra of CO desorbed from Pd/ZnO upon O₂ exposure at 25 °C (a) and during heating process to 200 °C (b).

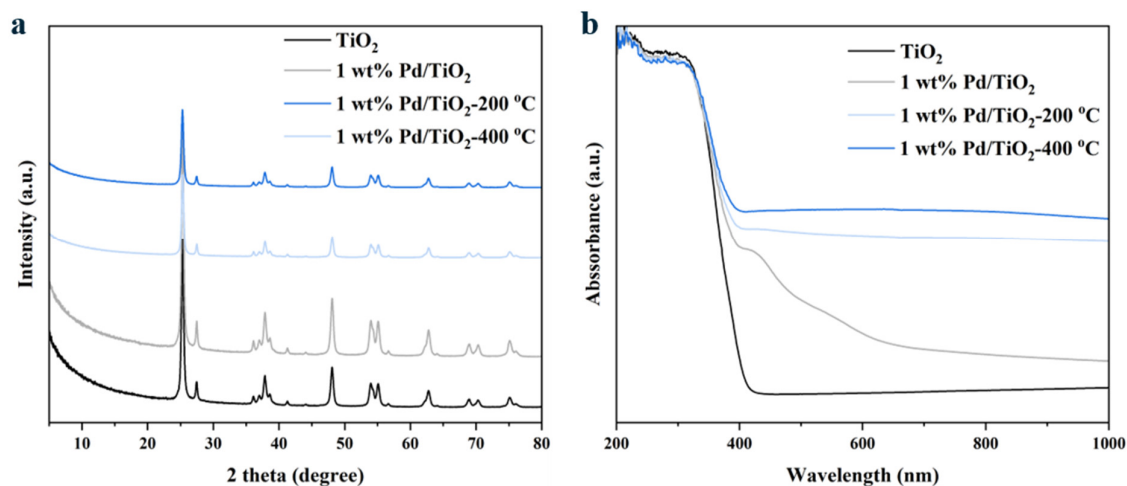


Figure A. 19. (a) XRD patterns and (b) UV-Vis DRS spectra of 1 wt% Pd/ TiO_2 -200 °C and 1 wt% Pd/ TiO_2 -400 °C.

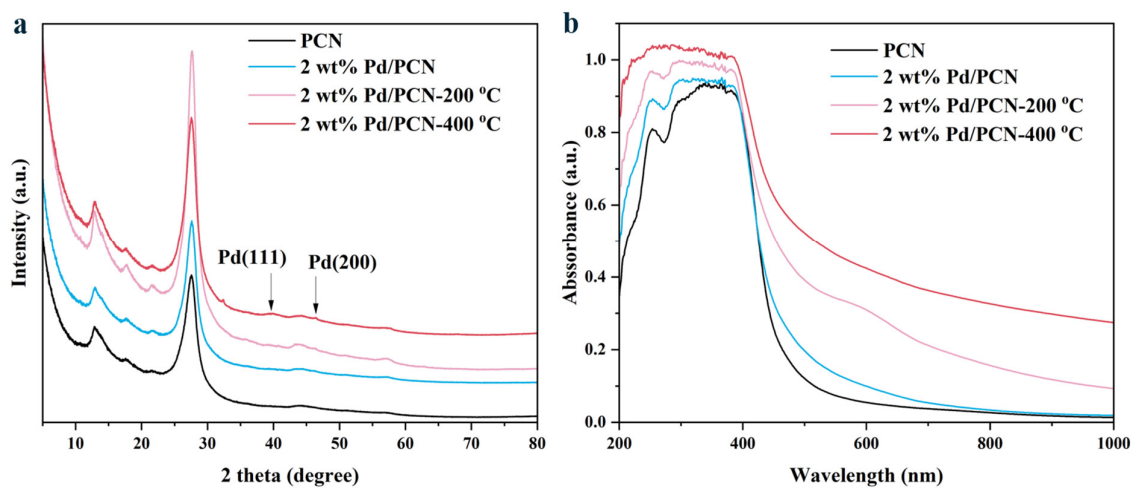


Figure A. 20. (a) XRD patterns and (b) UV-Vis DRS spectra of 2 wt% Pd/PCN-200 °C and 2 wt% Pd/PCN-400 °C.

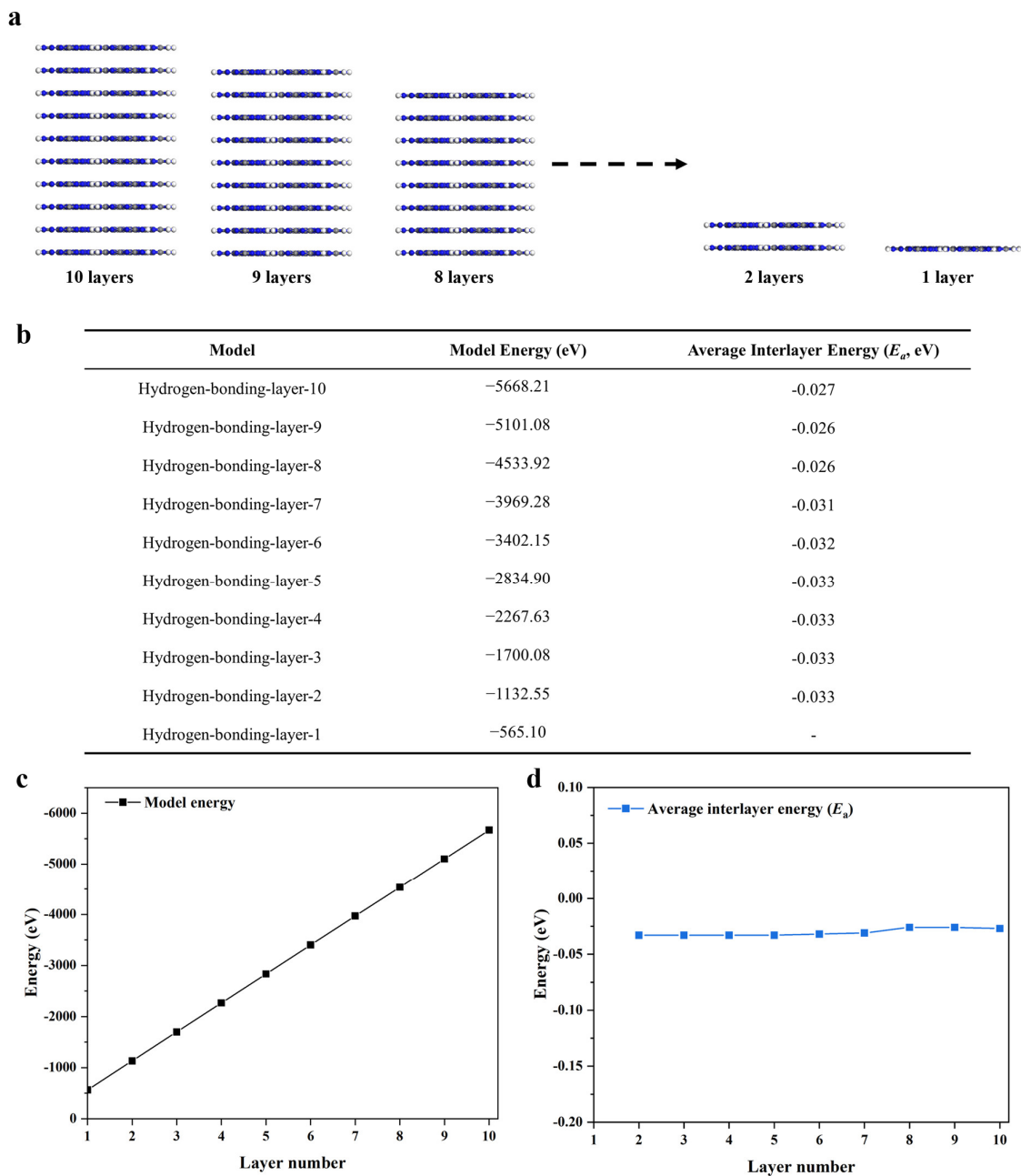


Figure A. 21. (a) Layer-by-layer exfoliation diagram of the hydrogen-bonded PCN model. (b) the calculated model energy and average interlayer energy. (c) optimized model energy and (d) average interlayer energy over different layer number.

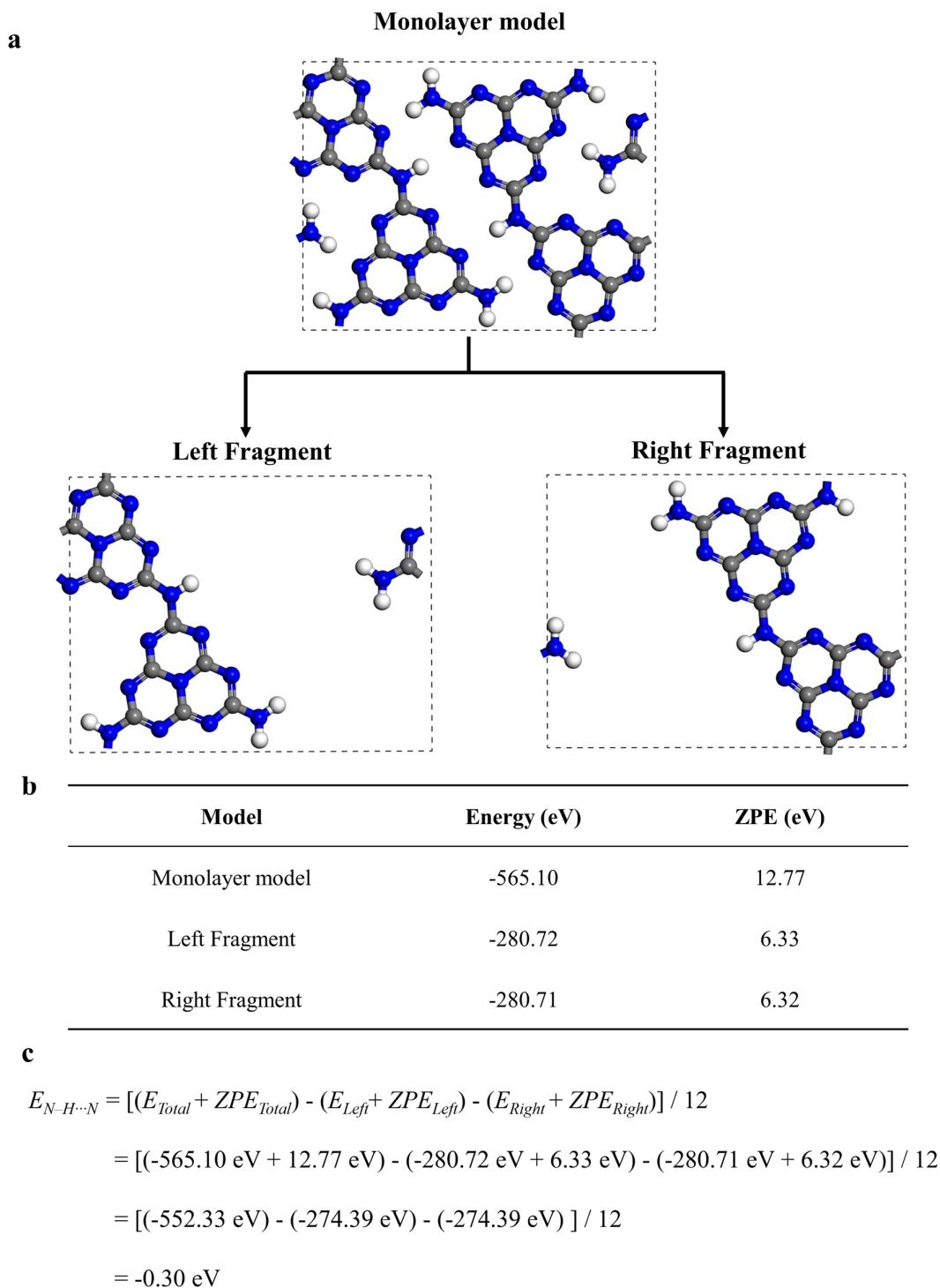


Figure A. 22. (a) Schematic illustration of the process of hydrogen bond calculation. (b) the calculated model energy and zero-point energy (ZPE). (c) hydrogen bond energy calculation process. The energy of in-plane hydrogen bonds (12 H atoms in one unit) for the monolayer model, $E_{N-H\cdots N}$, was determined by the above equation. Where E_{Total} is the energy of the monolayer model, E_{Left} is the corresponding energy of the left fragment of the monolayer model, and E_{Right} is the corresponding energy of the right fragment of the monolayer model. The zero-point energies (ZPE) were determined independently for each model to correct the lowest energy state.

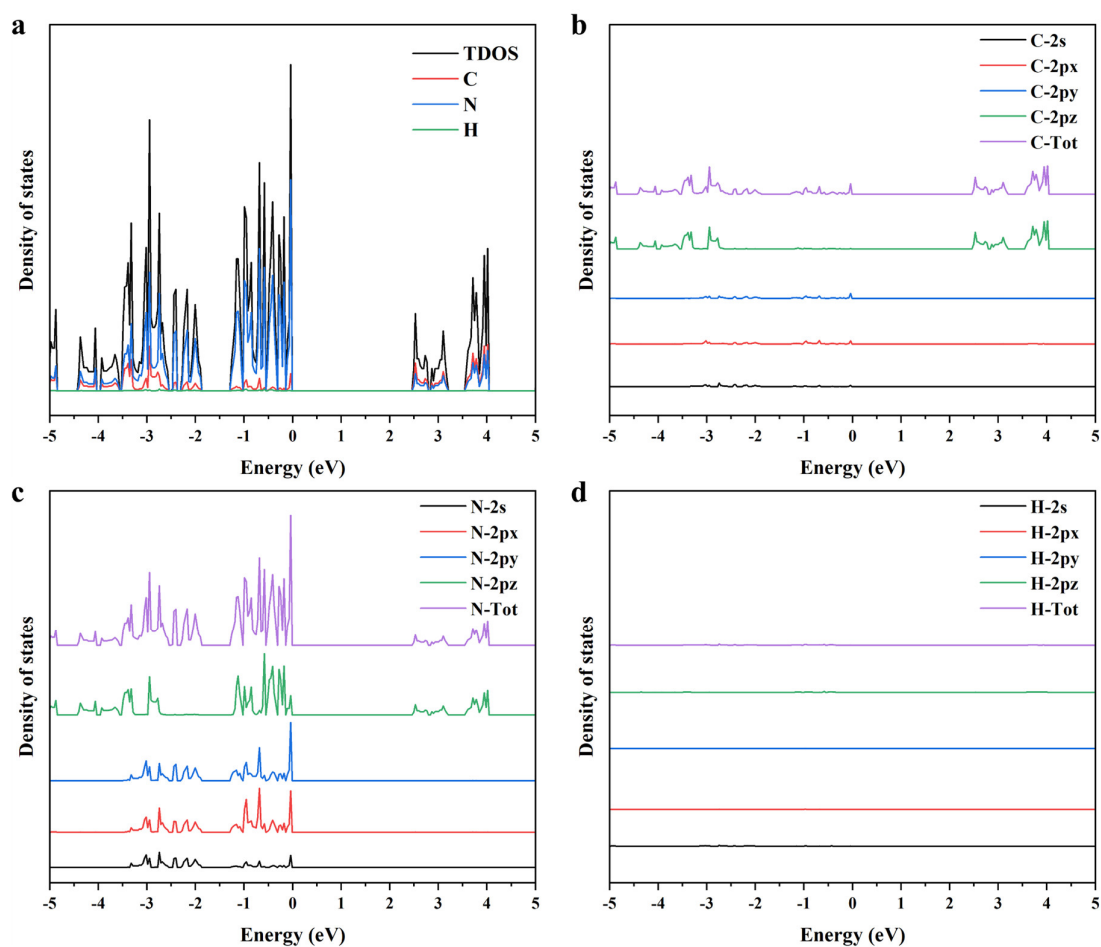


Figure A. 23. Projected density of states (PDOS) of the monolayer hydrogen-bonded PCN.

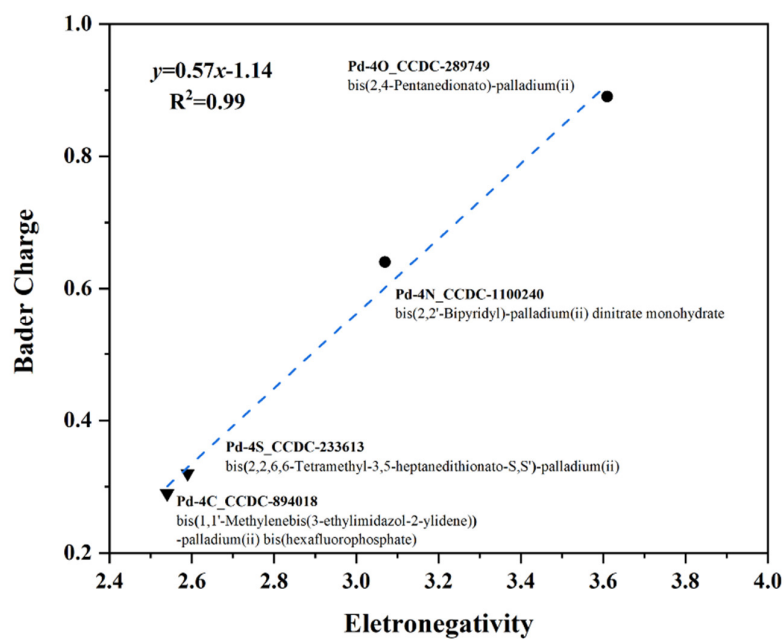


Figure A. 24. Bader charge for different Pd²⁺ models, plotted against the electronegativity of different type of bonding atom (C, S, N, and O). All models are obtained from the Cambridge Crystallographic Data Centre (CCDC).

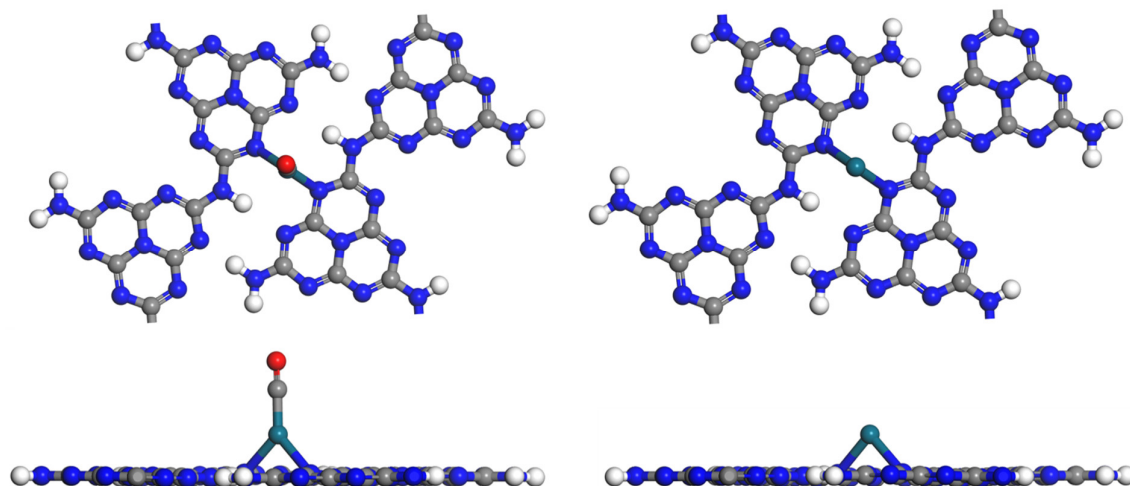


Figure A. 25. CO adsorbed (left) on $(\text{PdN}_2)_{\text{surface}}$ and $(\text{PdN}_2)_{\text{surface}}$ (right) with top view (top) and side view (bottom). Pd, C, N, O, H atoms are dark green, grey, blue, red and white spheres, respectively.

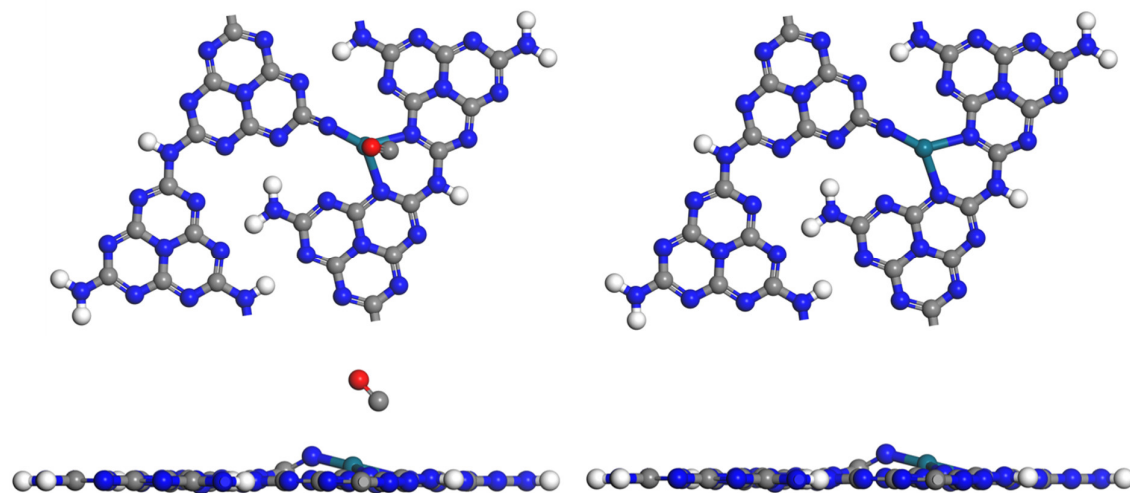


Figure A. 26. CO adsorbed (left) on $(\text{PdN}_3)_{\text{surface}}$ and $(\text{PdN}_3)_{\text{surface}}$ (right) with top view (top) and side view (bottom). Pd, C, N, O, H atoms are dark green, grey, blue, red and white spheres, respectively.

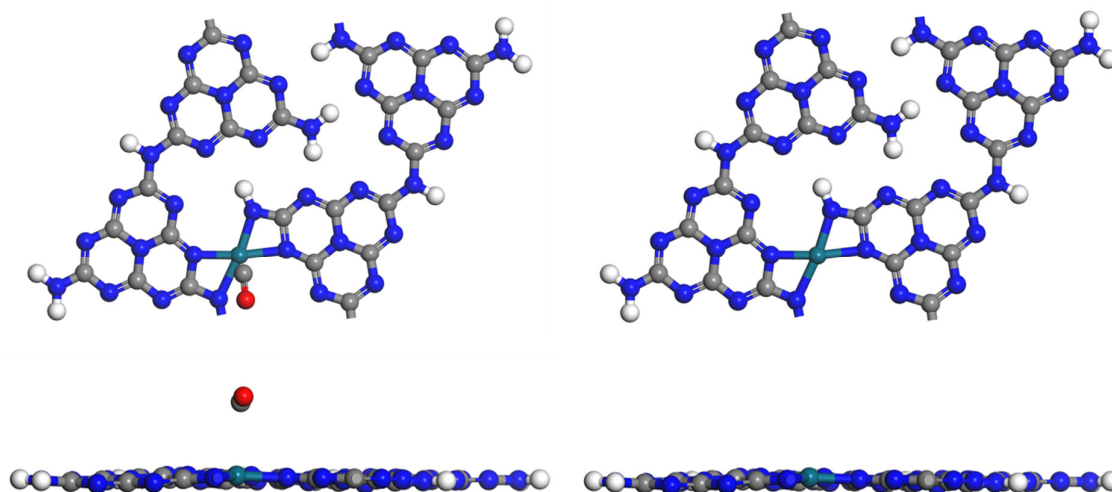


Figure A. 27. CO adsorbed (left) on $(\text{PdN}_4)_{\text{surface}}$ and $(\text{PdN}_4)_{\text{surface}}$ (right) with top view (top) and side view (bottom). Pd, C, N, O, H atoms are dark green, grey, blue, red and white spheres, respectively.

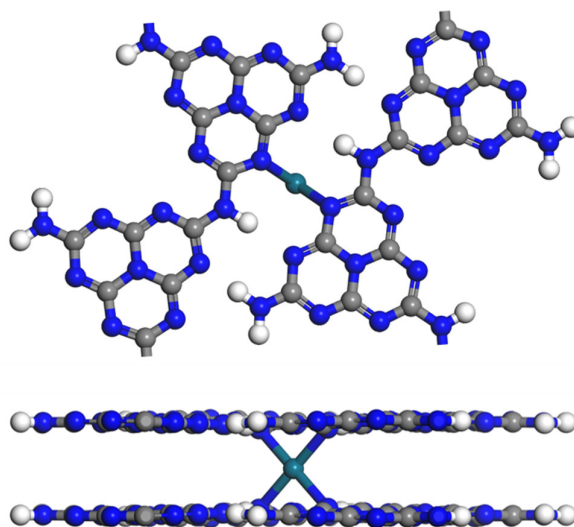


Figure A. 28. $(\text{PdN}_4)_{\text{interlayer}}$ with top view (top) and side view (bottom). Pd, C, N, H atoms are dark green, grey, blue and white spheres, respectively. The Bader charge of the model is $+0.51e$, and the calculated oxidation state is $+1.84$. CO vibrational frequency analysis was not performed in this model because the CO molecules would interact with the PCN support rather than with the palladium atoms beneath the surface layer.

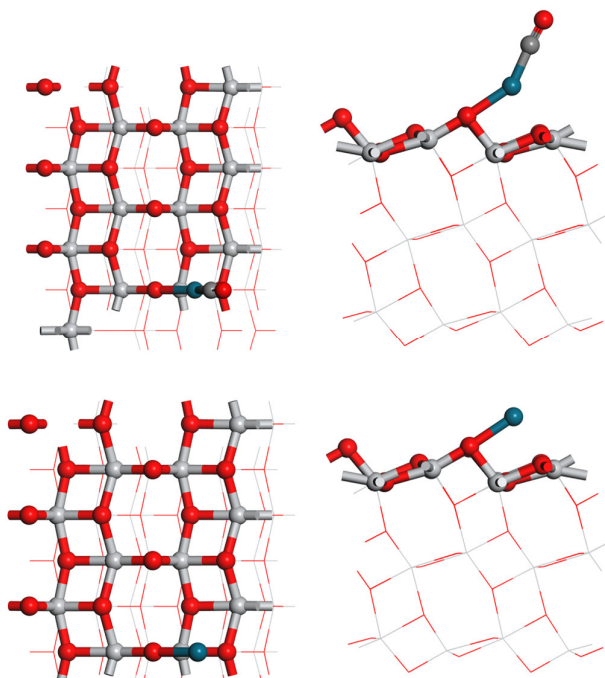


Figure A. 29. CO adsorbed (top) on Pd (Atop) model and Pd (Atop) model (bottom) with top view (left) and side view (right). Pd, Ti, C, O atoms are dark green, light-grey, grey, and red spheres, respectively.

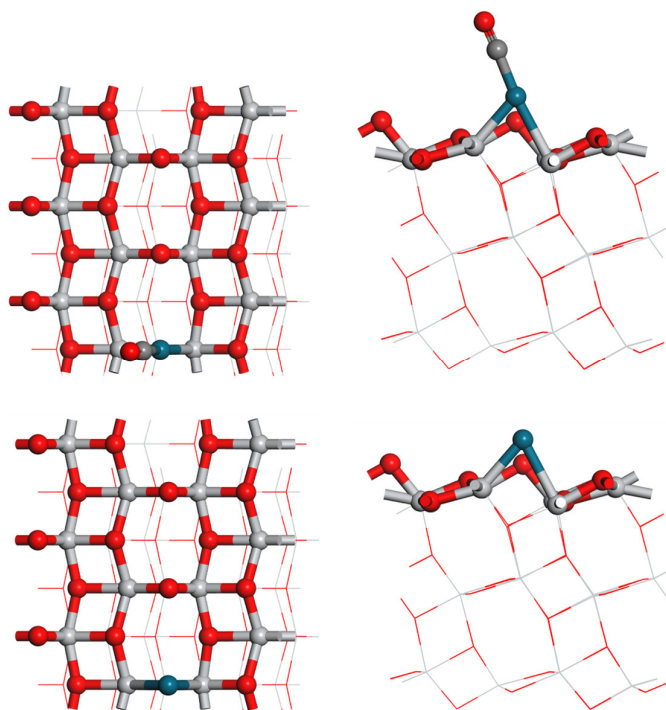


Figure A. 30. CO adsorbed (top) on Pd(O_{2c} -vacancy) model and Pd(O_{2c} -vacancy) model (bottom) with top view (left) and side view (right). Pd, Ti, C, O atoms are dark green, light-grey, grey, and red spheres, respectively.

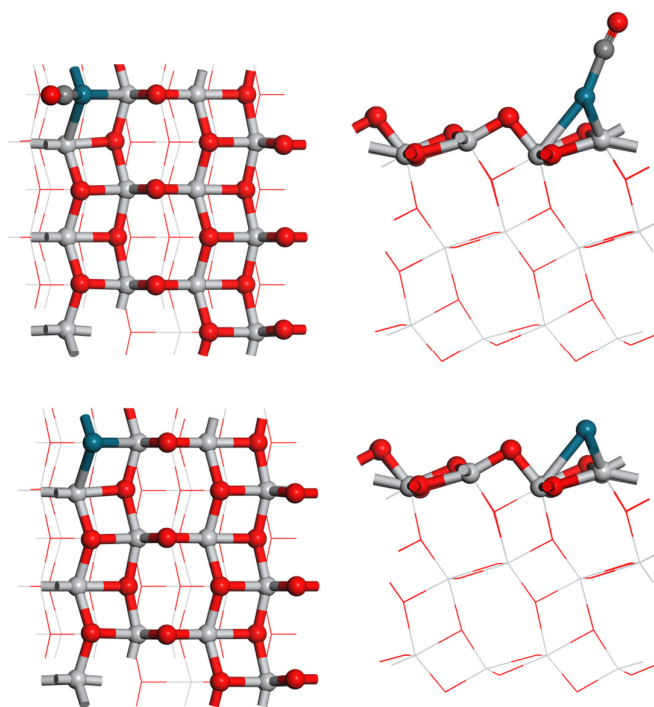


Figure A. 31. CO adsorbed (top) on Pd(O_{3c}-vacancy) model and Pd(O_{3c}-vacancy) model (bottom) with top view (left) and side view (right). Pd, Ti, C, O atoms are dark green, light-grey, grey, and red spheres, respectively.

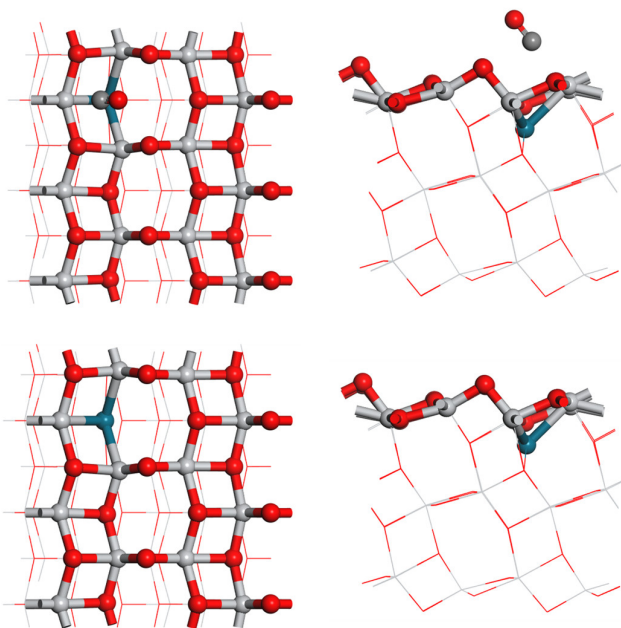


Figure A. 32. CO adsorbed (top) on Pd(O_{3c}*-vacancy) model and Pd(O_{3c}*-vacancy) model (bottom) with top view (left) and side view (right). Pd, Ti, C, O atoms are dark green, light-grey, grey, and red spheres, respectively.

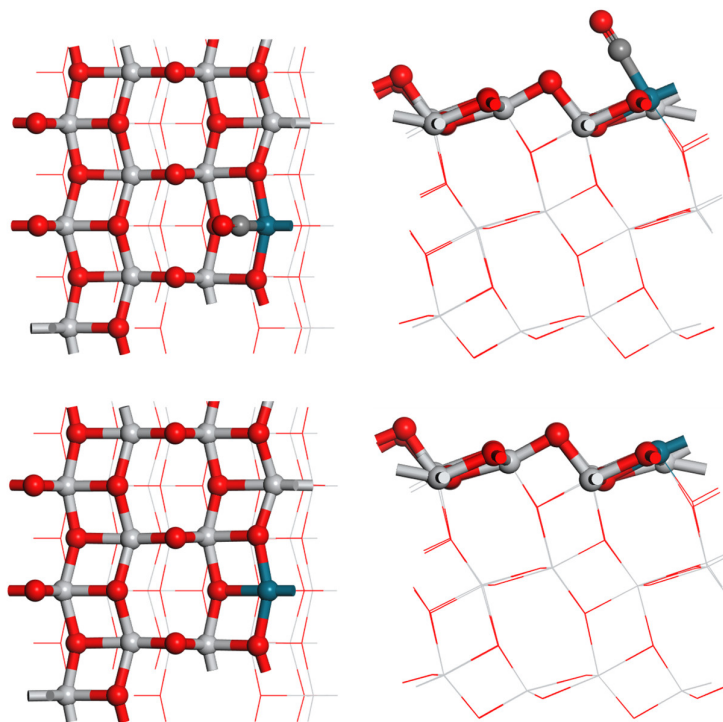


Figure A. 33. CO adsorbed (top) on Pd(Ti_{5c}-vacancy) model and Pd(Ti_{5c}-vacancy) model (bottom) with top view (left) and side view (right). Pd, Ti, C, O atoms are dark green, light-grey, grey, and red spheres, respectively.

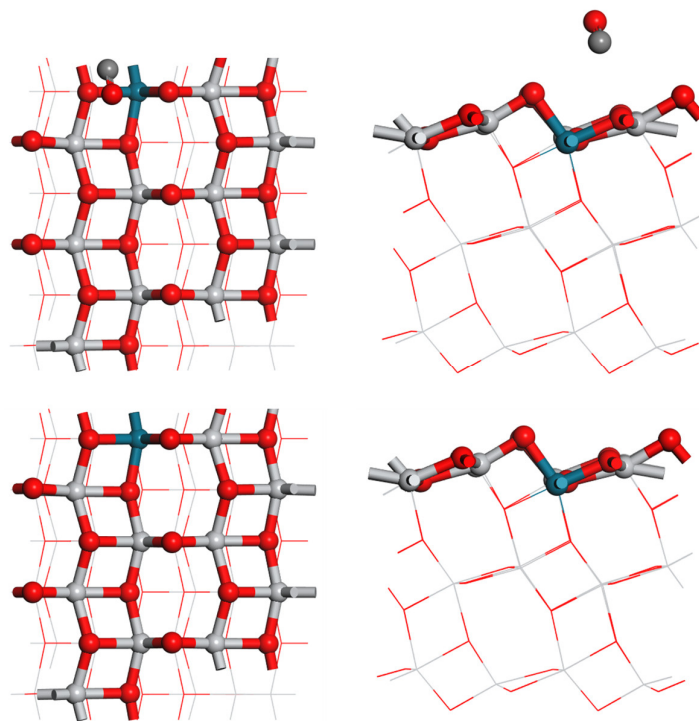


Figure A. 34. CO adsorbed (top) on Pd(Ti_{6c}-vacancy) model and Pd(Ti_{6c}-vacancy) model (bottom) with top view (left) and side view (right). Pd, Ti, C, O atoms are dark green, light-grey, grey, and red spheres, respectively.

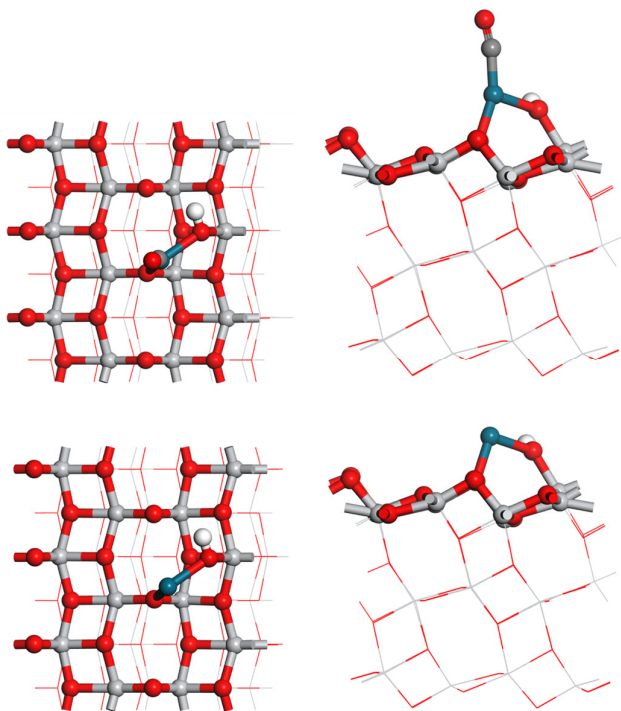


Figure A. 35. CO adsorbed (top) on PdOH model and PdOH model (bottom) with top view (left) and side view (right). Pd, Ti, C, O, H atoms are dark green, light-grey, grey, red, and white spheres, respectively.

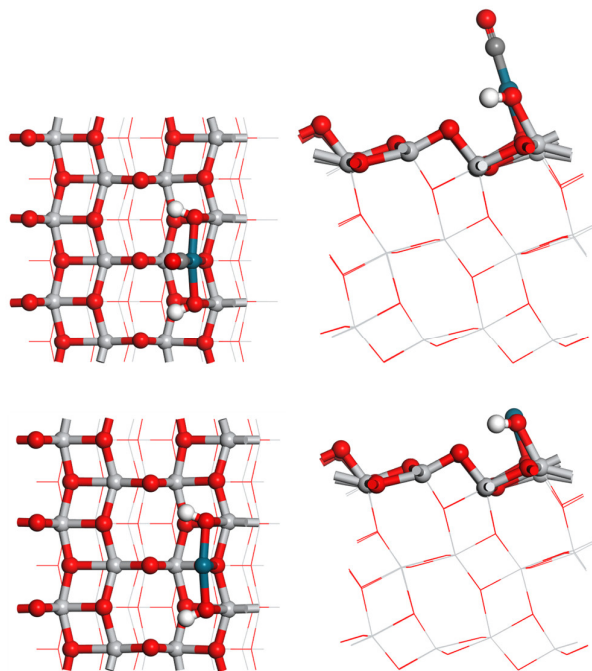


Figure A. 36. CO adsorbed (top) on Pd(OH)₂ model and Pd(OH)₂ model (bottom) with top view (left) and side view (right). Pd, Ti, C, O, H atoms are dark green, light-grey, grey, red, and white spheres, respectively.

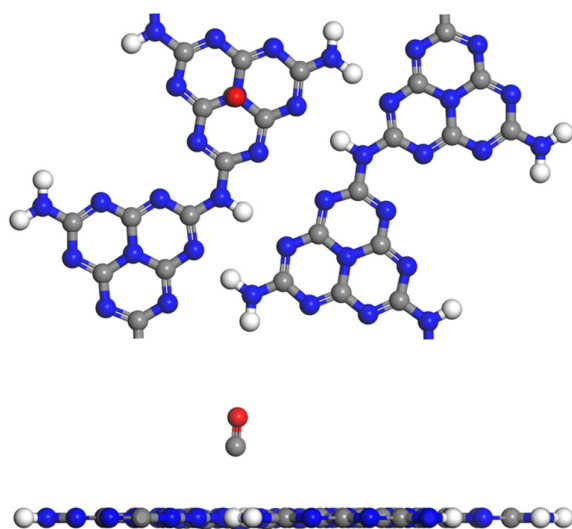


Figure A. 37. CO adsorbed on PCN-position 1 with top view (top) and side view (bottom). C, N, O, H atoms are grey, blue, red and white spheres, respectively.

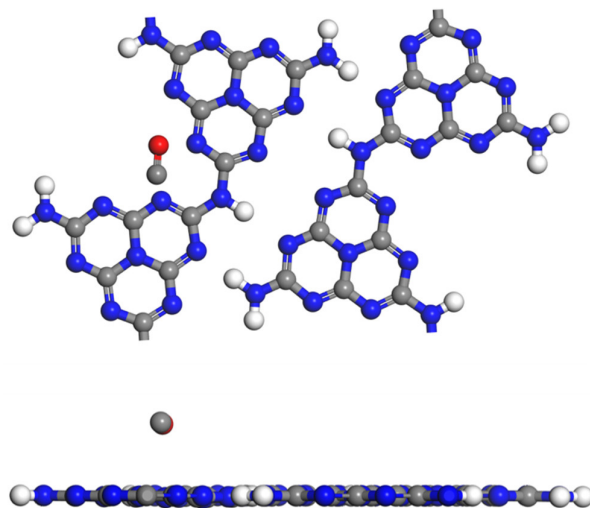


Figure A. 38. CO adsorbed on PCN-position 2 with top view (top) and side view (bottom). C, N, O, H atoms are grey, blue, red and white spheres, respectively.

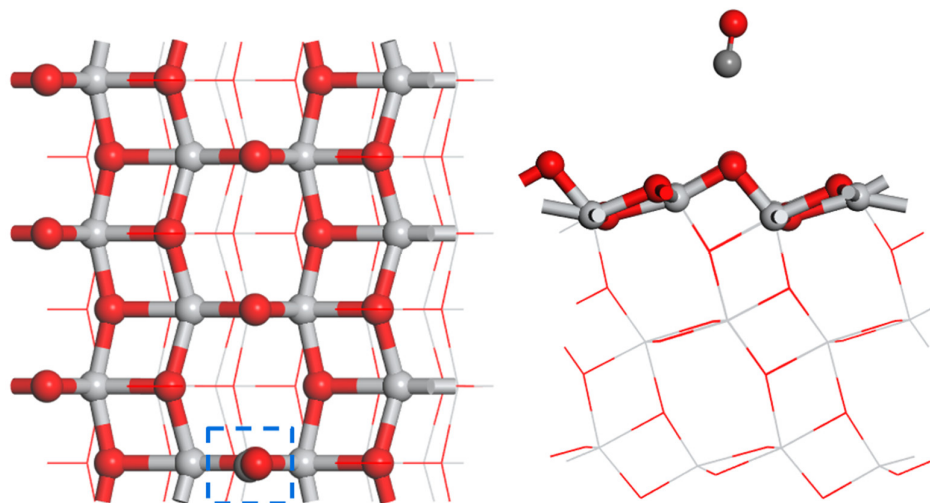


Figure A. 39. CO adsorbed (top) on TiO₂ (101)-position 1 with top view (left) and side view (right). Ti, C, O, H atoms are light-grey, grey, red, and white spheres, respectively.

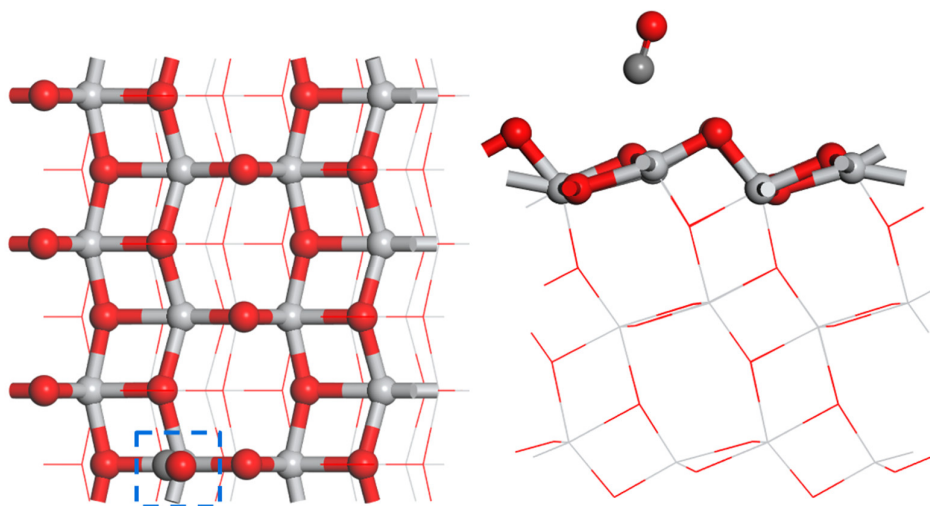


Figure A. 40. CO adsorbed on TiO₂ (101)-position 2 with top view (left) and side view (right). Ti, C, O, H atoms are light-grey, grey, red, and white spheres, respectively.

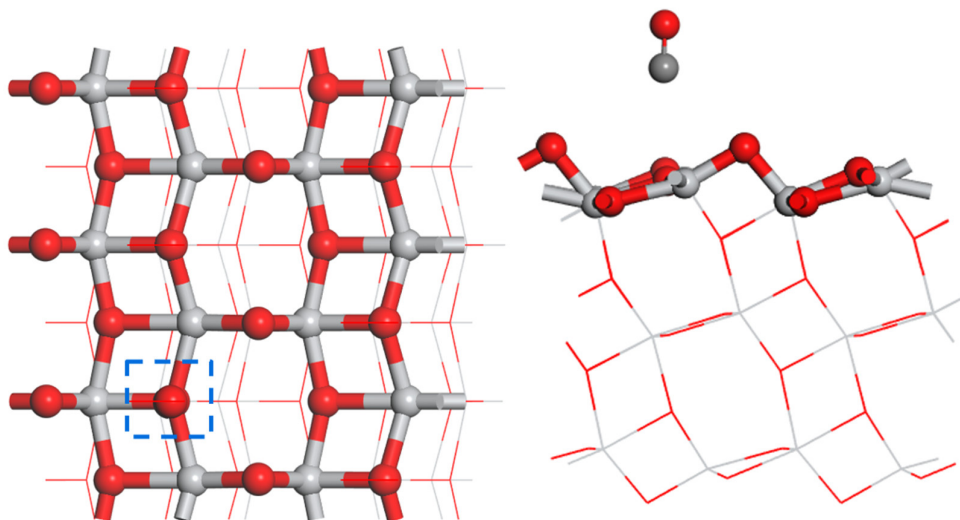


Figure A. 41. CO adsorbed on TiO_2 (101)-position 3 with top view (left) and side view (right). Ti, C, O, H atoms are light-grey, grey, red, and white spheres, respectively.

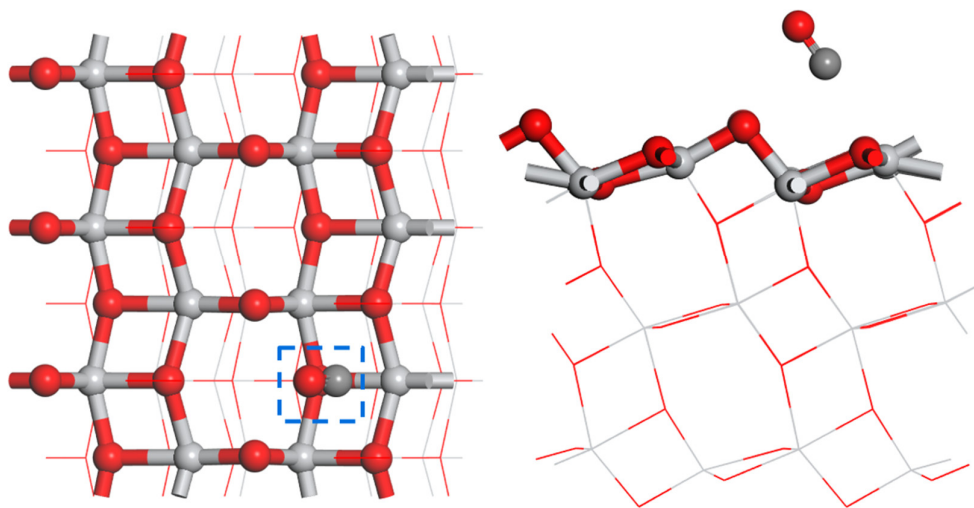


Figure A. 42. CO adsorbed on TiO_2 (101)-position 4 with top view (left) and side view (right). Ti, C, O, H atoms are light-grey, grey, red, and white spheres, respectively.

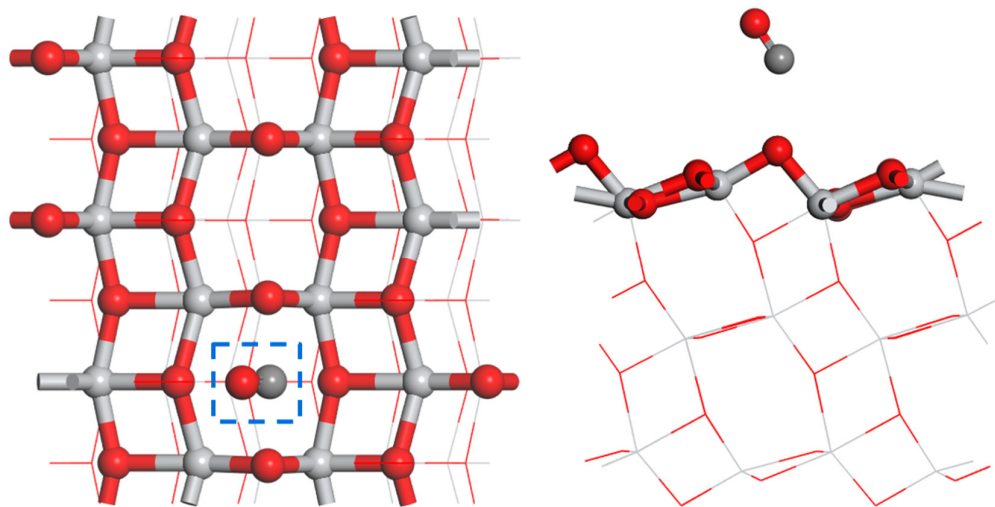


Figure A. 43. CO adsorbed on TiO₂ (101)-position 5 with top view (left) and side view (right). Ti, C, O, H atoms are light-grey, grey, red, and white spheres, respectively.

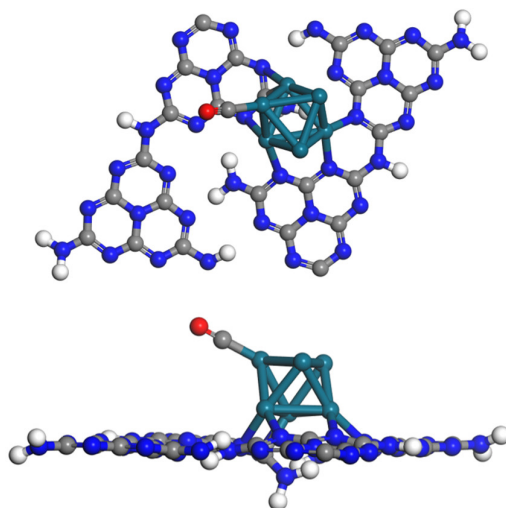


Figure A. 44. CO bonded to one Pd atom of Pd_{cluster}/PCN with top view (top) and side view (bottom). Pd, C, N, O, H atoms are dark green, grey, blue, red and white spheres, respectively.

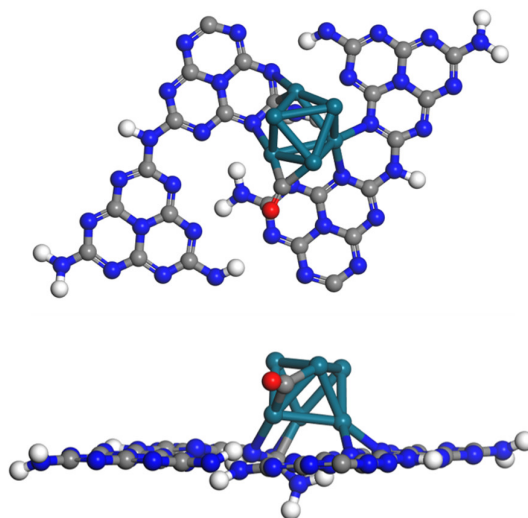


Figure A. 45. CO bonded to two Pd atom of Pd_{cluster}/PCN with top view (top) and side view (bottom). Pd, C, N, O, H atoms are dark green, grey, blue, red and white spheres, respectively.

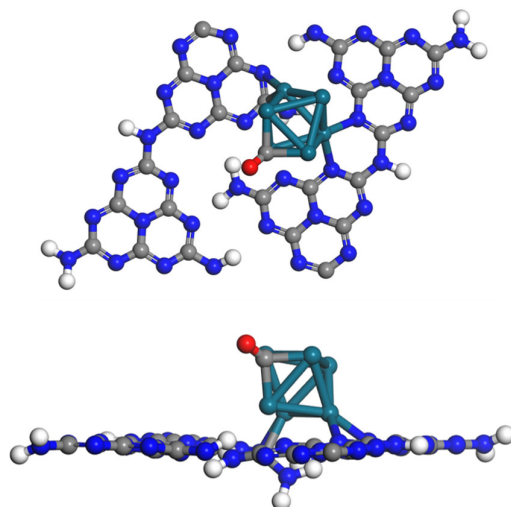


Figure A. 46. CO bonded to three Pd atom of Pd_{cluster}/PCN with top view (top) and side view (bottom). Pd, C, N, O, H atoms are dark green, grey, blue, red and white spheres, respectively.

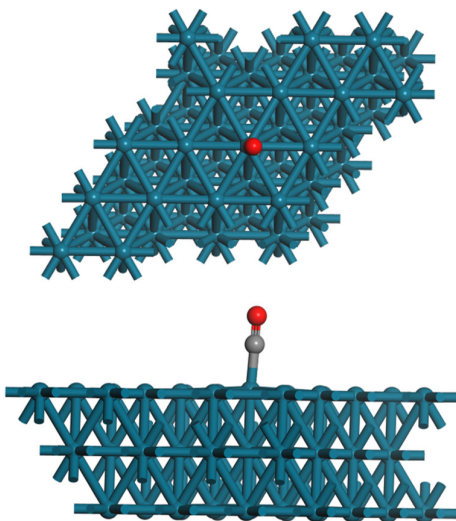


Figure A. 47. CO bonded to one Pd atom of bulk Pd (111) with top view (top) and side view (bottom). Pd, C, O atoms are dark green, grey, and red spheres, respectively.

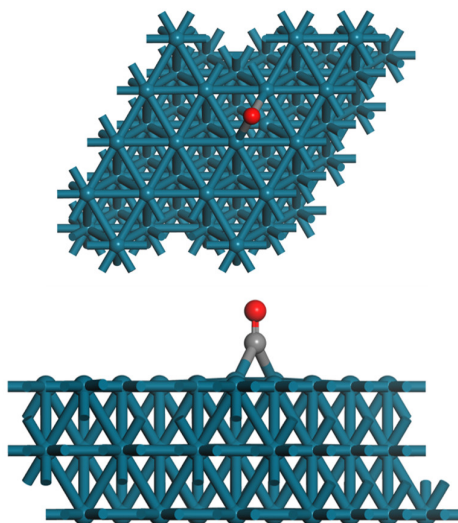


Figure A. 48. CO bonded to two Pd atom of bulk Pd (111) with top view (top) and side view (bottom). Pd, C, O atoms are dark green, grey, and red spheres, respectively.

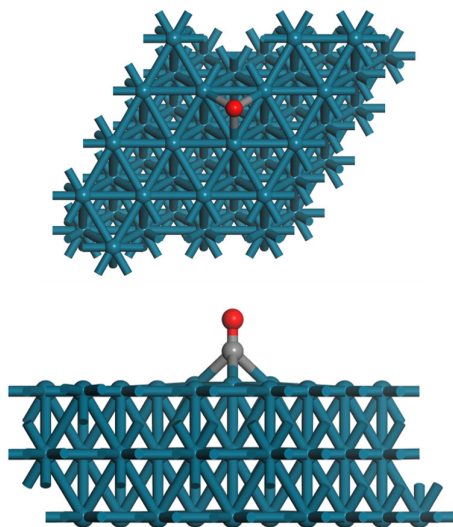


Figure A. 49. CO bonded to three Pd atom of bulk Pd (111) with top view (top) and side view (bottom). Pd, C, O atoms are dark green, grey, and red spheres, respectively.

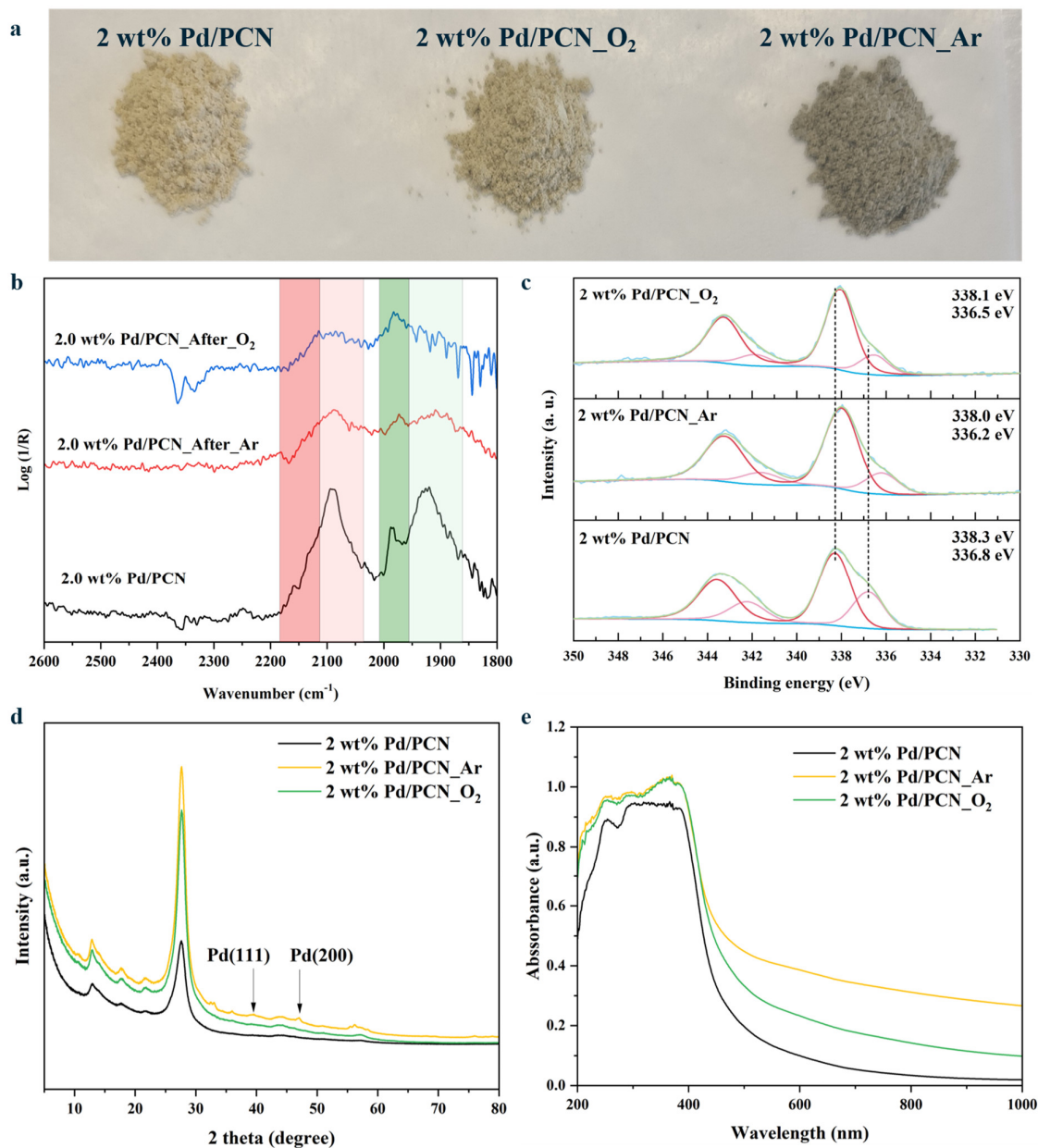


Figure A. 50. (a) Sample photographs (b) CO-DRIFTS spectra, (c) Pd 3d photoemission spectra, (d) XRD pattern, and (e) UV-Vis DRS spectra for 2 wt% Pd/PCN_Ar and 2 wt% Pd/PCN_O₂.

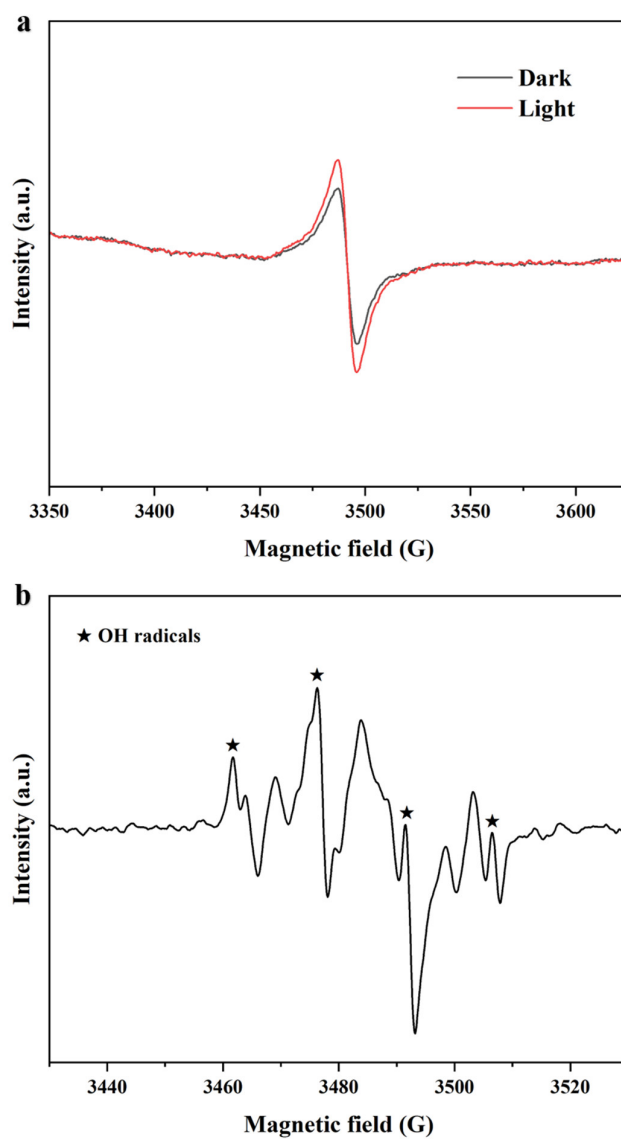


Figure A. 51.(a) EPR spectra of t-CN-3 before and after visible-light irradiation and (b) Selected DMPO spin trapping EPR spectra of t-CN-3 suspension under successive treatment of O₂ during the visible-light irradiation.

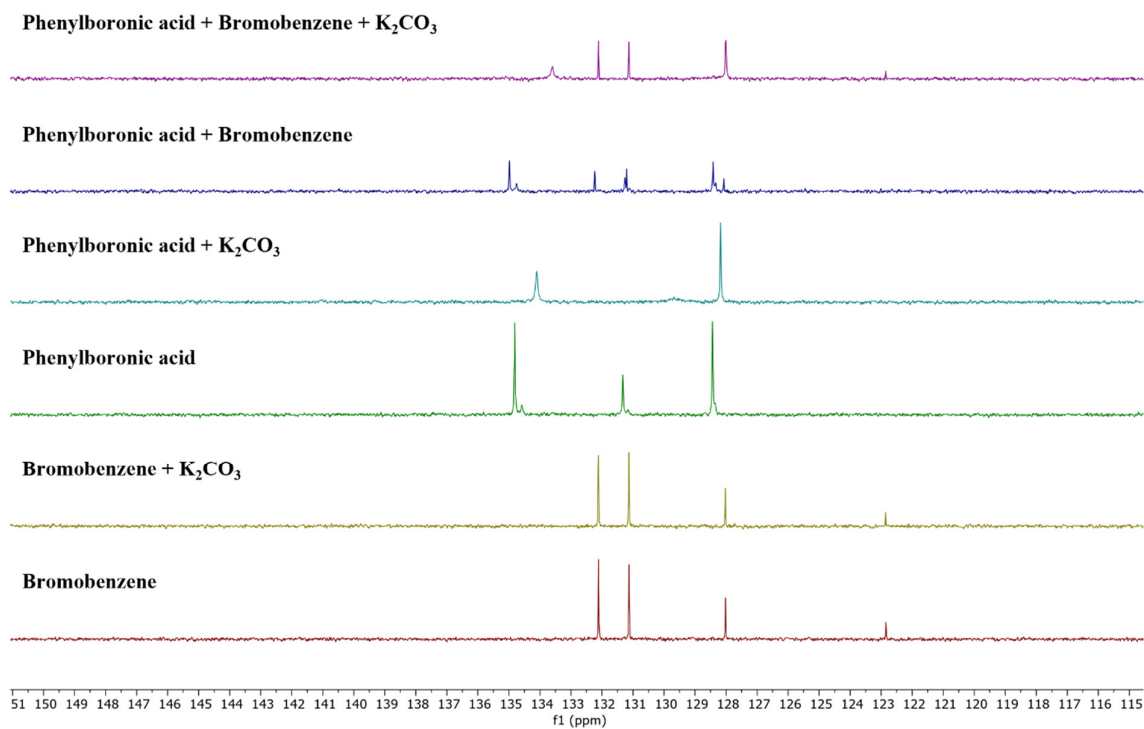


Figure A. 52. ^{13}C NMR spectra of substrates, referenced to Ethanol- d_1 (58.05 ppm).

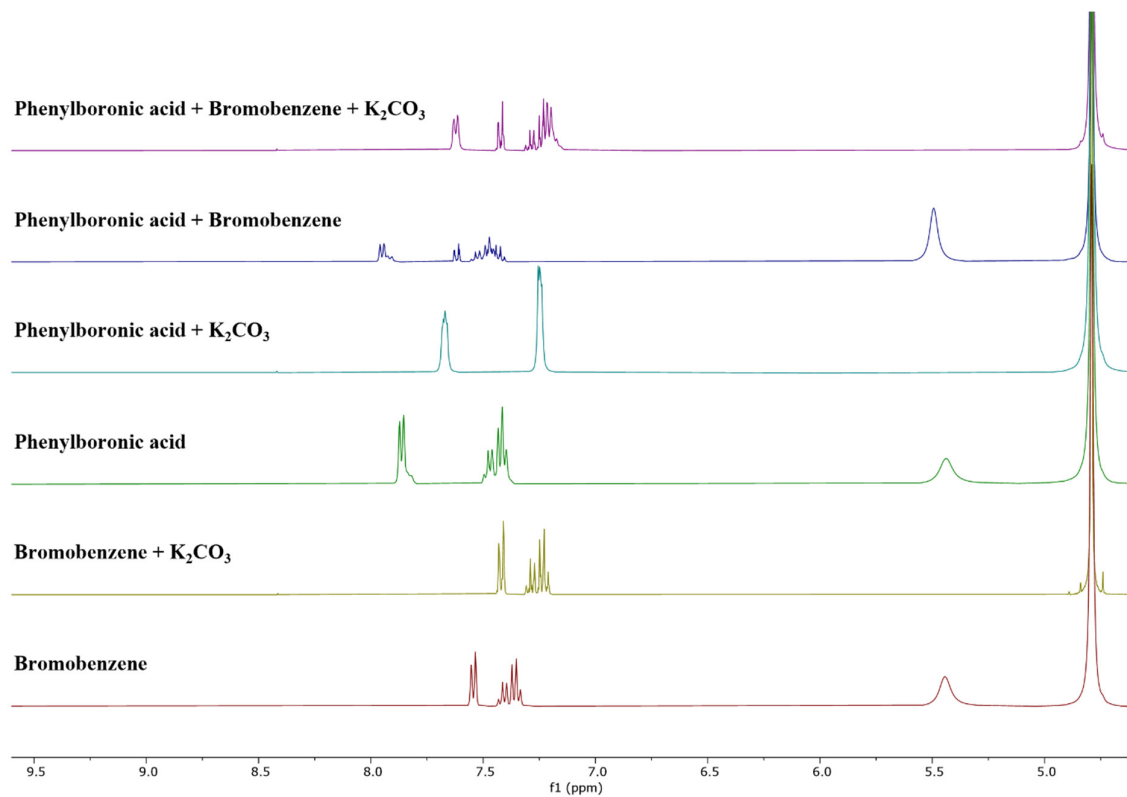


Figure A. 53. ^1H NMR spectra of substrates, referenced to D_2O (4.79 ppm).

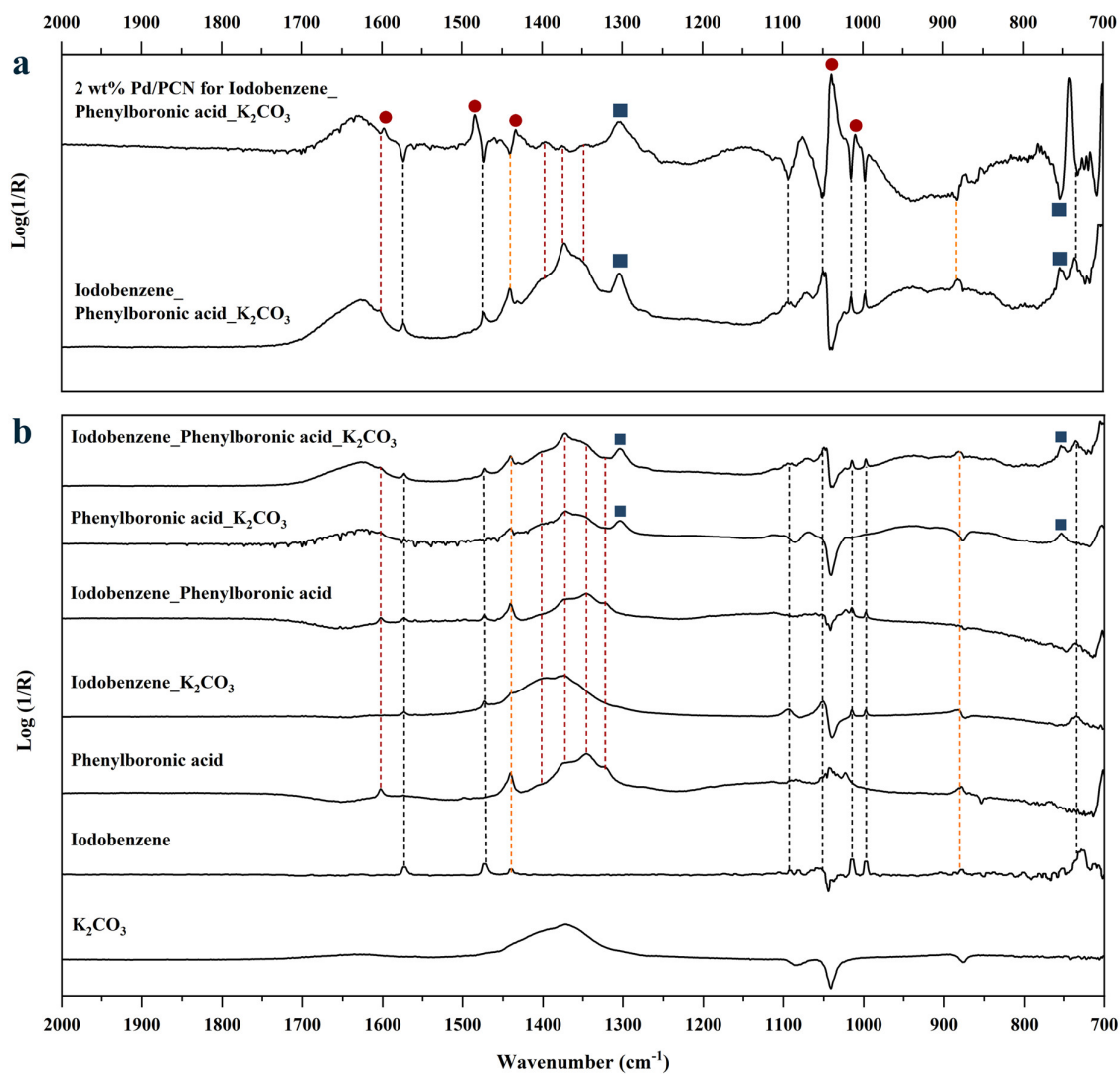


Figure A. 54. (a) *In situ* ATR-IR spectra of 2 wt% Pd/PCN for the coupling reaction of iodobenzene and phenylboronic acid. (b) *In situ* ATR-IR spectra of the substrate calibration (Iodobenzene, Phenylboronic acid, and K₂CO₃). The bands related to the functional groups from bromobenzene and phenylboronic acid are marked with black and red dashed lines, respectively. The yellow dashed lines mark the IR bands present in both substrates. New bands derived from boron-related group are marked with dark blue square, and new bands related to biphenyl is marked with dark red spheres.

Table A. 1. XPS high-resolution C1s data of differently exfoliated g-C₃N₄

Sample	Pt*		N-C=O		N-C=N		N(C) ₃		C-C	
	Binding energy	Area %	Binding energy	Area %	Binding energy	Area %	Binding energy	Area %	Binding energy	Area %
PCN	294.0 eV	5.3 %	289.3 eV	4.2 %	288.3 eV	87.5 %	286.4 eV	0.7 %	284.8 eV	2.4 %
t-CN-3	294.1 eV	2.7 %	289.3 eV	13.6 %	288.4 eV	73.2 %	286.2 eV	0.8 %	284.8 eV	1.0 %
t-CN-6	293.9 eV	9.9 %	289.3 eV	5.7 %	288.2 eV	80.3 %	286.2 eV	1.1 %	284.8 eV	3.1 %
e-CN-8	294.2 eV	3.2 %	289.3 eV	13.3 %	288.4 eV	70.8 %	286.3 eV	4.6 %	284.8 eV	8.1 %
e-CN-16	294.1 eV	5.7 %	289.3 eV	4.8 %	288.3 eV	79.0 %	286.2 eV	2.7 %	284.8 eV	7.8 %
u-CN-8	294.1 eV	5.3 %	289.3 eV	7.0 %	288.3 eV	84.4 %	286.4 eV	1.7 %	284.8 eV	1.5 %
u-CN-16	293.7 eV	7.4 %	289.3 eV	1.8 %	288.2 eV	87.1 %	286.2 eV	0.7 %	284.8 eV	3.1 %
h-CN-12	-	-	289.9 eV	36.0 %	288.7 eV	49.4 %	-	-	284.8 eV	14.6 %
h-CN-S12	-	-	289.0 eV	21.1 %	287.8 eV	43.9 %	286.2 eV	6.2 %	284.8 eV	28.8 %
h-CN-24	-	-	289.6 eV	40.7 %	288.4 eV	49.4 %	286.2 eV	0.9 %	284.8 eV	8.9 %
h-CN-S24	-	-	289.1 eV	29.4 %	287.8 eV	48.3 %	286.2 eV	3.7 %	284.8 eV	18.6 %

Table A. 2. XPS high-resolution N1s data of differently exfoliated g-C₃N₄

Sample	H-excitation		C-N-H		N-(C) ₃		C-N=C	
	Binding energy	Area %	Binding energy	Area %	Binding energy	Area %	Binding energy	Area %
PCN	404.6 eV	7.0 %	401.2 eV	10.4 %	400.1 eV	13.0 %	398.8 eV	69.6 %
t-CN-3	403.7 eV	14.1 %	401.4 eV	14.1 %	400.2 eV	16.3 %	398.9 eV	55.5 %
t-CN-6	404.4 eV	6.5 %	401.0 eV	10.2 %	399.9 eV	13.6 %	398.6 eV	69.7 %
c-CN-8	404.9 eV	5.3 %	401.2 eV	10.9 %	400.0 eV	18.9 %	398.9 eV	64.9 %
c-CN-16	404.7 eV	6.8 %	401.2 eV	10.9 %	400.0 eV	16.8 %	398.8 eV	65.6 %
u-CN-8	404.5 eV	7.8 %	401.1 eV	10.9 %	400.0 eV	15.1 %	398.7 eV	66.2 %
u-CN-16	404.3 eV	8.4 %	401.1 eV	11.0 %	399.9 eV	13.0 %	398.7 eV	67.6 %
h-CN-12	407.3 eV	2.2 %	401.6 eV	0.4 %	400.6 eV	39.4 %	399.4 eV	57.9 %
h-CN-S12	406.4 eV	4.3 %	400.8 eV	1.4 %	399.8 eV	41.6 %	398.6 eV	52.7 %
h-CN-24	406.8 eV	5.6 %	401.1 eV	3.1 %	400.1 eV	43.2 %	398.9 eV	48.2 %
h-CN-S24	406.8 eV	7.4 %	400.8 eV	2.9 %	398.8 eV	44.6 %	398.6 eV	45.1 %

Table A. 3. ICP and XPS data of Pd/PCN samples with different loading.

	Sample	Pd (wt%) from ICP	Pd (at.%) from XPS
Nitride support	1 wt% Pd/PCN	1.05	0.49
	1 wt% Pd/hBN	0.73	0.29
	1 wt% Pd/Si ₃ N ₄	1.06	0.20
	1 wt% Pd/TiN	1.08	0.55
Oxide support	1 wt% Pd/TiO ₂	1.11	0.93
	1 wt% Pd/Al ₂ O ₃	1.00	0.37
	1wt% Pd/ZnO	1.07	0.98
	1wt% Pd/SiO ₂	1.10	0.27
	1wt% Pd/B ₂ O ₃	0.67	2.05

Table A. 4. Comparison of atomic ratio of F to Pd over different Pd samples.

	Sample	Atomic ratio of F to Pd (Elemental analysis)	Atomic ratio of F to Pd (XPS)
Pd precursor	Pd(TFA) ₂	6 (theoretical value)	6 (theoretical value)
Nitride support	1 wt% Pd/PCN	1.6	2
	1 wt% Pd/hBN	0.3	2.6
	1 wt% Pd/Si ₃ N ₄	0	0
	1 wt% Pd/TiN	2.8	6.9
Oxide support	1 wt% Pd/TiO ₂	3.7	5.4
	1 wt% Pd/Al ₂ O ₃	11.2	16.5
	1wt% Pd/ZnO	3.2	4.6
	1wt% Pd/SiO ₂	3.6	1.9
	1wt% Pd/B ₂ O ₃	7.3	1.3

Table A. 5. ICP and XPS data of Pd/PCN samples with different loading.

Sample	Pd (wt%) from ICP		Pd (at.%) from XPS	
	Unwashed	Washed	Unwashed	Washed
0.5 wt% Pd/PCN	0.52	0.52	0.31	0.31
1.0 wt% Pd/PCN	1.05	1.05	0.49	0.49
2.0 wt% Pd/PCN	2.04	2.02	1.06	1.10
4.0 wt% Pd/PCN	3.34	2.83	1.67	1.50
8.0 wt% Pd/PCN	5.01	3.47	2.24	1.78
16.0 wt% Pd/PCN	10.11	5.46	2.94	2.06

Table A. 6. Comparison of atomic ratio of F to Pd over Pd/PCN samples.

Sample	Atomic ratio of F to Pd (Elemental analysis)		Atomic ratio of F to Pd (XPS)	
	Unwashed	Washed	Unwashed	Washed
0.5 wt% Pd/PCN	1.2	0.4	2	1.4
1.0 wt% Pd/PCN	1.6	0.7	2	1.6
2.0 wt% Pd/PCN	1.6	0.7	2	0
4.0 wt% Pd/PCN	1.4	0.4	1.6	0.7
8.0 wt% Pd/PCN	1.7	0.6	1.8	0.9
16.0 wt% Pd/PCN	1.4	0.3	2.2	0.7

Table A. 7. CO adsorption energy (E_{ads} , eV), C–Pd distance (R_{PdC} , Å), C–O bond length (R_{CO} , Å), and CO stretching frequency (ω_e , cm^{-1}) for CO adsorption on support PCN and TiO_2 (101) terrace sites. The corresponding structure is shown in Figure A.37 – A.43.

Model	E_{ads} (kJ mol ⁻¹)	R_{PdC} (Å)	R_{CO} (Å)	ω_e (cm ⁻¹)
PCN-CO position-1	9	2.80 to plane	1.126	2149
PCN-CO position-2	13	2.80 to plane	1.126	2121
TiO ₂ -CO position-1	12	2.933 to nearest atom	1.141	2143
TiO ₂ -CO position-2	45	2.522 to nearest atom	1.138	2168
TiO ₂ -CO position-3	19	3.000 to nearest atom	1.142	2137
TiO ₂ -CO position-4	49	2.809 to nearest atom	1.138	2165
TiO ₂ -CO position-5	18	3.116 to nearest atom	1.145	2109

Table A. 8. Comparison of Bader charge and CO stretching frequencies of Pd/PCN and Pd/TiO₂ with different Pd oxidation state (+4, +2, +1, and 0). Bader charge of Pd ($Q|e|$), experimental CO stretching frequency (ω).

Formal Pd oxidation state	Pd/PCN		Pd/TiO ₂	
	$Q e $	ω (cm ⁻¹)	$Q e $	ω (cm ⁻¹)
+4	1.00	2129	1.47	2167
+3	0.79	2099	1.19	2136
+2	0.55	2064	0.85	2098
+1	0.28	2025	0.45	2053
0	-0.01	1981	-0.01	2001

Table A. 9. CO adsorption energy (E_{ads} , eV), C–Pd distance (R_{PdC} , Å), C–O bond length (R_{CO} , Å), and CO stretching frequency (ω_{e} , cm^{-1}) for CO adsorption on Pd nanoparticle (0.5 nm) on PCN model and bulk Pd (111). The corresponding structure is shown in Figure A.44 – A.49.

Model	E_{ads} (kJ mol ⁻¹)	R_{PdC} (Å)	R_{CO} (Å)	ω_{e} (cm ⁻¹)
Pd _{cluster} on PCN-CO (Pd)	182	1.863	1.157	1990
Pd _{cluster} on PCN-CO (2Pd)	225	1.922, 1.954	1.190	1801
Pd _{cluster} on PCN-CO (3Pd)	252	1.983, 1.985, 1.990	1.208	1654
Bulk Pd(111)-CO (Pd)	175	1.853	1.141	2049
Bulk Pd(111)-CO (2Pd)	219	1.998, 1.999	1.165	1858
Bulk Pd(111)-CO (3Pd)	232	2.090, 2.100, 2.103	1.164	1856

Table A. 10. High performance liquid chromatography (HPLC) data of 2 wt% Pd/PCN for continuous flow reaction in Ar and O₂ atmosphere after 2h.

Reaction Atmosphere	Substrate	HPLC signal	Reaction time		Conversion	Comment
			0 hour	2 hour		
Ar	Phenylboronic acid	1.836	4.28E+04	3.35E+04	22%	Cross-coupling of bromobenzene and phenylboronic acid
	Toluene	7.581	5.05E+04	4.95E+04	-	
	Bromobenzene	8.778	5.05E+04	2.42E+04	52%	
	Biphenyl	20.054	4.42	1.12E+04	-	
O ₂	Phenylboronic acid	1.836	4.32E+04	2.71E+04	37%	Self-coupling of bromobenzene and phenylboronic acid
	Toluene	7.581	4.85E+04	4.92E+04	-	
	Bromobenzene	8.778	4.85E+04	4.92E+04	0%	
	Biphenyl	20.054	0	1.22E+04	-	

Table A. 11. XPS and ICP data of spent catalysts.

Sample	Metal content from XPS		Metal content from ICP	
	Pd (at.%)	K (at.%)	Pd (wt%)	K (wt%)
2 wt% Pd/PCN_Ar	0.59	1.81	1.97	1.76
2 wt% Pd/PCN_O ₂	0.62	1.78	1.98	2.4

List of Writing/Experiments/Calculations to Highlight Own Work and Contributions by Other Researchers

Part	Type	Specific	Wrote/Calculated/Measured by	Discussion
1	Thesis writing	Whole thesis	Junhao Huang	Junhao Huang, Jennifer Strunk, Marcus Klahn
2	DFT calculation	All calculations	Junhao Huang	Junhao Huang, Andrew Logsdail, Haijun Jiao, Xinxin Tian
3	Materials synthesis	All catalysts	Junhao Huang	Junhao Huang, Jennifer Strunk, Marcus Klahn
4	Performance test	All tests	Junhao Huang	Junhao Huang, Jennifer Strunk, Marcus Klahn, Norbert Steinfeldt, Michael Sebek
5	Materials characterization	ATR	Junhao Huang	Junhao Huang, Jennifer Strunk, Marcus Klahn
		DRIFTS	Junhao Huang	Junhao Huang, Jennifer Strunk, Marcus Klahn
		Electrochemical measurements	Junhao Huang	Junhao Huang, Shuoping Ding, Jennifer Strunk, Marcus Klahn
		PL	Junhao Huang	Junhao Huang, Jennifer Strunk, Marcus Klahn
		TPDE	Junhao Huang	Junhao Huang, Jennifer Strunk, Marcus Klahn
		UV-Vis DRS	Junhao Huang	Junhao Huang, Jennifer Strunk, Marcus Klahn
		EPR	Xinchao Dai, Jabor Rabeah	Junhao Huang, Xingchao Dai, Jabor Rabeah

		Elemental analysis	Astrid Lehmann	Junhao Huang, Astrid Lehmann
		Electron microscope	Tim Peppel, Armin Springer, Nils Rockstroh, Kevin Oldenburg, Song Hong, Zhenyu Sun	Junhao Huang, Tim Peppel, Armin Springer, Nils Rockstroh, Kevin Oldenburg, Song Hong, Zhenyu Sun
		ICP-OES	Anja Simmula	Junhao Huang, Anja Simmula
		NMR	Susann Buchholz	Junhao Huang, Susann Buchholz
		N ₂ adsorption-desorption isotherms	Reinhard Eckelt	Junhao Huang, Reinhard Eckelt
		Solid-State NMR	Victoria Aladin, Björn Corzilius	Junhao Huang, Victoria Aladin, Björn Corzilius, Jennifer Strunk, Marcus Klahn
		TGA-MS	Christine Rautenberg	Junhao Huang, Christine Rautenberg
		XRD	Henrik Lund	Junhao Huang, Henrik Lund, Jennifer Strunk, Marcus Klahn
		XPS	Stephan Bartling	Junhao Huang, Stephan Bartling, Jennifer Strunk, Marcus Klahn
		XAS	Jan-Dierk Grunwaldt, Anna Zimina, Martin Radtke	Junhao Huang, Jan-Dierk Grunwaldt, Anna Zimina, Dmitry Doronkin, Martin Radtke, Jennifer Strunk, Marcus Klahn

In summary, I designed, planned and performed the experimental and theoretical work, including the **Material Synthesis**, part of **Materials Characterization**, **Performance Test**, and **DFT Calculation**. I was involved in the discussions about the characterization results obtained from the LIKAT Analytical Services Group and other collaborators. I evaluated all analytical data and **independently wrote this monograph thesis**.

Curriculum Vitae

Personal details

Name Junhao Huang

Date of birth: 27th January, 1994

Place of Birth Qingdao, China

Nationality Chinese



Education

2020-present Ph.D. in Chemistry, Leibniz-Institute for Catalysis, Germany
(Supervisor: Prof. Jennifer Strunk)

2022.10-2022.11 Visiting student in Cardiff University and UK Catalysis Hub, United Kingdom (Supervisor: Dr. Andrew Logsdail)

2017-2019 M.Sc. in Chemistry, China Agricultural University, China
(Supervisor: Prof. Xia Liu)

2012-2016 B.Sc. in Food Science and Engineering, Qilu University of Technology, China

Scientific Contributions

List of publications

1. **Junhao Huang**, Pengcheng Meng, Xia Liu, “Porous nanostructure and enhanced charge transfer in graphitic carbon nitride fabricated by polyoxometalate oxidation etching” *Journal of Alloys and Compounds*, 2019, 805: 654-662.
2. Pengcheng Meng, **Junhao Huang**, Xia Liu, “Extended Light Absorption and Enhanced Visible-Light Photocatalytic Degradation Capacity of Phosphotungstate/Polyimide Photocatalyst Based on Intense Interfacial Interaction and Alternate Stacking Structure” *Applied Surface Science*, 2019, 465: 125-135.
3. Pengcheng Meng, Huimin Heng, Yanhong Sun, **Junhao Huang**, Jinpeng Yang, Xia Liu, “Positive effects of phosphotungstic acid on the in-situ solid-state polymerization and visible light photocatalytic activity of polyimide-based photocatalyst” *Applied Catalysis B: Environmental*. 2018, 226: 487-498.

Oral presentations

1. **Junhao Huang**, Pawel Naliwajko, Haijun Jiao, Marcus Klahn, Jennifer Strunk, “Atomically dispersed Pd on few-layer polymeric carbon nitride for Suzuki coupling”, EUROMAT 2021 (European Congress And Exhibition On Advanced Materials And Processes), Graz, Austria, 13 – 17 September 2021.
2. **Junhao Huang**, Pawel Naliwajko, Marcus Klahn, Jennifer Strunk, “Atomically dispersed Pd on few-layer polymeric carbon nitride for (photo)catalytic application”, ICES-LIKAT Workshop on Catalysis and Sustainability, Rostock, Germany, 29 – 30 June 2021.
3. **Junhao Huang**, Pawel Naliwajko, Marcus Klahn, Jennifer Strunk, “Atomically dispersed Pd on few-layer polymeric carbon nitride for (photo)catalytic application”, LIKAT workshop: Structure-Reactivity Relationships in Single-Site Catalysis for Sustainable Chemistry, Rostock, Germany, 23 March 2021.

Poster presentations

1. **Junhao Huang**, Marcus Klahn, Xinxin Tian, Pawel Naliwajko, Andrew J. Logsdail, Haijun Jiao and Jennifer Strunk, “Atomically dispersed Pd on few-layer polymeric carbon nitride for (photo)catalytic Suzuki coupling”, 23rd International Conference on Photochemical Conversion and Storage of Solar Energy (IPS-23), Lausanne, Switzerland, 2 – 5 August 2022
2. **Junhao Huang**, Marcus Klahn, Xinxin Tian, Pawel Naliwajko, Andrew J. Logsdail, Haijun Jiao and Jennifer Strunk, “Atomically dispersed Pd on few-layer polymeric carbon nitride for Suzuki coupling”, 55th German Catalysis Meeting, Weimar, Germany, 27 – 29 June 2022